Synthesis and Modifications of Biocompatible Materials Having Potential Therapeutic Properties Against Pathogenic Infections and Carcinogenic Cells

Thesis submitted to

Jadavpur University

By

Debbethi Bera

In partial fulfillment of the requirements

For the degree of

Doctor of Philosophy (Ph.D.)

In Science

Department of Physics

Jadavpur University

Kolkata – 700032

2023

CERTIFICATE FROM THE SUPERVISOR(S)

This is to certify that the thesis entitled **"Synthesis and modifications of biocompatible materials have potential therapeutic property against the pathogenic infection and carcinogenic cells"** Submitted by **Smt. Debbethi Bera** who got her name registered on 18/03/2021 (Index no.: 18/21/Phys./27) for the award of Ph. D. (Science) Degree of Jadavpur University, is absolutely based upon her own work under the supervision of **Prof. (Dr.) Sukhen Das** and **Prof. (Dr.) Papiya Nandy** and that neither this thesis nor any part of it has been submitted for either any degree/diploma or any other academic award anywhere before.

Prof. (Dr.) Sukhen Das
Department of Physics
Jadavpur University
Kolkata- 700032

Prof. Sukhen Das
Department of Physics,
Jadavpur University
Kolkata - 700 032

Prof. (Dr.) Papiya Nandy
Former Professor
Department of Physics
Jadavpur University
Kolkata- 700032

Prof. (Dr.) Papiya S. Nandy
M.Sc. (Cal Univ.), M.A.(Univ. Calif),
Ph.D. (Kent State Univ.)
Centre for Interdisciplinary Research
and Education, Kolkata-700068, India
Formerly, Emeritus Fellow & Professor of Physics,
Jadavpur University, Kol-32, India

Dedicated to

Maa, Mammi, Grand Mother
Babai, Dadabhai, Grand Father

ABSTRACT

Synthesis and modifications of biocompatible materials having potential therapeutic properties against pathogenic infections and carcinogenic cells.

INDEX No: 18/21/PhyS./27

Nanomaterials have emerged as an indispensable option in therapeutic and biomedical applications in recent years. The two major challenges in the medical field, antibiotic resistance and the malignancy of tumors are undergoing exponential escalation globally. Our study involves the development of nano-sized materials having dual therapeutic properties. Fabrication of these nanoparticles involves polymer or fluorescence materials, along with unconventional drug integration. In the pursuit of methods that are cost-effective and environmentally conscious, naturally abundant polymers and natural extracts have been harnessed for the synthesis of these nanoparticles. The green synthesis method has been pursued to generate nano-sized materials, which are considered for developing an efficient therapeutic system specific to the targeted cell with less toxicity.

Here we reported some nanoscale materials like Hydroxyapatite, Zinc Oxide, Silver, herbo-metallic medicine, and Zinc Sulfide, that are biocompatible with human normal cell lines and have potential activities against pathogenic bacterial strains and cancer cells. We have used synthetic vehicles like hydroxyapatite and natural polymers like gum acacia for capping the biomimetic nanoparticles to enhance their biocompatibility and feasibility. In addition, we used antibiotics and different therapeutics to target the specific cell and used fluorescence material for bioimaging.

Along with synthesis we have also observed and analyzed the physical characterizations of the materials and done different in vitro biological characterizations. These functionalized nanomaterials are thoroughly characterized by employing Field Emission Scanning Electron Microscopy (FESEM), Transmission Electron Microscopy (TEM), Powder X-Ray Diffraction (XRD), Thermogravimetric analysis (TGA), Fourier-Transform Infrared Spectroscopy (FTIR), Ultraviolet-Visible Spectroscopy (UV-Vis) and Dynamic light scattering (DLS) techniques etc.

To establish the efficacy of these functionalized antibacterial agents we have performed methods like minimum inhibitory concentration (MIC), minimum bactericidal concentration (MBC), agar well diffusion method, evaluation of intracellular reactive oxygen species (ROS) generation, bacterial cell survivability assay, etc. To evaluate the biocompatible properties of our nanomaterials we have performed cytotoxicity assay.

To assess the effectivity of functionalized anticancer nanoparticles we performed methods like MTT assay and estimation of Intracellular ROS generations by DCFDA method. We observed the comparative targeted delivery of the nanomaterials depending on pH.

To understand the mechanism of the therapeutics apoptotic cell quantification was done by Annexin V-FITC staining. The mitochondrial membrane potential was examined with the help of JC1 staining. The intracellular GSH (Glutathione) and NADPH levels were evaluated using sensing luminescence GSH-Glo™. Glutathione Assay kit (Promega) for GSH measurement and Amplite™ Fluorometric NADPH Assay kit (Advancing Assay & Test technologies [AAT] Bioquest, USA) for NADPH was used. Mitochondrial ROS measurement was estimated with the help of MitoSOX™ and nuclear morphology was examined with the help of DAPI staining (these later experiments were performed for Gum acacia capped Zinc oxide nanoparticles and herbo-metallic drug only).

So, our research is focused on the synthesis of therapeutic materials, their modifications, and their effective delivery against pathogenic infections and cancer cells. Our research has a comprehensive and dynamic approach. We followed meticulous synthesis procedures where we encapsulate nanomaterials with natural therapeutics and modified their properties for strategic development for precise targeting. With cutting-edge techniques and a profound commitment to advancing biomedical science, our endeavors stand poised to reshape the landscape of medical interventions, offering new hope in the battle against pathogenic infections and the relentless progression of cancer.

Date - 21.08.23

Prof. Sukhen Das
Department of Physics,
Jadavpur University
Kolkata-700 032

Prof. (Dr.) Papiya S. Nandy
M.Sc. (Cal Univ.), M.A.(Univ. Calif),
Ph.D. (Kent State Univ.)
Centre for Interdisciplinary Research
and Education, Kolkata-700068, India
Formerly, Emeritus Fellow & Professor of Physics,
Jadavpur University, Kol-32, India

Acknowledgment

This PhD journey could not be initiated without Dr. Suman Bhandary, Dr. Souravi Bardhan, and Dr. Shubham Roy. My Day 1 in research life came because of you three. Thank you!

I am also grateful to Mrs. Angelina Naik, Mr. Pradip Naik, and Mrs. Maitreyee Sengupta, whose unwavering and constant encouragement made me secure. I am grateful to Ayan Da and Babu Da for their contribution to this thesis.

I extend my sincere thanks to all my labmates, friends, and my dear juniors who have shared this academic odyssey with me. Your camaraderie, shared experiences, and collaborative spirit have enriched my research and made this journey a memorable one.

To all those who have supported me, both in visible and invisible ways, your contributions have been immeasurable, and I am truly indebted to each one of you. Thank you for being an integral part of this incredible journey.

I am highly grateful to Jadavpur University for giving me the opportunity for completing my thesis work and Swami Vivekananda Non-NET fellowship, Govt. of West Bengal for financial support.

I would like to express my love, respect, and deepest gratitude to 'The Almighty'.

CONTENTS

Abbreviations

Ag	:	Silver
AgNPs	:	Silver nanoparticles
ATCC	:	America Type Culture Collection
BOD	:	Biochemical Oxygen Demand
BSC	:	Biological Safety Cabinets
B. subtilis	:	*Bacillus subtilis*
CFU	:	Colony Forming Unit
DCF	:	Dichlorofluorescein
DCFH2-DA	:	2, 7 -dichlorodihydrofluoresceindiacetate
DLS	:	Dynamic Light Scattering
DTA	:	Differential Thermal Analyzer
E. coli	:	*Escherichia coli*
E. faecalis	:	*Enterococcus faecalis*
EDAX	:	Energy Dispersive X-ray
FA	:	Folic Acid
FES	:	Field Emission Source
FESEM	:	Field Emission Electron Microscope
FIB	:	Focused Ion Beam
FTIR	:	Fourier Transform Infrared spectroscopy
GA	:	Gum Acacia
GA@ZnO NPs	:	Gum Acacia capped Zinc oxide nanoparticles
GA@ZnO@RB	:	Gum Acacia capped Zinc oxide nanoparticles conjugated with Rodamine-B
Gd	:	Gadolinium
HAp	:	Hydroxyapatite

HAP	:	Hydroxyapatite
HAP@VAN@FA NPs	:	Hydroxyapatite encapsulated with Vancomycin conjugated with folic acid nanoparticles
HAP@VAN NPs	:	Hydroxyapatite encapsulated with Vancomycin nanoparticles
HAPNPs	:	Hydroxyapatite nanoparticles
HEPA	:	High-Efficiency Particulate Air
IR	:	Infrared
JCPDS	:	Joint Commission of Powder Diffraction Standards
KeV	:	Kilo electron Volt
KV	:	Kilovolt
LAF	:	Laminar airflow
LD_{50}	:	Lethal Dose 50
LED	:	Light-Emitting Diodes
MBC	:	Minimum Bactericidal Concentration
MDR	:	Multidrug Resistance
MHA	:	Mueller Hinton Agar
MIC	:	Minimum Inhibitory Concentration
MRI	:	Magnetic Resonance Imaging
MRSA	:	*Methicillin-resistant Staphylococcus aureus*
MTCC	:	Microbial Type Culture Collection
MTT	:	3- (4, 5- dimethylthiazol-2-yl)-2, 5-diphenyltetrazolium bromide
NCCS	:	National Center for Cell Science (NCCS)
NP	:	Nanoparticle
NPs	:	Nanoparticles
O. sanctum	:	*Ocimum sanctum*
P. aeruginosa	:	*Pseudomonas aeruginosa*

PXRD	:	Powder X-Ray diffraction
PBS	:	Phosphate-buffered saline
PDI	:	Polydispersity index
PDT	:	Photodynamic Therapy
PL	:	Photoluminescence
ROS	:	Reactive Oxygen Species
S. aureus	:	*Staphylococcus aureus*
SAED	:	Selected Area Electron Diffraction
SEM	:	Scanning Electron Microscope
TEM	:	Transmission Electron Microscopy
TGA	:	Thermogravimetric Analyzer
UV	:	Ultra Violet
VAN	:	Vancomycin
VB	:	Vanga Bhasma
VBNPs	:	Vanga Bhasma nanoparticles
XRD	:	X-Ray diffraction
ZnO	:	Zinc oxide
ZnO NPs	:	Zinc oxide nanoparticles
ZnS	:	Zinc Sulfide Nanoparticles
ZnS@Gd@Ag	:	Gadolinium doped Zinc Sulfide with silver Nanoparticles
ZnS@Gd NPs	:	Gadolinium doped Zinc Sulfide Nanoparticles

List of Publications

1. Gum acacia capped ZnO nanoparticles, a smart biomaterial for cell imaging and therapeutic applications. **Debbethi Bera**, Kunal Pal, Dheeraj Mondal, Parimal Karmakar, Sukhen Das and Papiya Nandy. Advances in Natural Sciences: Nanoscience and Nanotechnology. 2020, 11(3):035015. DOI: 10.1088/2043-6254/aba895.

2. A mechanistic insight into the bioaccesible herbometallic nanodrug as potential dual therapeutic agent. **Debbethi Bera**, Kunal Pal, Bhuban Ruidas, Dheeraj Mondal, Shinjini Pal, Biplab Kumar Paul, Parimal Karmakar, Sukhen Das and Papiya Nandy. Materials Today Communications. 2020, 24:101099. DOI: 10.1016/j.mtcomm.2020.101099.

3. Functionalised biomimetic hydroxyapatite NPs as potential agent against pathogenic multidrug- resistant bacteria. **Debbethi Bera**, Kunal Pal, Souravi Bardhan, Shubham Roy, Rubia Parvin, Parimal Karmakar, Papiya Nandy and Sukhen Das. Advances in Natural Sciences: Nanoscience and Nanotechnology 2019, 10(4):045017. DOI: 10.1088/2043-6254/ab5104.

4. Phytofabrication of silver nano particles using *Ocimum sanctum* leaf extract and their antibacterial and anticancer activity through oxidative damage. **Debbethi Bera**, Kunal Pal, Parimal Karmakar, Sukhen Das and Papiya Nandy. MOL2NET 2020, International Conference on Multidisciplinary Sciences, 6th edition 2020. DOI: 10.3390/mol2net-06-06781.

5. Bimodal Surface Modification Strategies towards Improving the Antibacterial Activity of Graphene Oxide. Finaz Khan, Susmita Prusty, Pritha Saha, **Debbethi Bera**, Bandita Datta, Sherley Saraffin R, Arijit Kapuria, Kajari Dutta, and Susmita Das. Journal of Materials Research (JMRS). 2023

6. The effect of temperature on the activity and stability of the thermostable enzyme caffeine dehydrogenase from *Pichia manshurica* CD1. Rubia Parvin , Khushnood Fatma , **Debbethi Bera** Jyotirmayee Dash, Joydeep Mukherjee, Ratan Gachhui. Biologia. 2023, 1-10. DOI: 10.1007/S11756-023-01473-9

7. Thymoquinone incotporated chitosan-sodium alginate/psyllium husk derived biopolymeric composite films: A comparative antibacterial and anticancer profile. Sanghita Das, **Debbethi Bera**, Debojyoti De, Dheeraj Mondal, Parimal Karmakar,

Sukhen Das, Anindita Dey. European Polymer Journal 2022, 180:111608. DOI: 10/1016/j.eurpolymj.2022.111608.

8. Design, development and mechanistic insights into the enhanced antibacterial activity of mono and bis-phosphonium fluoresceinate ionic liquids. Susmita Das, Anindita Paul, **Debbethi Bera**, Abira Dey, Ahitagni Roy, Avisek Dutta, Debabani Ganguly. Material Today Communications 2021, 28:102672. DOI: 10/1016/j.mtcomm.2021.102672.

9. Enhanced antibacterial activity of a novel biocompatible triarylmethane based ionic liquid-graphene oxide nanocomposite. Susmita Prusty, Kunal Pal, **Debbethi Bera**, Anindita Paul, Modhubroto Mukherjee, Finaz Khan, Anindita Dey, Susmita Das. Colloids and surfaces B: Biointerfaces. 2021, 203:111729. DOI: 10.1016/j.colsurfb.2021.111729.

10. Chemicals Arms Race: Occurrence of Chemical Defense and Growth Regulatory Phytochemical Gradients in Insect-Induced Folier Galls. Sampurna Roy, Ashutosh Mukherjee, Arunodaya Gautam, **Debbethi Bera**, Amlan Das. Proceedings of the National Academy of Sciences, India Section B: Biological Sciences 2022, 92:415-429. DOI: 10.1007/s40011-021-01322-2.

11. Bimodal Surface Modification Strategies towards Improving the Antibacterial Activity of Graphene Oxide.Finaz Khan, Susmita Prusty,Pritha Saha, **Debbethi Bera**, Bandita Datta,Sherley Saraffin R, Arijit Kapuria, Kajari Dutta, and Susmita Das. Journal of Materials Research (JMRS). 2023

12. The effect of temperature on the activity and stability of the thermostable enzyme caffeine dehydrogenase from *Pichia manshurica* CD1. Rubia Parvin , Khushnood Fatma , **Debbethi Bera** Jyotirmayee Dash, Joydeep Mukherjee, Ratan Gachhui. Biologia. 2023, 1-10. DOI: 10.1007/S11756-023-01473-9

13. Guar gum micro-vehicle mediated delivery strategy and synergistic activity of thymoquinone and piperine: an in vitro study on bacterial and hepatocellular carcinoma cells. Sanghita Das, **Debbethi Bera**, Kunal Pal, Dheeraj Mondal, Parimal Karmakar, Sukhen Das and Anindita Dey. Journal of Drug Delivery Science and Technology.

14. Remarkably high Pb2+ binding capacity of a novel, regenerable bioremediator Papiliotrema laurentii RY1: Functional in both alkaline and neutral environments. Avishek Mukherjee, Soumyadev Sarkar, Rubia Parvin, **Debbethi Bera**, Uttariya Roy and Ratan Gachhuia. Ecotoxicology and Environmental Safety. 2020, 195:110439. DOI: 10.1016/j.ecoenv.2020.110439.

15. Fabrication of Morphologically Modified Strong Supramolecular Nanocomposite Antibacterial Hydrogels based on Sodium Deoxycholate with Inverted Optical Activity and Sustained Release. Susmita Biswas, Udita Chatterjee, Sriparnika Sarkar, Finaz Khan, **Debbethi Bera**, Madhumita Mukhopadhyay, Soumyabrata Goswami, Sandip Chakrabarti and Susmita Das. Colloids and surfaces B: Biointerfaces. 2020, 188:110803. DOI: 10.1016/j.colsurfb.2020.110803.

16. Dual release kinetics in a single dosage from core– shell hydrogel scaffolds. Finaz Khan, **Debbethi Bera**, Santanu Palchaudhuri, Rajesh Bera, Madhumita Mukhopadhyay, Anindita Dey, Soumyabrata Goswami and Susmita Das. RSC Advances. 2018, (8):32695. DOI: 10.1039/c8ra05358h.

Conference Papers:

17. A novel approach to utilise nanopartilees on agricultural sector: A brief review. Anindita Dey, **Debbethi Bera**, Papiya Nandy. MOL2NET 2020. DOI: 10.3390/mol2net-06-06801.

List of Seminars Attended

1. Oral representation in "6th National Congress on Plant Science and Biology" on 9th-10th November 2020

2. Oral representation in "India International Science Festival 2020" on 22nd-24th December 2020.

3. Presented a poster in "One-Day National Symposium on Nanotechnology From Material to Medicine and their Social Impact on 25th March 2017 held at the Centre For Interdisciplinary Research and Education.

4. Participated in a One-Day seminar titled "Recent Trend in Frontier Research in Physics" on 6th March 2018.

5. Participated in "India International Science Festival 2019" on 5th-8th November 2019.

6. Participated in UGC-SAP Sponsored National symposium on" Modern Perspectives of Research and Development in Biochemistry and Biophysics" on 14th-15th March 2019 held at the Department of Biochemistry and Biophysics, University of Kalyani.

7. Presented a poster in a National seminar named "New Directions in Physical Sciences 2020" on 25th February 2020.

8. Participated in a One-Day DST-SERB Sponsored workshop named "Material Synthesis and Characterization Techniques "on 29th February 2020.

9. Participated in the "Young Scientist Conference "of "India International Science Festival 2020" on 22nd – 25th December 2020.

10. Participated in One-Day seminar named "Young Scientists Colloquium 2022 "on 16th December 2022 held at CGCRI Kolkata.

List of Figures

Chapter 1

Chapter 2

Chapter 5

Chapter 6

List of Tables

CHAPTER 1

Introduction and Literature Review

In the medical field, several significant threats are associated with both antibiotics and cancer therapy, posing challenges to effective treatment and patient well-being. Two major concerns are the growing problem of antibiotic resistance and conventional, high-cost, less specific cancer therapies. [1-10]

1.1. Standard Therapies

1.1.1. Antibacterial therapies

The treatment of pathogenic bacterial infections typically involves using antibiotics and other medical interventions. Here are some common remedies against pathogenic bacteria:

- Antibiotics

- Antibacterial creams and or ointments

- Antiseptics

- Vaccines

- Hygiene practices

- Probiotics

- Phage therapy

- Supportive care

The following are common problems associated with various remedies against pathogenic bacteria: [11-20]

1. Antibiotic resistance: Overuse or inappropriate use of antibiotics can lead to the development of antibiotic-resistant bacteria, making future infections harder to treat.

2. Side effects: Antibiotics can cause side effects like nausea, diarrhea, allergic reactions, and disruptions to the balance of beneficial bacteria in the gut.

3. Broad-spectrum antibiotics: Some antibiotics target a wide range of bacteria, which can disrupt the natural balance of the microbiome and lead to opportunistic infections.

4. Some people may experience allergic reactions to topical antibiotics.

5. Vaccines are specific to certain bacterial strains and may not protect against all types of bacterial infections. Vaccine effectiveness can vary, and booster shots may be required for continued protection.

6. The effectiveness of probiotics in preventing or treating bacterial infection is still an area of ongoing research and not all probiotics are equally effective.

7. Phage therapy is a specialized and experimental treatment that may not be widely available in all regions. Bacteriophages are often specific to certain bacterial strains, so finding the appropriate phage for a particular infection can be challenging.

1.1.2. Anticancer therapies

Cancer, characterized by uncontrolled cell growth and the potential to invade other tissues, represents a complex group of diseases. Treatment options for cancer can vary widely depending on the type and stage of cancer, as well as individual factors [21-30].

Some common cancer treatment options include:

- Surgery

- Chemotherapy

- Radiation therapy

- Immunotherapy

- Targeted therapy

- Hormone therapy

These clinical trials can be effective in managing and treating carcinoma, but they also came with certain drawbacks and potential side effects. Here are some common drawbacks associated with various cancer treatment methods.

- Surgery:

  a) Risk of infection bleeding and complications related to anesthesia.

  b) Possible damage to nearby organs or tissues during surgery.

  c) Depending on the extent of surgery, cosmetic changes, or functional limitations may occur.

Chapter 1

- Chemotherapy:

  a) Side effects like nausea, vomiting, fatigue, hair loss, and decreased immunity due to damage to healthy cells.

  b) Long-term effects on fertility and potential impact on organs like the heart, kidney, and nervous system.

  c) Risk of drug resistance and recurrence of cancer.

- Radiation therapy-

  a) Skin irritation and burns in the treated area.

- Immunotherapy:

  Immune-related side effects like inflammation of organs (e.g., lungs, colon) known as immune-related adverse events.

Nanotechnology offers several solutions to these problems tackling bacterial infection and cancer compared to traditional therapeutic approaches.

1.2. Nanoparticles and their effects

In the biological field, nanoparticles have been extensively studied and found to possess unique physical, chemical, and biological properties at the nanoscale. Various applications have been demonstrated, ranging from drug delivery and imaging to diagnostics and tissue engineering, where nanoparticles have been employed [31-40]. Nanoparticles have shown:

1. Drug Delivery: nanoparticles have been designed to encapsulate drugs and deliver them to specific target sites in the body, resulting in reduced side effects and enhanced therapeutic efficacy. Drug delivery applications have been facilitated using lipid-based, polymeric, and metallic nanoparticles.

2. Imaging: Nanoparticles have been utilized as contrast agents for various imaging techniques such as magnet resonance imaging (MRI), computed tomography (CT), and fluorescence imaging. Their unique optical and magnetic property has enabled better visualization of tissues and cells, contributing to early disease detection and monitoring.

3. Cancer Therapy: Nanoparticles have been fabricated to selectively target cancer cells allowing for more effective treatments with minimized damage to healthy tissues. Gold

nanoparticles, for instance, have been utilized for the local destruction of cancer cells through external stimuli (e.g., laser).

4. Diagnostics: Nanoparticles have been incorporated into biosensors and diagnostic assays to detect specific biomolecules or pathogens with enhanced sensitivity and specificity. Their utilization has contributed to early diagnosis.

5. Antimicrobial Applications: Nanoparticles have exhibited antimicrobial properties and have been employed in the development of coatings for medical devices, surfaces, and textiles to prevent microbial growth and reduced infections.

6. Environmental Monitoring: nanoparticles have been utilized for detecting pollutants and toxins in the environment, contributing to improved monitoring and management of ecological and public health aspects.

1.3. Types of nanoparticles

Nanoparticles come in various types, each with their unique properties and potential applications [41]. Here are some common types of nanoparticles:

1. Metallic nanoparticles

2. Metal oxide nanoparticles

3. Quantum dots

4. Magnetic nanoparticles

5. Lipid-based nanoparticles

6. Polymeric nanoparticles

7. Carbon-based nanoparticles

8. Silica nanoparticles

9. Hybrid nanoparticles

10. Biopolymer-based nanoparticles

A wide range of materials can be used to produce nanoparticles, each with its unique properties and potential applications. These materials can be broadly categorized into organic, inorganic, and hybrid materials. Here are some examples:

➢ Organic Nanoparticles:

1. Polymeric nanoparticles: poly (lactic-co-glycolic acid) (PLGA), polyethylene glycol (PEG), and chitosan are commonly used to create nanoparticles for drug delivery and other biomedical applications.

2. Lipid-based nanoparticles: liposomes, micelles, and lipid nanoparticles are formed from lipid molecules and are used for drug delivery and gene therapy due to their biocompatibility.

3. Protein-based Nanoparticles: Proteins and peptides can self-assemble into nanoparticles with specific functions.

➢ Inorganic nanoparticles:

1. Metallic nanoparticles: Gold, silver, platinum, and other metal nanoparticles have unique optical and catalytic properties. They are used in imaging, sensing, catalysis, and medical applications.

2. Magnetic nanoparticles: Iron oxide nanoparticles and other magnetic materials are used in biomedical applications such as targeted drug delivery and magnetic resonance imaging (MRI).

3. Quantum Dots: Semiconductor nanoparticles with quantum confinement effects. They have tunable fluorescence properties and final applications in imaging and display technologies.

4. Metal Oxide Nanoparticles: nanoparticles of materials like titanium dioxide (TiO_2) and zinc oxide (ZnO) have photocatalytic properties and are used in applications like photocatalysis and sunscreens.

➢ Hybrid Nanoparticles:

1. Silica-coated nanoparticles: Inorganic nanoparticles coated with a silica shell for improved stability and biocompatibility. They are used in drug delivery and imaging.

2. Polymer-coated nanoparticles: Inorganic nanoparticles coated layer of polymer for controlled release and targeting in drug delivery applications.

3. Core-Shell nanoparticles: combinations of different materials where one material forms the core, and another material forms the shell.

➢ Carbon-based nanoparticles:

1. Carbon nanotubes: cylindrical carbon structures with remarkable mechanical, electrical, and thermal properties. They find applications in electronics, materials, and nanomedicine.

2. Graphene nanoparticles: Single layers of carbon atoms with excellent electrical and mechanical properties. They are being exploited for various applications including electronics and energy storage.

1.4. Nanoparticles Synthesis Process

The synthesis method depends on the desired nanoparticle type size, shape, and intended applications [41]. Here are some common nanoparticle synthesis methods:

1. Chemical Reduction: This method involves reducing metal ions in a solution to form metallic nanoparticles.

2. Sol-gel Method: A solution of precursor compounds undergoes hydrolysis and condensation reaction to form a sol (a colloidal suspension of nanoparticles) which then forms a gel, eventually yielding solid nanoparticles.

3. Co-precipitation: metal ions are simultaneously precipitated from the solution by a suitable base, leading to the formation of nanoparticles.

4. Emulsion-based methods: Emulsions of oil and water containing precursors are used to generate nanoparticles when the precursors react under specific conditions.

5. Microfluidic synthesis: nanoparticles formed within tiny channels with controlled mixing of reactants, enabling precise control over particle size and properties.

6. Electrochemical synthesis: Nanoparticles are formed at the electrode surface during electrochemical reactions.

7. Pyrolysis: Precursor compounds are heated to high temperatures in an inert atmosphere, leading to nanoparticle formation through decomposition and nucleation.

8. Spray Pyrolysis: Precursor solutions are atomized and sprayed into a hot furnace, where they decompose and nucleate to form nanoparticles.

9. Hydrothermal Synthesis: Nanoparticles are synthesized in an aqueous at elevated temperatures and pressure, leading to controlled crystal growth.

10. Green Synthesis of Nanoparticles: Biomolecules such as plant extracts or microorganisms are used to reduce and stabilize metal ions, resulting in nanoparticle formation. Green synthesis refers to the production of nanoparticles using environmentally friendly and sustainable methods, often involving plant extracts, microbes, or other natural resources.

The green synthesis process typically involves the following steps [41-45]:

1. Selection of Natural Resources such as extracts, fungi, bacteria, algae, or agricultural waste materials were chosen as reducing agents or stabilizers for nanoparticle synthesis.

2. Preparation of Extracts: The selected green resources were processed to extract bioactive compounds that can act as reducing and stabilizing agents for nanoparticle formation.

3. Purifications: the extracted bioactive compounds were used to purify or reduce metal ions to form desirable metal nanoparticles.

All these steps were followed by characterization using various analytic techniques to determine their size, shape, stability, and other properties.

Green synthesis offers several advantages over traditional chemical synthesis methods. It avoided the use of hazardous chemicals and minimizes waste generation. Moreover, green synthesis often requires milder reaction conditions and can be cost-effective. Moreover, green-synthesized nanoparticles have shown potential applications in various fields, including medicines, agriculture, and environmental remediation. Their biocompatibility and reduced toxicity make them promising candidates for drug delivery, antimicrobial agents, and other biomedical applications.

1.5. Instrumentation

1.5.1 X-Ray Diffraction
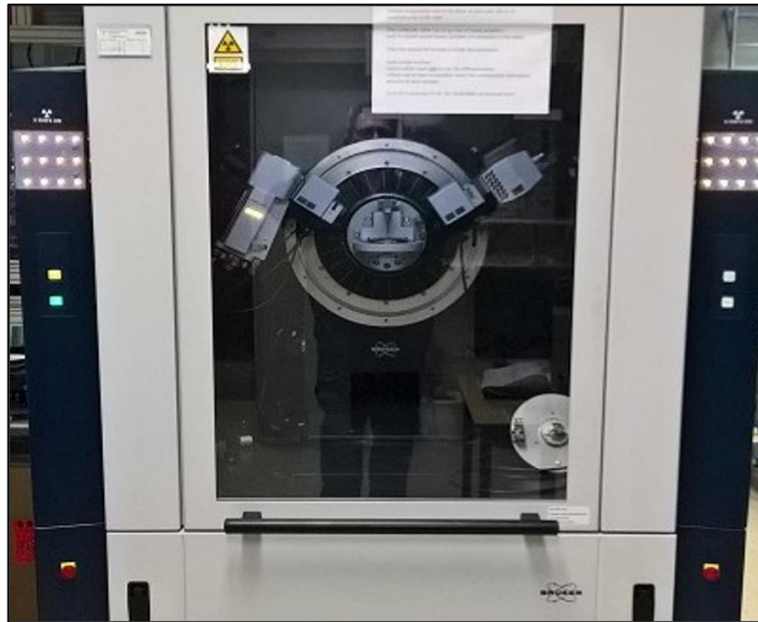
Figure.1.1. X Ray Diffractometer

The working principle of X-Ray diffraction (XRD) (Figure: 1.1.) can be explained using the equation known as Bragg's law. Bragg's law describes the relationship between the scattering angle (θ), the wavelength of X-rays (λ), and the spacing between crystal lattice planes (d). The equation for Bragg's law:

$$n \lambda = 2d \sin(\theta)$$

Where n is an integer representing the order of the diffraction peak, λ is the wavelength of the incident X-rays, D is the spacing between crystal planes and θ was the angle between the incident X-ray beam and the crystal plane. This equation relates the properties of X-rays and the crystal lattice to the diffraction pattern observation in XRD.

According to Bragg's law, when X-rays strike a crystal at a specific angle (θ), they are diffracted by the crystal planes that satisfy the condition for constructive interference. Constructive interference occurs when the path difference between the scattered waves from adjacent crystal planes was an integer multiple of the X-ray wavelength ($n\lambda$). This leads to the formation of diffraction peaks in the XRD pattern. By measuring the angle (θ) at which the diffraction peaks occur and knowing the wavelength of the X-rays, researchers can determine

the spacing between the crystal lattice parameters and the presence of specific crystalline phases can be obtained [46].

We have used model-D8 Bruker AXS, Wisconsin, USA with Cu-Kα target and a target wavelength of 1.5418λ. The XRD was operated at 35 kV with a scan speed of 1 s/step.

Importance:

1. Structural Analysis: By employing XRD, the structural analysis of biological nanoparticles can be facilitated.

2. Crystallographic information about the biological nanoparticles can be obtained through XRD.

3. The determination of the atomic arrangement within the biological nanoparticles can be achieved through XRD.

4. The lattice parameters of the crystalline structure in the biological nanoparticles can be determined using XRD.

5. Specific crystalline phases present in the biological nanoparticles can be identified with the aid of XRD.

1.5.2. Fourier Transform Infrared Spectroscopy (FTIR)

Figure.1.2. FTIR Spectrophotometer

Fourier Transform Infrared spectroscopy (FTIR) (Figure: 1.2.) was based on the interaction between matter and electromagnetic radiation in the infrared region of the electromagnetic spectrum. The working principle can be described using physics terms and equations as follows:

Infrared radiator was described by the electromagnetic wave equation:

$$E(t) = EO * \cos (2\pi vt + \varphi)$$

Where E(t) represents the electric field of the wave, EO was the amplitude, v was the frequency, t was time and φ was the phase.

Molecules have vibrational modes characterized by the equation of motion:

$$m \, d^2x/dt^2 = -kx$$

Where m is the mass of the atoms, x is the displacement from the equilibrium position, k is the force constant and d^2x/dt^2 was the acceleration.

In our studies, the Fourier transform infrared spectroscopy (FTIR) study was conducted using FTIR-8400S, Shimadzu, Japan, in the wave number range from 400 cm^{-1} to 4000 cm^{-1} [47].

Importance:

In the characterization of biological nanoparticles, several benefits were offered by FTIR spectroscopy, as it provides valuable insights into their composition, and structure properties. Some of the key benefits include:

1. Composition Analysis: The composition of biological nanoparticles can be identified and analyzed by FTIR spectroscopy. The presence of specific biomolecules such as proteins, nucleic acids, lipids, and carbohydrates can be detected in the nanoparticles. This information aids in understanding the biomolecular components and their interactions within the nanoparticles.

2. Surface Functionalization: The functional groups present on the surface of biological nanoparticles can be studied using FTIR spectroscopy. Information about the chemical moieties and surface modifications such as functionalized ligands or coating was provided. This characterization helps in assessing the stability, reactivity, and potential applications of nanoparticles.

11

3. Structural Characterization: Insights into the structural properties of biological nanoparticles can be obtained through FTIR spectroscopy. This information was crucial for understanding the stability, assembly, and functionality of the nanoparticles.

4. Encapsulation and Drug Delivery: The presence of the encapsulated molecule and its interaction with the nanoparticle matrix can be confirmed. This characterization aids in the development of nanoparticle-based drug delivery systems with controlled release properties.

5. Stability and Degradation Analysis: Changes in the chemical composition, degradation products, and structural integrity of the nanoparticles can be detected. This analysis helps in evaluating the shelf life, storage conditions, and potential degradation pathways of the nanoparticles.

6. Quality control: FTIR spectroscopy serves as a valuable tool for quality control in the production of biological nanoparticles. It enables the assessment of batch-to-batch consistency, purity, and sample integrity.

7. Non-Destructive Analysis: FTIR spectroscopy was a non-destructive technique that allows repeated measurements on the same biological nanoparticles without altering their integrity. This was advantageous when studying dynamics processes, changes over time, or performing longitudinal studies on the nanoparticles.

1.5.3. Transmission Electron Microscopy (TEM)

Figure.1.3. TEM

In TEM (Figure: 1.3.), a beam of electrons was accelerated by applying a voltage (V) between an electron source and an anode. The kinetic energy (E) of the electrons was determined by the accelerating voltage. The equation relating voltage, kinetic energy, and electron charge (e) were as follows:

$$E = eV,$$

where E represents the kinetic energy, E is the elementary charge (1.602×10^{-19} C) and

V was the accelerating voltage. In TEM, the electron beam interacts with a sample, leading to several phenomena such as elastic scattering, inelastic scattering, and absorption. These interactions can be described by equations such as the Rutherford scattering equation and the Bethe-Bloch equation, which account for electron-sample interaction and energy loss mechanisms. The interaction of electrons with the sample results in the formation of an image or a diffraction pattern. Electron scattering by the sample and subsequent focusing of the scattered electrons onto a detector or photographic film was involved in image formation in TEM [48].

Importance:

1. High-resolution imaging: The exceptionally high resolution was provided by TEM, allowing the visualization of biological structures and details at the nanoscale. The precise examination of cellular components, organelles, viruses, protein complexes, and other subcellular structures was enabled. The ultrastructure and morphology of biological samples can be understood through the high-resolution images obtained via TEM.

2. Visualization of ultrastructure details: Fine details of biological materials that were not easily discernible with other imaging techniques can be observed using TEM. Intricate cellular structures, such as membranes, vesicles, microtubules, and filaments can be revealed, providing insights into their organization, arrangements, and interactions.

3. Subcellular localization studies: The localization of specific molecules or structures within cells can be facilitated by TEM. Through techniques such as immunolabeling or gold nanoparticle tagging, the distribution and localization of proteins, nucleic acids and other biomolecules within cellular compartments can be visualized.

4. Examination of cellular dynamics: Dynamics processes within cells can be captured using TEM. Techniques like time-lapse imaging or freeze-fracture TEM enable the observation of cellular events, including cell division, endocytosis, and membrane dynamics.

5. Analysis of structural changes: Structural changes and alterations in biological materials can be detected using TEM. Insight into disease mechanisms, progression, and the effects of treatments can be gained through TEM.

6. Elemental analysis: TEM can be combined with energy-dispersive X-ray spectroscopy (EDAX) to obtain elemental composition information. This enables the determination of elemental distribution within biological samples, identifying the presence and localization of specific elements or nanoparticles.

1.5.6. Ultra Visible Spectroscopy (UV-Vis Spectroscopy)

The working principle of UV-Vis spectroscopy (Figure: 1.4.), can be explained by the Beer-Lambert Law, which relates the absorbance of a sample to its concentration and the path length of the sample cell. The equation was as follows:

$$A = \varepsilon c l$$

where A was the absorbance of the sample, E was the molar absorptivity (also known as the molar absorption coefficient), which represents the ability of a substance to absorb light at a specific wavelength, C was the concentration of the sample in moles per liter (M), I was the path length of the sample cell in centimeters (CM).

Figure.1.4. UV-Vis Spectrophotometer

In UV-Vis spectroscopy, the incident light intensity (l_O) and the transmitted light intensity (l) were related to the absorbance using the equation: A = -log(l/l_O)

By different wavelengths, the absorbance was measured, and a UV-Vis spectrum can be obtained which represents the absorbance characteristics of the sample across the UV and visible range.

The absorbance intensity of our nanoparticles was estimated by an Epoch microplate reader, BioTek, USA) .

1.5.5. Dynamic Light Scattering (DLS)

The correlation function, g2(t) was defined as the auto-correlation function of the intensity fluctuations, which was normalized and relates the intensity fluctuations of the scattered light to the size and diffusion properties of the particles.

The correlation function, g2(t) was given by: $g2(t) = <I(t) * I(t+\tau)> / <I(t)>^2$

where I(t) represent the intensity of the scattered light at time T, τ denotes the time delay and

$<...>$ signifies the ensemble average over different time intervals.

The correlation function represents the degree of correlation between the intensity values at different time intervals. In DLS, it was utilized to extract information about the size and diffusion properties of the particles. The size of the particles was related to the correlation function through the following equation:

$$g2(t) = 1 + \beta \mid q^2 D\tau$$

where β was a constant related to the optical setup, q corresponds to the scattering vector (which was proportional to the scattering angle), D represents the diffusion coefficient of the particles and T signifies the time delay.

From this equation, it can be observed that the correlation function was dependent on the diffusion coefficient of the particles, which was associated with their size. By fitting the experimental correlation function to theoretical models, such as the Stokes-Einstein equation, the size distribution and diffusion properties of the particles can be determined [50].

Figure.1.5. DLS Analyzer

Importance:

1. Size Determination: The determination of the size distribution of biological particles, such as proteins viruses, liposomes, and nanoparticles, can be accomplished using DLS. The hydrodynamics radius of these particles in solution can be measured, aiding in the understanding of their structure and behavior.

2. Sensitivity: Detection and analysis of particles ranging from a few nanometers to several micrometers can be achieved using DLA. This vast size range makes it suitable for the characterization of various biological materials, including macromolecules and subcellular structures.

3. Real-Time Monitoring: Real-time information about changes in particle size or aggregation state can be provided by DLS. This was particularly valuable for the monitoring of dynamic biological processes, such as protein folding, self-assembly, and interaction studies.

4. Non-Destructive: DLS was a non-destructive technique that does not require any labeling or sample preparation, preserving the integrity and functionality of the biological materials under investigation.

5. Complementary Technique: DLS can be used in conjunction with other analytical techniques, such as static light scattering, zeta potential measurement, and fluorescence spectroscopy.

The average particle diameter, size distribution, and zeta potential of HAP NPs were measured using Zetasizer (NANO ZS90, Malvern Instruments Ltd, UK).

1.5.6. Photoluminescence Spectroscopy (PL Spectroscopy)
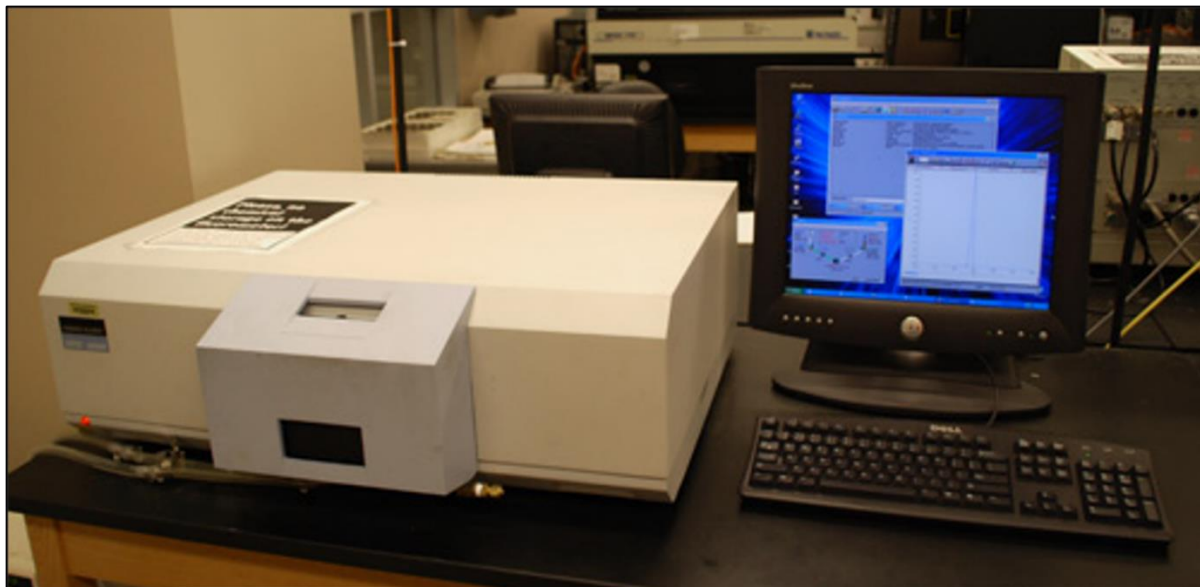
Figure.1.6. PL Spectrophotometer

Photoluminescence (Figure.1.6.) was a form of luminescence that results from photoexcitation. Photoluminescence spectroscopy was a non-destructive and non-contact method of probing the structure of any material. The light was directed onto a sample material and absorbed. In photoluminescence spectroscopy, by employing an <u>optical spectrometer,</u> we can measure the intensity of emitted light as a function of wavelength.

By Photo-excitation electrons within a material can move into permissible excited states. When these electrons return to their equilibrium states, they can lose energy through radiative or non-radiative emissions. In a radiative process, the excess energy was released through the emission of photons.

The energy of the emitted light represents the difference in energy levels between the two electron states which were involved in the transition between the equilibrium state and the excited state. The quantity of the emitted light corresponds to the relative contribution of the radiative emissions [51].

Importance

1. Detection of Aggregation-caused quenching (ACQ) properties where it was necessary to use and study fluorophores in dilute solutions or as isolated molecules.

2. Detection of Aggregation-induced emission (AIE) properties.

1.5.7. Field Emission Scanning Electron (FESEM)

Figure.1.7. FESEM

FESEM was one of the most versatile analytical techniques for observing the surface morphology of specimens. The mode of operation of FESEM microscopes was similar to the conventional scanning electron microscopes. An electron beam was focused by electromagnetic lenses and scans the surface of any sample, where the reflected electrons create an image of the surface and topography of sample materials by generating many low-energy secondary electrons. The secondary electron yield was the number of secondary electrons emitted per incident primary electrons. It depends on the properties of the sample surface and the incident electron energy [].

The morphological studies were carried out by the field emission electron microscope (FESEM) INSPECT F50 (FEI, the Netherlands).

Importance:

1. High-resolution imaging: Excellent spatial resolution was provided by the FE-SEM, allowing biological samples to be visualized at the nanoscale. Detailed surface morphology can capture, revealing intricate structures and features of biological materials.

2. Surface topography analysis: Accurate analysis of the surface topography of biological samples can be performed by the FESEM. Surface roughness, texture, and the presence of surface irregularities can be revealed, which were crucial for understanding the structure-function relationships of biological materials.

3. Elemental composition analysis: The FESEM was equipped with energy-dispersive X-ray spectroscopy (EDAX) detectors, which enable elemental analysis of biological samples. Identification and mapping of the distribution of various elements within the sample can be achieved using EDAX, providing insights into the chemical composition and elemental concentrations.

4. Subcellular imaging: Subcellular structures and organelles can be imaged by the FESEM due to its high-resolution capabilities. Cellular processes, organelle interaction, and cellular ultrastructure can be studied, providing valuable information for cell biology and biomedical research.

5. Sample versatility: A wide range of biological samples, including cells, tissues, biomaterials, and nanoparticles, can be accommodated by the FESEM. Flexibility in sample preparation methods, allowing for imaging of both fixed and live samples, as well as samples with different sizes and shapes.

6. 3D imaging and reconstruction: Advanced FESEM techniques, such as focused ion beam (FIB) milling and serial block-face imaging enable 3D imaging and reconstruction of biological samples.

7. Correlative imaging: Integration with other imaging modalities, such as light microscopy or transmission electron microscopy, can be achieved with the FE-SEM, enabling correlative imaging. The advantages of different techniques can be combined and complementary information about the biological sample can be obtained.

1.5.8. Thermogravimetric Analysis (TGA)

Figure.1.8. TGA

TGA Figure.1.8. was one of the thermal analysis methods where a change in mass of the substance under study was noted concerning a linear change in temperature in an inert atmosphere. The initial mass of the sample was known. It was possible to quantitatively analyze any thermally induced mass change in the sample as a response to the temperature change. The plot of mass vs. temperature was known as a thermogram. A thermogram can be divided into horizontal and vertical sections. The horizontal sections denote a stable relation between the sample mass and the temperature range as there was no mass loss here. However, the vertical sections denote temperature ranges in which the sample loses mass. This mass loss can be attributed to causes such as moisture loss, other component loss, physical changes in the sample, and the building and breaking of chemical bonds. The order of physical transitions and chemical reactions for any particular sample has a distinct order. Hence, the TGA thermogram for a given sample was unique to it.

Here, the TGA analysis has been carried out using the DTG-60H, Simultaneous DTA-TG Apparatus, Shimadzu.

Importance:

1. TGA analysis can be used to investigate the thermal stability, sample purity, moisture content, and decomposition mechanism of samples.

2. It can be used to determine the evaporation rates of liquid mixtures.

It can be used for the estimation of the composition of various alloys and mixtures if the decomposition temperature data was available.

1.5.9. Biological Safety Cabinet

Figure.1.9. A biological incubator was used in laboratories and research facilities to provide controlled conditions for the growth and cultivation of microorganisms, cells, and tissues. It was designed to create an environment with precise temperature, humidity, and sometimes even gas composition to support optimal growth and development.

Figure.1.9. Biosafety cabinet with Laminar Air Flow

1.5.10. Laminar Airflow (LAF)

Laminar airflow systems were commonly utilized in biological laboratories to create a controlled and sterile environment for various applications, including cell culture, tissue

culture, microbiology, and other sensitive experiments. The implementation of laminar airflow in biological labs assists in minimizing the risk of contamination and maintaining the integrity of samples and cultures [54].

- **Features and components:**

    1. Clean benches or Biological Safety Cabinets (BSCs): Laminar airflow was often incorporated into clean benches or biological safety cabinets. These cabinets provide both sterile airflow and containment to protect the user and the samples. The flow also air creates a barrier that prevents airborne contaminants from reaching the samples while also minimizing the dispersion of any contaminants generated within the cabinet.

    2. HEPA Filters: Laminar airflow systems in biological labs rely on high-efficiency particulate air (HEPA) filters to remove particles and microorganisms from the incoming air. Particles as small as 0.3 micrometers can be effectively trapped by HEPA filters.

    3. Unidirectional Flow: Laminar airflow systems in biological labs were designed to provide a unidirectional flow of air. It means that the air was moved in a single direction, typically from the top to the bottom of the workspace. Unidirectional flow helps in minimizing the disruption of air patterns and reduces the chances of contaminants entering the sterile area.

    4. Creation of a sterile working area: The primary objective of laminar airflow in biological labs was the creation of a sterile working environment. The controlled airflow helps in reducing the number of airborne particles, microorganisms, and other contaminants that could interfere with cell cultures, tissue cultures, or other biological processes.

    5. Utilization of aseptic techniques: Laminar airflow systems should be used in conjunction with proper aseptic techniques to ensure the sterility of the work environment.

1.5.11. BOD Incubator

Figure.1.10. BOD Incubator

- **Features and components:**

Figure.1.10. shows the BOD incubator.

1. Temperature control: The temperature within the incubator was controlled to maintain a stable range, typically between 5 °C and 60 °C, depending on the specific application. Heating elements were utilized to raise the internal temperature evenly.

2. Heating elements: Heating coils or heating pads were used to raise the internal temperature, ensuring even distribution through the incubator, and preventing temperature variations.

3. Temperature monitoring and regulation: The incubator incorporates internal temperature sensors to continuously monitor and regulate the temperature. This ensures the maintenance of the set temperature and prompt correction of any deviations.

4. Sterilization: To minimize contamination, incubators often include sterilization features like HEPA filters, UV lights, or high-temperature sterilization cycles.

5. Programmable settings: Advanced incubators can be programmed with specific temperature and humidity profiles over time. This functionality was particularly useful for experiments requiring precise growth conditions or cyclic variations [55].

1.6. The objective of the present work:

Addressing the medical threats demands a multidisciplinary approach. So, we tried to synthesize and modify the therapeutic agents keeping in mind the following factors:

1. Against Drug Resistance: Over time antibiotics were getting Resistance against the bacteria and diminishing the effectiveness of treatments, limiting their abilities. In this study, we synthesize needle-shaped hydroxyapatite nanoparticles (HAP NPs) encapsulated with vancomycin (VAN) conjugated with folic acid (FA) against multidrug Resistance (MDR) *Enterococcus faecalis*.

2. Against Side Effects: Side effects of the drugs were leading to discontinuation or reducing the concentrations of the dose. Synthesized materials in our studies were less toxic than conventional drugs. Zinc oxide nanoparticles (ZnO NPs) and (AgNPs) were synthesized from *Tulsi*.

3. low cost: These materials were synthesized with very common chemical and natural ingredients.

4. Targeted therapies: each nanoparticle shows a different pH depending on drug release and was conjugated with various materials that help to track the drug pathways.

CHAPTER 2

Functionalized Biomimetic Hydroxyapatite Nanoparticles as Potential Agents Against Pathogenic Multidrug-Resistant Bacteria

Summary

The grave contemporary global impediment of hospital-acquired infections caused by the persistent dissemination of resistant bacterial strains needed to be mitigated with immediate effect. Special attention was attracted to infections caused by pathogenic multidrug-resistant (MDR) Gram-positive bacteria, such as *Enterococcus faecalis*, which exhibit resistance to conventional antibiotic therapy. Here, the synthesis of nanoscale hydroxyapatites (HAPNPs), well-known biomimetic ceramic materials characterized by needle-shaped morphologies, was reported. Vancomycin (VAN) has been encapsulated within these nanoparticles, and the targeting ligand (folic acid) has been conjugated using a facile synthesis process to enhance therapeutic efficacy against MDR *E. faecalis*. Characterizations of these functionalized HAPNPs were conducted through field emission scanning electron microscopy (FESEM), powder X-Ray diffraction (PXRD), ultraviolet-visible spectroscopy (UV-Vis), and dynamic light scattering (DLS) techniques. It is suggested by the results that these functionalized HAPNPs could successfully transport vancomycin across the cell wall of MDR *E. faecalis* through endocytosis. The determination of selective antibacterial activity was envisaged with the help of extensive in-vitro assays such as the minimum inhibitory concentration (MIC), minimum bactericidal concentration (MBC), and the generation of reactive oxygen species (ROS). This study vividly establishes that folic acid-conjugated HAPNPs are promising antibacterial agents against MDR *E. faecalis* and related pathogenic-resistant bacterial strains.

2.1. Introduction

The emergence of drug-resistant bacteria was highlighted as a grave threat in modern society. Millions of deaths worldwide were caused by antibiotic-resistant bacteria, as mentioned in previous reports [55,56]. Furthermore, an incessant decline in approved antibiotics over the past decade exacerbated this issue. This led to the need for the development of alternate strategies to overcome bacterial strain resistance. Various active strategies, including the development of novel antibiotics, were implemented for the treatment of multidrug-resistant (MDR) bacteria. The process of functionalizing nanomaterials was found to be highly effective in the development of antibacterial agents for MDR bacteria treatment. Li et al., successfully developed fluorescent-carbon quantum dots capped with spermidine against MDR bacteria [57]. Additionally, different approaches mediated by nanoparticles were being implemented as ameliorative agents for infections caused by MDR bacteria [58]. However, these nanoparticles were found to be undesirably hazardous, antibacterial agents.

Enterococcus faecalis was identified as a predominant pathogen responsible for infection in the urinary tract, nosocomial bacteremia, and post-surgical infections. It gradually developed resistance towards conventional therapies, and the lack of proper diagnosis and treatment for such infections resulted in the loss of innumerable lives. Furthermore, its MDR phenotype posed a grave threat to global public health [59]. To cure *E. faecalis* infection, various antibiotics were used, but recently none were found to be effective against different strains of *E. faecalis* [60,61]. Resistance to different antibiotics like penicillin, vancomycin, and methicillin was found in over 90% of *E. faecalis*, strains [62]. The antibiotic drug vancomycin, which was clinically used to treat *E. faecalis* infections, joined the list of antibiotics that developed resistance after penicillin (in 1940) and methicillin (in 1961) [63,64]. Overcoming this drug resistance and combating MDR *E. faecalis* infection required the development of an antibacterial agent that could effectively address MDR *E. faecalis*. Although some recent work had been carried out on the modifications of materials effective against MDR pathogenic strains like *S. aureus* [65-67]. There was an urgent need to amplify the antibacterial activities of glycopeptide antibiotics like vancomycin (VAN) [68]. Vancomycin was predominantly used for the treatment of Gram-positive, such as *S. aureus* and *E. faecalis*. Unfortunately, these bacterial strains also exhibited resistance to vancomycin. To combat this problem, a series of VAN-modified nanoparticles were implemented by several researchers that could be employed against multidrug-resistant *S. aureus* (MRSA) [69-73]. Taking a cue from their work, the

development of nanoscale hydroxyapatite (HAPNPs) conjugated with VAN for the treatment of MDR *E. faecalis* was reported in the study.

In recent years, HAPNPs have shown great potential in various applications, particularly in the delivery of bioactive molecules [74,75]. The modification of HAPNPs for therapeutic applications had drawn considerable interest due to their attributes such as large surface area, high porosity, and easily modifiable surface [76,77]. It had been established by Wu et al. and Ghosh et al. that hydroxyapatite possessed the ability to enhance the antibacterial effects of common antibiotics like vancomycin [78,79]. Based on these attributes, the development of functionalized HAPNPs for the treatment of MDR *E. faecalis* was emphasized. Folic acid (FA) was a vital nutrient required for nucleotide synthesis in bacteria. Therefore, folic acid-conjugated antibiotic-encapsulated nanoparticles were readily internalized by bacteria through the process of endocytosis, greatly facilitating the delivery of the encapsulated antibiotic to bacterial cells. Folic acid targeting had previously been implemented for the delivery of antibiotics to resistant cells [69,70].

In the present study, folic acid-modified HAP nanoparticles conjugated with VAN were designed as ameliorative agents against vancomycin-resistant bacterial strains. Detailed in vitro assays, such as minimum inhibitory concentration (MIC), minimum bactericidal concentration (MBC), and the agar diffusion method were used to assess the antibacterial efficacy of our prepared samples.

The results strongly indicated that our prepared material harbored the potential to arise as a promising remedial agent against various disease-causing MDR bacterial strains. Our current study portrayed that functionalized HAPNPs possessed characteristics that could unlock novel possibilities in the treatment of MDR *E. faecalis* as well as other comparable pathogenic resistant bacterial strains.

2.2. Experimental Section

2.2.1. Materials

2.2.1.1. Chemical Ingredients

Calcium nitrate tetrahydrate [Ca $(NO_3)_2.4H_2O$] (0.1M) and di-ammonium hydrogen phosphate [$(NH_4)_2.HPO_4$] (0.1M) were obtained from Merck, India. The antibiotic, Vancomycin, a pure drug was procured from HiMedia, India. Ultrapure grades of bacterial culture media,

fluorescence stains, various chemicals, and reagents used for biological purposes were procured from Merck and SRL, Mumbai, India. Therefore, mentioned reagents were utilized without any type of purification or modification. All the experiments were performed with de-ionized (Millipore) water with a resistivity of at least 18 MΩ-cm. The glass wares were thoroughly cleaned with aqua regia solution and were subsequently rinsed with ultrapure water.

2.2.1.2. Bacterial strain

MDR pathogenic bacterial strains and antibiotic sensitive strains were used throughout the antibacterial study. The antibiotic resistant *E. faecalis* (ATCC 52199) and antibiotic sensitive *E. faecalis* bacteria (ATCC 29212) were obtained from ATCC. The resistant strain, *E. faecalis* (ATCC 52199) was resistant to the various traditional antibiotics like Vancomycin, amikacin, ciprofloxacin, tetracycline, penicillin, methicillin, and erythromycin.

2.2.1.3. Cell line

WI38 (human lung fibroblast) was used to determine the cytotoxicity assay obtained from the Central Cell repository of the National Center for Cell Science (NCCS), Pune, India. All the above cell lines were cultured in the presence of Dulbecco's Modified Eagles Media (DMEM) supplemented with 10% FBS, 1mM sodium pyruvate, 2 mM L-glutamine, non–essential amino acids, in the presence of antibiotic solution comprising 100 mg/L penicillin and 100 mg/L streptomycin. The cells were grown in a humidified atmosphere at a temperature of 37 ^{0} C in the presence of 5% CO_2.

2.2.2. Experimental methods

2.2.2.1. Synthesis of nano-Hydroxyapatite

The stock solution was prepared by dissolving calcium nitrate tetrahydrate [$Ca(NO_3)_2.4H_2O$] (0.1 M) and di-ammonium hydrogen phosphate [$(NH_4)_2.HPO_4$] (0.1 M) in 50 ml of distilled water. To yield the final solution, di-ammonium hydrogen phosphate was added dropwise to calcium nitrate tetrahydrate. The pH of the reacting suspension was maintained at 5. After vigorous stirring for 2-3 hours, the solution was transferred to a Teflon-lined stainless-steel hydrothermal reactor. The unit was placed in a dust-free electric oven and reactions were performed for 48 hours at a temperature of 200 $^°$C and then naturally cooled to room temperature. The reacted solutions were washed several times with distilled water, followed by

air drying at ~50 °C for 72 hours. The obtained sample was named HAP and was sent further characterizations.

2.2.2.2. Synthesis of vancomycin encapsulated nanoscale HAP (HAP@VAN)

The HAP synthesized earlier was dissolved in millipore water and stirred vigorously for 24 hours. In another glass tube, vancomycin solution was introduced dropwise into the HAP solution. The resulting solution was vigorously stirred for 24 hours. Vancomycin-encapsulated HAP nanoparticles were collected through centrifugation at a speed of 10,000 rpm for 10 minutes. Afterward, the solution was dried using the normal lyophilization method. Finally, the dried powder was ground in an agate mortar to achieve finer grains. The sample, HAP@VAN was used for further characterizations.

2.2.2.3. Folic acid tailoring on vancomycin loaded HAP NPs (HAP@VAN@FA)

The carboxyl group (-COOH) of folic acid (FA) was activated using the ethyl (dimethylaminopropyl) carbodiimide/N-hydroxysuccinimide (EDC/NHS) reaction. Firstly, FA was solubilized in dimethylformamide (DMF). The EDC/NHS was then incorporated into the FA solution to activate FA. Under dark conditions, the activated FA was added dropwise into the HAP@VAN solution, maintaining the pH of the solution at 7. The FA-conjugated HAP@VAN NPs (HAP@VAN@FA) were subjected to centrifugation at 10,000 rpm for about 10 minutes and thoroughly washed. Ultimately, the FA-conjugated HAP@VAN was obtained by employing the lyophilization method.

2.2.3. Physical Characterizations

The XRD (X-Ray Diffractometer) patterns of the powdered nanoparticle samples were analyzed by XRD model-D8 Bruker AXS, Wisconsin, USA, employing Cu-Kα target with the help of a target wavelength of 1.5418 Å. The XRD was operated at 35 kV with a scan speed of 1 sec/step. The Fourier transform infrared spectroscopy (FTIR) study was done using FTIR-8400S, Shimadzu, Japan in the wavenumber range from 400 cm^{-1} to 4000 cm^{-1}. The Field emission scanning electron microscope (FESEM) was carried out for the morphological study employing INSPECT F50 (FEI, Netherland). The nanoparticles were thoroughly dispersed in MilliQ water in a bath-type ultrasonicator for 30 minutes to form a suspension having a concentration of 2 mg/ml. The UV visible spectrophotometer (Epoch microplate reader, Bio-Tek, U.S.A) was used to estimate the absorbance intensity of the nanoparticles after being dispersed completely in MilliQ water. The average particle diameter, size distribution, and zeta

potential of HAP NPs were measured by employing Zetasizer (NANO ZS90, Malvern Instruments Ltd, UK). All the synthesized HAPNPs and drugs were sterilized by UV radiation technique before the antibacterial experiments. To determine the shape and size of the material we have performed the TEM analysis using JEOL JEM 2100h.

2.2.4. Evaluation of antibacterial activity

2.2.4.1. Determination of minimum inhibitory concentration (MIC) and minimum bactericidal concentration (MBC).

The minimum inhibitory concentration (MIC) and minimum bactericidal concentration (MBC) were determined using the microdilution method [80]. A bacterial culture containing 2.5 x 10^5 CFU/ml bacteria (10 µl) was individually added to several 1ml nutrient broths (NBs) exposed to different concentrations of the synthesized HAPNPs. The solutions were then incubated at 37 °C for 24 hours. The HAPNPs nanoparticles were thoroughly sonicated to prepare a pure suspension before the experiment. The MIC values were estimated by examining the turbidity of bacterial growth, indicating near absolute (99%) inhibition of bacterial growth.

For the MBC, bacterial cultures were grown onto agar plates using MIC dilutions. The cultures were then incubated at 37 °C for 24 hours. The minimum concentration required for total bacterial killing was considered its MBC value. The assays were meticulously performed in a bio-safety cabinet.

2.2.4.2. Tolerance level

The MIC and MBC values indicated the tolerance levels of each bacterial strain towards the synthesized samples using the following formula [81].

Tolerance level = (MBC) / (MIC)………………………………….…………………………..[eq.1]

2.2.4.3. Agar well diffusion method

The Agar well diffusion method gives a clear indication of the efficacy of our samples HAP@VAN and HAP@VAN@FA against the pathogenic MDR bacterial strain *E. faecalis*. The strain was grown until the turbidity of the bacterial culture reached 0.5 Mac Farland standards which were approximately 10^8 CFU per ml. Then 100 µl of this bacterial culture was inoculated on petridish having a diameter of 90 mm and was filled with 30 ml of Mueller Hinton Agar (MHA). Afterward, the wells having a diameter of approximately 0.563 cm were

punched within the agar plates and were treated with HAP, HAP@VAN, and HAP@VAN@FA NPs at their respective MBC concentrations. The resistant *E. faecalis* strains were grown on the MHA and incubated overnight at a temperature of 37 °C. Then, the zone of inhibition or the inhibitory diameter was measured [82]. The autoclaved distilled water was used as negative control and the standard antibiotic, Methicillin was used as positive control in this experiment.

2.2.4.4. Bacterial cell-survivability assay

The bacterial cell survivability was envisaged with the help of the 3-(4, 5-dimethylthiazol-2-yl) -2, 5-diphenyltetrazolium bromide (MTT) assay following a standard protocol [80]. The cell viability was examined after exposure to different concentrations of HAPNPs and was incubated for 24 hours at 37 °C. The bacterial cells were then collected and centrifuged at 1400 rpm for 10mins at 4 °C. The collected cells were then washed thrice with the help of autoclaved phosphate buffered saline (PBS, pH 7.4). The fresh culture media containing 0.5 mg.ml^{-1} of MTT reagent was then added by replacing the previous medium and was incubated for 3 hours at a temperature of 37 °C. The solution of HCl-isopropanol was added and was incubated for 15mins at room temperature. Then the absorbance of solubilized MTT formazan product was estimated by UV-Vis spectrophotometer (Epoch microplate reader, Bio-Tek, U.S.A) at a wavelength of 570 nm.

2.2.4.5. Determination of Intracellular uptake

Bacterial cells were treated with HAPNPs and incubated for 24 hours at 37 °C. Afterward, the bacterial cells were collected, washed with phosphate-buffered saline (PBS, pH 7.4), and treated with QS-labeled HAPNPs. The cells were then incubated in the dark at 37 °C for 12 hours. Unlabeled HAP nanoparticles were used as a negative control. The cells were washed and resuspended in PBS and the suspension was placed on a glass slide for imaging with a fluorescence microscope (DM 2500, Leica, Germany) at excitation wavelengths of 330-360 nm.

2.2.4.6. Determination of Intracellular ROS generation

Intracellular ROS generation was determined using the 2,7-dichlorofluorescein diacetate (DCFH$_2$-DA) assay. Bacterial cells were exposed to HAPNPs, cultured overnight, and then incubated with DCFH$_2$-DA in the dark at 37 °C for 30 minutes. The amount of intracellular

ROS generated within the bacteria was assessed using a fluorescence microscope (DM 2500, Leica, Germany) at an excitation wavelength of 504 nm and emission wavelength of 529 nm.

2.2.4.7. Morphological Change of Bacterial Cell Observed by FESEM

The bacterial cells were grown in 5ml culture media and were incubated in shaking conditions at 198 rpm at 37 °C for 12hrs [80]. Then the cells were treated with three different concentrations of HAP@VAN@FA (concerning the MBC concentration). The cells which were not treated with the HAPNPs were taken as a negative control. Then the cells were centrifuged at 5000 rpm for 5 minutes and were washed thoroughly with PBS. The obtained bacterial pellet was later fixed with the help of 2.5% glutaraldehyde and was then washed thrice with sterile PBS. Afterward, one drop of the fixed pellet was placed on the surface of a glass plate and was vacuum oven dried. The plate was then gold coated and alterations in the bacterial cell morphology were observed with a scanning electron microscope.

2.2.5. Cytotoxicity assay

The cell survivability of the human lung fibroblast cells WI-38 when treated with HAP nanoparticles 4s was envisaged by employing a standard protocol [83,84]. Briefly, the WI-38 cells were exposed to different concentrations of HAP nanoparticles and were then examined by MTT assay. The cells were grown in each well of 96-well plates at a density of 1×10^4 cells per well at 37 °C for 22-24 hours. The cells were then exposed to HAP NPs at different concentrations of 0-500 µg/ml for 24 hours. The cells after incubation were thoroughly washed with 1×PBS and incubated with a solution of MTT at a concentration of 450 µg/ml for a period of 3-4 hours at 37 °C. The resulting formazan crystals were then dissolved in a buffer that could solubilize the crystals. Then, the absorbances were measured at a wavelength of 570 nm with the help of a spectrophotometer (Epoch microplate reader, BioTek, U.S.A).

2.3. Statistical analysis

We repeated these experiments three times, and the data were expressed by calculating the standard deviation of all the experiments.

2.4. Results and Discussion

2.4.1. Physical Characterizations

2.4.1.1. X-ray Diffraction (XRD)
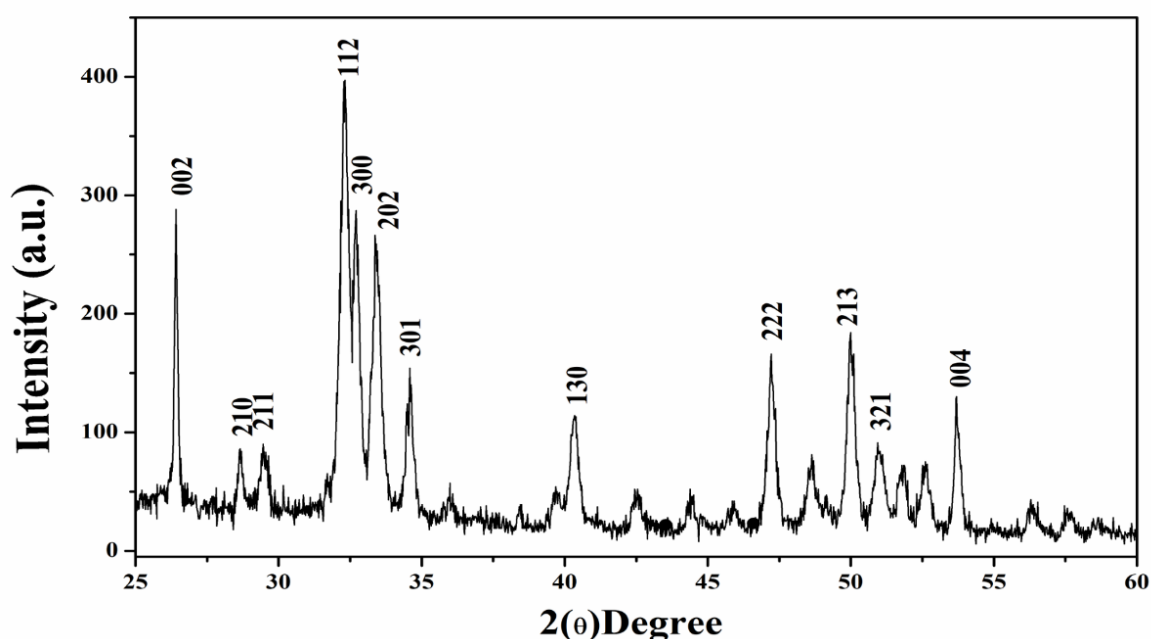
Figure.2.1. XRD analysis of Hydroxyapatite capped Vancomycin conjugated with Folic acid nanoparticles

Prominent diffraction maxima were shown by the synthesized nano-HAP sample, indicating that this ceramic nanomaterial was well crystalline (Figure.2.1.) [86,87]. The formation of hexagonal phase pure synthesized HAP nano-needles has been confirmed by using the JCPDS card (No: 74-0566). The absence of any unwanted diffraction maxima confirms the purity of the sample.

2.4.1.2. Fourier Transform Infrared Spectroscopy (FTIR)
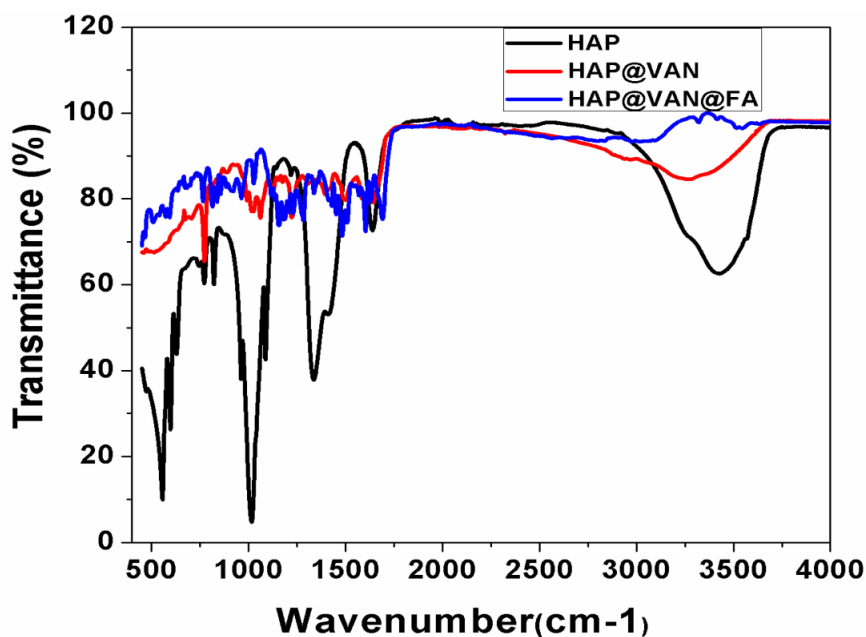
Figure.2.2. FTIR analysis of Hydroxyapatite capped Vancomycin conjugated with Folic acid nanoparticles

In FTIR spectra of our synthesized HAP nanoneedles, absorption peaks at 1460, 882 and 670 cm^{-1} correspond to the presence of the carbonate ions [88,89]. The carbonate ions may arise due to a reaction between atmospheric carbon dioxide and the solution during the synthesis process (Figure 2.2). The characteristic bands for $-PO_4^{3-}$ were exhibited at 471.2 (v_2 PO_4^{3-}) [90], 565 and 602.7 (v_4 PO_4^{3-}) [36], 962 (v_1 PO_4^{3-}), 1031 and 1095 (v_3 PO_4^{3-}) [92] and 1248 cm^{-1} (P-O stretching vibration of PO_4^{3-}) [93]. The band at 1382 cm^{-1} occurs due to the N-O stretching mode of NO^{3-} [94]. A broad band at 1633 and 3197 cm^{-1} corresponds to the presence of adsorbed water [92,93]. The medium band at 1355 cm^{-1} was attributed due to the OH in-plane bend [95].

The presence of the characteristic peaks of the bare folic acid at 3549, 3115, 1679, 1600, and 834 cm^{-1} established that folic acid was successfully attached to the surface of the HAP nanoparticles as shown in Figure.2.2. The peak of vancomycin and folic acid in the case of HAP@VAN@FA gets almost emerged because of similar functional groups. The broadness of the region 2900-3300 cm^{-1} with prominent FA peaks confirms the presence of VAN within the matrix of HAP nanoparticles and the folic acid conjugation on the surface of HAP nanoparticles. Thus, data of FTIR spectra confirm the conjugation of the drug molecule (VAN) and targeting ligand (FA) with the HAPNPs i.e., HAP@VAN@FA.

35

2.4.1.3. Field Emission Scanning Electron Microscope (FESEM)
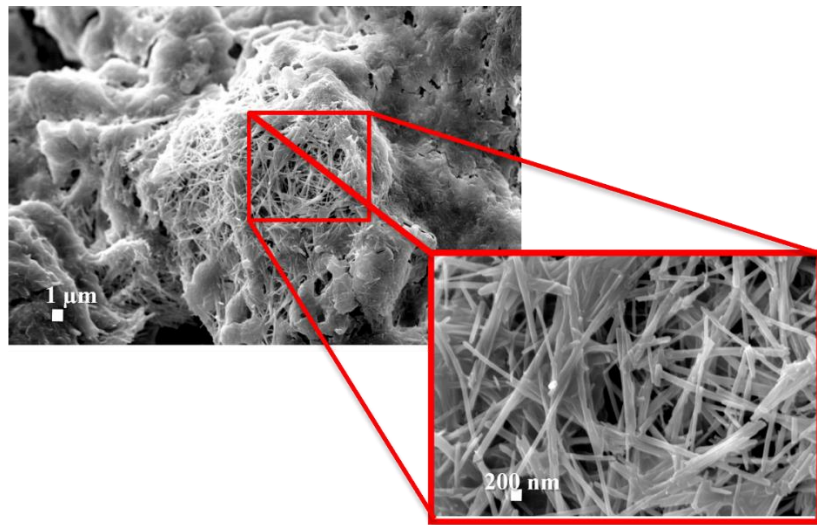
Figure.2.3. FESEM analysis of Hydroxyapatite nanoparticles

FESEM analysis was employed to investigate the surface morphology and size of the biomimetic HAP nano-carrier as shown in Figure 2.3. The synthesized HAP NPs were represented by a very well-dispersed and nearly needle-like uniform nanostructure, having a thickness of 70-80 nm and a length in the range of 1 μm for these needles. The small size of these HAP nanoneedles results in the highest amount of cohesive force between the grains of this sample, which may be the reason for the high agglomeration rate in HAP.

2.4.1.4. Transmission Electron Microscope
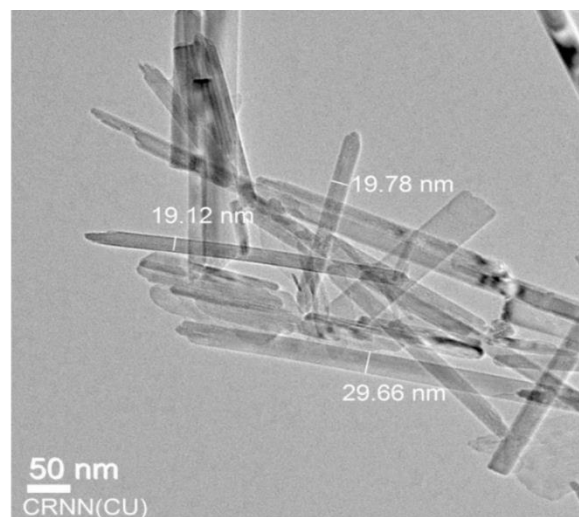
Figure.2.4. TEM analysis of Hydroxyapatite nanoparticles

36

TEM image reveals the nanosized crystal needle-shaped form of the HAPNPs in Figure.2.4. The average diameter of the particles is 20 nm approximately

2.4.1.5. DLS Analysis

Table: 2.1. Hydrodynamic Size Distribution

SAMPLE NAME	DLS SIZE (d. nm)	PDI	ZETA POTENTIAL (mV)
HAP	83.8	0.225	11.23
HAP@VAN	181.4	0.461	4.84
HAP @VAN@FA	343.9	0.585	-9.87

The hydrodynamic diameter of 181.14 ± 3.47 d. nm and zeta potential of 4.84 ± 1.97 mV were shown by the vancomycin-encapsulated HAP NPs (Table.2.1.). The zeta potential was not reversed by the encapsulation of vancomycin but it does enhance the hydrodynamic diameter. The bare HAP nanoparticles have a hydrodynamic size of 83.8 ± 2.43 d. nm. The conjugation of folic acid to the HAP nanoparticles increases the hydrodynamic diameter to 343.9 ± 4.86 d. nm and the zeta potential of the nanoparticles was reduced to -9.87 ± 2.35 mV [86]. This moderate negative zeta potential increases the stability of the nanoparticles. The samples have low polydispersity index (PDI) values, indicating that they form a homogenous solution [85]. This homogenous solution was conducive to biological applications.

2.4.2 Antibacterial activity

2.4.2.1. Determination of MIC and MBC

Figure.2.5.
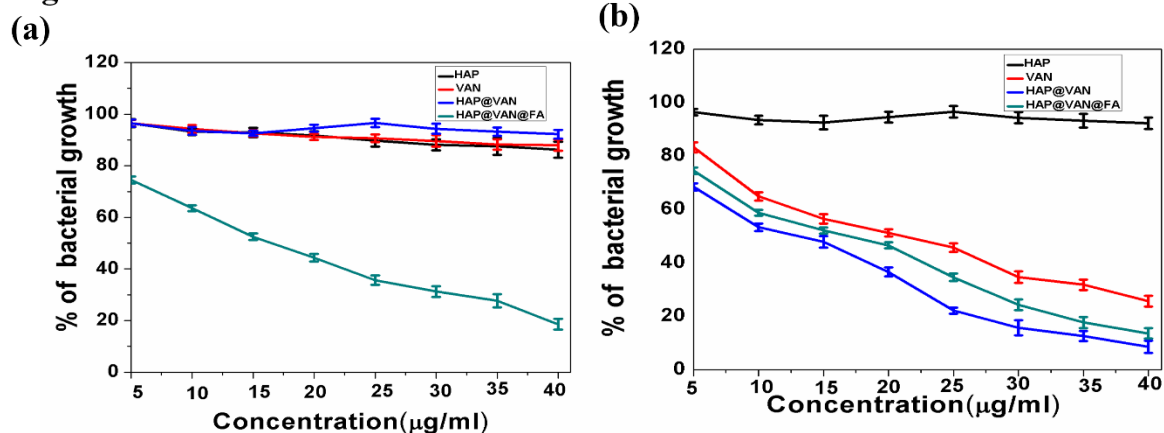
Figure.2.5. **Activity by MIC of Hydroxyapatite nanoparticles capped Vancomycin conjugated with Folic acid against pathogenic strains (a) MDR.** *Enterococcus faecalis* **(b)** *Enterococcus faecalis* **Vancomycin sensitive**

Table: 2.2. MIC values of synthesized nanoparticles

Name of Samples	MDR. *E. faecalis*	*E. faecalis*
VAN	NIL	$22.77 \pm 1.03 \mu g\ ml^{-1}$
HAP@VAN	$19.88 \pm 2.04\ \mu g\ ml^{-1}$	$18.46 \pm 1.2\ \mu g\ ml{-1}$
HAP@VAN@FA	$19.88 \pm 2.04\ \mu g\ ml^{-1}$	$15.54 \pm 1.43 \mu g/ml$

Bare vancomycin does not exhibit any antibacterial activity against MDR *E. faecalis* [96]. Additionally, no antibacterial activity was shown by HAP nanoparticles and the targeting ligand folic acid (Table.2.2). However, antibacterial activity to combat bacterial resistance in the case of *E. faecalis* was demonstrated by VAN encapsulated HAP (HAP@VAN) and folic acid conjugated HAP@VAN (HAP@VAN@FA). The bactericidal activity of the synthesized HAPNPs, HAP@VAN and HAP@VAN@FA was separately tested against vancomycin-sensitive *E. faecalis* and vancomycin-resistance *E. faecalis* strains. In case of the vancomycin-sensitive *E. faecalis* strain, the MIC values of $18.46 \pm 1.2\ \mu g\ ml{-1}$ and $15.54 \pm 1.43\ \mu g\ ml{-1}$ were observed for HAP@VAN and HAP@VAN@FA respectively, while bare vancomycin

exhibited a MIC value of 22.77 ± 1.03μg ml^{-1}. In contrast, no effect was observed when vancomycin and HAP@VAN nanoparticles were used against the resistant *E. faecalis* strain, whereas HAP@VAN@FA showed considerable antibacterial effect with a MIC value of 19.88 ± 2.04 μg ml^{-1} shown in Figure.2.5 (a) and (b).
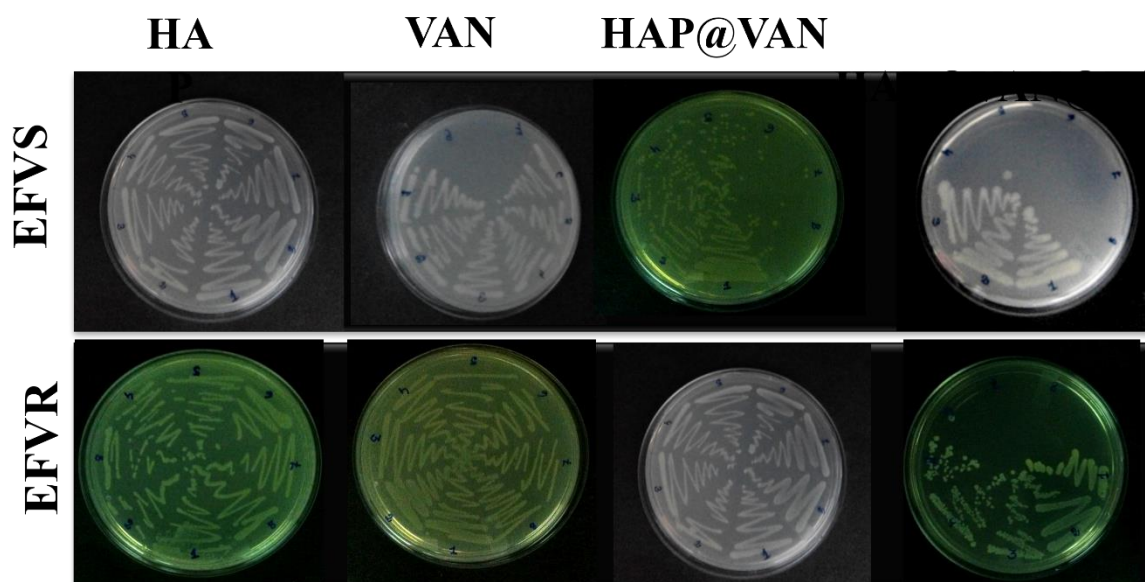
Figure.2.6. MBC plate of Hydroxyapatite nanoparticles capped Vancomycin conjugated with Folic acid against pathogenic strains

To avoid misinterpretation due to the turbidity of insoluble HAPNPs in the broth tube, the MBC assay was performed. Briefly, both the bacterial strains were cultured with the MIC dilutions on sterile agar plates and we examined the MBC [80]. The MBC concentrations were noted in cases where no visible bacteria growth was observed on the agar plates. The MBC values of HAP@VAN@FA were observed to be 70 μg ml^{-1} in the case of the resistant *E. faecalis* strains as shown in Figure2.6. The decrease in bacterial growth was contingent upon the increase in the concentration of HAP@VAN@FA. In this method, bacterial growths were effectively inhibited by the internalization of HAP@VAN@FA into the resistant *E. faecalis* cells. The MIC value of folic acid conjugated vancomycin-encapsulated chitosan nanoparticles against vancomycin-resistant *S. aureus* strain was reported at 2 μg/ml by Chakroborty et al., [69]. Qi et al found that in the case of mesoporous silica encapsulated vancomycin nanoparticles the MIC value against *S. aureus* was 200 μg ml−1 [71]. Chowdhuri et al developed folic acid conjugated mesoporous ZIF nanoparticles for the delivery of vancomycin to multidrug-resistant *Staphylococcus aureus* strains (MRSA) and reported their MIC and

MBC values as 8µg ml^{-1} and 16µg ml^{-1} respectively [73]. Previous findings have depicted that hydroxyapatite nanoparticles have augmented the activity of vancomycin [78,79]. Wu et al reported that antibacterial activity at 0.5–10 µg ml^{-1} against common non-resistant pathogenic bacterial strains was shown by the vancomycin-loaded hydroxyapatites [78]. Furthermore, Ghosh et al observed that antibacterial activity against the pathogenic bacterial strains was achieved by a composite containing 0.02 grams of vancomycin and hydroxyapatite [79]. Therefore, from this study, it can be concluded that significant bactericidal activity was exhibited by the HAP@VAN@FA nanoparticles against resistant *E. faecalis* strains.

2.4.2.2. Agar well diffusion study
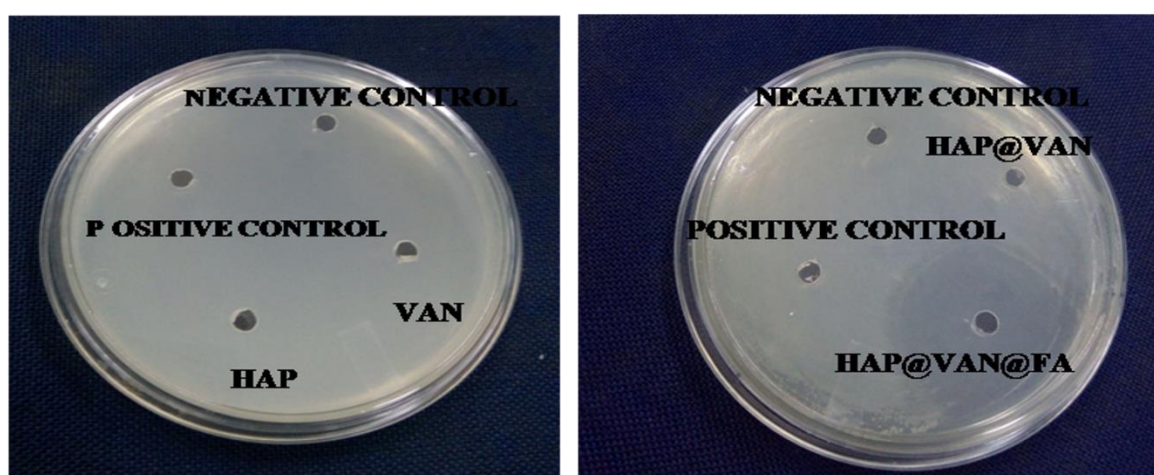
Figure.2.7. MBC plate of Hydroxyapatite nanoparticles capped Vancomycin conjugated with Folic acid against pathogenic strains

This study was performed to visualize the comparison of the antibacterial activity of different HAP samples. The zone of inhibition of Gram-positive vancomycin resistant *E. faecalis* against HAP@VAN@FA, HAP@VAN, VAN, distilled water (as a negative control), standard antibiotic, methicillin (as a positive control) was shown in Figure2.7. No zone of inhibition was observed in the case of the HAP@VAN, VAN, and distilled water, but a clear zone of inhibition was observed around the disc in the case of HAP@VAN@FA. A Zone of inhibition having a diameter of around 18 ± 0.5 mm was observed when the MDR *E. faecalis* strain was treated with HAP@VAN@FA at a concentration of 70 µg ml−1 (MBC). The zone of inhibition in the case of disc agar diffusion study of ZIF@VAN@FA in MRSA was reported to be 14 ±

0.5 mm by Chowdhuri et al [73]. This study vividly elucidates the efficacy of HAP@VAN@FA against the resistant *E. faecalis*.

2.4.2.3. Determination of tolerance level

The tolerance level of *E. faecalis* strains against HAP@VAN@FA was estimated from the respective MIC and MBC values. Our results suggest that the tolerance level of Gram-positive vancomycin resistant *E. faecalis* to HAP@VAN@FA was 4.02. The values of the tolerance level help in the differentiation between the bactericidal agents and bacteriostatic agents. The folic acid conjugated vancomycin loaded chitosan nanoparticles were reported to exhibit a tolerance level of 5 towards vancomycin resistant *S. aureus* strains [69]. The value of tolerance level in the case of the ZIF@VAN@FA against resistant *S. aureus* strain was observed to be 2.0 by Chowdhuri et al [73]. The bactericidal agents were known to be responsible for the killing of the bacteria while the bacteriostatic agents lead to the inhibition of bacterial growth. Antibacterial agents were noted as bacteriostatic when this ratio of MIC/MBC was more than or equivalent to 16 for a specific bacterium and bactericidal agents when this ratio was equal to or less than 4 [81]. Here, the MBC/MIC ratio was considered an important paradigm in examining the antibacterial capability of our synthesized nanoparticles, HAP@VAN@FA. Our results reflect that HAP@VAN@FA has the potential to be considered an effective bactericidal agent against MDR *E. faecalis*.

2.4.2.4. Intracellular internalization of functionalized HAP
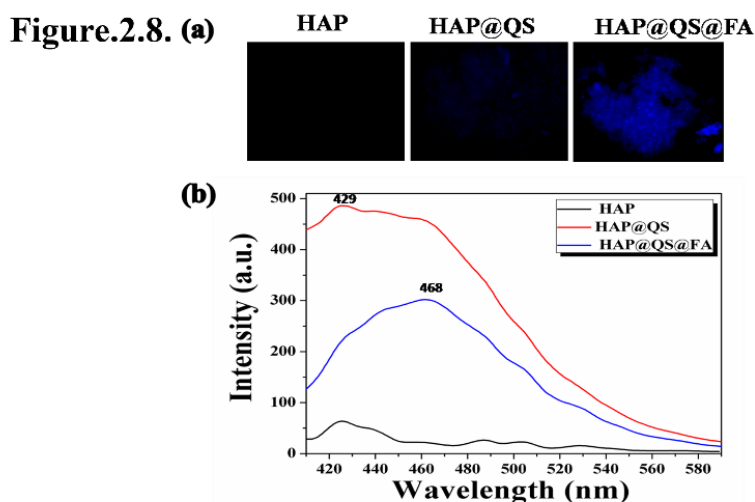
Figure.2.8. Intracellular uptake of HAP@QS@FA (a) Fluoresence image (b) Photoluminescence spectra in vancomycin resistant *Enterococcus faecalis* strain

The primary requisite for the action of an antibiotic was binding with the cell wall and subsequent cellular internalization. To demonstrate the uptake of HAP by MDR *E. faecalis*, QS-labelled HAPNPs were exposed to bacterial strains, and fluorescence images were captured (Figure.2.8(a)). The results show that QS-labelled HAP@FA was successfully internalized into the resistant *E. faecalis* cells, whereas the QS-labelled HAP failed to do so. The QS labeled HAP@FA was found to be uniformly dispersed within the cytoplasm, providing its successful internalization within the *E. faecalis* cells. The internalization of nanoparticles was generally contingent upon various physical characteristics such as size, shape, and surface charge. Typically, this internalization occurs in two steps with the nanoparticles first binding to the cell membrane, followed by their subsequent internalization into the cells. In this scenario, the internalization of QS labeled HAP@FA was mediated by endocytosis facilitated by the folate receptors present on the membrane of *E. faecalis*. The endocytosis process involves the uptake of HAPNPs through membrane invagination, leading to the formation of intracellular vesicles that encapsulate the nanoparticles and facilitate their transportation within the cells [73]. Similar internalization mechanisms were observed in *E. coli* and *S. aureus* bacterial strains treated with FITC-tagged vancomycin encapsulated mesoporous silica nanoparticles by Qi et al [71]. Chowdhuri et al also delineated a similar mechanism of internalization of their synthesized functionalized nanoparticles, ZIF@VAN@FA [73]. From these observations, we can conclude that HAP@VAN@FA nanoparticles can successfully deliver vancomycin inside the MDR *E. faecalis* by following a similar endocytotic pathway.

The photoluminescence studies confirm the distinct peak at 429 nm in the case of the sample HAP@QS Figure.2.8. (b). This peak was congruent with that of the emission spectra of quinine sulfate [98,99] indicating the successful encapsulation of quinine sulfate within the HAP nanoparticles. The bare HAP nanoparticles were optically inactive. However, a prominent bend was observed at 468 nm in the case of HAP@QS@FA which was possibly due to the conjugation of folic acid which has an emission spectrum at 490 nm [100].

2.4.2.5. Bacterial cell viability assay

HAP@VAN@FA decreased the viability of the MDR *E. faecalis* to 37.57% in comparison to the control group at 70 µg ml−1 (MBC) as displayed in Figure.2.9 (a). This decrease may be attributed to the successful internalization of HAP@VAN@FA within the *E. faecalis* cells, which, in turn, inhibits bacterial growth and causes bacterial cell death. According to the previous report of Chowdhuri et al., the cell viability of multidrug-resistant *S. aureus* was

diminished by 38.57% and 84.03%, at 8 µg ml−1 (MIC) 16 µg ml−1 (MBC) of ZIF-8@FA@VAN treatment, respectively [73]. The results suggest that the folic acid conjugated vancomycin-encapsulated HAP nanoparticles exhibit both bacteriostatic and bactericidal activities.

2.4.2.6. Determination of ROS Generation
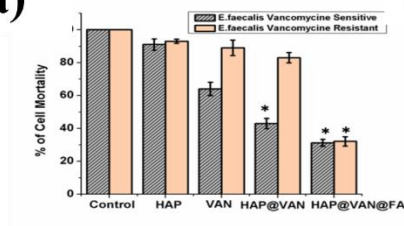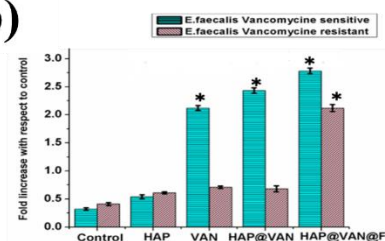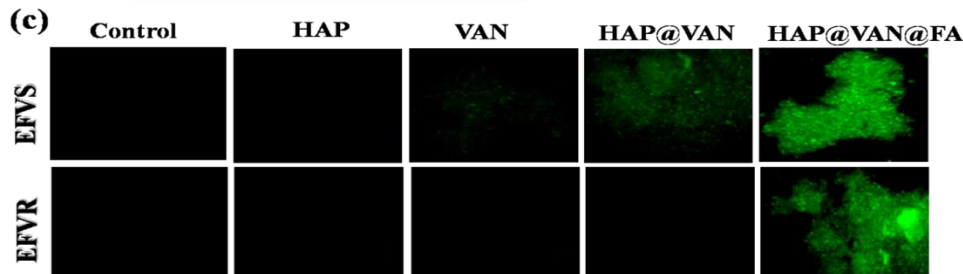
Figure.2.9. (a) Bacterial cell viability by MTT (b) Intracellular ROS generation (c) Fluorescence microscopic image of intracellular ROS generation

The production of intracellular ROS was thoroughly examined to delve into the mechanisms behind the bactericidal activities of HAP@VAN@FA, as elucidated in Figure2.9. (b) and (c). The DCFH-DA was used as an intracellular ROS indicator to estimate ROS levels in HAP@VAN@FA treated bacterial cells. The results clearly depict the enhanced generation of ROS, indicated by the augmented fluorescence intensity in the bacterial cells treated with HAP@VAN@FA, while the untreated cells exhibit negligible fluorescence intensity. Enhancement of ROS also occurred upon delivery of vancomycin via ZIF@FA as observed by Chowdhuri et al [73]. Thus, we can conclude enhancement of intracellular ROS generation was responsible for the antibacterial activity of the HAP@VAN@FA. Increased production of intracellular ROS disrupts the electronic transport chain, degrades genetic materials, and damages the bacterial cell membrane [80].

2.4.2.7. Bacterial morphology study by FESEM

Figure.2.10. (a)
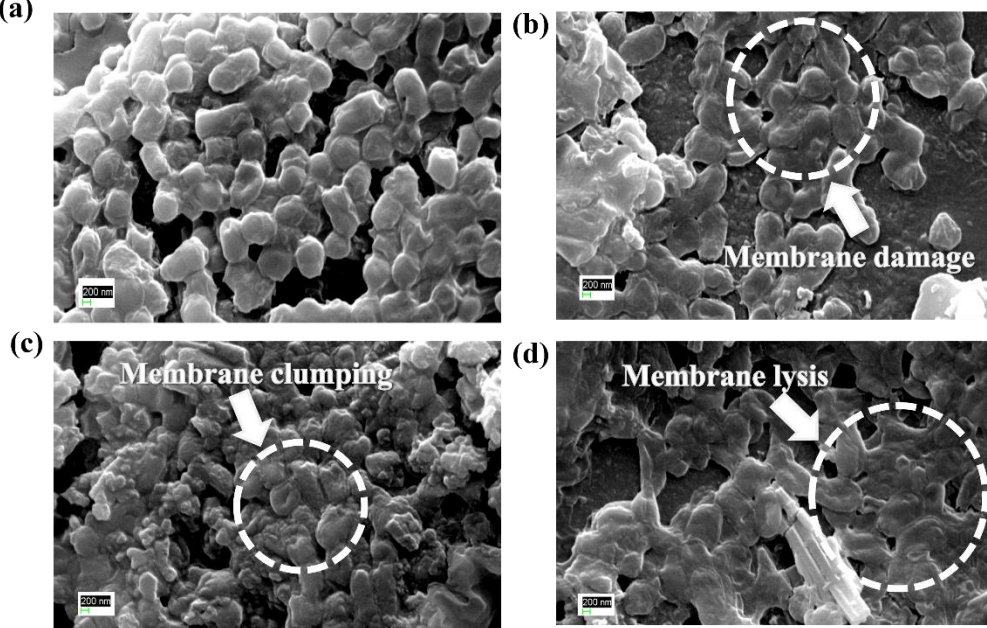
Figure.2.10. FESEM image of (a) Untreated and treated Vancomycin resistant *Enterococcus faecalis* with HAP@VAN@FA at concentration (b) 20µl/ml (c) 40µl/ml and (d) 70µl/ml with cells

The images obtained from SEM of vancomycin resistant *E. faecalis* cells treated with HAP@VAN@FA and untreated cells were displayed in Figure.2.10. The SEM images reveal that the untreated cells were smooth, unaltered, and possess features that were like the native cells. On the other hand, the treated resistant *E. faecalis* cell shows signs of maximum membrane damage. A substantial number of treated *E. faecalis* cells exhibit signs of fragmentation, leakage, perforation, and innumerable gaps in the cell membrane. Our study clearly depicts that the treatment with HAP@VAN@FA was the reason behind the aberration in the bacterial membrane morphology. This, in turn, leads to enhanced permeability, which favors the cell membrane-mediated transport of the nanoparticles. The damage to DNA and the perturbance of cellular response were due to the penetration of the HAP@VAN@FA into the bacterial cells and its subsequent interaction with DNA. According to the previous report by Qi et al vancomycin encapsulated mesoporous silica caused intense membrane damage in *E. coli* and *S. aureus* bacterial strains [71]. Chowdhuri et al also reported that ZIF@VAN@FA caused cell membrane damage in multidrug-resistant *S. aureus* [73]. The most probable mechanism behind the antibacterial activity of HAP@VAN@FA was its easy penetration into the cell through endocytosis via the folate receptors and its effective production, leading to the inhibition of bacterial cell growth.

2.4.3. Biocompatibility study
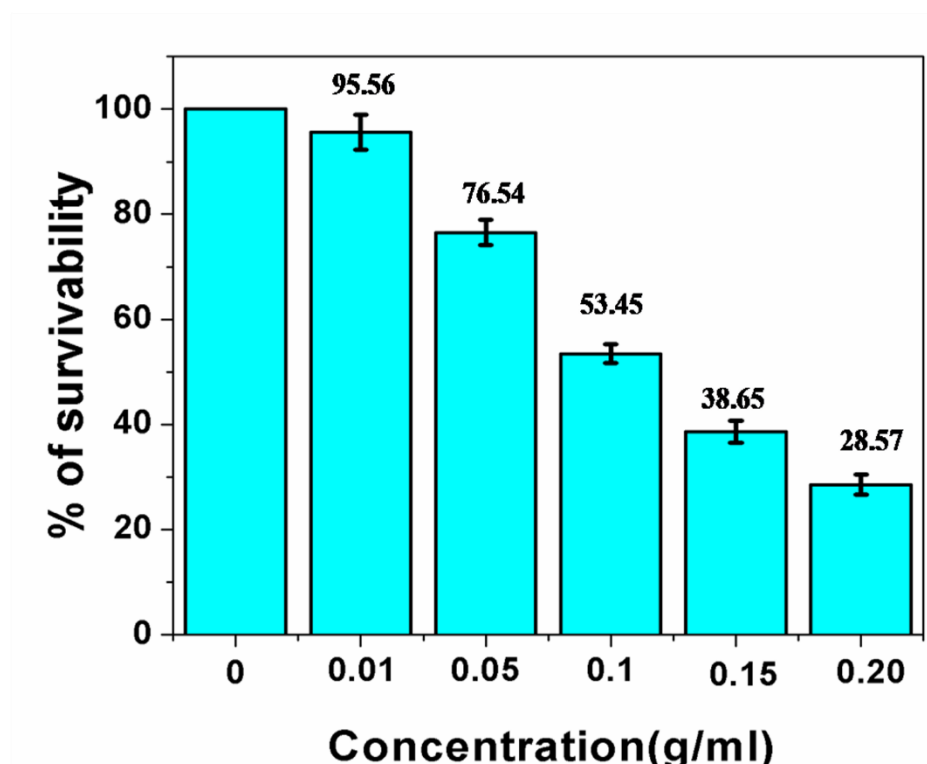
Figure.2.11. Cell viability assay by treatment with Hydroxyapatite nanoparticles

The in vitro cytotoxicity of the HAP nanoparticles was estimated for biocompatibility assay on the WI-38 cell line (Figure.2.11). Toxicity at a very high concentration of 0.1 g ml^{-1} is exhibited by the HAP nanoparticles. However, no such toxicities were observed when the cells were treated with HAP nanoparticles at lower concentrations. Therefore, it can be concluded that the HAP NP has commendable biocompatibility and was ideal for biological applications. According to a previous report, the LD$_{50}$ value of hydroxyapatite-silica nanocomposite was reported as 0.1g ml^{-1} [97]. In this case, the LD$_{50}$ value of our synthesized hydroxyapatite nanoparticles was 0.127 g ml^{-1}.

2.5. Conclusion

Here vancomycin has been successfully encapsulated within the HAP nanoparticles, and their surface has been modified through folic acid conjugation using a facile synthesis process. Emphasis has been placed on the functionalized of biocompatible hydroxyapatite nanoparticles through folic acid conjugation to facilitate the delivery of vancomycin to the resistant

pathogenic MDR *E. faecalis*. Our results clearly depict that the functionalized HAPNPs exhibit good biocompatibility and demonstrate excellent selective antibacterial activity against MDR *E. faecalis*. Our strategy can be instrumental in the delivery of various conventional antibiotics such as penicillin, methicillin, erythromycin, amikacin, ciprofloxacin, tetracycline, oxacillin, cefotaxime, etc., to numerous multidrug-resistant strains like *E. faecalis*. Thus, it can be concluded that our synthesized biocompatible HAPNPs fulfill all the criteria to emerge as a promising ameliorative agent against a wide range of multidrug-resistant bacteria infections that cripple modern society.

CHAPTER 3

Gum Acacia Capped Zinc oxide Nanoparticles, A Smart Biomaterial For Cell Imaging And Therapeutic Applications

Summary

Zinc oxide nanoparticles (ZnONPs) have become increasingly prominent in various biomedical applications. To achieve a cost-effective and environment-friendly synthesis, we utilized the leaf extract of *Ocimum sanctum* (Tulsi), a widely available medicinal plant, for the phytosynthesis of ZnONPs. This green synthesis method was not only facile but also generates negligible hazardous impact. To improve the bioavailability and therapeutic efficacy of the biogenic ZnONPs, we employed gum acacia, a well-known natural polymer, as a capping agent. Additionally, we tagged these nanoparticles with a fluorescent dye, rhodamine-B, enabling cellular imaging applications. The characterization of the nanoparticles was conducted using various biophysical methods such as UV-vis spectroscopy, X-ray diffraction (XRD), Fourier-transform infrared spectroscopy (FTIR), and field-emission scanning electron microscopy (FESEM) to confirm their successful synthesis. Subsequently, we evaluated their antibacterial and anticancer efficacy. The results demonstrated that these nanoparticles induce oxidative stress in both eukaryotic and prokaryotic cells, making them effective against pathogenic bacterial strains and hepatocellular cancer cells. Moreover, the nanoparticles exhibited a pH-responsive behavior, qualifying them as a potential cancer therapeutic delivery system. The rhodamine-B tagged nanoparticles also possess fluorescence properties, making them suitable for bioimaging applications. In the future, these nanoparticles could be conjugated with cancer-specific targeting ligands, further enhancing their therapeutic and diagnostic capabilities.

3.1. Introduction

Zinc oxide nanoparticles (ZnONPs) have garnered significant attention in the biomedical field. Researchers have been actively exploring ways to modify Zinc oxide to enhance its properties and improve its biocompatibility. Notably, ZnONPs have been recognized as effective antimicrobial agents [100,101]. In recent times, there has been growing interest in utilizing natural polymers and green-synthesized metals for various biological applications [102-111]. Numerous efforts have been made to increase the bioavailability of zinc by incorporating it within natural or synthetic polymer matrices [112-139]. For instance, combining ZnONPs with different natural polymers and synthetic materials has been an area of exploration for improving its functionality and applicability in various biomedical contexts. Enhancing the functionality of Zinc Oxide Nanoparticles Encapsulated in Biopolymers for biomedical applications. Various polymers, including collagen, dextran, gelatin, and polyvinyl alcohol, have been extensively studied as wound dressing materials by researchers [140-150]. Gum acacia (GA), a natural polymer extracted from the acacia tree, has recently gained popularity in biomedical applications due to its excellent biocompatibility and biodegradability [151-159]. Chopra et al. [160] developed alginate/gum acacia encapsulated GA@ZnONPs and demonstrated their antibacterial effectiveness against pathogenic *Pseudomonas aeruginosa*. Similarly, Bajpai et al. [161] fabricated ZnONPs loaded gum acacia/poly sodium acrylate hydrogels and validated their antibacterial efficacy against *E. coli.*

However, until now, there have been no efforts to further enhance the functionalities of these polymer-encapsulated ZnONPs. Moreover, various studies have explored the extraction of zinc from different plants [162-165].

In this study, we adopted an eco-friendly and cost-effective approach to synthesize ZnONPs using the well-known medicinal plant, *Ocimum sanctum* (Tulsi). The aromatic and cooling leaves of Tulsi possess anticancer, anti-inflammatory, diuretic, and various other medicinal properties [166-170]. These leaves contain several phenolic phytochemicals, such as quercetin, luteolin, cyclopropylidene, eugenol, germacrene, β-caryophyllene, β-element, and carvacrol [171]. The prevalence of flavonoids like quercetin in *Ocimum sanctum* facilitates the formation of chelating complexes with zinc ions, thereby stabilizing these metallic ions [172]. Furthermore, these phenolic compounds have the capability to reduce metallic salts into metal oxides through electron transfer and functionalize the particle surface. Hence, the aqueous extract of *O. sanctum* plays a vital role in the colloidal precipitation synthesis of ZnONPs [171].

3.2. Experimental section

3.2.1. Materials

3.2.1.1. Chemical Ingredients

All the reagents and chemicals (except the zinc salt) used for this study including bacterial culture media, fluorescence stains, MTT reagent, glutaraldehyde, and Rhodamine-B were purchased from Merck Ltd, HiMedia, and SRL Pvt. Ltd, Mumbai, India. AR-grade Zinc nitrate ($ZnNO_3$) was purchased from Sigma-Aldrich Chemicals. Fresh *Ocimum sanctum* (Tulsi) leaves were purchased from the nearby market. Throughout the study deionized (Millipore) water of resistivity at least 18 MΩ-cm has been used. The glass wares were thoroughly washed before the performance of each experiment by using the aqua regia solution and then were rinsed with distilled water.

3.2.1.2. Bacterial Strain

The Gram-positive strains used in microbiological experiments were *Staphylococcus aureus* 740 and *Enterococcus faecalis* 441. *Escherichia coli* 443 and *Pseudomonas aeruginosa* 1688 were the Gram-negative strains used in this study. These bacterial strains were procured from the Microbial Type Culture Collection (MTCC), IMTECH, Chandigarh, India.

3.2.1.3. Cell line

Hep G2 (Hepatocellular carcinoma cell) and WI38 (human lung fibroblast) were used to determine the cytotoxicity assay obtained from the Central Cell Repository of the National Center for Cell Science (NCCS), Pune, India. All the above cell lines were cultured in the presence of Dulbecco's Modified Eagles Media (DMEM) supplemented with 10% FBS, 1 mM sodium pyruvate, 2 mM L-glutamine, non–essential amino acids, in the presence of antibiotic solution comprising 100 mg/L penicillin and 100 mg/L streptomycin. The cells were grown in a humidified atmosphere at a temperature of 37 ^{0} C in the presence of 5% CO_2.

3.2.2. Experimental methods

3.2.2.1. Preparation of Tulsi leaf extract

The leaves of Tulsi were thoroughly washed with deionized water and dried at room temperature. The dried leaves were then powdered using a mortar and pestle. Approximately 2 grams of the powdered leaves were added to 100 ml of distilled water and boiled for 2–3

minutes. After boiling the solution was cooled at room temperature and filtered using Whatman filter paper.

3.2.2.2. Preparation of Zinc Nitrate solution

1.0 mM ZnNO₃ was added to 20 ml of distilled water and continuously stirred for 2 to 4 hours.

3.2.2.3. Synthesis of Zinc Oxide nanoparticles

A dropwise addition of 10 ml filtered leaf extracts was made into 200 ml of prepared Zinc Nitrate stock solution. Subsequently, it was heated in a water bath at 90 °C for 1 hour.

3.2.2.4. Purification of synthesized Zinc Oxide nanoparticles

The ZnONPs obtained were purified by centrifugation at 9000 rpm for 25 minutes at room temperature. After removing the supernatant, the precipitate was re-dispersed in distilled water. The entire purification procedure was performed thrice.

3.2.2.5. Capping of ZnONPs with Gum Acacia and tagging with Rhodamine-B

GA was dissolved in lukewarm distilled water (kept at 45 °C) and continuously stirred for 24 hours. Then the solution of ZnONPs was added to the GA solution in a 2:1 w/v ratio. The Rhodamine-B was solubilized in water and was mixed thoroughly by constant stirring for 12 hours in a separate test tube. This Rhodamine-B solution was then slowly added to the GA@ZnSONPs solution in a 1:4 w/v ratio and continuously stirred for another 24 hours. Ultimately, the final solution was centrifuged at 10000 rpm for 10 minutes at room temperature to obtain the Rhodamine-B labeled GA@ZnONP (GA@ZnONP@RB). After discarding the supernatant, the precipitate was placed in a vacuum desiccator at room temperature for drying. Finally, the dried powder was mortared to achieve fine grains for further characterization.

3.2.3. Physical Characterization of GA@ZnONPs

The GA@ZnONPs were characterized with the help of Ultraviolet-visible spectrophotometer (Bio-tek), X-ray powder Diffractometer model D8, Bruker AXS, Wisconsin, USA, using Cu-Kα target operating at 35kV (wavelength -1.5418 Å and scan speed-1s/step), Field emission Scanning Electron Microscope (FESEM) using INSPECTF50 (FEI, Netherland) and EVO 18 Special Edition, Carl Zeiss, Germany for bacterial image, Image J software for size distribution analysis, Fourier transform infrared spectroscope (FTIR)-8400S, Shimadzu, DLS (Dynamic

light Scattering) (NANO ZS90, Malvern Instruments Ltd., UK). Fluorescence microscope (DM 2500 Leica, Japan).

3.2.4. Evaluation of antibacterial activity

3.2.4.1 Determination of minimum inhibitory concentration (MIC) and minimum bactericidal concentration (MBC)

The microdilution method was applied to determine the MIC and MBC values [80]. Total assays were performed in a biosafety cabinet to prevent any undesirable contamination.

3.2.4.2. Tolerance level

The tolerance level of each bacterial strain towards GA@ZnONPs can be predicted by the values of MIC and MBC. The tolerance level was determined by using the following formula [80].

Tolerance= (MBC) / (MIC)…………………………………………………………… (eq.1)

3.2.4.3. Agar well diffusion method

The susceptibility of pathogenic bacteria to GA@ZnONPs was examined by the Mueller-Hinton agar well diffusion method according to a previously reported protocol [80].

3.2.4.4. Intracellular ROS generation in Bacterial cells

The bacterial intracellular ROS generation was measured using 2, 7-dichlorofluorescein diacetate ($DCFH_2$-DA), following our previously reported protocol [128]. The $DCFH_2$-DA was to passively enter the cells, reacting with the generated ROS and undergoing oxidation, thereby forming a highly fluorescent compound 2, 7-dichlorofluorescein (DCF). After exposure to GA@ZnO@NPs, the bacteria cells were cultured overnight and washed with PBS solutions. Subsequently, the cells were incubated with the required amount of $DCFH_2$-DA at 37 °C for 30 minutes. Finally, the bacteria cells were visualized under a fluorescence microscope.

3.2.4.5. .Morphological change of Bacterial cells observed by FESEM

The treated (at their MBC value) and untreated (control) four bacterial strains were incubated for 16 hours at 37 ^{0} C. Next, the cells were prepared following a standard protocol [179].

3.2.5. Evaluation of anticancer activity

3.2.5.1. Cytotoxicity assay

The viability of Hep G2 cells after exposure to various concentrations of GA@ZnONPs was determined by 3- (4, 5-dimethylthiazol-2-yl)-2,5-diphenyltetrazolium bromide (MTT) assay [130-132]. Briefly, around 1×104 cells per well of 96-well plates were exposed to our synthesized sample at the concentrations of untreated as control, 20, 40, 60, 80, and 100 μg/ml for 24 hours of incubation at 37 ^{0} C and 5% CO_2. Following this, the cells were incubated again with 10 μl MTT solution (stock 1 mg/ml) for 4 hours at 37^0 C and 5% CO_2 following a wash with $1\times$ phosphate-buffered saline (PBS), and the resulting formazan crystals were dissolved in MTT solubilization buffer to measure the absorbance at 570 nm by using a microplate reader (Biorad). The data were formulated compared with the control ones.

3.2.5.2. Intracellular ROS generations in Hep G2 cells

Normally, the DCFDA enters the cell and reacts with the reactive oxygen to give a green fluorescent color compound dichlorofluorescein (DCF). Briefly, a stock solution of DCFDA (10 mM) was prepared in methanol and was further diluted with PBS to a working concentration of 100 μM. Hep G2 cells were treated with our synthesized sample at LD_{50} for 12 hours at 37 ^{0} C and washed with ice-cold $1\times$ PBS followed by incubation with 100 μM of DCFDA for 30 minutes in the dark at 37 ^{0} C [131,132]. The fluorescence intensity was measured both spectroscopically and under a fluorescence microscope in Hep G2 cells excitation and emission wavelengths of 485 nm and 520 nm respectively.

3.2.5.3. Study of intracellular uptake

Biogenic GA@ZnONPs were labeled with the fluorescent dye, Rhodamine-B for confirming the internalization of nanoparticles within the bacterial surface [157-160]. The images were obtained under a fluorescence microscope at an excitation wavelength of 510–550 nm.

3.2.5.4. Apoptotic cell quantification by AnnexinV-FITC staining

The quantification of the apoptotic cells was conducted with the help of the annexin V-FITC/PI double staining method by following a standard protocol [155].

3.2.6. Drug release study

Rhodamine-B released from the core of GA@ZnONP@RB was in vitro to confirm the release at different intervals, following a standard protocol [175,176] and measuring the absorbance at 544 nm using a standard curve of rhodamine-B [180].

3.3. Statistical analysis

We repeated these experiments three times and the data were expressed by calculating the standard deviation of all the experiments. Comparisons of the mean were done with the help of a model I ANOVA test (using a statistical package, Origin Pro 8, Northampton, MA 01060, USA) with multiple comparison t-tests, $p < 0.05$ as a limit of significance. The data was the average of three experiments $\pm$ SD. $*$ = represents p value < 0.05, $**$ = represents p value < 0.01, $***$ = represents p value < 0.001.

3.4. Results and Discussion

3.4.1. Physical Characterizations

3.4.1.1. X-Ray Diffraction (XRD)

XRD pattern of the biosynthesized GA@ZnONPs clearly indicates their crystalline nature, in Figure.3.1. The prominent diffraction peaks (2θ) were found at 31.48, 34.32, 36.36, 47.53, 56.52, 62.88, 67.82, and 76.5 degrees. The average size of ZnONPs was determined using the Debye–Scherrer equation considering the highest intense peak.

$$D = 0.9\lambda/\beta\cos\theta \dots\dots\dots\dots\dots\dots\dots\dots\dots\dots\dots\dots\dots\dots\dots\dots\dots\dots\dots\dots\dots\dots \text{(eq.2)}$$

where β represents the full width at half maxima of the diffraction peak (radian), Bragg's angle was denoted by θ in degree.
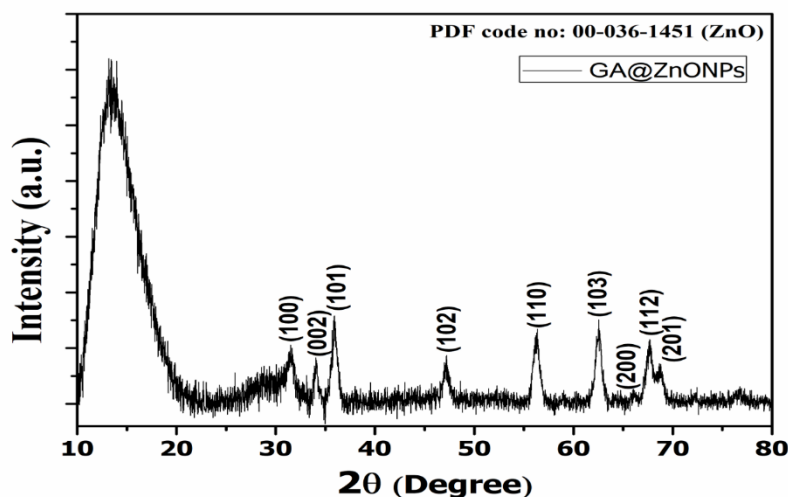
Figure.3.1. XRD analysis of Gum Acacia capped Zinc Oxide nanoparticles

The particle size of these GA@ZnONPs was in accordance with the relevant literature [101, 140]. FWHM (β) = 0.011 17. Average diameter $\langle D_{101}\rangle$ of ZnO = 13.04 nm. These peaks were attributed to the crystallization of GA@ZnONPs. All the peaks can be assigned with the PDF code No. #00-036-1451. The XRD pattern also exhibits an amorphous nature in the diffraction pattern for the 2θ value ranges from 10 to 20°, indicating low crystallization of gum acacia extract.

3.4.1.2. Fourier Transform Infrared Spectroscopy (FTIR)
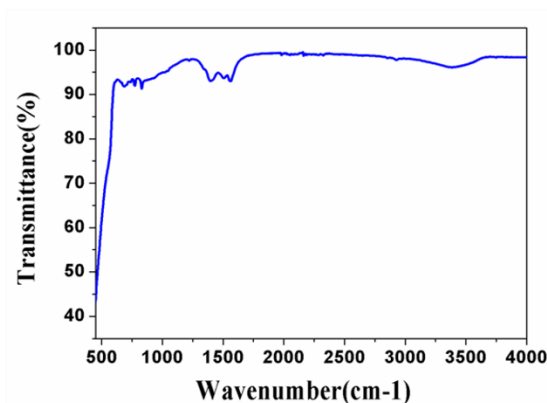
Figure.3.2. FTIR spectra of Gum Acacia capped Zinc Oxide nanoparticles

The FTIR spectra of the biosynthesized GA@ZnONPs were displayed in Figure.3.2. FTIR was performed to determine the purity of the nanoparticles and confirmed the prevalence of different phytochemicals in the *O. sanctum* leaf extract. The characteristic peaks at 1634 and

(600, 450) cm^{-1} for the synthesized ZnONPs were congruent with that of the Zn–O vibration arising due to stretching and deformation [168, 169]. The prominent bands were at 3408 cm^{-1} (–OH stretching), 2936 cm^{-1} (stretching of –CH) and characteristic peaks of vibration at 1624 cm^{-1} and 1427 cm^{-1} (asymmetric as well as symmetric stretching of -COO^{-}) also suggest the presence of GA@ZnONPs.

3.4.1.3. UV Visible Spectroscopy
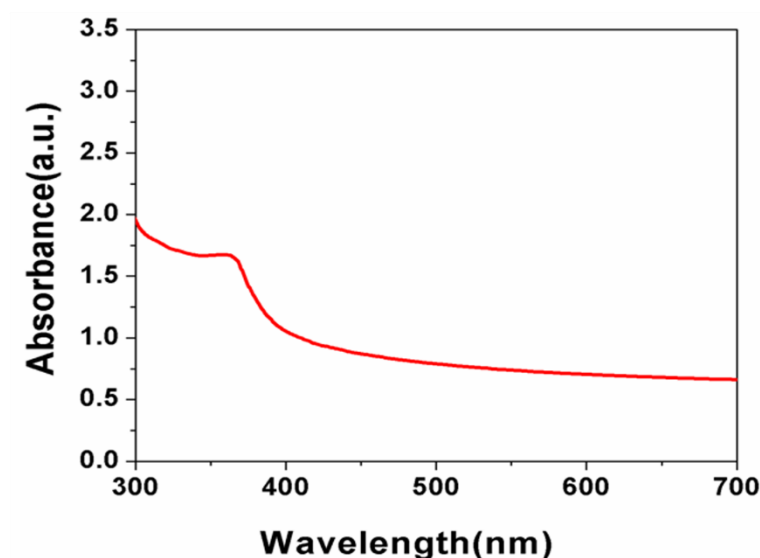
Figure.3.3. UV-Visible spectra of Gum Acacia capped Zinc Oxide nanoparticles

The results of UV−visible absorption is shown in Figure.3.3. confirming the formation of GA@ZnONPs. The characteristic peak of GA@ZnONPs was found around 350 nm, indicating their large excitation binding energy at room temperature [168].

3.4.1.4. Field Emission Scanning Electron Microscope (FESEM) analysis

The morphological modification of synthesized GA@ZnONPs was determined by the FESEM analysis Figures.3.4. (a) and (b). The micrograph of GA@ZnONPs shows that they had a spherical shape and uniform distribution. The FESEM results confirm the presence of spherical ZnONPs within a sheath of the biopolymer gum acacia with a size range between 300–380 nm, Figure.3.4. (c) (average particle size of 340 nm). From the FESEM images GA@ZnONPs capping was confirmed.

Figure.3.4.(a)   **(b)**

(c)
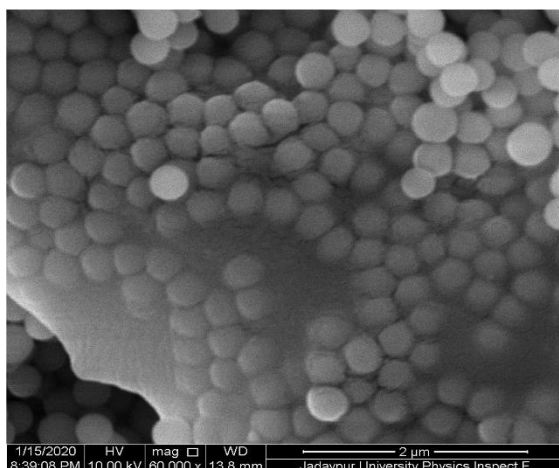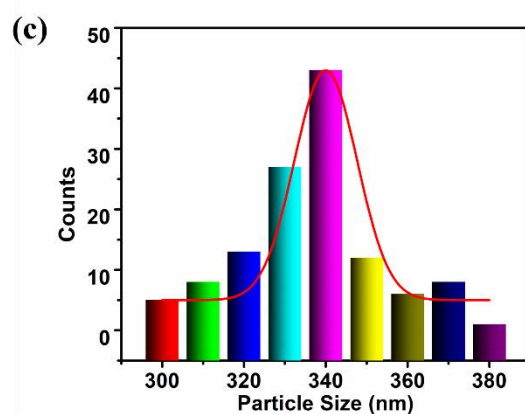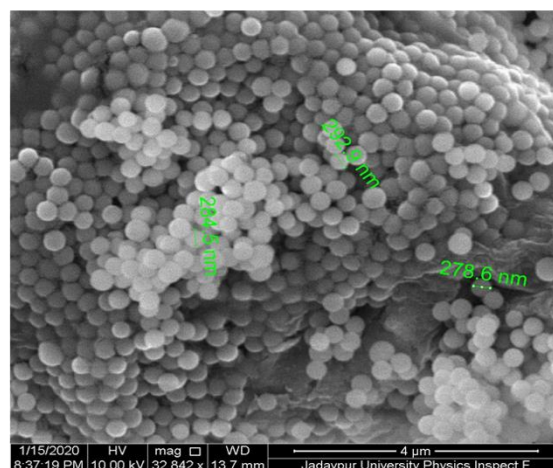
Figure.3.4. FESEM analysis (a) Gum Acacia capped Zinc Oxide nanoparticles (b) Zinc Oxide nanoparticles (c) Size distribution curve

3.4.1.5. DLS Analysis

Table.3.1. **Hydrodynamic Size Distribution**

SAMPLE NAME	DLS SIZE (d.nm)	PDI	ZETA POTENTIAL (mV)
GA@ZnONPs	253.8±4.4	0.225±0.075	12.23±1.4

The size distribution of the GA@ZnONPs was determined by DLS (Table.3.1). The Particle size distribution curve reveals that GA@ZnONPs obtained were homogeneous in nature, having a polydispersity index (PDI) of 0.225 with an average diameter of about 254 nm. The zeta potential of the GA@ZnONPs was measured at 12.23 mV indicating the moderate stability

of the sample. DLS and Zeta potential study suggests that the particles were quite conducive to biological applications.

3.4.2. Evaluation of antibacterial activity

3.4.2.1. Determination of MIC and MBC

Table.3.2. Determination of MIC and MBC values

Name of Samples	Bacterial Strain	MIC	MBC
GA@ZnONPs	*Staphylococcus aureus*	15.54 ± 1.37µg/ml	59 µg/ml
	Enterococcus faecalis	22.48 ± 2.4 µg/ml	81 µg/ml
	Escherichia coli	36.46 ± 1.8µg/ml	135 µg/ml
	Pseudomonas aeruginosa	42.32 ± 2.9µg/ml	148 µg/ml
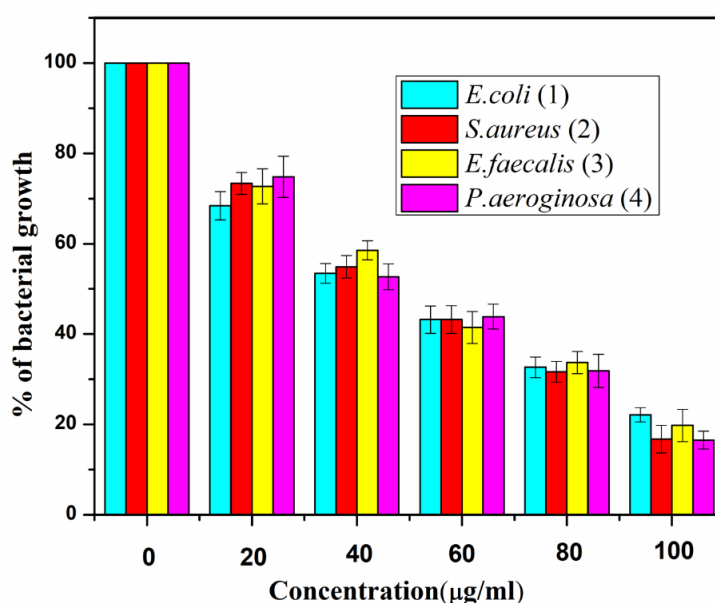
Figure.3.5. Bacterial viability by treatment with Gum Acacia capped Zinc Oxide nanoparticles in pathogenic bacterial strains.

The antibacterial activity of the synthesized GA@ZnONPs was determined by separate treatment against Gram-negative and Gram-positive bacterial strains. MIC values of

58

GA@ZnONPs against *E. coli, P. aeruginosa, E. faecalis, S. aureus* were 36.46 ± 1.8, 42.32 ± 2.9, 15.54 ± 1.37, and 22.48 ± 2.4 µg/ml respectively as shown in Figure.3.5 and Table.3.2. The MIC dilutions of all the bacterial strains were streaked on sterile agar plates and incubated at 37 °C for 18–22 hours to evaluate their respective minimum bactericidal concentrations (MBC) [175, 179].

The concentration at which no visible bacterial growth was observed on the agar plate after treatment with GA@ZnONPs was considered as the MBC. The MBC values of GA@ZnONPs for *E. coli, P. aeruginosa, S. aureus, and E. faecalis* were found to be 135, 148, 59, and 81 µg/ml, respectively. Significant bactericidal activity of GA@ZnONPs against different bacterial strains was clearly depicted by the result.

3.4.2.2. Determination of tolerance level

The tolerance level of bacterial strains *E. coli, P. aeruginosa, S. aureus, and E. faecalis* against GA@ZnONPs was 3.7, 3.5, 3.9, and 3.6, respectively. The tolerance level represents the difference between bacteriostatic agents and bactericidal agents. When the value of MBC / MIC for a particular strain was greater than or equal to 16, this may be considered a bacteriostatic type and when the value was less than or equal to 4, it may be considered a bactericidal agent [175, 179]. The result clearly suggests that GA@ZnONPs exhibit significant bactericidal activity against pathogenic bacterial strains.

3.4.2.3. Agar well diffusion study
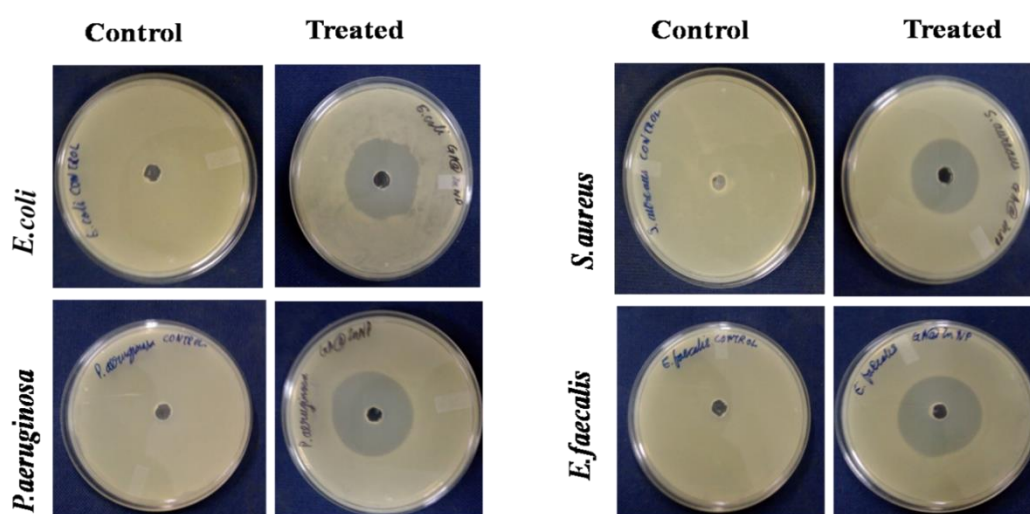
Figure.3.6. Agar well diffusion study of Gum Acacia capped Zinc oxide nanoparticles against pathogenic strains

The agar diffusion study was performed to compare the antibacterial activity of different strains treated with GA@ZnONPs. The inhibition zone of Gram-positive and Gram-negative bacteria was shown in Figure.3.6. This study reconfirms the bactericidal activity of GA@ZnONPs against different pathogenic bacterial strains.

3.4.2.4. Bacterial morphology study by FESEM
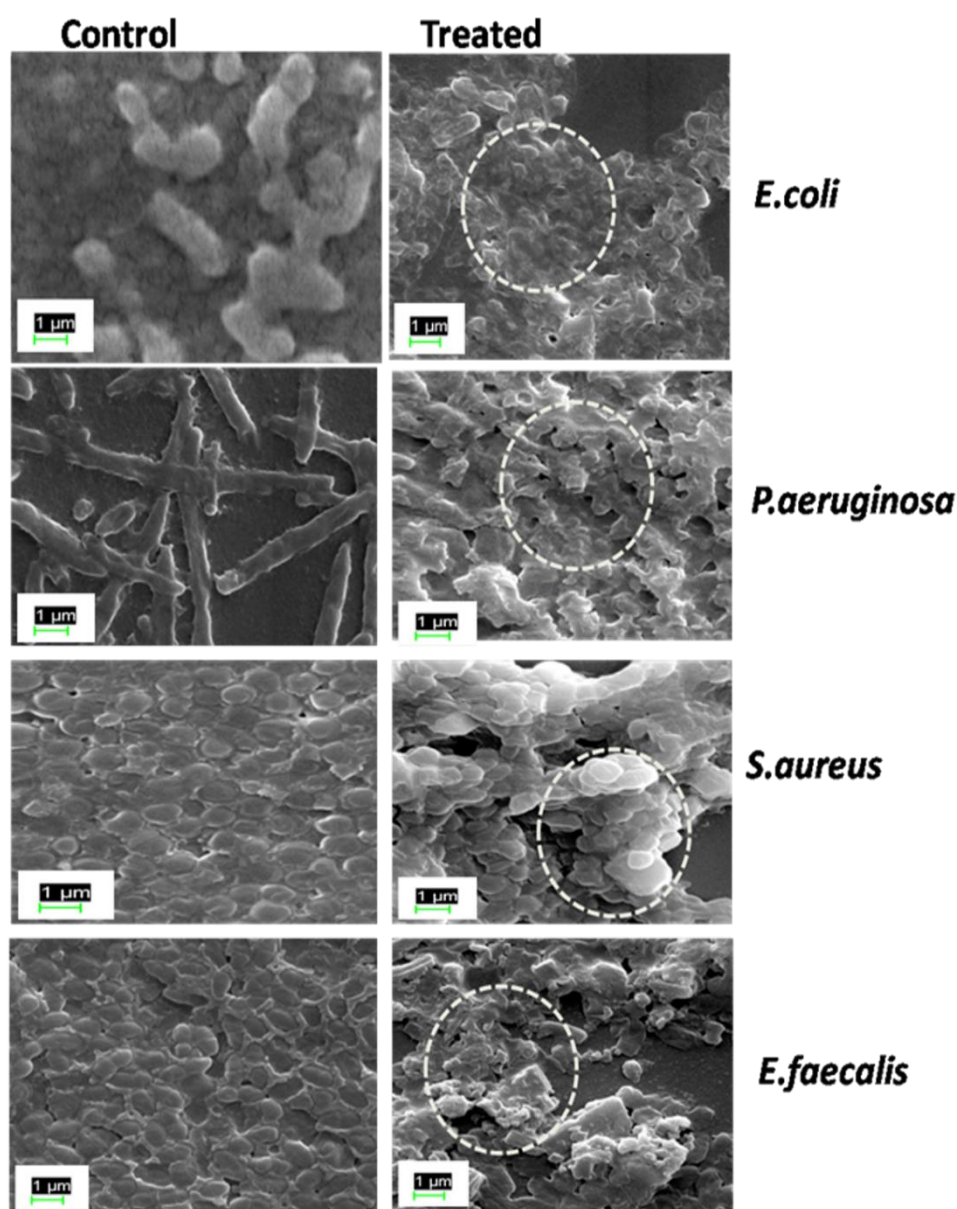
Figure.3.7. FESEM of Gum Acacia capped Zinc Oxide nanoparticles treated pathogenic bacterial strains.

The treatment with GA@ZnONPs causes alterations in the structural morphology of the bacterial cells, as shown in the FESEM results. The respective morphology was retained by the untreated bacterial strains, as shown in Figure.3.7. However, in the case of treated bacterial

cells, it was observed that the membrane was damaged, and cytoplasmic leakage led to agglomerated cell debris. The bacterial membrane was confirmed to be disrupted and perforated due to penetration of GA@ZnONPs or due to ROS generation as evidenced by FESEM.

3.4.2.5. Determination of ROS Generation
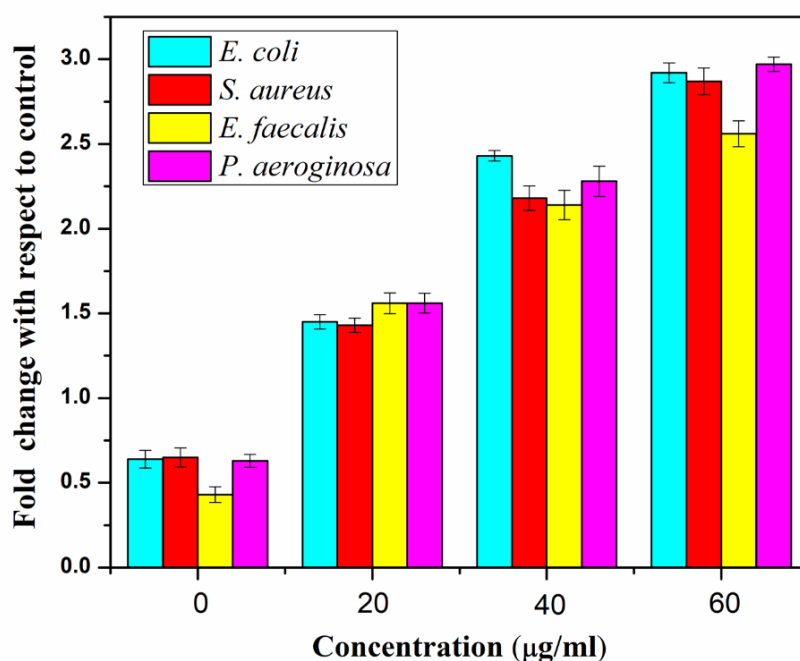
Figure.3.8. Intracellular ROS generation by treatment with Gum Acacia capped Zinc Oxide nanoparticles in pathogenic bacterial strains.

The Phytofabricated GA@ZnONPs could induce intracellular ROS generation, leading to bacterial cell death. The intracellular ROS generation in the bacterial cells was determined by employing DCFH-DA as an intracellular ROS indicator, as shown in Figure.3.8. The results indicated that the GA@ZnONPs treated pathogenic bacterial cells augmented ROS generation, which was responsible for bacterial cell death. The enhanced ROS production was correlated with the bacterial cell membrane, disruption in the electronic transport chain, and genetic material detonation [128, 129].

3.4.3. Anticancer activity against Hep G2 cells

3.4.3.1. Cytotoxicity Study

The in vitro cytotoxicity was estimated by exposing the HepG2 cells to different concentrations of GA@ZnONPs for 24 hours. This was followed by an MTT assay. It was noted that the GA@ZnONPs exhibit significant anticancer activity with an LD_{50} of 48 ± 3.24 µg/ml as shown in Figure.3.9. Therefore, we can conclude that the GA@ZnONPs have promising anticancer properties.
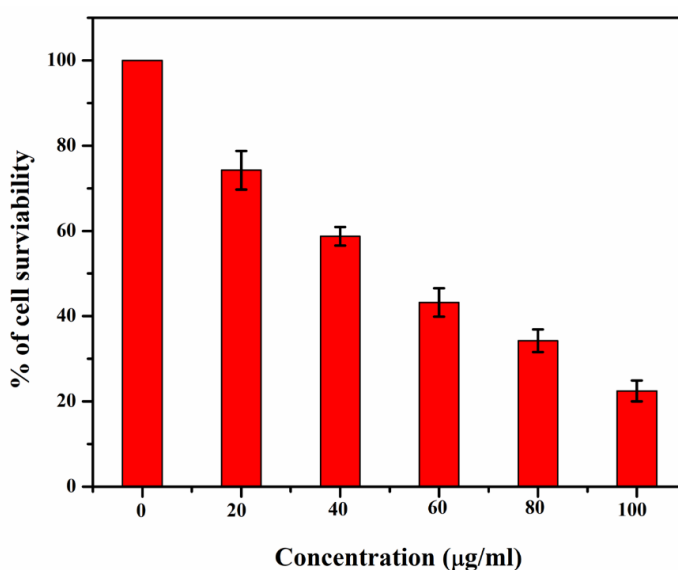
Figure.3.9. Cell viability assay by treatment with Gum Acacia capped Zinc Oxide nanoparticles in cancer cells

3.4.3.2. Study of Intracellular ROS generation

The content of intracellular ROS was intricately evaluated to investigate the cellular mechanisms responsible for the antibacterial activity of GA@ZnONPs as depicted in Figure.3.10. (a). The enhanced fluorescence intensity in the case of GA@ZnONPs treated bacterial cells was a positive indicator of increased levels of intracellular ROS. On the other hand, the untreated bacterial cells exhibit negligible fluorescence intensity. The increased production of intracellular ROS was responsible for the disruption in the electronic transport chain, degradation of the genetic material, and damage to the bacterial cell membrane [174, 175, 179]. Similarly, in the case of the eukaryotic cells, 2′, 7′ dichlorofluorescein diacetate (DCF-DA) was employed as a specific probe to envisage the reactive oxygen species (ROS) [176, 177]. The reactive oxygen production was measured in the case of hepatocellular cancer

cells, HepG2 where the cells were treated with GA@ZnONPs at their LD$_{50}$ dose for a period of 12 hours. The results procured from the fluorescence microscope and spectrofluorometer delineate the enhancement of green color fluorescent intensity in the case of the treated HepG2 cells after the incubation time of 12 hours, as depicted in Figures.3.10. (a) and (b).

Figure.3.10.(a)
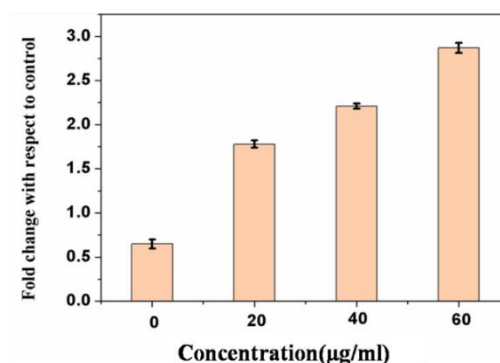
(b)
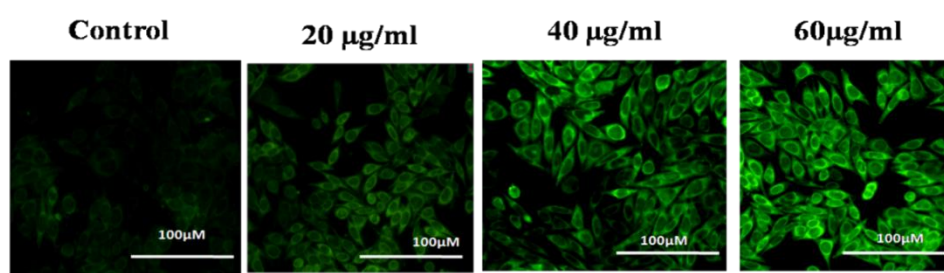
Figure.3.10. (a) Intracellular ROS generation (b) Fluorescence microscopic image by treatment with Gum Acacia capped Zinc Oxide nanoparticles in carcinoma cells

3.4.3.3. Quantification of apoptotic cells

Figure.3.11. (a)
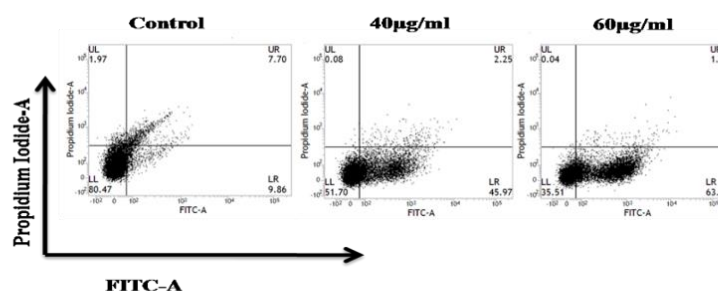
(b)
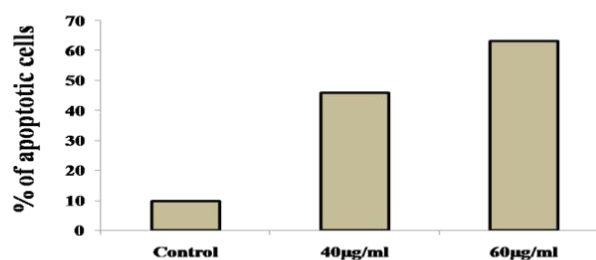
Figure.3.11. (a) Annexin-FITC analysis (b) Quantitative analysis of apoptotic cells by treatment with Gum Acacia capped Zinc Oxide nanoparticles in carcinoma cells

63

The confirmation of apoptosis was conducted with the aid of AnnexinV-FITC staining and was estimated by FACS Verse. Figure.3.11 (a) and (b) depict that upon treatment with 40 and 60 µg ml^{-1} of NPs, cells shifted towards early to late apoptosis with time. Almost 43% and 62.5% apoptotic cells were observed in 40 and 60 µg ml^{-1} of GA@ZnONPs treated HepG2 cells for 24 hours respectively.

3.4.3.4. Intracellular uptake of Rhodamine-B encapsulated GA@ZnONPs
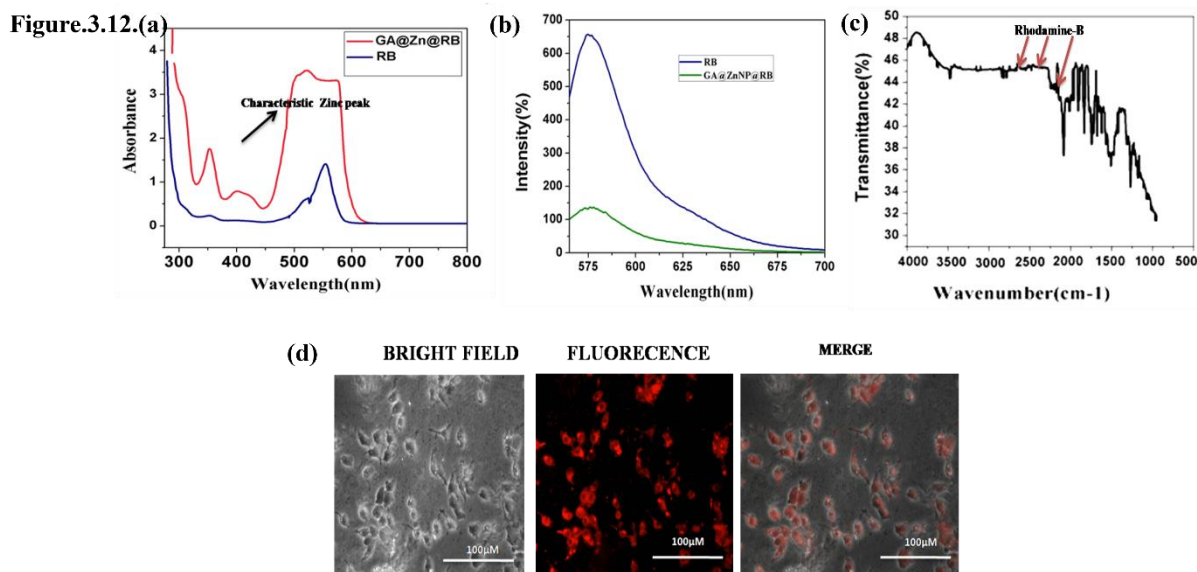
Figure.3.12. (a) UV-Vis analysis (b) Photoluminescence spectra (c) FTIR spectra of GA@ZnONP@RB which confirms Rhodamine-B (d) Cellular internalization of GA@ZnONP@RB in HepG2 cells.

The Rhodamine-B encapsulated GA@ZnONPs exhibit an absorbance peak at 544 nm, which was quite like that of bare Rhodamine-B, as shown in Figure.3.12. (a). This confirms the encapsulation of rhodamine-B within the GA@ZnONPs. The photoluminescence spectra of our synthesized GA@ZnONPs show a luminescent maximum centered at 575 nm shown in Figure.3.12. (b).

The incorporation of the Rhodamine-B dye in GA@ZnONP@RB was indicated by the peaks at 2740, 2407, and 1362 cm^{-1}, respectively corresponding to C–H stretching, NH^{+3} symmetric and C=S stretching vibration, which were like the absorbance peaks of rhodamine-B Figure.3.12. (c). This result confirms the conjugation of rhodamine-B within the matrix of GA@ZnONPs.

GA@ZnONPs tagged with Rhodamine-B were successfully internalized into the HepG2 cells, as seen in Figure.3.12. (d). The result exhibits that the GA@ZnONP@RB was distributed

throughout the cytoplasm, which indicates its successful internalization into HepG2 cells. These nanoparticles possibly penetrate the cells through the endocytosis pathway. Thus, these fluorescent biocompatible nano-platforms were quite conducive to bioimaging applications.

3.4.4. Drug release study
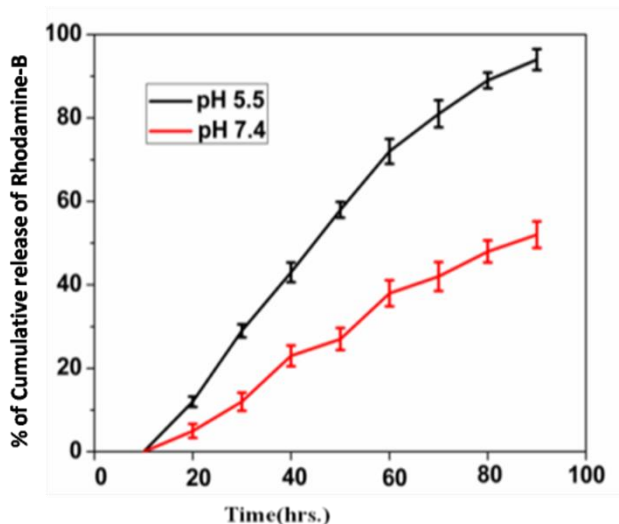
Figure.3.13. Drug release profile of Gum Acacia capped Zinc Oxide nanoparticles

Approximately 25 and 31% of Rhodamine-B were released from GA@ZnONP@RB after 12 and 24 hours, respectively at pH 7.4 as shown in Figure.3.13. On the other hand, the release values were 41 and 55% respectively in the case of pH 5.5. The results indicate that the discharge of rhodamine-B at pH 5.5 (like the pH of the cancer cells) was faster than that of the physiological pH of 7.4. This pH sensitive attribute was quite conducive to cancer amelioration and circumvents adverse effects on the normal cells.

3.5. Conclusion

The synthesis, detailed physical characterization, and determination of the biological activity of gum acacia capped green-synthesized ZnO nanoparticles (GA@ZnONPs) and depicted in the present study. The cell wall synthesis or cross-linking of polymers, as well as the degradation of intracellular DNA, lipids, and proteins, were disrupted by these nanoparticles, resulting in pathogenic cell death. Significant activity against pathogenic bacterial strains both Gram-positive (*S. aureus, E. faecalis*) and Gram-negative (*E. coli and P. aeruginosa*) was exhibited by GA@ZnONPs as confirmed through MIC, MBC, and agar well diffusion studies. The initiation of augmented intracellular ROS by GA@ZnONPs was clearly suggested by the DCFDA assay, leading to bacterial cell death. Additionally, the DCFDA assay demonstrated

enhanced ROS generation in human hepatoma cells induced by GA@ZnONPs, confirming oxidative stress-mediated apoptosis in HepG2 cells. For facilitating bioimaging applications, Rhodamine-B was tagged to these nanoparticles. A pH-responsive drug release assay was performed at two pH levels (5.5 and 7.4) using Rhodamine-B as the model drug. The results indicated significantly higher discharge of rhodamine-B at lower pH (corresponding to the intracellular pH of cancer cells) demonstrating the potential for targeted delivery of anticancer therapeutics specifically to cancer cells without adverse effects on normal cells. Future efforts could see the conjugation of various cancer specific targeting molecules, such as folic acid, lactobionic acid, etc., to specific delivery therapeutics to cancer cells. Cancer-specific labeling may be achieved by attaching these targeting moieties to Rhodamine-B tagged nanoparticles, allowing for discrimination of cancer cells.

To the best of our knowledge, this was the first instance of enhancing the therapeutic and diagnostic attributes of biogenic GA@ZnONPs. This combination of therapeutic and diagnostic potential represents a significant advancement. Consequently, these hydrophilic GA@ZnONPs have undeniably paved the way for the development of a cost-effective platform catering to multiple therapeutic and bioimaging applications.

CHAPTER 4

A Mechanistic Insight into The Inaccessible Herbometallic Nanodrug as Potential Dual Therapeutic Agent

Summary

The bio-accessibility of Vanga Bhasma, a herbometallic mixture compound used in Ayurveda as a gastrointestinal digestive medicine, has been investigated for its potential efficacy as an antibacterial and anti-cancer agent. The characteristic XRD, FTIR, UV-Vis, FESEM, and TEM of the nanoparticles were determined, revealing a high mineral content. The antibacterial property of the nanoparticles was evaluated through MIC and MBC studies, which demonstrated their ability to enhance bacterial ROS generation, leading to the degradation of the peptidoglycan layer in bacterial cell walls.

Furthermore, the anti-cancer potential of the synthesized herbometallic nanoparticles was examined on the breast cancer cell line. The results indicated that the nanoparticles could induce apoptosis through oxidative damage and damage to the mitochondrial membrane. In conclusion, the dual therapeutic attributes of herbometallic nanoparticles as anticancer and antibacterial agent have been successfully established through our studies.

4.1. Introduction

Conventional antibiotic treatments are widely available in the global market today. However, their rampant use and occasional incomplete prescribed courses have led to the development of bacterial strains that are resistant to these antibiotics. Additionally, many antibiotics are not utilized due to their side effects. Evidence shows that resistant pathogenic strains like *Staphylococcus aureus* and *Pseudomonas aeruginosa* have the potential to cause significant mortality. Over the years, various strains such as vancomycin-resistant *S. aureus* have been found to be resistant to antibiotics like penicillin and methicillin.

The emergence of antibiotic resistance poses a significant challenge to researchers, as they strive to develop new drugs or modify existing ones. Recently, metal-organic frameworks have shown promise in the biological field. Herbometallic compounds have also gained attention due to their novel synthesis processes.

For centuries, metal and metallic ions have been utilized in low concentrations as antimicrobial and anticancer agents due to their minimal toxic effects. Eastern countries have traditionally used herbometallic drugs against diseases without fully understanding their mechanisms of action. In our study, we attempt to comprehend the mechanism and physical characteristics of one such drug, locally named Vanga Bhasma (VB), using advanced technologies.

VB, mainly used as an ayurvedic medicine, is an organometallic compound with reduced particle size. It comprises elements essential for the body, with Tin oxide (SnO_2) and zinc oxide (ZnO_2) being major components. VBNPs are tasteless and odorless fine powders with a pH of 8.75. It is carefully prepared to focus on immunomodulation and drug targeting abilities at specific sites. Previous studies have observed the synthesis, purification, physical characterization, and biocompatibility of VB for gastric and gastrointestinal digestion. VB has been traditionally used as a gastrointestinal drug for diabetes, urinary disorders, anemia, asthma, and gastric ulcers. However, its antibacterial and anticancer activities have not been thoroughly explored.

In our current study, the mechanism of a naturally processed drug, VB, which has been used for years as an ameliorative agent against gastrointestinal diseases in oriental medicine, was investigated. Additionally, the potencies of Vanga Bhasma nanoparticles (VBNPs) as an antibacterial and anticancer agent were established [178-202].

4.2. Experimental section

4.2.1. Materials

4.2.1.1. Chemical Ingredient

All analytical grades of chemicals were used for mentioned experiments and were purchased from Sigma-Aldrich. Reagents used for bacterial studies, MTT reagents, glutaraldehyde, and fluorescence stains were from HiMedia. All the glass wares were washed with Aqua regia solution, then rinsed with the aid of ultrapure water, and were ultimately dried. For the synthesis and characterization of material ion-free water (Millipore) was employed with a minimum resistivity at 18MΩ. For further use, deionized water was utilized.

4.2.1.2. Bacterial strain

Bacterial strains used in our study are Gram-negative *Pseudomonas aeruginosa* 1688, *Escherichia coli* 443 and Gram positive *Staphylococcus aureus* 740, *Enterococcus faecalis* 441. Bacterial strains were procured from the Microbial Type Culture Collection (MTCC), IMTECH, Chandigarh, India.

4.2.1.3. Cell line

MDA-MB-468 and MCF-7 (human breast cancer cell) and WI38 (human lung fibroblast) cell lines were procured from the Central Cell repository of the National Center for Cell Science (NCCS), Pune, India. All the above cell lines were cultured in the presence of Dulbecco's Modified Eagles Media (DMEM) supplemented with 10% FBS, 1mM sodium pyruvate, 2 mM L-glutamine, non–essential amino acids, in the presence of antibiotic solution comprising of 100 mg/L penicillin and 100 mg/L streptomycin. The cells were grown in a humidified atmosphere at a temperature of 37 ^{0} C in the presence of 5% CO_2.

4.2.2. Drug Description

Vanga Bhasma (VB) was provided by the Department of Pharmacy, J. B. Roy State Ayurvedic Medical College and Hospital, Kolkata, West Bengal, India. It was further purified following other improved extraction methods [196].

4.2.3. Experimental methods

4.2.3.1. Extraction procedure of VBNPs

The extraction procedure of Vanga Bhasma nanoparticles (VBNPs) consists of three stages, namely purification and incineration. In summary, the general purification involved washing with lime water seven times. Subsequently, the specific purification process was carried out by adding Nirgundi (*Vitex nigundo Linn*.) and powdered Haridra (*Curcuma longa Linn.*, Turmeric) three times. Then the mixture was incinerated by heating and rubbing the purified Vanga with the whole plant of *Achyranthes aspera* in an open atmosphere. Next, the roasted Vanga was triturated with Aloe vera juice and incinerated using an electric muffle furnace at a temperature of 600 °C for an hour. This process was repeated six times to obtain Vanga Bhasma following classical literature [19].

4.2.4. Physical Characterizations of VBNPs

Inductively coupled plasma optical emission spectra (ICP-OES); Thermo iCAP 7000 series, (Thermo Fisher Scientific, USA), and atomic absorption spectra (AAS; Perkin Elmer 2800, USA) were checked to find out the total caption concentration of the VBNPs after acid digestion (HNO_3: HCl; 1:3 ratio) reported elsewhere [199]. To perform ICP-OES, a standard solution (1000μg/ml) compatible with multiple parameters was procured from Merck, Kolkata, India. Each element was characterized at RF power 1160 W, plasma, and nebulizer argon flow rate of 10.00 and 0.50 l/minute, respectively, at an auxiliary argon flow rate of 0.50 l/minute. During each cycle of operation, the calibration was supported by an intermediate standard after every five samples and was repeated thrice. The AAS analysis was performed by keeping VBNPs in water at a horizontal shaker for 6 hours at room temperature following 18 hours equilibration for filtration of the aqueous solution. The instruments were fine-tuned using standard solutions (analytical grade) of each element and the analytical procedure was checked by blank analyzing reagents routinely as per the manufacturer's protocol. Elemental detection ranges were varied from 1 to 0.001μg/ml for the experiment. Final data were recorded following the formula: (Instrument reading × final volume makeup) / actual weight or volume of sample. To investigate the functional groups in the biomolecules possibly present in the material, we have examined the Fourier transform infrared spectroscopy (FTIR) with the help of FTIR-8400S (Shimadzu) between the wavelengths of 400 cm^{-1} and 4000 cm^{-1}. To observe the crystalline property of VBNP, the X-ray diffraction (XRD) pattern was analyzed using the Model D8, Bruker AXS, Wincosin, USA with a voltage of 40kv having a scan speed of 0.2

s/step in the range of 2θ from 20^0 to 80^0 and with Cu Kα radiation- 1.5418 Å. To measure the absorbance spectra of VBNPs at a wavelength of 250-800 nm, an Ultraviolet-visible spectrophotometer was used (Bio-Tek, India). Dynamic light scattering (DLS) was performed by employing Zetasizer (NANO ZS90, Malvern Instruments Ltd., UK) to determine the size distribution of VB nanoparticles. Thermogravimetric analysis was done using Shimadzu Corp. Serial No. C305745. With the help of a Field Emission Scanning Electron Microscope, we visualize the fine morphological character of the material by using INSPECT F50 (FEI, Netherland). The biological effect of VBNP was confirmed by Bacterial SEM (ZEISS). Energy-dispersive X-ray (EDX) spectroscopy of synthesized VBNPs was examined with Supra 55 (ZEISS). For determining the shape and size of the material we have performed the TEM analysis using JEOL JEM 2100 HR.

4.2.5. Evaluation of Antibacterial Activity

4.2.5.1 Determination of minimum inhibitory concentration (MIC) and minimum bactericidal concentration (MBC)

Fresh culture of *E. coli, E. faecalis, S. aureus,* and *P. aeruginosa* were prepared in nutrient broth, which was used for treatment at different concentrations of VBNPs. These were kept in a shaker and incubated for 18-20 hours. After incubation UV-absorption spectrum was observed to obtain MIC against positive control. These four strains were streaked with MIC dilutions growth on an agar plate to observe the MBC. They were incubated for 18-20 hours at $37 ^0$ C. MBC is the minimum concentration of VBNP at which bacterial strain is completely killed. Bacterial assays were done in a biosafety cabinet in order to prevent contamination.

4.2.5.2. Tolerance Level

To evaluate the tolerance level of bacterial strain against VBNP, we use the following equation,

Tolerance = (MBC) / (MIC)……………………….………………………………...…….[eq.1]

4.2.5.3 Agar well diffusion method

Fresh culture of two Gram-negative and Gram-positive bacterial strains were spread on the Muller Hinton agar plate for well diffusion. After that wells of 9 mm were made to add VB at their MIC concentration along with a negative control i.e., sterile water, and a positive control, and incubated for overnight. A growth inhibition zone will be observed. To determine the

susceptibility of the drug VB, the zone of inhibition diameter was measured surrounding the well.

4.2.5.4. Intracellular ROS generation in Bacterial cell

The 2,7-dichlorofluorescein diacetate (DCFH$_2$-DA) was used as a specific probe for envisaging the amount of ROS generation within the bacterial cells. The DCFH$_2$-DA shows passive intracellular penetration and subsequently reacts with the cellular ROS, which in turn results in the generation of 2, 7-dichlorofluorescein (DCF), which is a fluorescent compound [203]. The bacterial cells were at first treated with different concentrations of VBNPs and were incubated overnight at 37 ^{0} C. The bacterial cells were collected with the help of centrifugation and were washed thoroughly with PBS solutions. Afterward, the cells were incubated with adequate DCFH$_2$-DA solution for 30 minutes at a temperature of 37 ^{0} C. Ultimately, the visualization of the bacterial cells was performed with the help of a fluorescence microscope.

4.2.5.5. Study of bacterial cell morphology by FESEM

The degree of damage to the bacterial cells, post-treatment, by VBNP, was analyzed by SEM. Samples subjected to SEM study were prepared following overnight incubation of both the treated and control bacterial cells at 37 ^{0} C [80]. Centrifugation (4 minutes, 4000 rpm) of 1ml of these incubated cultures (both control and treated) was performed to obtain the pellet. After washing the pellet three times with sterile and filtered PBS containing 2% glutaraldehyde, the bacterial cells were dehydrated serially. Bacterial cells were then fixed on coverslips using the drop-casting method and were finally dried by placing them under laminar airflow. SEM analysis was then performed followed by gold coating and placing on carbon tape.

3.2.6. Evaluation of Anticancer Activity

4.2.6.1. Cytotoxicity assay

The 3-(4, 5-dimethylthiazol-2-yl)-2,5-diphenyltetrazolium bromide (MTT) dye was used to determine the survivability of the breast cancer cells and normal lung fibroblast cells treated with different concentrations of VBNPs [203]. Briefly, around 1×10^4 cells per well of cell culture plates containing 96 wells were treated with different concentrations (0, 20, 40, 60, 80, 100 μg/ml) of VBNPs at 37 ^{0} C for 24 hours in the presence of 5% CO$_2$. Following this, 10 μl MTT solution at a temperature of 37 ^{0} C was kept for 4 hours in the presence of 5% CO$_2$. Thus, the generated crystals of MTT-formazan were dissolved in an MTT solubilization buffer.

Ultimately a microplate reader (Biorad) was employed to analyze the absorbance at a wavelength of 570 nm. The data were formulated compared with the control ones.

4.2.6.2. Intracellular ROS generations

Normally, the DCFDA makes intracellular penetration, and it subsequently reacts with the reactive oxygen which results in the generation of a green, fluorescent color compound, dichlorofluorescein (DCF). DCFDA stock solution (10 mM) was prepared in methanol. The stock solution was diluted in PBS to make a working concentration (100 μM). At first, MDA-MB 468 cells were exposed to VBNPs for a time span of 12 hours at a temperature of 37 ^{0} C. The cells were washed thoroughly with ice-cold 1× PBS and were then incubated with DCFDA for 30 minutes in dark conditions at a temperature of 37 ^{0} C [83]. The fluorescence intensity was examined both spectroscopically (Hitachi, Japan) and under a fluorescence microscope in MDA-MB 468 cells (Leica) at wavelengths of 485 nm (excitation) and 520 nm (emission).

4.2.6.3. Intracellular GSH & NADPH measurement

To examine the intracellular antioxidant level in MDA-MB-468 cells on treatment with different concentrations of VBNPs, the intracellular GSH (Glutathione) and NADPH sensing luminescence were performed. GSH-Glo™ is used to record the experimental data. Glutathione Assay kit (Promega) for GSH measurement and Amplite™ Fluorometric NADPH Assay kit (Advancing Assay & Test technologies [AAT] Bioquest, USA) for NADPH measurement with the aid of Microplate reader (Bio-Tek).

4.2.6.4. Assessment of Mitochondrial membrane potential

The mitochondrial membrane potential was examined with the help of JC1 staining [83]. JC-1 dye was used for specific indications of mitochondria depolarization. A cationic dye, JC-1 shows accumulation within the mitochondria in a potential-dependent manner. This is indicated by a transition of fluorescence from red to green which takes place due to the mitochondrial damage and subsequent loss of membrane potential. The treated MDA-MB-468 cells were afterward washed thoroughly with the help of phosphate buffered saline (PBS) and incubated in the dark for 30 minutes with (10 µg/ml) JC-1 at 37 ^{0} C. Finally, images were captured with the aid of a fluorescent microscope (Leica).

4.2.6.5. Mitochondrial ROS measurement

MitoSOX™ Red is a fluorescent dye that acts as a specific probe for quantifying the superoxide present within the mitochondria of live cells. At first, 5×10^4 cells were cultured on coverslips and were then exposed to the different concentrations of VBNPs. The cells were afterward fixed with the help of 3.7% formaldehyde and were thoroughly washed with $1 \times$ PBS. Subsequently, the cells were incubated for 10 minutes at $37 \ ^0$ C in the dark using a working solution of MitoSOX™ Red reagent (5 µM). Ultimately the coverslips were mounted on slides and were immediately observed with the help of a fluorescence microscope (Leica). Again, a spectro-fluorometer (Bio Tek) was used to analyze the fluorescence intensity at an excitation of 510 nm and emission at 580 nm.

4.2.6.6. Nuclear morphology examination

The nuclear morphology of the treated and untreated breast cancer cells was envisaged by DAPI staining. The cells were exposed to different doses (40 µg/ml and 60 µg/ml) of VBNPs for a time span of 12 hours. Afterward, the cells were washed with $1 \times$ PBS and were stained with the help of 4′,6-diamidino- 2-phenylindole (DAPI) (Vector Laboratories Inc.). The nuclear morphology of the cells was ultimately observed with the aid of a fluorescence microscope (Leica).

4.2.6.7. Quantification of apoptotic cell

The Annexin V-FITC/PI staining was performed after flow cytometry in order to confirm the initiation of apoptosis by employing the Thermo Fischer kit [206]. In brief, the cells were treated with different concentrations of VBNPs. Then the cells were washed thoroughly in ice-cold $1 \times$ PBS. These cells were then resuspended in a binding buffer (100 µl) and were incubated for 15 minutes after the addition of Annexin V-FITC (5µl) and PI (5 µl). The cells were incubated in dark conditions at room temperature following the guidelines of the manufacturer. Afterward, the flow cytometric analysis was performed by employing a FACS Verse instrument (BD).

4.3. Statistical analysis

We repeated these experiments three times and the data were expressed by calculating the standard deviation of all the experiments. Comparisons of the mean were done with the help of a model I ANOVA test (using a statistical package, Origin Pro 8, Northamptom, MA 01060,

USA) with multiple comparison t-tests, $p < 0.05$ as a limit of significance. The data is the average of three experiments $\pm$ SD. $*$ = represents p value < 0.05, $**$ = represents p value < 0.01, $***$ = represents p value < 0.001.

4.4. Results and Discussion

4.4.1. Physical Characterizations

4.4.1.1. X-ray diffraction (XRD)
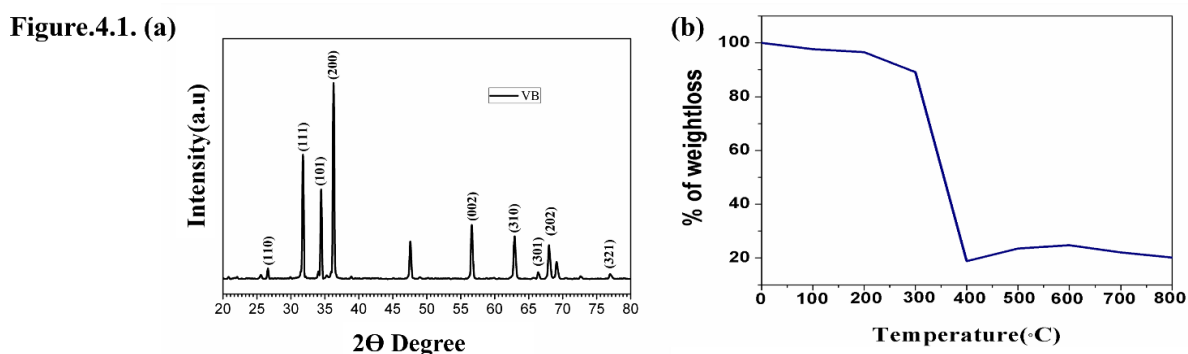
Figure.4.1. (a)

Figure.4.1. (a) XRD analysis (b) TGA analysis of Vanga Bhasma nanoparticles

The diffraction peaks are shown in Figure. 1a represents approximately 26.5^0 , 31.7^0 , 34.5^0 , 36.2^0 , 56.5^0 , 62.9^0 , 66.26^0 , 67.7^0 , 72.4^0 , 76.9^0 corresponding to (110), (111), (101), (200), (002), (310), (301), (202), (321) plane. The formation of VBNPs has been in good agreement with the Joint Committee on Powder Diffraction Standards (JCPDS) card no.- 71-0652 for SnO_2 and 37-1497 for CaO. The average nano-crystalline diameter of all the samples has been estimated using the Debye-Scherrer equation from the broadening of the most intense peak (200) present in the diffraction pattern.

$$< D >_{(200)} = \frac{K\lambda}{\beta_{1/2} \cos\theta} \dots\dots\dots\dots\dots\dots\dots\dots\dots\dots\dots\dots\dots\dots\dots\dots\dots\dots\dots\dots\dots\dots\dots\dots..\dots[eq.2]$$

Here, D is the average nanocrystalline size, λ is the wavelength of the incident Cu-Kα beam (λ =1.54Å), θ is the corresponding Bragg's angle, $\beta_{1/2}$ is the full width at half maximum (FWHM) of the (200) peak and K is the shape factor having the constant value of $\simeq 0.9$. The FWHM ($\beta_{1/2}$) of the sample has been calculated after broadening the (200) peak and it is around 0.00424. Also, the corresponding average nanocrystalline diameter (D) is found to be ~ 34.4 nm.

4.4.1.2. Thermogravimetric Analysis (TGA)

In thermogravimetric analysis, a substantial weight loss of approximately 85% weight loss was observed at 464 °C, which was attributed to the reduction in the labile organic and mineral contents of VBNPs Figure.4.1. (b). Other identified minerals were found to remain thermally stable within this temperature range. Based on the TGA data, it can be inferred that the major fractions of VBNPs consist of organic substances along with a relatively lower number of metallic components, making them highly capable of exhibiting antibacterial and anticancer activities.
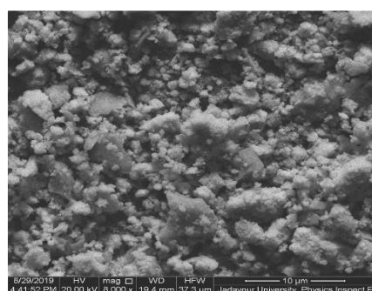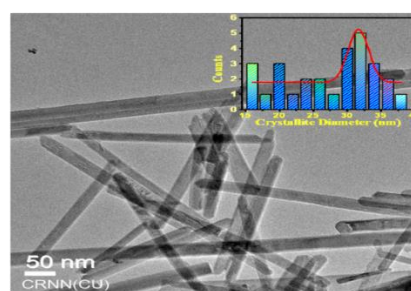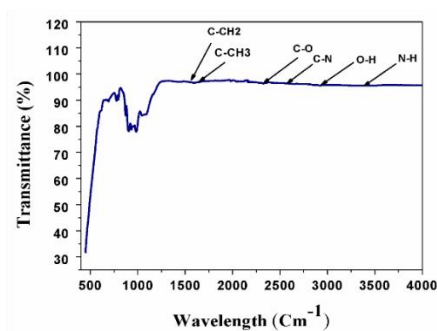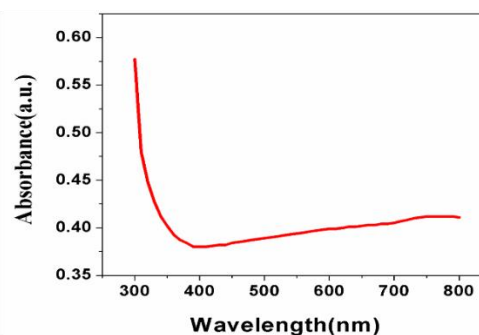
Figure.4.2. (a) FESEM (b) TEM and Size distribution curve (c) FTIR (d) UV-Vis analysis of Vanga Bhasma nanoparticles

4.4.1.3. Field Emission Scanning Electron Microscope (FESEM) analysis

The microstructure of VB was shown in Figure.4.2. (a) using FESEM, revealing a clustered rod-shaped morphology.

4.4.1.4. TEM image

The TEM image demonstrated that the VBNPs exhibit nearly monodisperse, nanosized crystals. The average crystallite diameter, estimated through Gaussian distribution, was found to be approximately 31.8 nm (Size histogram shown in Figure.4.2b. The particles exhibited

crystalline characteristics with minimal agglomeration, predominately appearing as regular rod structures.

4.4.1.5. Spectroscopic analysis of VBNPs

The presence of organic compounds in VBNPs was clearly observed by FTIR analysis reflecting the presence of different types of organic bonds like C-H, C-N, C-O, C=O, and so on in Figure.4.2c.

In Figure.4.2. (d), the UV-Visible spectrum of VBNP does not show any characteristic peak or hump upon spectral scanning within a range of 300-800 nm.

4.4.1.6. DLS Analysis

As depicted in Table.4.1. The DLS size and zeta potential of VBNPs. This low P.D.I value indicates that the aqueous solution of VBNP is homogenous in nature which is quite conducive for biological applications. The Zeta potential of VBNPs is 10.83 ± 1.48 mV. The colloidal stability of the prepared samples was studied by dynamic light scattering (DLS) measurements.

Table.4.1. Determination of hydrodynamic size and surface charge of synthesized VBNP nanoparticles

SAMPLE NAME	DLS SIZE (d.nm)	PDI	ZETA POTENTIAL (mV)
VBNPs	124.8 ± 2.13	0.185 ± 0.09	10.83 ± 1.48

4.4.1.7. EDAX analysis
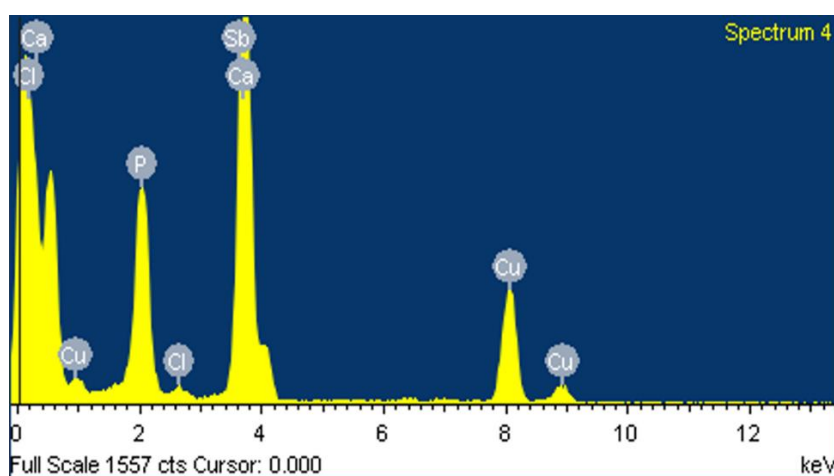
Figure.4.3. EDAX analysis of Vanga Bhasma nanoparticles

The elemental composition of VBNPs was determined using EDAX analysis and predominant elements such as Tin, Zinc, Calcium, and Iron which are shown in EDAX spectra in Figure.4.3.

4.4.2 Antibacterial Activity

4.4.2.1. Determination of MIC and MBC

Table.4.2. Determination of MIC and MBC values of VBNPs

Antibacterial effectiveness of VBNPs		
Bacterial strain	**MIC value (µg/ml)**	**MBC value (µg/ml)**
Enterococcus faecalis	26.0 ± 2.64	100.88 ± 2.12
Staphylococcus aureus	24.8 ± 1.64	98.2 ± 2.43
Pseudomonas aeruginosa	38.7 ± 2.51	147.06 ± 3.23
Escherichia coli	34.0 ± 1.70	122.4 ± 4.56
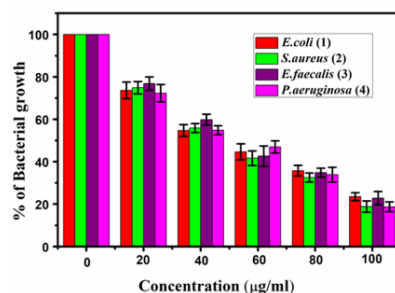
Figure.4.4 (a)   **(b)**
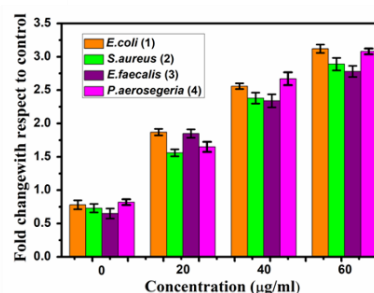
Figure.4.4 (a) Antibacterial activity by MIC (b) Intracellular ROS generation of bacterial cell treated Vanga Bhasma nanoparticles

To determine the bactericidal activity of VBNPs against both the Gram negative as well as and Gram positive strains were treated with different concentrations of VBNPs. Figure.4.4. (a) depicts a dose dependent inhibition of growth in different bacterial strains due to the treatment with VBNPs. Table-4.2. represents the respective MIC values in the case of *E. coli, E. faecalis, S. aureus, and P. aeruginosa* strains.

MIC dilution was streaked to sterile agar plates to estimate the MBC value. The respective MBC values for *E. coli, E. faecalis, S. aureus, and P. aeruginosa* are also given in Table.4.2. The results clearly depicts that the VBNPs exhibit significant bactericidal activity against a wide range of bacterial strains.

4.4.2.2. Determination of tolerance level

The tolerance level was calculated from MBC and MIC values [80]. When the MBC/MIC ratio is greater or equal to 16, the agent is considered to be bacteriostatic for specific bacteria. On the other hand, when this ratio is less than or equal to 4 it is bactericidal for that specific bacterium. The values of the tolerance level of VBNPs in the case of *E. faecalis, S. aureus, P. aeruginosa, and E. coli* were 3.88, 3.96, 3.8, 3.6 which further confirms the bactericidal characteristics of VBNPs.

4.4.2.3. Determination of ROS Generation

The VBNPs had the capability to induce intracellular ROS generation which in results culminates in bacterial cell death. In order to envisage the mechanisms behind the bactericidal activities of VBNPs, the DCF-DA solution was used as a specific probe for determining the amount of ROS generated within the bacterial cells as depicted in Figure.4.4. (b). The results indicate that the treated pathogenic bacterial cells enhanced the generation of ROS. This augmented intracellular ROS production contributes to the bacterial cell membrane, disruption in the cellular genetic content which subsequently leads to the death of the bacterial cells [207].

4.4.2.4. Agar well diffusion study
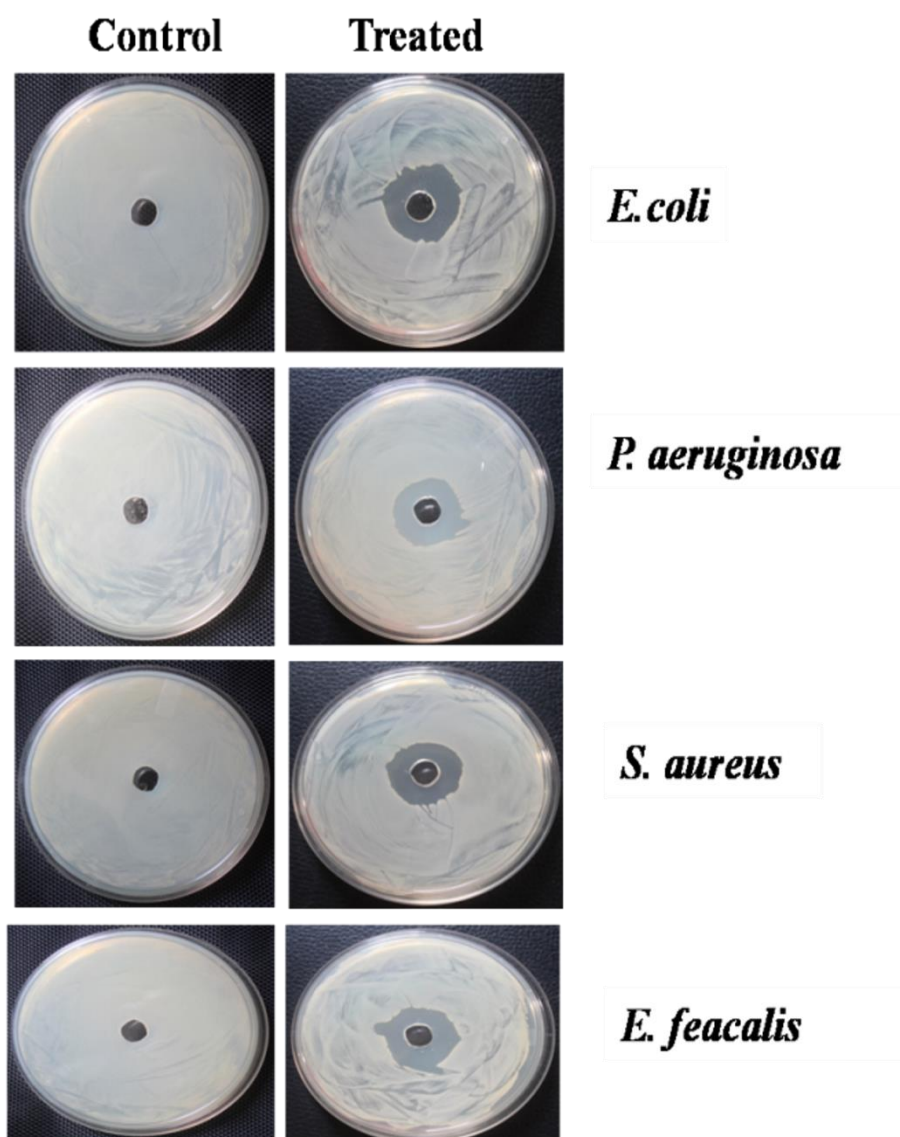
Figure.4.5. Agar well diffusion plate of Vanga Bhasma nanoparticles

The agar well diffusion method was performed to confirm the growth inhibition of different strains at their MIC concentration with the control treated with sterile water [80]. As depicted in Figure.4.5. distinct zones of inhibition are observed in the case of pathogenic strains like *E. coli, E. faecalis, S. aureus,* and *P. aeruginosa.*

4.4.2.5. Bacterial morphology study by FESEM

After analyzing the FESEM images (Figure.4.6.) it can easily be concluded that the membrane was severely damaged in the case of VBNP treated bacterial cells resulting in the loss of morphological integrity of the cells. On the other hand, membrane integrity was intact in the case of control cells. Bacterial cell death was an obvious consequence because of membrane destruction and perforations leading to the expulsion of cytoplasmic contents [80].

4.4.3. Anticancer Activity

4.4.3.1. Cytotoxicity Study
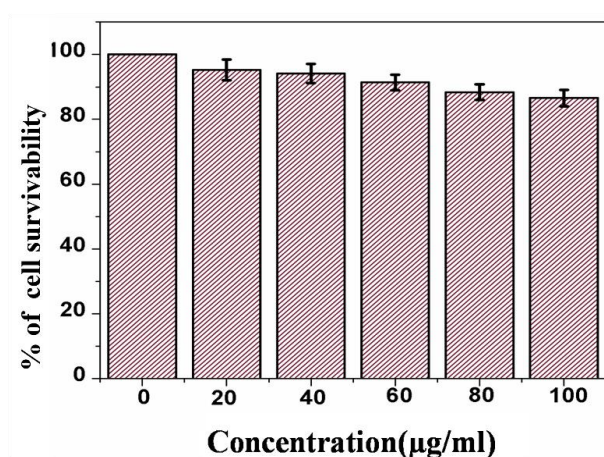
Figure.4.7. (a) **(b)**
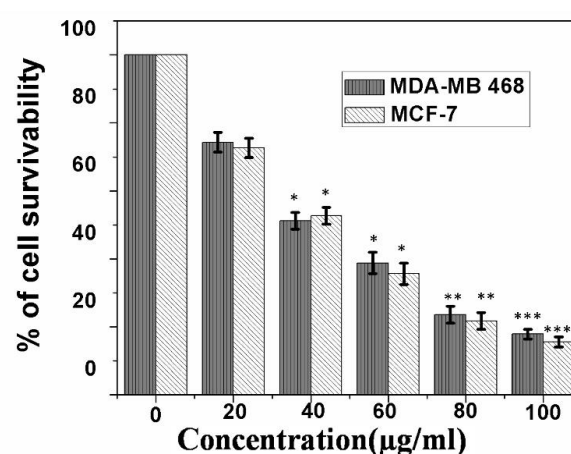
Figure.4.7. (a) Cell viability assay by treatment with Vanga Bhasma nanoparticles (a) Normal (b) Carcinoma cells

Table 3. Determination of LD$_{50}$ values

Compound	MDA-MB 468	MCF-7
VBNPs	58.7 ± 3.4	60.2 ± 4.8

In-vitro cytotoxicity of the VBNPs is evaluated for determining the cytotoxic effects on MDA-MB 468 and MCF-7 cell lines [203]. The cells were treated with various concentrations of VBNPs (0-120 µg/ml) for a time span of 24 hours and were afterward followed by MTT assay. It was observed that VBNPs depicted a decrease in the cell survivability in a dose dependent manner. The details of LD$_{50}$ values in the case of these two cell lines are provided in Table.4.3.

The VBNPs showed negligible toxicities on the normal WI38 cells. Therefore, the results clearly suggest that the VBNPs could exert encouraging anticancer activity without exhibiting any significant toxicity on the normal cells exhibited in Figure.4.7. (a) and (b).

4.4.3.2. Study of Intracellular ROS generation
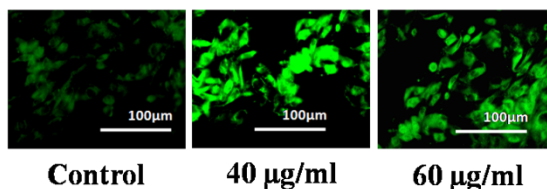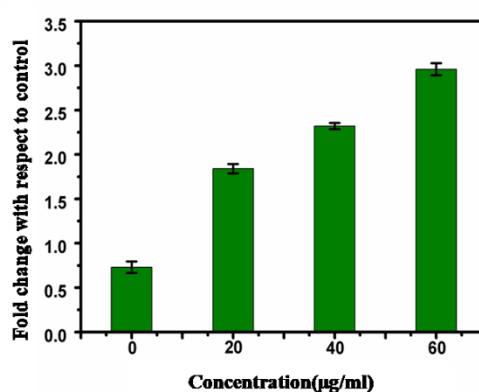
Figure.4.8. (a) Fluorescence microscopic image (b) Intracellular ROS generation by treatment with Vanga Bhasma nanoparticles in carcinoma cells

The Reactive oxygen species (ROS) is examined with the help of both a Spectro fluorometer and fluorescence microscopy with the help of 2′, 7′ dichlorofluorescein diacetate (DCF-DA) as a probe [206]. The generation of reactive oxygen species is evaluated in the case of human breast carcinoma cells, MDA-MB 468 with VBNPs at concentrations of 40 µg/ml and 60 µg/ml for 12 hours. The fluorescence microscopic images clearly depict the occurrence of enhanced green fluorescence intensity in the case of treated MDA-MB 468 cell lines after 12 hours (Figure.4.8).

4.4.3.3. Evaluation of intracellular NADPH and GSH level
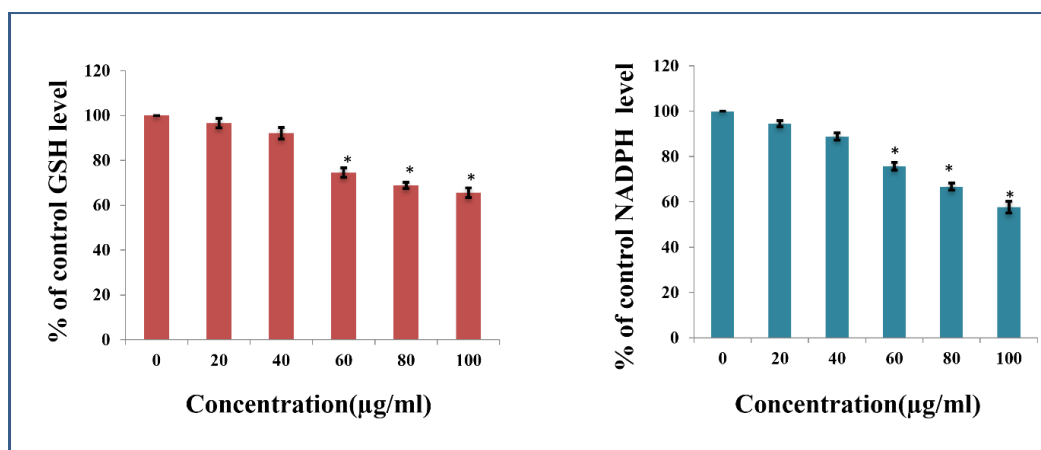
**Figure.4.9. Intracellular antioxidant level in MDA-
MB 468 treated with Vanga Bhasma nanoparticles**

The homeostasis of the ROS level is critically maintained inside the cell and solely regulated by intracellular antioxidant levels (NADPH and GSH) in mitochondria and cytosol. Therefore, the investigation of the intracellular antioxidant system was of central concern, as it eliminates NADPH and GSH, which are very important antioxidants in mitochondria and cytosol to defend cells against oxidative stress mediated cellular death [8,9]. In this experiment, the results exhibit a drastic dose-dependent diminishment in the percentage of GSH and NADPH levels with 100 μg/ml of VBNP treatment compared with control one (Figure.4.9.).

4.4.3.4. Evaluation of mitochondrial membrane potential
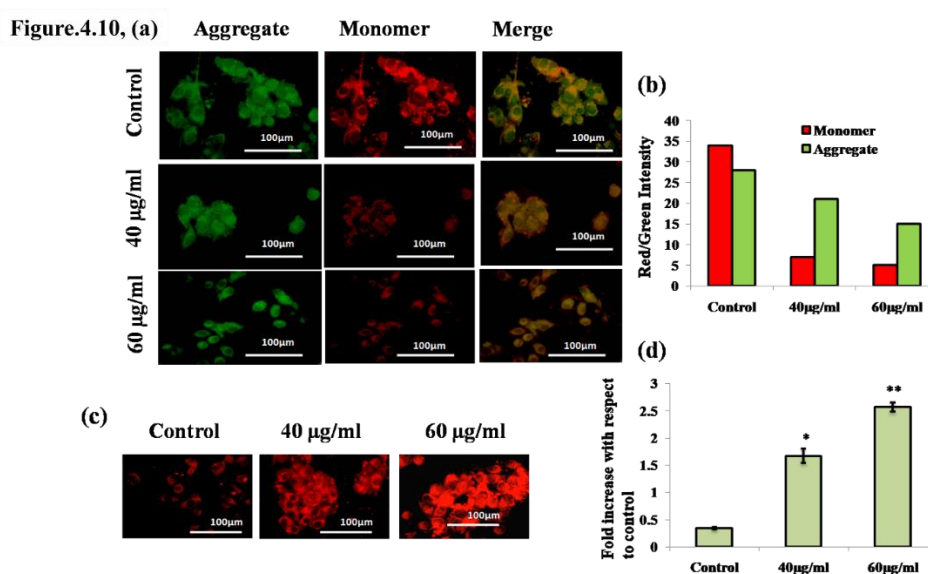
**Figure.4.10. (a) Mitochondrial membrane potential (b) along with quantification data
(c) Mitochondrial ROS generation (d) along with quantification data of MDA-MB 468 cells
treated with Vanga Bhasma nanoparticles**

84

Furthermore, it has been suggested by reports that intracellular ROS plays a pivotal role in altering mitochondrial permeability [85]. Thus, mitochondrial damage was investigated by JC-1 upon treatment with VBNPs Figure.4.10. (a) and (b)**.** The drastic transition of fluorescence from red to green and the decreased red/green ratio depicted the mitochondrial membrane permeability transition. Therefore, these results confirm that the intracellular ROS generation, mediated by VBNPs, drastically disrupts the mitochondrial membrane potential [85].

4.4.3.5. Mitochondrial ROS measurement

The production of mitochondrial ROS in the presence of the MitoSOX™ Red reagent was also envisaged. MitoSOX™ Red reagent effectively penetrated the mitochondria of the live cells and was immediately oxidized by the mitochondrial superoxide. The oxidized product emitted a prominent red fluorescence upon binding to nucleic acid. An evident increase in fluorescence was observed in cells treated with different concentrations of VBNPs, as seen in Figure.4.10. (c) and (d). Hence, it can conclude that VBNPs mediate enhanced mitochondrial ROS production, leading to apoptosis-mediated cell death.

4.4.3.6. Quantification of apoptotic cell

Figure.4.11. (a)
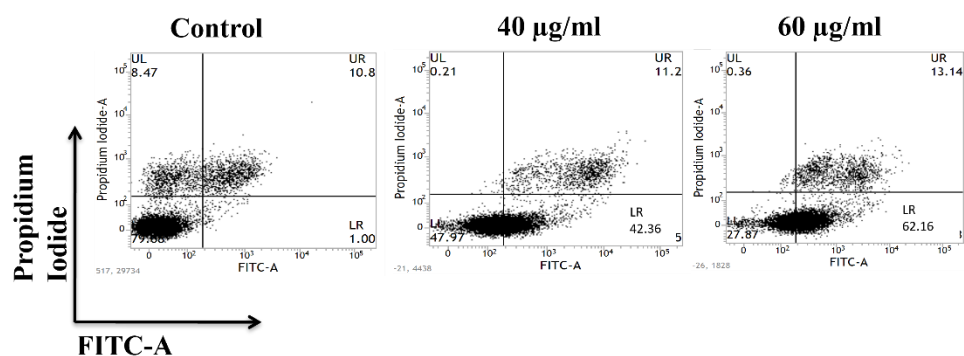
(b)
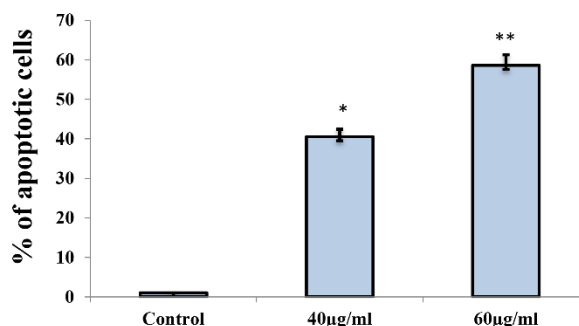
Figure.4. 11. (a) Annexin-FITC analysis (b) Quantitative analysis of apoptotic cells in MDA-MB 468 treated with Vanga Bhasma nanoparticles

As a confirmation of apoptosis, Annexin V-FITC staining was carried out with the help of FACS Caliber. As depicted in Figure.4.11. (a) and (b), the treatment with LD_{50} dose of VBNPs resulted in the drastic transition of the cells shifted towards early to late apoptosis. The percentage (%) of apoptotic cells was predominant in the case of the breast carcinoma cells treated VBNPs for 24 hours compared to the untreated cells. In the case of the MDA-MB 468 cells treated with VBNP, approximately 60% of the cells depicted signs of apoptosis after 24 hours. On the other hand, only 1% of apoptotic cells were observed in the case of the normal control cells. The results suggest that the VBNPs are capable of initiating apoptosis-mediated cell death in breast cancer cells via a series of intracellular events like enhancement of ROS generation, impairment of the intracellular redox balance, and mitochondrial membrane damage [206-208].

4.4.3.7. Nuclear morphology examination
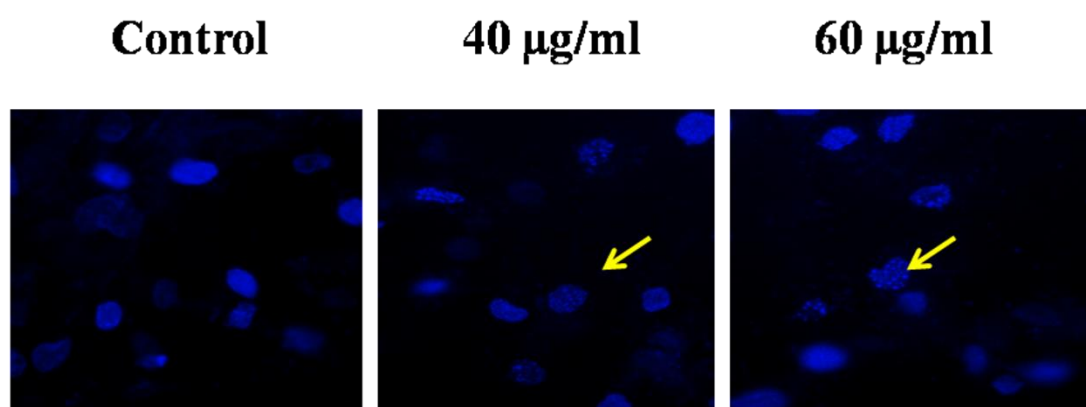
Figure.4.12. Nuclear morphology by DAPI staining

Apoptotic morphology was evaluated in the case of breast cancer cells treated with VBNPs for 12 hours with the aid of DAPI staining. In the case of untreated cells, no morphological anomalies like nucleus shrinking or polynuclear fragmentation were observed. While in the case of the treated cells, distinct polynuclear fragmentation and nucleus shrinking were prevalent [Figure.4.12]. Our results show that 34% and 46% of cells showed dominant signs of apoptosis when treated with a dose of 40 ug/ml and 60 ug/ml of VBNPS.

4.5. Conclusion

The fields of cancer and antibiotic resistance are currently posing challenges, but we believe that promising advancements in chemotherapy can address these concerns more efficiently and

with fewer side effects. Our studies confirm the applicability of Vanga Bhasma nanoparticles (VBNPs) as a combined therapeutic system, which is in great demand nowadays.

We firmly believe that these nanoparticles hold the potential to emerge as promising ameliorative agents against a broad range of diseases, including cancer and bacterial infections such as urinary tract infections, surgical infections, and skin infections. In the present study with VBNPs, the destruction of bacterial cell walls is likely due to the disruption of signaling cascades, leading to impaired cell wall synthesis caused by enhanced ROS generation, observed in both Gram-negative and Gram-positive bacterial strains.

Furthermore, our study clearly depicts the enhancement of intracellular ROS generation in breast carcinoma cells upon treatment with Vanga Bhasma nanoparticles. This heightened ROS production is responsible for inducing changes in the mitochondrial membrane potential of the cells, ultimately resulting in apoptosis-mediated breast cancer death. In conclusion, our studies suggest that these Vanga Bhasma nanoparticles hold the promise of emerging as a dual ameliorative agent against pathogenic bacterial strains and breast cancer cells.

CHAPTER 5

Phytofabrication of Silver Nanoparticles Using *Ocimum Sanctum Leaf* Extract and Their Antibacterial and Anticancer Activity Through Oxidative Damage

Summary

Prominence has been gained by silver nanoparticles in various fields like medicine, catalysis, nanoelectronics, textiles, pollution, and water treatment, owing to their unique attributes. The applications of silver nanoparticles in medical purposes, including drug delivery, treatment, diagnosis, and medical device coating are experiencing rapid growth. Conventionally, various chemical and physical methods have been utilized to synthesize silver nanoparticles (AgNPs). However, these synthesis processes are not only expensive but also involve side effects. To address these significant issues and enhance safety and efficiency, green nanotechnology has emerged as a crucial approach for silver nanoparticle synthesis. The synthesis of biogenic silver nanoparticles from plant extracts is referred to as green nanotechnology.

In this study, the green synthesis of silver nanoparticles was achieved using *Ocimum sanctum* (Tulsi) leaf extract, which served as both the reducing agent and capping agent. The synthesized silver (Ag) nanoparticles (NPs) were thoroughly characterized, and their antibacterial and anticancer activities were observed. The formation of silver nanoparticles was confirmed by the development of a brown color upon the addition of *Ocimum sanctum* (Tulsi) extract. To quantify the formation of silver nanoparticles, UV-Vis absorption spectroscopy, X-ray diffraction (XRD), and zeta potential measurements were performed. Furthermore, Fourier-transform infrared (FTIR) analysis revealed that the silver nanoparticles (AgNPs) were stabilized by eugenols, terpenes, and other aromatic compounds present in the extract. The antimicrobial and anticancer properties of silver nanoparticles (AgNPs) were evaluated through various in vitro cellular assays. The findings from our present study confirm that silver nanoparticles (AgNPs) can serve as a dual therapeutic option for combating pathogenic microbial strains and hepatocellular cancer.

5.1. Introduction

Nanotechnology is regarded as the field responsible for the development of more consistent processes for the synthesis of nanomaterials across a wide range of sizes, ensuring good mono dispersity and precise chemical composition [209]. Metallic nanoparticles attract significant importance in recent years due to their wide application in physics, chemistry, medicine, biology, and material science [210]. Exceptional physiochemical characteristics, encompassing optical, catalytic, electronic, magnetic, and antibacterial properties are being raised due to the high specific surface area and surface atoms of metallic nanoparticles. [42]. Particularly, noble metals, like silver nanoparticles, stand out due to their dominant optical absorption in the visible region, resulting from the exciting group of the free electron gas [212]. Silver nanoparticles exhibit a diverse range of compelling attributes, including nonlinear optics, spectrally selective coating for solar energy absorption, excellent electrical conductivity, bio-labeling capabilities, antibacterial properties, intercalation materials for electrical batteries, optical receptors, chemically stable materials, and catalysts in chemical reactions [43,44].

The broad applications of silver nanoparticles are found in the medical field, especially in skin ointments and creams to prevent infections in burn wounds and open wounds. Silver exhibits inhibitory action against many bacterial strains and microorganisms commonly found in medical and industrial processes [45]. The general method for synthesizing silver nanoparticles is through chemical reduction, leading to colloidal dispersions in water or organic solvents [213].

The imperative technique of green synthesis involves the utilization of nontoxic chemicals, eco-friendly solvents, and renewable materials, with the capability to reduce metals through specific metabolic pathways [214]. Various biological approaches for green synthesis using plant leaf extracts from different plants have been reported [214-216]. These biologically-synthesized nanoparticles are known to exhibit antibacterial properties [217-223].

The leaves of *Ocimum sanctum* (Tulsi), have been employed as a remedy for stomachaches, headaches, diarrhea, dysentery, coughs, colds, and intestinal infections, for centuries [224-229]. The leaves have aroma, cooling, mucilaginous, diuretic, and anti-inflammatory attributes that have been utilized in the treatment of digestive and carminative issues, spasmodic affections, vitiated inflammatory conditions, and even as an anticancer agent [230-232]. The major phytochemicals found in *O. sanctum* such as eugenol, β-elemene, cyclopropylidene,

carvacrol, linalool, germacrene, etc., are believed to play a crucial role in the bio-reduction of silver metal ions and the stabilization of the resulting nanoparticles.

In this study, we observed how prokaryotic and eukaryotic cells were affected by biogenic AgNPs. Positive effects of the phytofabricated AgNPs against Gram positive (*S. aureus*, *B. subtilis*) and Gram-negative (*E.coli, P. aeruginosa*) pathogenic bacterial species were also demonstrated. The mechanism of bacterial growth inhibition was investigated thoroughly. The biogenic AgNPs likely destroyed bacterial cell walls through signaling cascades, resulting in defective cell wall synthesis or impaired cross-linking of polymer units. This effect may have been caused by ROS generation in both Gram-positive and Gram-negative bacterial strains [80].

Furthermore, cellular metabolism, inhibiting proliferation and metastasis of cancer cells was altered significantly by silver ions. The generation of reactive oxygen species (ROS) played a crucial role in maintaining reduction-oxidation balance in most cancer cells, elevated ROS levels may promote oxidative damage leading to cellular abnormalities or death [235-236]. The antimicrobial and anticancer activities of AgNPs against different pathogenic bacterial strains and hepatocellular cancer cell lines were investigated in this study.

Phytofabricated, non-hazardous, and eco-friendly AgNPs have great potential as an effective dual therapeutic agent.

5.2. Experimental section

5.2.1. Materials

5.2.1.1. Chemical Ingredients

AR-grade silver nitrate ($AgNO_3$) was purchased from Sigma-Aldrich Chemicals and fresh *Ocimum sanctum* leaves were collected locally from Kolkata, India. All the chemicals and reagents required for bacterial culture media, MTT reagent, glutaraldehyde, fluorescence stains, and different chemicals and reagents used for biological purposes were purchased from Merck Ltd and SRL Pvt. Ltd, Mumbai, India, and HiMedia at the highest grade available. All the reagents were used without further purification. Deionized (Millipore) water was used throughout the experiment with a resistivity of at least 18 MΩ-cm. The cleaning was done by aqua regia solution followed by rinsing with ultrapure water for all the glass-wares used in our experiments were cleaned with.

5.2.1.2. Bacterial strain

Gram-positive (*Staphylococcus aureus* 740 and *Bacillus subtilis* 441) and Gram negative (*Escherichia coli* 443 and *Pseudomonas aeruginosa* 1688) used for the bacterial experiment were procured from Microbial Type Culture Collection (MTCC), IMTECH, Chandigarh, India.

5.2.1.3. Cell line

Hep G2 (Hepatocellular carcinoma cell) and WI38 (human lung fibroblast) are used to determine the cytotoxicity assay obtained from the Central Cell repository of the National Center for Cell Science (NCCS), Pune, India. All the above cell lines were cultured in the presence of Dulbecco's Modified Eagles Media (DMEM) supplemented with 10% FBS, 1mM sodium pyruvate, 2 mM L-glutamine, non–essential amino acids, in the presence of antibiotic solution comprising of 100mg/L penicillin and 100mg/L streptomycin. The cells were grown in a humidified atmosphere at a temperature of 37 ^{0} C in the presence of 5% CO_2.

5.2.2. Experimental methods

5.2.2.1 Preparation of plant leaf extract

Ocimum sanctum leaves were washed with deionized water to remove the dust and dirt particles. Subsequently, the leaves are then dried at room temperature. Approximately 2 grams of the dried powdered leaves were taken and mixed with 100ml distilled water. The mixture was then boiled for 5 minutes and allowed to cool down. Afterward, the solution was filtered and stored at 4 °C. All syntheses were performed within a week after the preparation of the leaf extract.

5.2.2.2. Preparation of Silver Nitrate Solution

1.0 mM $AgNO_3$ was added into distilled water and stirred continuously for 2 to 4 hours.

5.2.2.3. Synthesis of Silver Nanoparticles

In a 250 ml beaker, 150 ml of prepared silver nitrate stock solution was taken. Subsequently, 10 ml of leaf extract was added to the breaker. The mixture was then heated in a water bath at 90 °C for 1 hour.

5.2.2.4. Purification of synthesized particles

After heating, the precipitation was obtained by centrifugation at 9000 rpm for 25 minutes. Then the precipitation was then repeatedly washed by centrifuging (3 times). Thus, purified silver nanoparticles (AgNPs) were obtained.

5.2.3. Physical Characterizations of Silver Nanoparticles

The absorbance spectra were measured using an Ultraviolet-visible spectrophotometer (Bio-Tek) at a wavelength of 250-800 nm. Silver nanoparticles were synthesized by reducing silver metal ions solution with Tulsi leaf extract and were initially characterized using UV-Visible Spectrophotometer. The XRD (X-Ray Diffractometer) patterns of the silver nanoparticle samples were recorded by X-ray powder Diffractometer model D8, Bruker AXS, Wisconsin, USA, using Cu-Kα target employing wavelength of 1.5418 Å and operating at 35 kV with a scan speed of 2s/step. Particle size and its distribution were assessed with Field Emission Scanning Electron Microscope (FESEM) using ZEISS. Electrons interact with the electrons in the sample, producing various signals that can be detected and that contain information about the surface topography and composition of the samples. The Fourier transform infrared spectroscopy (FTIR) study was done using FTIR-8400S, Shimadzu in the wavenumber range from 400 cm^{-1} to 4000 cm^{-1}. FTIR Spectrometer to detect the possible functional groups in biomolecules present in the plant extract. The particle size distribution and stability were measured by DLS (Dynamic light Scattering) using Zetasizer (NANO ZS90, Malvern Instruments Ltd., UK). The surface charges of the nanoparticles were also measured by the Zetasizer.

5.2.4. Evaluation of antibacterial activity

5.2.4.1. Determination of minimum inhibitory concentration (MIC) and minimum bactericidal concentration (MBC)

As per our previously reported protocol [80], the microdilution method in Luria broth was used to evaluate the MIC and MBC. Bacterial media containing the inoculums were supplemented with different concentrations of AgNPs and incubated for 24 hours. After incubation, the MIC values were obtained by assessing the turbidity of the bacterial growth through UV absorption.

To determine the MBC values the MIC dilutions of growth i.e., 10 µl of a bacterial strain containing 2.5×10^5 CFU ml^{-1} bacteria, were separately added to the several 1 ml nutrient

broths (NBs) onto agar plates, and then they were incubated for 24 hours at 37 °C. The MBC value was noted as the lowest concentration of AgNPs, at which the bacterial strains were completely inhibited. This MBC value signifies the minimum concentration of particles required for 100% bacterial killing compared to the positive control (no treatment). All assays were performed in laminar airflow.

5.2.4.2. Tolerance level

The tolerance levels of each bacterial strain against AgNPs were determined by using the following formula [235].

Tolerance= (MBC) / (MIC) …………………………………………………………………(eq.1)

5.2.4.3. Agar well diffusion method

The susceptibility of pathogenic bacteria to AgNPs was examined using the Agar well diffusion method, following a previously reported protocol. The pathogenic strains were grown in LB Broth at 37 °C overnight until turbidity of 0.5 Mac Farland standards (10^8 CFU/ml) was achieved. A 90mm diameter Petri dish filled with 30 ml of Mueller Hinton Agar was then inoculated with 50 µl of this bacterial suspension. Wells were punched into the agar plates and treated with AgNPs at their MBC concentrations. The zone of inhibition diameter in the bacterial growth surrounding the disc (including the disc) was measured [235].

5.2.4.4. Intracellular ROS generation in Bacterial cell

The bacterial intracellular ROS generation was measured using 2, 7-dichlorofluorescein diacetate ($DCFH_2$-DA), following our previously reported protocol [80]. The $DCFH_2$-DA was to passively enter the cells, reacting with the generated ROS and undergoing oxidation, thereby forming a highly fluorescent compound 2, 7-dichlorofluorescein (DCF). After exposure to AgNPs, the bacteria cells were cultured overnight and washed with PBS solutions. Subsequently, the cells were incubated with the required amount of $DCFH_2$-DA at 37 °C for 30 minutes. Finally, the bacteria cells were visualized under a fluorescence microscope.

5.2.5. Evaluation of Anticancer Activity

5.2.5.1. Cytotoxicity assay

The viability of Hep G2 cells after exposure to various concentrations of AgNPs was determined by 3- (4, 5-dimethylthiazol-2-yl)-2,5-diphenyltetrazolium bromide (MTT) assay

[231, 83,85]. Briefly, around 1×104 cells per well of 96-well plates were exposed to AgNPs at the concentrations of untreated as control, 20, 40, 60, 80, 100µg/ml for 24 hours of incubation at 37^0 C and 5% CO_2. Following this, the cells were incubated again with 10µl MTT solution (stock 1 mg/ml) for 4 h at 37^0 C and 5% CO_2 following a wash with $1\times$ phosphate-buffered saline (PBS), and the resulting formazan crystals were dissolved in MTT solubilization buffer to measure the absorbance at 570nm by using a microplate reader (Biorad). The data were formulated compared with the control ones.

5.2.5.2. Intracellular ROS generations in Hep G2 cells

Normally, the DCFDA enters the cell and reacts with the reactive oxygen to give a green, fluorescent color compound dichlorofluorescein (DCF). Briefly, a stock solution of DCFDA (10 mM) was prepared in methanol and was further diluted with PBS to a working concentration of 100 µM. Hep G2 cells were treated with AgNPs at LD_{50} for 12 hours at 37^0 C and washed with ice-cold $1\times$ PBS followed by incubation with 100 µM of DCFDA for 30 minutes in the dark at 37^0 C [83,85]. The fluorescence intensity was measured both spectroscopically and under a fluorescence microscope in Hep G2 cell excitation and emission wavelengths of 485 nm and 520 nm respectively.

5.3. Statistical analysis

We repeated these experiments three times, and the data were expressed by calculating the standard deviation of all the experiments. Comparisons of the mean were done with the help of a model I ANOVA test (using a statistical package, Origin Pro 8, Northamptom, MA 01060, USA) with multiple comparison t-tests, $p < 0.05$ as a limit of significance. The data is the average of three experiments ± SD. $*$ = represents p value < 0.05, $**$ = represents p value $<$ 0.01, $***$ = represents p value < 0.001.

5.4. Results and Discussion

5.4.1. Physical Characterizations

5.4.1.1. X-ray diffraction (XRD)

The crystalline character of the synthesized nanoparticles is confirmed through X-ray crystallography. The XRD pattern of AgNPs is given in Figure.5.1. (a). The pattern clearly shows the main peaks at (2θ) 38.19º, and 44.37º corresponding to the (111) and (200) planes,

respectively. By comparison with JCPDS (file no: 89- 3722), the typical pattern of green-synthesized AgNPs was found to possess a prominent structure. The average crystalline size of the silver nanoparticles was estimated using (Eq. 2), the Debye–Scherrer's equation:

$$D=0.9\lambda/\beta \cos\theta\dots\dots\dots\dots\dots\dots\dots\dots\dots\dots\dots\dots\dots\dots\dots\dots\dots\dots\dots\dots\dots\dots(eq.2)$$

By calculating the width of (111) Bragg's reflection, the average particle size was 14 nm. In addition, three unassigned peaks appeared at 27.78^0 , 32.34^0 , and 46.29^0 . These peaks were weaker than those of silver possibly due to the presence of bioorganic compounds on the surface of the AgNPs.
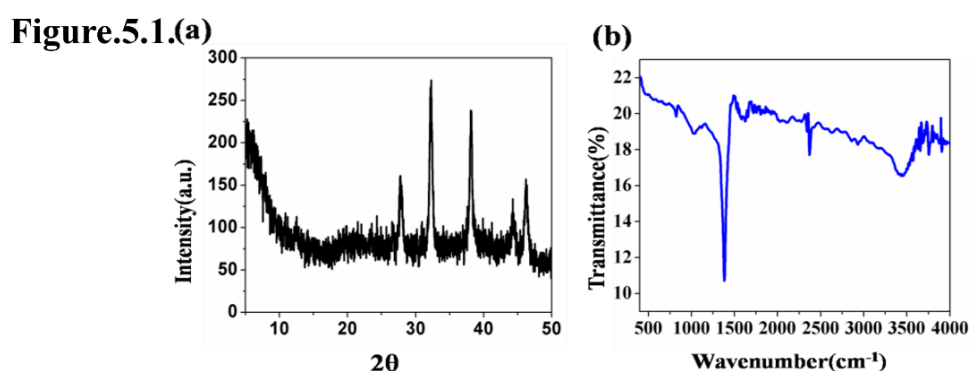
Figure.5.1.(a)

Figure.5.1. (a) XRD analysis of silver nanoparticles and (b) FTIR spectra

5.4.1.2. Fourier Transform Infrared Spectroscopy (FTIR)

FTIR experiment was conducted to identify the presence of various functional groups in biomolecules responsible for the bio-reduction of silver nanoparticles (AgNPs) and capping/stabilization of silver nanoparticles. The intense bands obtained were compared with standard values to identify the functional groups, as shown in Figure.5.1. (b). The bands at $3422cm^{-1}$ in the spectra correspond to O–H stretching vibration, indicating the presence of alcohol and phenol group. Bands at 2921 cm^{-1} arising from C–H stretching of aromatic compounds, were observed. The band at $1631cm^{-1}$ was assigned to C–N and C–C stretching, indicating the presence of proteins. The band at 1450 cm^{-1} represents N–H stretch vibration, present in the amide linkages of the proteins. These functional groups play a role in the stability/capping of AgNPs, as reported in other studies. Additionally, the bands at 1450 cm^{-1} correspond to the N–H and C–N (amines) stretch vibration of the proteins while the band at 1377 cm^{-1} exemplifies the N-O symmetry stretching typical of the nitro group. The strong bands at 1074 cm^{-1} correspond to ether linkages and suggest the presence of flavanones adsorbed on the surface of the synthesized metal nanoparticles. The immediate reduction and

capping of silver ions into silver nanoparticles in this analysis might be due to flavonoids and proteins. The flavonoids present in the leaf extract are powerful reducing agents, which may be actively involved and responsible for the reduction of Ag^+ to Ag^0.

5.4.1.3. UV-Visible absorption studies

The absorption spectra of the synthesized AgNPs in aqueous solution were monitored in a wavelength range of 250-800 nm as shown in Figure.5.2a. It was observed that the solution of silver nitrate turned dark brown on the addition of leaf extract, indicating the formation of AgNPs, while no color change was observed in the absence of plant extract. The UV-Vis spectrum exhibited a single, strong, and broad Surface Plasmon Resonance (SPR) peak at 450 nm, which confirmed the synthesis of AgNPs.
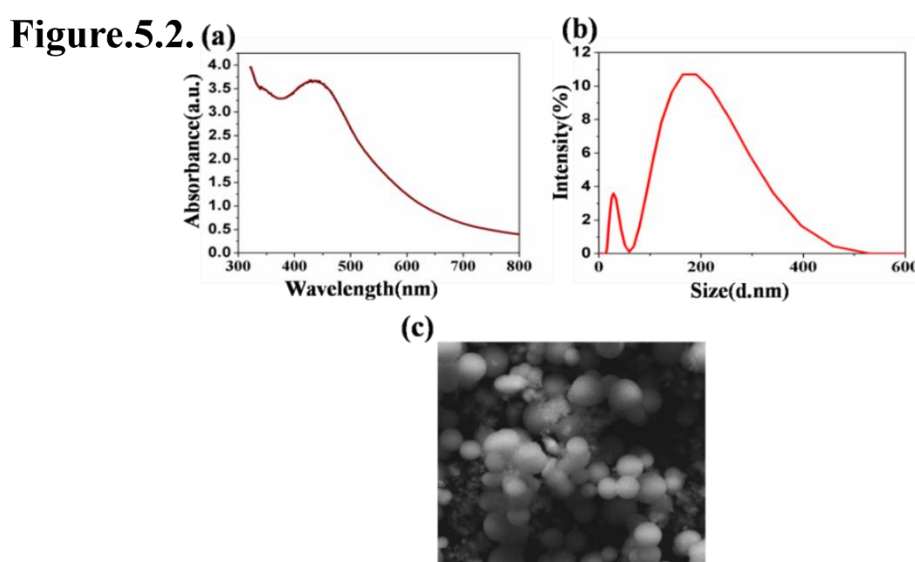
Figure.5.2. (a) UV-Vis spectra, (b) Hydradynamic size distribution study by DLS and (c) FESEM analysis of silver nanoparticles

5.4.1.4. DLS Analysis

Table.5.1. Hydrodynamic Size Distribution

SAMPLE NAME	DLS SIZE (d.nm)	PDI	ZETA POTENTIAL (mV)
AgNPs	101.8	0.231	-21.4

DLS was performed to determine the size distribution of AgNPs Figure.5.2. (b). In the case of AgNPs the particle size distribution curve revealed the P.D.I (Polydispersity Index) is 0.231 and the average diameter that is approximately ~100 nm. The low P.D.I value indicates that the solution is homogenous in nature which is ideal for biological applications. A quite high negative zeta potential is exhibited by silver nanoparticles, indicating the stability of the particles in the aqueous solution. The details are given in Table.5.1.

5.4.1.5. FESEM analysis

The FESEM images of the silver nanoparticles are shown in Figure.5.2. ©, revealing the spherical morphology of AgNPs. The particle size in the present study ranged from 25 to 100 nm.

5.4.2. Antibacterial activity

5.4.2.1. Determination of MIC and MBC
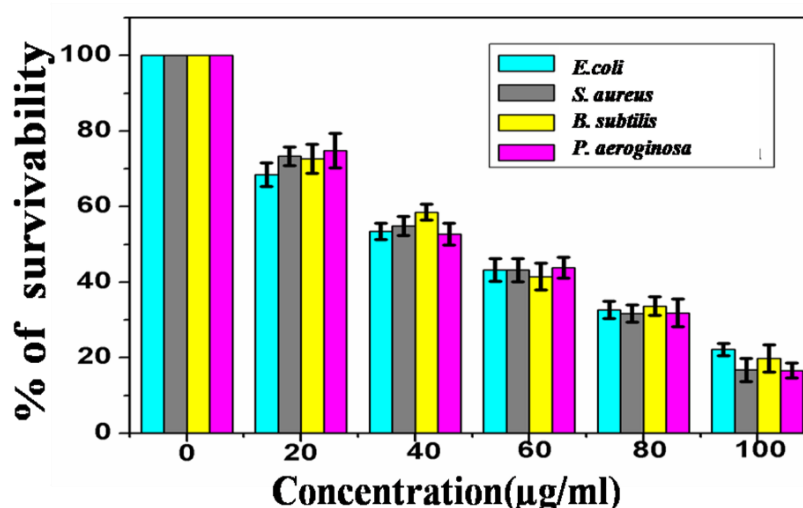
Figure.5.3. Bacterial viability study of pathogenic bacterial strains by treatment with analysis of silver nanoparticles

Table.5.2. Determination of MIC and MBC values

Antibacterial effectiveness of AgNPs		
Bacterial strain	**MIC value (µg/ml)**	**MBC value (µg/ml)**
Bacillus subtilis	41.3 ± 2.83	140 ± 3.7
Staphylococcus aureus	35.54 ± 1.43	132 ± 1.8
Pseudomonas aeruginosa	44.65 ± 2.2	143 ± 4.2
Escherichia coli	38.460 ± 1.2	135 ± 3.2

The bactericidal activity of the synthesized AgNPs has been treated separately against Gram negative *E.coli, P.aeruginosa,* and Gram-positive *S.aureus, B.subtilis*. In the case of *E.coli, and P.aeruginosa* strains the MIC values of AgNPs are 38.46 ± 1.2 µg/ml, 44.65 ± 2.2 µg/ml, and that in the case of *S.aureus, B.subtilis* the MIC values are 35.54 ± 1.43µg/ml, 41.3 ± 2.83 µg/ml respectively as shown in Table 2. The MBC values, where complete bacterial growth was inhibited on the sterile agar plates with treatment of AgNPs were recorded as 135 ± 3.2 µg/ml, 143 ± 4.2 µg/ml, 132 ± 1.8 µg/ml, 140 ± 3.7µg/ml in case of *E. coli, P. aeruginosa, S. aureus, B. subtilis* bacterial strains respectively [80]. Decreases in bacterial growth with the increase in the concentration of AgNPs are shown in Figure.5.3. The microdilution method indicated that the easy penetration of AgNPs into the cells followed by bacteriostatic action in different bacterial strains might be responsible for the inhibition.

5.4.2.2. Determination of tolerance level

The tolerance levels of pathogenic strains against AgNPs were evaluated based on the respective MIC and MBC values. From these results, the tolerance level to AgNPs was found to be 3.5, 3.2 for *E. coli, P. aeruginosa* and 3.7, 3.4 for *S. aureus, B. subtilis* respectively. The MBC/MIC ratio is an important parameter reflecting the bactericidal capacity of the AgNPs. In this study, AgNPs exhibited significant bactericidal activity against pathogenic strains i.e., *E. coli, P. aeruginosa, S. aureus,* and *B. subtilis*. This might be attributed to the ingression of AgNPs into the bacterial cells, hindering growth and acting as an ideal bactericidal agent.

5.4.2.3 Determination of agar well diffusion method
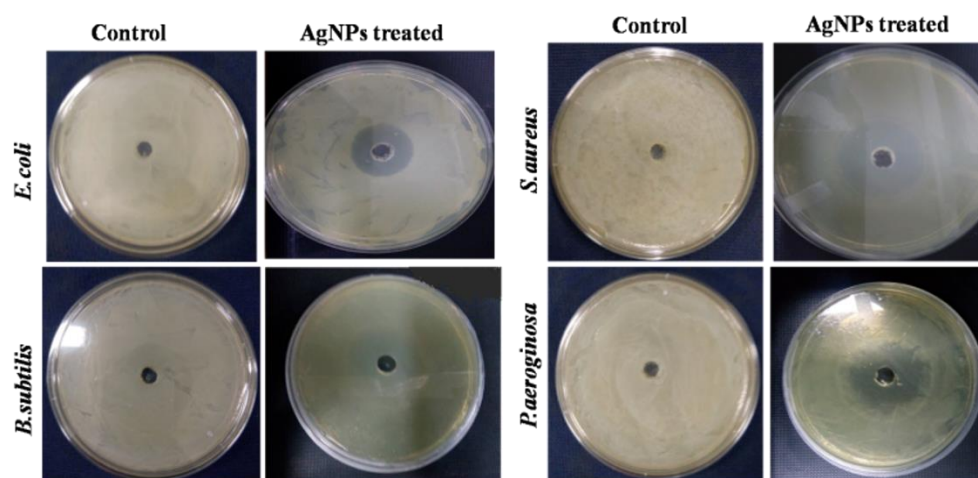
Figure.5.4. Antibacterial assessment of biogenic silver nanoparticles in pathogenic strains be disc agar diffusion method

The selective bactericidal activity of AgNPs was confirmed by the good diffusion method, as shown in Figure.5.4. The zone of inhibitions exhibited significant diameters when strains were treated with AgNPs at their MBC dose. Thus, the AgNPs demonstrated effective growth inhibition for pathogenic *E.coli, S.aureus, B.subtilis, and P.aeruginosa*.

5.4.2.4. Determination of ROS Generation
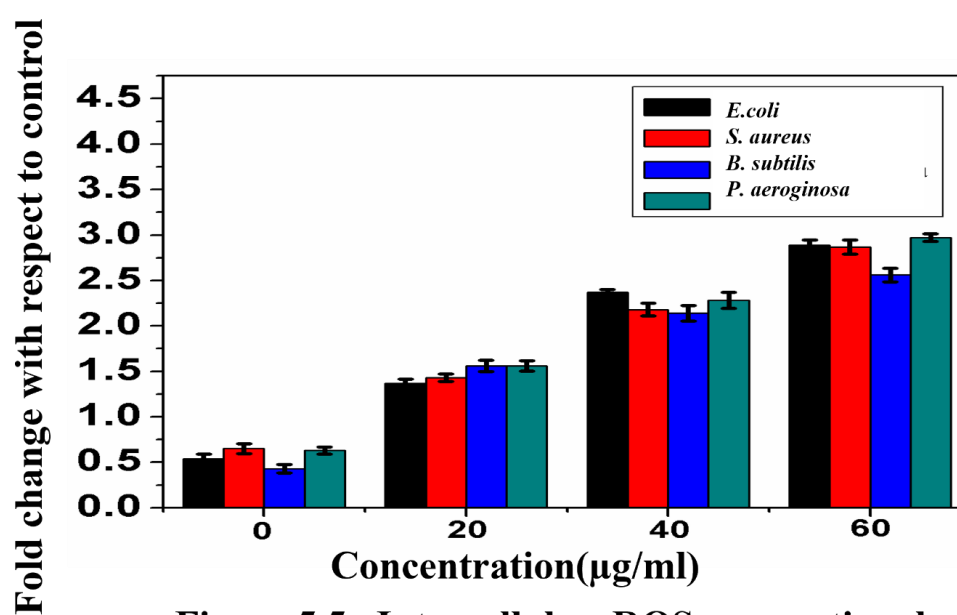
Figure.5.5. Intracellular ROS generation by treatment with AgNPs in pathogenic bacterial strains

100

The phytofabricated AgNPs had the capability to induce intracellular ROS generation, leading to bacterial cell death. The intracellular ROS generation in the bacterial cells was determined by employing DCFH-DA as an intracellular ROS indicator, as shown in Figure.5.5. The results indicated that the AgNPs treated pathogenic bacterial cells augmented ROS generation, which was responsible for bacterial cell death. The enhanced ROS production was correlated with the bacterial cell membrane, disruption in the electronic transport chain, and genetic material detonation [80, 235].

5.4.3. Anticancer activity against Hep G2 cells

5.4.3.1. Cytotoxicity Study
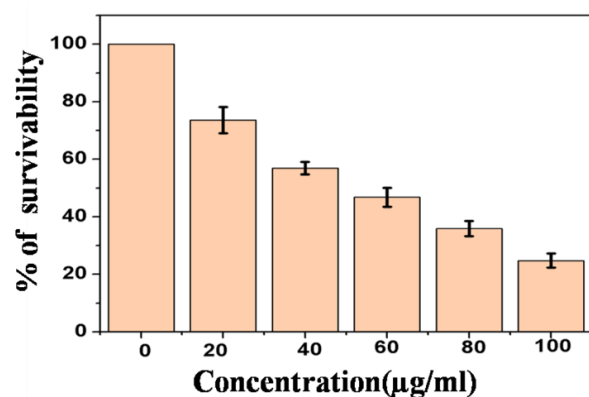
Figure.5.6. Cell viability assay of AgNPs in human hepatocellular cancer HepG2 cells

The in vitro cytotoxicity of the AgNPs was evaluated to determine effects on HepG2 cell line. The cells were exposed to different concentrations of AgNPs (0-120 µg/ml) for 24 hours, followed by an MTT assay. It was observed that the AgNPs exhibited a dose-dependent decrease in cell survivability. The LD_{50} of AgNPs was calculated to be 46 ± 3.2 µM. Therefore, it can be concluded that the synthesized phytofabricated AgNPs could potentially exert encouraging anticancer activity as shown in Figure.5.6.

5.4.3.2 Study of Intracellular ROS generation
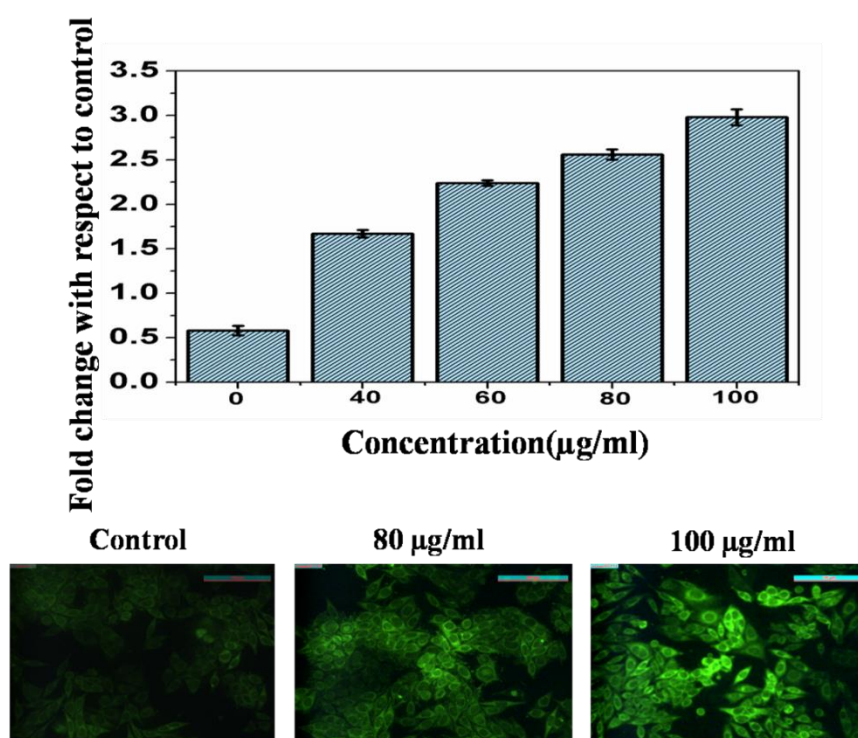
Figure.5.7. Intracellular ROS generation by treatment with AgNPs in human hepatocellular cancer HepG2 cells

The analysis of Reactive oxygen species (ROS) was performed using both fluorescence microscopy and a spectrofluorometer with the aid of 2′, 7′ dichlorofluorescein diacetate (DCF-DA) as a probe. The generation of reactive oxygen species was evaluated in hepatocellular carcinoma cells (Hep G2) with AgNPs at concentrations of 80 µg/ml and 100 µg/ml for 12 hours. The fluorescence microscopic images clearly depict the enhancement of green color fluorescent intensity in the treated HepG2 cell lines after 12 hours Figure.5.7. (a) and (b) [232].

5.5. Conclusions

The synthesis of phyto-fabricated silver nanoparticles is inexpensive, nontoxic, and eco-friendly. The AgNPs were thoroughly characterized using UV-Vis, FTIR, XRD, DLS, and FESEM. The results from UV−Vis spectral studies confirmed the presence of surface plasmon resonance of these biogenic silver nanoparticles. The biomolecules predominant in the *O. sanctum* leaves were primarily responsible for reducing and capping the AgNPs as analyzed by FTIR measurements. Particle size and stabilization were determined with the aid of DLS

and zeta potential techniques. FESEM studies depicted the formation of spherical and uniform-shaped silver nanoparticles with a size range of 25-100 nm. The XRD pattern additionally confirmed the development of the silver nanoparticles through the eco-friendly green synthetic route. Despite significant progress in cancer diagnosis and treatment, cancer still poses a grave worldwide threat. Conversely, the global dissemination of pathogenic bacterial strains has emerged as a serious contemporary challenge to public health. Our results clearly indicate that the biogenic AgNPs initiate oxidative damage through augmented ROS generations in both prokaryotic and eukaryotic cells. The generated reactive oxygen or superoxide can directly interact with the cell metabolism to generate hydroxyl radicals, leading to damage to DNA, lipid, and proteins. Our results strongly suggest that these phytofabricated AgNPs can be considered potential antibacterial agents against Gram-positive (*S. aureus*, *B. subtilis*) and Gram-negative (*E. coli*, *P. aeruginosa*) pathogenic bacterial strains. In the present study with AgNPs, the probable reason behind the destruction of the bacterial cell wall might be due to the disruption in the signaling cascades that lead to defective cell wall synthesis. This phenomenon occurs due to enhanced ROS generation in both Gram-positive and Gram-negative bacterial strains. Additionally, the AgNPs lead to the damage of human liver cancer cells due to enhanced intracellular ROS. In conclusion, our studies suggest that our phytofabricated AgNPs have the potential to emerge as potent anticancer and antibacterial agents.

CHAPTER 6

Gadolinium-Capped Zinc sulfide Conjugated Silver Nanoparticles: A Potential Nanocomposite having Antibacterial Properties

Summary

Zinc sulfide (ZnS) nanoparticles are highly considerable for their inherent antibacterial properties, making them promising material for combating bacterial infections. This study explores the potential of enhancing their therapeutic efficacy by incorporating Gadolinium (Gd), a well-known fluorophore with unique properties. The addition of silver aims to enhance the effectiveness of the ZnS nanoparticles. Successful synthesis of ZnS@Ag nanoparticles capped with Gadolinium (ZnS@Gd@Ag) was confirmed using various biophysical methods such as UV-Vis spectroscopy, X-ray Diffraction (XRD), Fourier Transform Infrared (FTIR), Field Emission Scanning Electron Microscopy (FESEM), Photoluminescence (PL), Transmission electron microscope (TEM) and zeta potential. The antibacterial efficacy of the Gadolinium-doped ZnS nanoparticles was evaluated, revealing their ability to induce oxidative stress in bacterial cell membranes, leading to the eradication of pathogenic bacterial strains. Furthermore, the Gadolinium-tagged nanoparticles exhibited fluorescence properties, potentially enabling their utilization in bioimaging applications. The potential conjugation with silver opens up exciting possibilities for enhancing their therapeutic and diagnostic credentials, presenting these nanoparticles as a merging intervention for various biomedical applications.

6.1. Introduction

Zinc sulfide nanoparticles (ZnS) are well known for their optoelectronic property but nowadays they have been studied for their bacterial properties against various pathogenic bacteria [233]. When Zinc sulfide nanoparticles are capped to enhance their antibacterial property with 1-(carboxymethyl)-4-[(E)-2-(1,2-oxazol-3-yl)etheylpyridin-1-ium, it has been observed that capped ZnS are more potential than uncapped ZnS [234]. In the study of C. Chaliha et al., zinc sulfide nanoparticle was dopped with copper through a solvothermal approach using Mercapotosuccinic (MSA) and sodium citrate (SC) as differential capping agents. They confirmed MSA@Cu: ZnS nanoparticles as a potential antibacterial agent. [235]. ZnS nanoparticles synthesized by G.R Amir et al., using the chemical precipitation method are cubic in shape. Their study confirmed that with the increasing concentration of ZnS nanoparticles bacterial growth was affected. [236]. Previous research validates the antibacterial potential of ZnS nanoparticles but no such augment was done to enhance the efficacy and to encapsulate the ZnS. Gadolinium is a rare earth element that is used to fabricate to modify the properties of ZnS@Ag such as magnetic, optical, and luminescence characteristics. Gadolinium doping has the potential to increase the photolytic activity of the nanoparticles by increasing the surface area and charge separation [237]. Gadolinium is also capable of improving the sensitivity and selectivity of the nanoparticles by providing more active sites and enhancing electron transfer [232-242]. ZnS@Ag nanoparticles may be used as luminescent materials for bioimaging, and drug delivery and conjugation of Gadolinium can increase the intensity and stability of these nanoparticles by introducing energy levels and reducing quenching effects.

There are several studies on synthesizing Zinc Sulfide nanoparticles [233-238]. But in this study, we attached Gadolinium for its fluorescence property to track the nanoparticle and silver to increase the antibacterial potential. Previously this type of functionalized ZnS nanoparticles was not synthesized against pathogenic bacterial cells.

Silver nanoparticles are conventionally used against pathogenic bacterial cells [240]. AgNPs are highly efficient and have potential antibacterial properties. Here we have observed the effect of these biogenic ZnS@Gd@AgNPs on the prokaryotic cells. The fabricated ZnS@Gd@AgNPs had a remarkable antimicrobial efficacy against Gram-positive (*S. aureus, E. faecalis*) and Gram-negative (*E. coli, P. aeruginosa*) pathogenic bacterial species. We have also studied the mechanism behind bacterial growth inhibition. In our present experiments with biogenic ZnS@Gd@AgNPs, the destruction of bacterial cell walls might have caused due to

one or multiple steps of signaling cascades resulting in defective cell wall synthesis or impaired cross-linking of polymer units, which have occurred due to the ROS generation in both Gram-positive and Gram-negative bacterial strains [80].

6.2. Experimental Section

6.2.1. Materials

6.2.1.1. Chemical Ingredients

All the reagents and chemicals used for this study including bacterial culture media, fluorescence stains, MTT reagent, Zinc acetate, Thiourea, Gadolinium, and Ethylene diamine were purchased from Merck, India, and SRL Pvt. Ltd, Mumbai, India. Throughout the study deionized (Millipore) water of resistivity at least 18 MΩ-cm has been used.

6.2.1.2. Bacterial Strains

The Gram-positive strains used in microbiological experiments were *Staphylococcus aureus* 740 and *Enterococcus faecalis* 441. *Escherichia coli* 443 and *Pseudomonas aeruginosa* 1688 were the Gram-negative strains used in this study. These bacterial strains were procured from the Microbial Type Culture Collection (MTCC), IMTECH, Chandigarh, India.

6.2.2. Experimental Methods

6.2.2.1. Synthesis of nano-ZnS@Gd@Ag

Stock solution was prepared by dissolving Zinc acetate and thiourea (1:1 ratio) was added in 50 ml distilled water. To yield the final solution, Ethylene diamine solution was added dropwise to maintain the pH. Gadolinium was added about 5% and 7% of silver nitrate. Each step is done under a continuous stirring process. After stirring for 2 hours the solution was transferred to a Teflon-lined stainless steel hydrothermal reactor. Reactions were performed by placing the unit in a dust-free electric oven for 8-6 hours at a temperature of 150 °C and then allowing it to cool down at room temperature. The reacted solution was centrifuged and then washed several times with distilled water followed by drying. The obtained samples were sent for characterization.

6.2.3. Physical Characterization of ZnS@Gd@AgNPs

Synthesized nanoparticles were characterized with the help of X-ray powder Diffractometer model D8, Bruker AXS, Wisconsin, USA, using Cu-Kα target operating at 35 kV (wavelength -1.5418 Å and scan speed-1s/step), Fourier transform infrared spectroscope (FTIR)-8400S, Shimadzu, DLS (Dynamic light Scattering) (NANO ZS90, Malvern Instruments Ltd., UK). Fluorescence microscope (DM 2500 Leica, Japan), Field emission Scanning Electron Microscope (FESEM) using INSPECTF50 (FEI, Netherland) and EVO 18 Special Edition, Carl Zeiss, Germany, Image J software for size distribution analysis. Energy Dispersive X-ray (EDAX) spectrum is also used to determine the elemental composition. The optical properties of the samples are studied using an Ultraviolet-visible spectrophotometer (Epoch microplate reader, Bio-Tek, USA)) and Photoluminescence (PL) spectroscopy (Cary Eclipse Fluorescence Spectrophotometer, Agilent). A fluorescence microscope (DM 2500, Leica, Germany) and Spectroscope (Hitachi, Japan) were employed for the ROS study. Ultrasonic bath sonicator is used for preparing different types of suspensions. All bacterial studies were performed in a biosafety cabinet.

6.2.4. Evaluation of antibacterial activity

6.2.4.1. Determination of minimum inhibitory concentration (MIC) and minimum bactericidal concentration (MBC)

The microdilution method was applied to determine the MIC and MBC values [80]. Total assays were performed in a biosafety cabinet to prevent any undesirable contamination.

6.2.4.2. Tolerance level

The tolerance level of each bacterial strain towards synthesized nanoparticles can be predicted by the values of MIC and MBC. The tolerance level was determined by using the following formula [80].

Tolerance level = (MBC) / (MIC)………………………………………………...………(eq.1.)

6.2.4.3. Agar well diffusion method

The susceptibility of pathogenic bacteria to synthesized nanoparticles was examined by the Mueller-Hinton Agar well diffusion method according to a previously reported protocol [80].

Intracellular ROS generation

2, 7-dichlorofluorescein diacetate (DCFH$_2$-DA) assay was employed to determine the bacterial intracellular ROS generation [237].

Morphological changes of bacterial cells observed by FESEM

The treated (at their MBC value) and untreated (control) 4 bacterial strains were incubated for 16 hours at 37 ^{0} C. Next, the cells were prepared following a standard protocol [238].

6.3. Statistical analysis

We repeated these experiments three times and the data were expressed by calculating the standard deviation of all the experiments. Comparisons of the mean were done with the help of a model I ANOVA test (using a statistical package, Origin Pro 8, Northamptom, MA 01060, USA) with multiple comparison t-tests, p < 0.05 as a limit of significance. The data is the average of three experiments ± SD. ∗ = represents p value < 0.05, ∗∗ = represents p value < 0.01, ∗∗∗ = represents p value < 0.001.

6.4. Results and Discussion

6.4.1. Physical characterization

6.4.1.1. XRD analysis
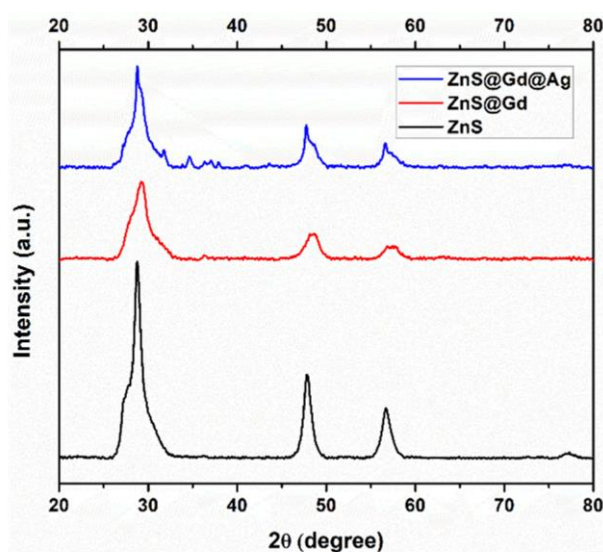
Figure.6.1. XRD analysis nanoparticles

From XRD graph of the biosynthesized ZnS@Gd@AgNPs clearly indicates their crystalline nature (Figure.6.1a). The prominent diffraction peaks (2θ) were found at 29^0 ,48^0 , and 57^0 in the case of ZnS. Doping with Gd causes these to be lowered and wider in the case of ZnS@Gd and ZnS@Gd@Ag NPs. The substitution doping becomes favorable between the comparable ionic radii of two elements. As the ionic radius of Ag^{2+} is comparatively close to Zn^{2+} than to S^{2-}, Ag^{2+} can simply substitute with Zn^{2+} in the ZnS lattices [235-245]. The highest intense peak was considered for determining the average size of ZnS@Gd@Ag NPs by employing the Debye–Scherer equation (eq.1)

$$D = 0.9\, k/\beta\, \cos\theta, \ B = (B^2_M - B^2_S)^{1/2} \dots\dots\dots\dots\dots\dots\dots\dots\dots\dots\dots\dots\dots\dots\dots\dots\dots\dots..\dots\dots\dots (eq.1)$$

where D is the diameter of the nanoparticle, k is the X-ray wavelength (1.5418 Å), B_M and B_S are the measured peak broadening and the instrumental broadening in radian respectively, the full width at half maximum (FWHM) of the diffraction peak and 'θ' is the Bragg angle of the reflection. The calculated average particle sizes are shown in Table.6.1.

Sample	FWHM	Avg Crystallite Diameter
Gd@ZnS@Ag	0.022784	6.28 nm
Gd@ZnS	0.037025	3.87 nm
ZnS	0.021167	6.76 nm

Table.1. Calculated average particle sizes

6.4.1.2. Fourier Transform Infrared spectroscopy analysis

FTIR analysis was carried out in order to determine the chemical structure and identify the presence of various functional groups in nanoparticles. The obtained intense bands $1102 cm^{-1}$,$1219\ cm^{-1}$, $1405\ cm^{-1}$and $2932\ cm^{-1}$ corresponds to the formation of ZnS@Gd@Ag NPs (figure.6.2.). The bands at $612\ cm^{-1}$ are assigned to the ZnS band due to Zn–S vibrations [1. (232,239)]. $1560\ cm^{-1}$ spectrum corresponds to O–H stretching vibration representing the water absorption. Bands between $420\ cm^{-1}$ and $430\ cm^{-1}$specifies that ZnS were not oxidized during synthesis [1. (234)]. Another peak at $1102 cm^{-1}$ cm stands for C–O stretching.
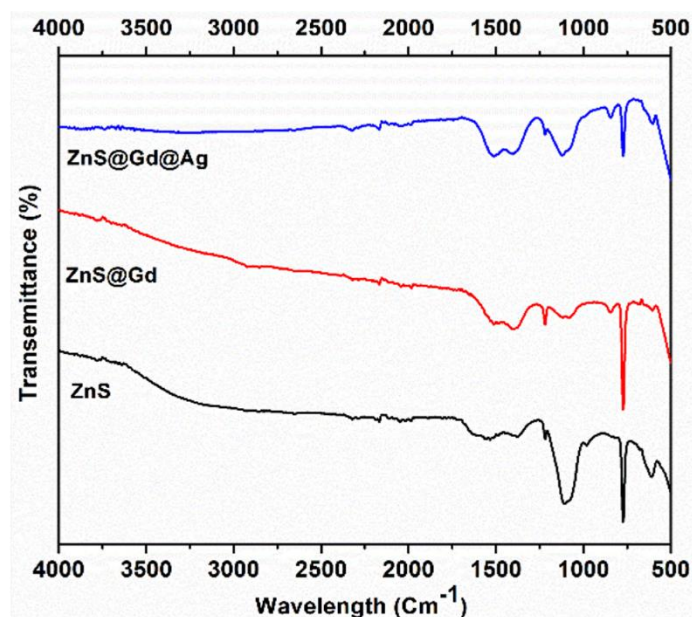
Figure.6.2. FTIR analysis nanoparticles

6.4.1.3. FESEM analysis and EDAX study

The FESEM micrograph is shown in Figure.6.3. clearly depicts the morphology of ZnS@Gd@Ag nanoparticles. The agglomeration reveals the weakly bound collection of nanoparticles. From the EDAX study Figure.6.3. (b) we obtain the elemental composition of the synthesized nanoparticles. Our sample mainly consists of Zn, Ag, S, Gd, and O without any impurity which confirms the formation of ZnS@Gd@Ag nanoparticles.
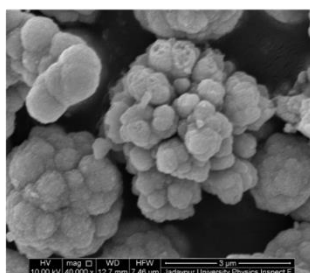
Figure.6.3. (a)   (b)
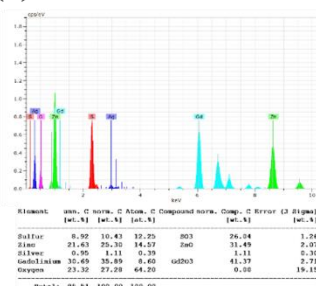
Figure.6.3. (a) FESEM micrograph and (b) EDAX study of ZnS@Gd@Ag nanoparticles

111

6.4.1.4. Dynamic Light Scattering (DLS) and Zeta Potential

The polydispersity index (PDI) and zeta potential of the nanoparticles were determined by DLS (Table 2). P.D.I of ZnS@Gd@Agis 0.254 which confirms the homogeneous nature. The zeta potential of the ZnS@Gd@Ag was 15.4 mV which indicates the moderate stability of the sample. DLS and zeta potential study suggests that the particle is suitable for biological applications.

Table.6.2. Zeta Potential

SAMPLE NAME	PDI	ZETA POTENTIAL (mV)
ZnS	0.571	12.8 ± 1.2
ZnS@Gd	0.506	14.7 ± 2.3
ZnS@Gd@Ag	0254	15.4 ± 1.9

6.4.1.5. Transmission Electron Microscopy

TEM image reveals the nanosized crystal form of the ZnS@Gd@Ag in Figure.6.4. (a). The shape of the ZnS@Gd@Ag nanoparticle is found to be spherical. The average diameter of the particles has been estimated through Gaussian distribution and found to be 12 nm approximately which is graphically represented in Figure.6.4. (b).
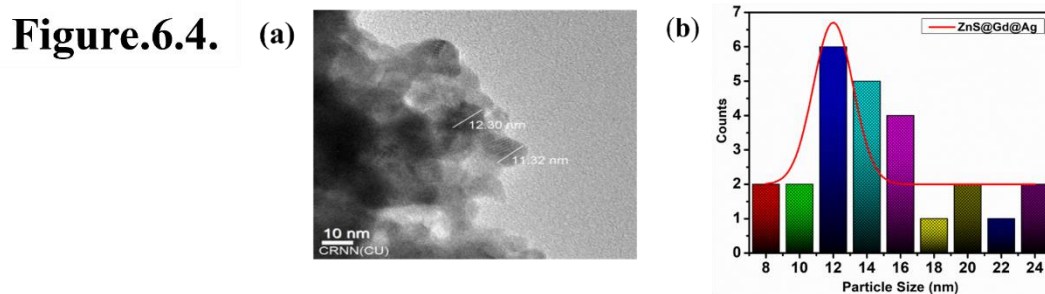
Figure.6.4. (a) TEM image and (b) Particle size analysis of ZnS@Gd@Ag nanoparticles

6.4.1.6. Photoluminance spectroscopy analysis

In our current investigation, we observed a distinct red shift in the photoluminescence (PL) peaks of the entire sample when excited at a specific excitation wavelength (λexc= 320nm), as depicted in Figure.6.5. Our study revealed that smaller-sized particles (ZnS@Gd) result in a wider band gap. The maximum PL emission occurs when the band gap of the particles closely matches the excitation wavelength. In other words, at a particular excitation wavelength, the PL emission corresponds to a specific value of band gap energy for particles of a certain dimension,
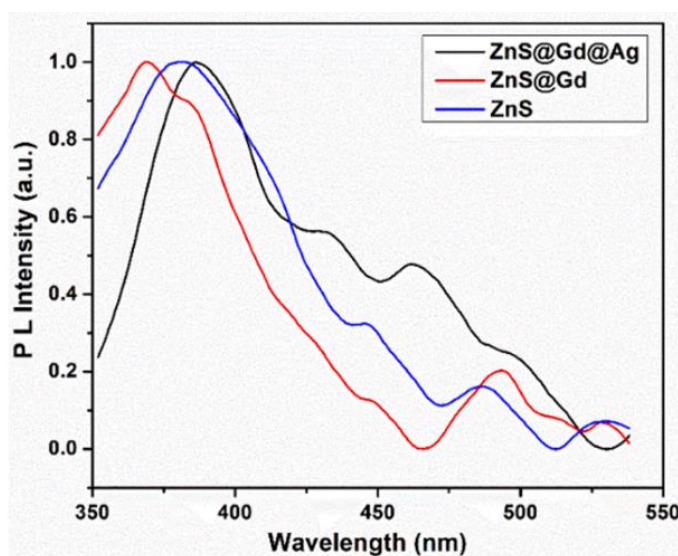
Figure.6.5. PL analysis of ZnS@Gd@Ag nanoparticles

and the intensity of emission depends on the number of particles involved in the process. Consequently, for a given sample, the maximum emission peaks shift towards higher wavelengths with an increase in the average particle diameter. This phenomenon consistently occurred across different particle sizes, with the emission spectra showing a similar trend for ZnS@Gd@Ag. Additionally, when the size of the particles deviates from the exact excitation wavelength, the peak intensity diminishes due to an incompatible bandgap with the excitation wavelength.

6.4.2. Antibacterial activity

6.4.2.1. Determination of MIC & MBC

Table.3. Determination of MIC and MBC values

Antibacterial effectiveness of ZnS@Gd@AgNPs		
Bacterial strain	**MIC value (µg/ml)**	**MBC value (µg/ml)**
Enterococcus faecalis	36.0±2.24	58.20 ± 2.30
Staphylococcus aureus	44.8±1.34	73.08 ± 1.92
Pseudomonas aeruginosa	48.7±2.31	70.95 ± 3.03
Escherichia coli	24.0±1.50	68.00 ± 3.65

Antimicrobial properties of ZnS@Gd@AgNPs were studied by colony counting method on *E. feacalis, S. aureus, P. aeroginosa, E. coli*. The bactericidal activity of ZnS@Gd@Ag NPs against both the Gram-positive and Gram-negative strains is confirmed from Table.6.3 which clearly depicts the MIC and MBC values of our sample against these bacterial strains.

6.4.2.2. Agar well diffusion
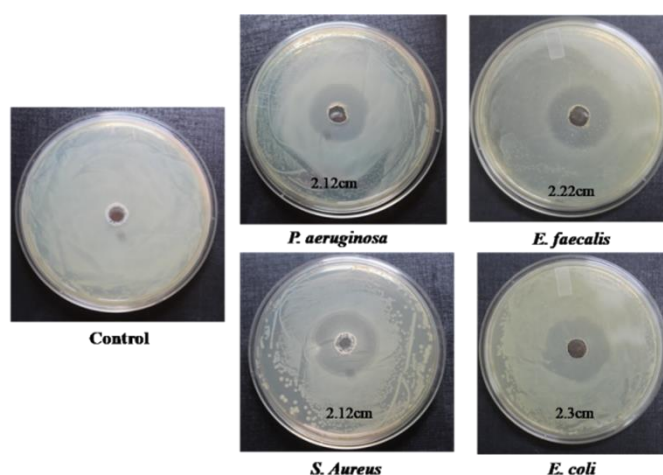
Figure.6.6. Agar plate diffusion treated with ZnS@Gd@Ag nanoparticles

For the agar well diffusion method, 100 µl of overnight grown bacterial culture (cell density 107 CFU ml^{-1}) was dispersed over the petri dish. The solution of the synthesized nanoparticle is placed into the well on the agar petri plate containing solid media. Then the plates were incubated at 37 ^{0} C overnight. Figure.6.6. confirms the distinct zone of inhibition against *E. feacalis, S. aureus, P. aeroginosa,* and *E. coli* against ZnS@Gd@Ag.

6.4.2.3. Tolerance level

Tolerance is a significant parameter that implies the bactericidal nature of any antibacterial agent. For a particular bacterial strain, if the MBC / MIC ratio is less than or equal to 4, then antibacterial agents are considered bactericidal agents. Table.6.3. we can clearly suggest the bactericidal potential of ZnS@Gd@AgNPs against four different bacterial strains.

6.4.2.4. Evaluation of ROS Generation
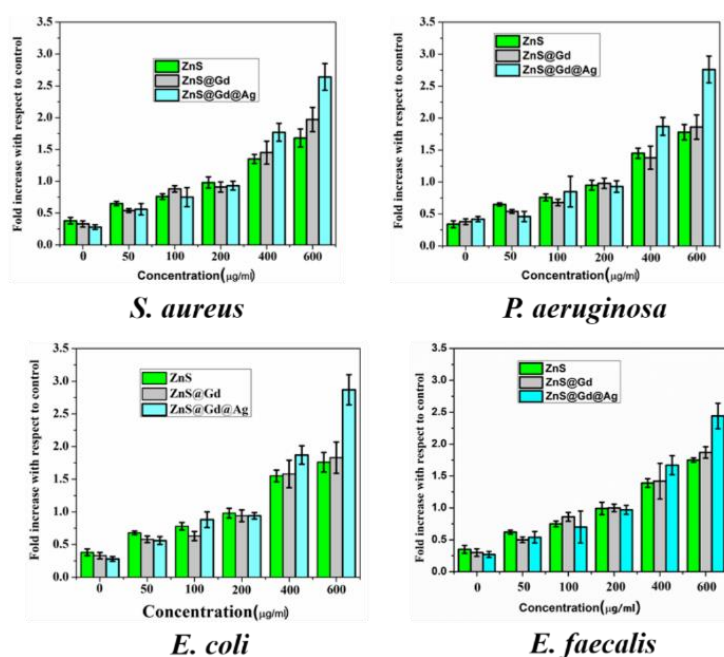
Figure.6.7. Bacterial ROS generation

The ZnS@Gd@Ag has the potential to reduce bacterial cell survivability at their respective MBC value. As shown in Figure.6.7, To envisage the mechanisms behind the bactericidal activities of our synthesized samples DCF-DA solution was used as a specific probe for determining the amount of ROS generated within the bacterial cells. As depicted in Figure.6.7. The results indicate that the treated pathogenic bacterial cells gradually enhanced ROS

generation with increasing concentrations of NPs. This augmented intracellular ROS production contributes to the bacterial cell membrane disruption that leads to bacterial cell lysis and leakage of the cellular content.

6.4.2.5. Bacterial morphology study by FESEM

E. coli Control | E. coli treated with Gd@ZnS@Ag

E. faecalis Control | E. faecalis treated with Gd@ZnS@Ag

S. Aureus Control | S. Aureus treated with Gd@ZnS@Ag

P. aeruginosa Control | P. aeruginosa treated with Gd@ZnS@Ag
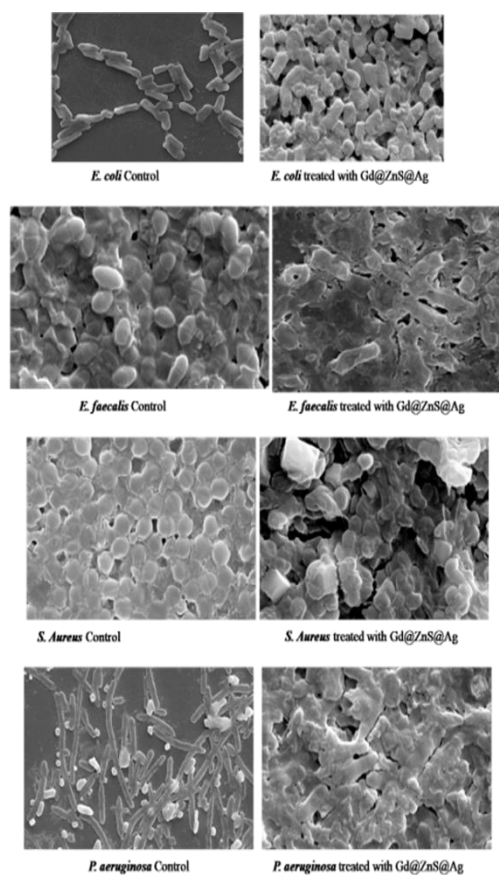
Figure.6.8. FESEM Bacterial image treated and untreated with ZnS@Gd@Ag nanoparticles

The treatment with ZnS@Gd@Ag causes alterations in the structural morphology of the bacterial cells as shown in the FESEM results. The untreated bacterial strains as shown in Figure.6.8. retain their respective morphology. But in the case of treated bacterial cells, we observe that the membrane is damaged, and cytoplasmic leakage leads to agglomerated cell debris. FESEM images confirm that the bacterial membrane is disrupted and perforated due to penetration of ZnS@Gd@AgNPs or might be due to ROS generation.

6.5. Conclusions

The present study reports the synthesis, comprehensive physical characterization and assessment of the biological activity of Gadolinium capped synthesized ZnS nanoparticles conjugated with silver (ZnS@Gd@AgNPs). These nanoparticles exhibit potent antimicrobial effects by disrupting cell wall synthesis or cross-linking of polymers as well as causing degradation of intracellular DNA, lipids, and proteins, ultimately leading to pathogenic bacterial cell death. Notably, ZnS@Gd@AgNPs demonstrated remarkable efficacy against both Gram-positive (*S. aureus, E. faecalis*) and Gram-negative (*E. coli, P. aeruginosa*), as confirmed through various assays including MIC, MBC, and Agar well diffusion studies. Furthermore, the DCFDA assay revealed that ZnS@Gd@AgNPs efficiently induce an increase in intracellular ROS levels, contributing to the demise of bacterial cells. Moreover, the nanoparticles were tagged with Gadolinium to enable facile bio-imaging applications. Remarkably, this study represents the first instance of biogenic ZnS@Gd@AgNPs with enhanced therapeutic and diagnostic attributes. Consequently, this ZnS@Gd@AgNPs holds significant potential as a cost-effective platform for numerous therapeutic and bio-imaging applications.

CHAPTER 7

Conclusion

In conclusion, the studies presented in our work highlight the significant potential of various nanomaterials, including Vanga Bhasma nanoparticles, phytofabricated silver nanoparticles, Hydroxyapatite, Gum Acacia capped Zinc nanoparticles, and Gadolinium doped Zinc sulfide conjugated with silver NPs as promising therapeutic agents against a broad range of diseases, such as cancer and different bacterial infections. These nanomaterials have demonstrated remarkable antimicrobial effects by inducing oxidative damage through increased ROS generation, leading to the disruption of bacterial cell wall synthesis and the death of pathogenic bacterial strains.

Table.7.1. Comparison of size, MIC, MBC and LD$_{50}$ of the synthesized nanoparticles.

NAME	DLS SIZE (d.nm)	MIC (µg/ml)	MBC (µg/ml)	LD$_{50}$ (µg/ml)
VBNPs	124.8	30	116.75	59 µg/ml
AgNPs	101.8	39.5	137.5	46 µg/ml
GA@ZnONPs	253.8	28.75	105.75	48 µg/ml
HAPNPs	343.9	19.88	70	0.1g/ml
Gd@ZnS@Ag	12 nm (from TEM)	38	67.25	

Furthermore, the biogenic nanoparticles have shown promising results in inducing apoptosis in breast cancer cells, providing a potential avenue for anticancer treatments. The use of eco-friendly green synthesis methods for these nanoparticles makes them cost-effective, non-toxic, and environmentally friendly, which adds to their appeal for various medical and biological applications. Additionally, the development of Hydroxyapatite encapsulating Vancomycin and folic acid for selective recognition and killing of pathogenic multi-drug resistant *Enterococcus faecalis* represents a significant advancement in treating drug-resistant bacterial infections. These functionalized HAPNPs have shown excellent antibacterial activity against MDR strains, making them potential candidates for preclinical applications in various disease treatments.

Moreover, the synthesis of Gadolinium-capped ZnS nanoparticles conjugated with silver (Gd@ZnS@AgNPs) demonstrates a novel approach to achieving both antimicrobial efficacy and bio-imaging capabilities. These nanoparticles have exhibited potent antimicrobial effects

against a wide range of bacteria and have the potential for future therapeutic and diagnostic applications.

Overall research data indicates that all these five types of nanomaterials have high potential in their antibacterial property and their cytotoxicity is negligible. Moreover, they are specific to cancer cells depending on pH sense, so they do less harm to normal cells.

The nanoparticles were tagged with fluorescence material to enable bio-imaging applications. This study represents enhanced therapeutic and diagnostic attributes. Consequently, these nanoparticles hold significant promise as a cost-effective platform for numerous therapeutic and bio-imaging applications.

Thus, in the course of our work, dual therapeutic, biocompatible, and non-conventional drug delivery have been successfully synthesized and modified which will be suited for advanced biomedical applications in the future.

Future Scope

1. Mechanistic Elucidation: Investigating the precise mechanism of action of functionalized nanoparticles against MDR bacteria can provide deeper insights into their antibacterial activity. For anticancer properties, more detail is required about the molecular pathways.

2. In vivo studies: Conducting animal studies to evaluate the therapeutic potential and safety profile of these functionalized nanoparticles in vivo can bridge the gap between in vitro experiments and clinical applications. This can include assessing the bio-distribution, pharmacokinetics, and efficacy of the nanoparticles in relevant animal models.

3. Clinical translation: Translating the findings from laboratory studies to clinical applications is crucial. Conducting clinical trials to evaluate the safety, efficacy, and feasibility of functionalized nanoparticles in human patients, can pave the way for their potential use as a novel therapeutic approach.

4. Combination Therapies: Exploring the synergistic effects of these nanoparticles in combination with other treatments, such as conventional chemotherapy or antibiotics, could lead to enhanced therapeutic outcomes. Combination therapies may also help mitigate potential resistance mechanisms.

BIBLIOGRAPHY

1.   Ventola, C. L. The antibiotic resistance crisis part 1: causes and threats. PT 40, 277–283 (2015).

2.   Michael, C. A., Dominey-Howes, D. & Labbate, M. The antimicrobial resistance crisis: Causes, consequences, and management. Front. Public Health 2, 145 (2014).

3.   CDC. Antibiotic Resistance threats in the United States, 2019. (Department of Health and Human Services, CDC, 2019).

4.   WHO. Global Antimicrobial Resistance Surveillance System (GLASS) (WHO, 2017).

5.   Naylor, N. R. et al. Estimating the burden of antimicrobial resistance: a systematic literature review. Antimicrob. Resist. Infect. Control. 7, 58 (2018).

6.   Wu S, Zhu W, Thompson P, Hannun YA (2018) Evaluating intrinsic and non-intrinsic cancer risk factors. Nat Commun 9(1):3490. https://doi. org/10.1038/s41467-018-05467-z

7.   Quazi S (2021) Telomerase gene therapy: a remission towards cancer. Preprints 2021, 2021100407. https://doi.org/10.20944/preprints2 02110.0407.v1

8.   Anand P, Kunnumakkara AB, Sundaram C, Harikumar KB, Tharakan ST, Lai OS, Sung B, Aggarwal BB (2008) Cancer is a preventable disease that requires major lifestyle changes. Pharm Res 25(9):2097–2116. https:// doi.org/10.1007/s11095-008-9661-9.

9.   Cancer Facts & Figures 2021 | American Cancer Society. (n.d.). https:// www.cancer.org. https://www.cancer.org/research/cancer-facts-stati stics/all-cancer-facts-fgures/cancer-facts-fgures-2021. html#:~:text=The%20Facts%20%26%20Figures%20annual%20report%20provides%3A%201.

10.   Park W, Heo YJ, Han DK (2018) New opportunities for nanoparticles in cancer immunotherapy. Biomater Res 22:24. https://doi.org/10.1186/ s40824-018-0133-y 6. Jovčevska I, Muyldermans S (2020) The therapeutic potential of nanobodies. BioDrugs Clin Immunotherap Biopharm Gene Therapy 34(1):11–26. https://doi.org/10.1007/s40259-019-00392-z.

11. Willyard, C. The drug-resistant bacteria that pose the greatest health threats. Nature 543, 15 (2017). This article ranks the most dangerous bacteria that pose urgent threats to public health.

12. Lebeaux, D., Chauhan, A., Rendueles, O. & Beloin, C. From in vitro to in vivo models of bacterial biofilm related infections. Pathogens 2, 288–356 (2013).

13. Lebeaux, D., Ghigo, J.-M. & Beloin, C. Biofilm-related infections: bridging the gap between clinical management and fundamental aspects of recalcitrance toward antibiotics. Microbiol. Mol. Biol. Rev. 78, 510–543 (2014).

14. Bjarnsholt, T. The role of bacterial biofilms in chronic infections. APMIS 121, 1–58 (2013).

15. Van Acker, H., Van Dijck, P. & Coenye, T. Molecular mechanisms of antimicrobial tolerance and resistance in bacterial and fungal biofilms. Trends Microbiol. 22, 326–333 (2014).

16. Flemming, H. & Wingender, J. The biofilm matrix. Nat. Rev. Microbiol. 8, 623–633 (2010).

17. Ventola, C. L. The antibiotic resistance crisis part 2: management strategies and new agents. PT 40, 344–352 (2015).

18. Aminov, R. I. A brief history of the antibiotic era: lessons learned and challenges for the future. Front. Microbiol. 134, 1–7 (2010).

19. Arciola, C. R., Campoccia, D. & Montanaro, L. Implant infections: adhesion, biofilm formation and immune evasion. Nat. Rev. Microbiol. 16, 397–409 (2018).

20. Wu, Y.-K., Cheng, N.-C. & Cheng, C.-M. Biofilms in chronic wounds: pathogenesis and diagnosis. Trends Biotechnol. 37, 505–517 (2019).

21. Jovčevska I, Muyldermans S (2020) The therapeutic potential of nanobodies. BioDrugs Clin Immunotherap Biopharm Gene Therapy 34(1):11–26. https://doi.org/10.1007/s40259-019-00392-z

22. Zitvogel L, Apetoh L, Ghiringhelli F, Kroemer G (2008) Immunological aspects of cancer chemotherapy. Nat Rev Immunol 8(1):59–73. https:// doi.org/10.1038/nri2216

23. Chan H-K, Ismail S (2014) Side efects of chemotherapy among cancer patients in a malaysian general hospital: experiences, perceptions and informational needs from

clinical pharmacists. Asian Pac J Cancer Prev 15(13):5305–5309. https://doi.org/10.7314/apjcp.2014.15.13.5305

24. Quazi S (2021) Artifcial intelligence and machine learning in precision and genomic medicine. Preprints 2021, 2021100011. https://doi.org/10.20944/preprints202110.0011.v1

25. Mahapatro A, Singh DK (2011) Biodegradable nanoparticles are excellent vehicle for site directed in-vivo delivery of drugs and vaccines. J Nanobiotechnol 9:55. https://doi.org/10.1186/1477-3155-9-55

26. Kroemer G, Zitvogel L (2018) The breakthrough of the microbiota. Nat Rev Immunol 18:87–88. https://doi.org/10.1038/nri.2018.4

27. Rosenberg SA, Restifo NP, Yang JC, Morgan RA, Dudley ME (2008) Adoptive cell transfer: a clinical path to efective cancer immunotherapy. Nat Rev Cancer 8(4):299–308. https://doi.org/10.1038/nrc2355.

28. 13. Melero I, Rouzaut A, Motz GT, Coukos G (2014) T-cell and NK-cell infltration into solid tumors: a key limiting factor for efcacious cancer immunotherapy. Cancer Discov 4(5):522–526. https://doi.org/10.1158/ 2159-8290.CD-13-0985.

29. Lacouture M, Sibaud V (2018) Toxic side efects of targeted therapies and immunotherapies afecting the skin, oral mucosa, hair, and nails. Am J Clin Dermatol 19(Suppl 1):31–39. https://doi.org/10.1007/ s40257-018-0384-3.

30. Dadwal A, Baldi A, Narang RK (2018) Nanoparticles as carriers for drug delivery in cancer. Artif Cells Nanomed Biotechnol 46(sup2):295–305. https://doi.org/10.1080/21691401.2018.1457039.

31. Palazzolo S, Bayda S, Hadla M, Caligiuri I, Corona G, Tofoli G, Rizzolio F (2018) The clinical translation of organic nanomaterials for cancer therapy: a focus on polymeric nanoparticles, micelles, liposomes and exosomes. Curr Med Chem 25(34):4224–4268. https://doi.org/10.2174/ 0929867324666170830113755.

32. Gupta, A., Landis, R. F. & Rotello, V. M. Nanoparticle ``based antimicrobials: surface functionality is critical. F1000Res. 5, 364 (2016).

33. Li W, Zhang H, Assaraf YG, Zhao K, Xu X, Xie J, Yang DH, Chen ZS (2016) Overcoming ABC transporter-mediated multidrug resistance: molecular mechanisms

and novel therapeutic drug strategies. Drug Resist Updates 27:14–29. https://doi.org/10.1016/j.drup.2016.05.001.

34. Pelgrift, R. Y. & Friedman, A. J. Nanotechnology as a therapeutic tool to combat microbial resistance. Adv. Drug Deliv. Rev. 65, 1803–1815 (2013).

35. Boisseau P, Loubaton B (2011) Nanomedicine, nanotechnology in medicine. ScienceDirect. https://www.sciencedirect.com/science/article/pii/S1631070511001538.

36. Soenen, S. J. et al. Cellular toxicity of inorganic nanoparticles: common aspects and guidelines for improved nanotoxicity evaluation. Nano Today 6, 446–465 (2011).

37. Laurent S, Forge D, Port M, Roch A, Robic C, Vander Elst L, Muller R (2008) Magnetic iron oxide nanoparticles: synthesis, stabilization, vectorization, physicochemical characterizations, and biological applications. https://doi.org/10.1021/Cr068445e. https://www.academia.edu/1082933/Magnetic_iron_oxide_nanoparticles_synthesis_stabilization_vectorization_physicochemical_characterizations_and_biological_ applications.

38. Baptista, P. V. et al. Nano-strategies to fight multidrug resistant bacteria — "a battle of the titans". Front. Microbiol. 9, 1–26 (2018).

39. Tiwari JN (2011) Zero-dimensional, one-dimensional, two-dimensional and three-dimensional nanostructured materials for advanced electrochemical energy devices. https://www.academia.edu/32389141/Zero_dimensional_one_dimensional_two_dimensional_and_three_dimensional_nanostructured_materials_for_advanced_electrochemical_ energy_devices

40. Gupta, A., Mumtaz, S., Li, C.-H., Hussain, I. & Rotello, V. M. Combatting antibiotic-resistant bacteria using nanomaterials. Chem. Soc. Rev. 48, 415–427 (2019).

41. S Hasan. A review on nanoparticles: Their synthesis and types. Research Jounrnal of recent Science. Vol. 4(ISC-2014), 1-3 (2015). ISSN 2277-2502.

42. A. Saxena, R.M. Tripathi, F. Zafar, P. Singh, Green synthesis of silver Nanoparticles using aqueous solution of Ficus benghalensis leaf extract and characterization of their antibacterial activity, Mater Lett. 67 91–94 (2012).

43. M. Zargar, S. Shameli, N. G. Reza, F. Farahani, Plant mediated green biosynthesis of silver nanoparticles using Vitex negundo L. extract. J Ind Eng Chem. 20(6) 4169–4175 (2014).

44. H. Jiang, S. Manolache, A.C.L. Wong, F.S. Denes, Plasma enhanced deposition of silver nanoparticles onto polymer and metal surfaces for the generation of antimicrobial characteristics, J Appl Polym Sci. 93 1411–1422 (2004).

45. V.K. Sharma, R.A. Yngard, Y. Liny, Silver nanoparticles; green synthesis and their antimicrobial activities, Adv Coll Interface Sci. 145 83–96 (2009). P. Raveendran, J. Fu, S.L. Wallen, Completely green synthesis and stabilization of metal nanoparticles J Am Chem Soc. 125 13940–13941(2003).

46. Chauhan, A. and Chauhan, P., 2014. Powder XRD technique and its applications in science and technology. J Anal Bioanal Tech, 5(5), pp.1-5.

47. Ismail, A.A., van de Voort, F.R. and Sedman, J., 1997. Fourier transform infrared spectroscopy: principles and applications. In Techniques and instrumentation in analytical chemistry (Vol. 18, pp. 93-139). Elsevier.

48. Flannigan, D.J. and Zewail, A.H., 2012. 4D electron microscopy: Principles and applications. Accounts of chemical research, 45(10), pp.1828-1839.

49. Perkampus, H.H., 2013. UV-VIS Spectroscopy and its Applications. Springer Science & Business Media.

50. Sandhu, R., Singh, N., Dhankhar, J., Kama, G. and Sharma, R., 2018. Dynamic light scattering (DLS) technique, principle, theoretical considerations and applications. Nanotechnol. Biochem. Tech. Assess. Qual. Saf. Milk Milk Prod, pp.135-137.

51. Borchert, H. and Borchert, H., 2014. Absorption and photoluminescence spectroscopy. Solar Cells Based on Colloidal Nanocrystals, pp.119-127.

52. Akhtar, K., Khan, S.A., Khan, S.B. and Asiri, A.M., 2018. Scanning electron microscopy: Principle and applications in nanomaterials characterization. Handbook of materials characterization, pp.113-145.

53. Lin, T., Zargar, O.A., Lin, K.Y., Juiña, O., Sabusap, D.L., Hu, S.C. and Leggett, G., 2020. An experimental study of the flow characteristics and velocity fields in an

operating room with laminar airflow ventilation. Journal of Building Engineering, 29, p.101184.

54. Jain, A., Jain, R., Jain, S., Jain, A., Jain, R. and Jain, S., 2020. BOD (Biochemical Oxygen Demand or Biological Oxygen Demand) Incubator. Basic Techniques in Biochemistry, Microbiology and Molecular Biology: Principles and Techniques, pp.3-4.

55. Li X, Robinson S M, Gupta A, Saha K, Jiang Z, Moyano D F, Sahar A, Riley M A and Rotello V M 2014 ACS Nano 810682–6

56. Neu H C 1992 Science 257 1064–73

57. Li Y J, Harroun S G, Su Y C, Huang C F, Unnikrishnan B, Lin H J, Lin C H and Huang C C 2016 Adv. Healthc. Mater. 5 2545–54

58. Chen C W, Hsu C Y, Lai S M, Syu W J, Wang T Y and Lai P S, 2014 Adv. Drug. Deliv. Rev. 78 88–104

59. Chambers H F 2001 Emerg. Infect. Dis. 7 178–82

60. Dickgiesser N and Kreiswirth B N 1986 Antimicrob. Agents Chemother. 29 930–2

61. Levin T P, Suh B, Axelrod P, Truant A L and Fekete T 2005 Agents Chemother. 49 1222–4

62. Schmitz F J, Sadurski R, Kray A, Boos M, Geisel R, Kohrer K, Verhoef J and Fluit A C 2000 J. Antimicrob. Chemother. 45 891–4

63. Hiramatsu K, Hanaki H, Ino T and Tenover F C 1997 J. Antimicrob. Chemother. 40 135–46

64. Chang S et al 2003 New Engl. J. Med. 348 1342–7

65. Singh R, Smitha M S and Singh S P 2014 J. Nanosci. Nanotechnol. 14 4745–56

66. Rai M K, Deshmukh S D, Ingle A P and Gade A K 2012. J. Appl. Microbiol. 112 841–52

67. Manikprabhu D, Cheng J, Chen W, Sunkara A K, Mane S B, Kumar R, Das M, Hozzein W, Duan N Y Q and Li W J 2016 J. Photochem. Photobiol. B 158 202–5

68. Eirich J, Orth R and Sieber S A 2011 J. Am. Chem. Soc. 133 12144–53

69. Chakraborty S P, Sahu S K, Kar Mahapatra S, Santra S, Bal M, Roy S and Pramanik P 2010 Nanotechnology 21 105103–11

70. Chakraborty S P, Sahu S K, Pramanik P and Roy S 2012 Int. J. Pharma. 436 659–76

71. Qi G, Li L, Yu F and Wang H 2013 ACS Appl. Mater. Interfaces 5 10874–81

72. Kell A J, Stewart G, Ryan S, Peytavi R, Boissinot M, Huletsky A, Bergeron M G and Simard B 2008 ACS Nano 2 1777–88

73. Chowdhuri A R, Das B, Kumar A, Tripathy S, Roy S and Sahu S K 2017 Nanotechnology 28 095102

74. Ren H, Zhang L, An J, Wang T, Li L, Si X, He L, Wu X, Wang C and Su Z 2014 Chem. Commun. 50 1000–2

75. Horcajada P, Serre C, Maurin G, Ramsahye A N, Balas F, Vallet-Regí M, Sebban M, Taulelle F and Férey G 2008. J. Am. Chem. Soc. 130 6774–80.

76. Taylor-Pashow K M L, Rocca J D, Xie Z, Tran S and Lin W 2009 J. Am. Chem. Soc. 131 14261–3

77. Tamames-Tabar C E, Guillou I N, Serre C, Miller S R, Elkaïm E, Horcajada P and Blanco-Prieto M J 2015 Cryst. Eng. Comm. 17 456–62

78. Wu V M, Tang S and Uskoković V 2018 ACS Appl. Mater. Interfaces 10 34013–28

79. Ghosh S, Wu V, Pernal S and Uskoković V 2016 ACS Appl.Mater. Interfaces 8 7691

80. Bardhan S, Pal K, Roy S, Das S, Chakraborty A, Karmakar P, Basu R and Das S 2019 J. Nanosci. Nanotechnol. 19 1–11

81. May J, Shannon K and King A 1998 J. Antimicrob. Chemother. 42 189–97

82. Bhattacharya D, Saha B, Mukherjee A, Santra C R and Karmakar P 2012 Nanoscience and Nanotechnology 2 14–21

83. Pal K, Laha D, Parida P K, Roy S, Bardhan S, Dutta A, Jana K and Karmakar P 2018 J. Nanosci. Nanotechnol. 19 3720–33

84. Pal K, Roy S, Parida P K, Dutta A, Bardhan S, Das S, Jana K and Karmakar P 2019 Materials Science & Engineering C 95 204–16

85. Roy S, Maity A, Mandal P, Chanda D K, Pal K, Bardhan S and Das S 2018 Cryst. Eng. Comm. 20 6338–50

86. Roy S, Bardhan S, Pal K, Ghosh S, Mandal P and Das S 2018. Journal of Alloys and Compounds 763 749–58

87. Liu J B, Ye X Y, Wang H, Zhu M K, Wang B and Yan H 2003. Ceram. Int. 29 629

88. Zapanta L R 1965 Nature 206 403–4

89. Banerjee S et al 2018 Colloids and Surfaces B: Biointerfaces 171 300–7

90. He Q J and Huang Z L 2007 Cryst. Res. Technol. 42 460

91. Panda R N, Hsieh M F, Chung R J and Chin T S 2003 J. Phys. Chem. Solids 64 193

92. Blakeslee K C and Condrate R A 1971 J. Am. Ceram. Soc. 54 559

93. Anee T K, Ashok M, Palanichamy M and Narayana K 2003. Mater. Chem. Phys. 80 725–30

94. Liu Y, Hou D and Wang G 2004 Mater. Chem. Phys. 86 69–73

95. Esmaeilia A and Ghobadianpour S 2016 Int. J. Pharm. 501. 326–30

96. Musa M, Kannan T P, Masudi S M and Rahman I A 2012 Mol. Cell. Toxicol. 8 53–60

97. Dixon J M, Taniguchi M and Lindsey J S 2005 Photochem. Photobiol. 81 212–3

98. Eaton D F 1988 Pure Appl. Chem. 60 1107–14

99. Tyagi A and Penzkofer A 2010 Chem. Phys. 367 83–92.

100. Patrinoiu G, Calderón-Moreno J M, Chifiriuc C M, Saviuc C, Birjega R and Carp O 2016 J. Colloid Interface Sci. 462 64.

101. Petrochenko P E, Skoog S A, Zhang Q, Comstock D J, Elam J W, Goering P L and Narayan R J 2013 Biomatter 3 e25528.

102. Vijayakumar S, Vinoj G, Malaikozhundan B, Shanthi S and Vaseeharan B 2015 Spectrochimica Acta Part A:Molecular and Biomolecular Spectroscopy 137 886.

103. Malekzadeh A M, Ramazani A, Rezaei S J T and Niknejad H 2017 J. Colloid Interface Sci. 490 64.

104. Gholibeloo E, Mortezazadeh T, Salehian F, Forootanfar H, Firoozpour L, Foroumadi A, Ramazani A and Khooti M 2019 J. Colloid Interface Sci. 556 128.

105. Dabbaghi A, Jahandideh A, Kabiri K, Ramazani A and Zohuriaan-mehr M J 2019 J. Polym. Environ. 27 1988.

106. Fardood S T, Ramazani A, Moradi S and Asiabi P A 2017. J. Mater. Sci.: Mater. Electron. 28 13596.

107. Singh G, Singh J, Jolly S S, Rawat R, Kukkar D, Kumar S, Basu S and Rawat M 2018 J. Mater. Sci.: Mater. Electron. 29 7364.

108. Rezaei S, Seyed J T, Asemeh M, Ali R and Hassan N 2019. Curr. Drug Deliv. 16 839.

109. Sadr S H, Davaran S, Alizadeh E, Salehi R and Ramazani A. 2018 J. Drug Deliv. Sci. Tec. 45 240.

110. Sadr S H, Davaran S, Alizadeh E, Salehi R and Ramazani A 2018 J. Biomater. Sci. Polym. Ed. 29 277.

111. Singh J, Kumar S, Alok A, Upadhyay S K, Rawat M, Tsang D C W, Bolan N and Kim K H 2019 J. Clean. Prod. 214 1061.

112. Sajjadifar S, Amini I and Amoozadeh T 2017 Chem. Method. 1 1.

113. Elumalaia K and Velmuruganb S 2015 Applied Surface Science 345 329. Selvarajan E and Mohanasrinivasan V 2013 Materials Letters 112 180.

114. Moradnia F, Ramazani A, Fardood S T and Gouranlou F 2019. Mater. Res. Express. 6 075057.

115. Yu C, Zheng-Jun Y, Ping-Ze Z and Xi-Xi L 2020 Mater. Res. Express 6 1250f4.

116. Fardood S T, Forootan R, Moradnia F, Afshari Z and Ramazani A 2020 Mater. Res. Express. 7 015086.

117. Dayyani N, Ramazani A, Khoee S and Shafiee A 2018 Silicon 10 595.

118. Hosseinzadeh Z, Ramazani A, Ahankar H, Ślepokura K and Lis T 2019 Silicon 11 2933.

119. Atrak K, Ramazani A and Fardood S T 2019 J. Photochem. Photobiol. A 382 111942.

120. Moradnia F, Fardood S T, Ali Ramazani A and Gupta V K. 2020 J. Photochem. Photobiol. A 392 112433.

121. Hassani H, Zakerinasab B and Nozarie A 2018 Asian J. Green Chem. 2 59.

122. Lakshmeesha T R, Sateesh M K, Prasad B D, Sharma S C, Kavyashree D, Chandrasekhar M and Nagabhushana H 2014 Cryst. Growth Des. 14.

123. Krishnaveni R and Thambidurai S 2013 Industrial Crops and Products 47 160.

124. Karvani Z E and Chehrazi P 2011 African Journal of Microbiology Resear. 5.

125. Raghupathi R, Koodali R T and Manna A C 2011 Langmuir 27 4020.

126. Sorbiun M, Mehr S E, Ramazani A and Fardood S T 2018. J. Mater. Sci.: Mater. Electron. 29 2806.

127. Atrak K, Ramazani A and Fardood S T 2018 J. Mater. Sci.: Mater. Electron. 29 6702.

128. Bhadra P, Mitra M K, Das G C, Dey R and Mukherjee S 2011. Mater Sci Eng C. 31 929.

129. Banoee M, Seif S, Nazari Z E, Fesharaki P J, Shahverdi H R, Moballegh A, Moghaddam K M and Shahverdi A R 2005. J. Biomed. Mater. Res. B Appl. Biomater. 93 557.

130. Dutta R K, Nenavathu B P and Gangishetty M K 2013 Journal of Photochemistry and Photobiology B: Biology 126105. Vikrant K, Roy K, Kim K H and Bhattacharya S S 2019. Environ. Res. 177 108569.

131. Fardood S T, Ramazani A and Moradi S 2017 Chem. J. Mold. 12 115.

132. Tarasi R, Khoobi M, Niknejad H, Ramazani A, Ma'mani L, Bahadorikhalili S and Shafiee A 2016 J. Magn. Magn. Mater. 417 451.

133. Singh J, Dutta T, Kim K H, Rawat M, Samddar P and Kumar P 2018 J. Nanobiotechnol. 16 84.

134. Singh J, Rathi A, Rawat M, Kumar V and Kim K H 2019. Compos. B Eng. 166 361.

135. Aghahosseini H, Ramazani A, Slepokura K and Lis T 2018. J. Colloid Interface Sci. 511 222.

136. Aghahosseini H and Ramazani A 2020 Eurasian Chem. Commun. 2 410.

137. Singh J, Kaur S, Kaur G, Basu S and Rawat M 2019 Green Processing and Synthesis 8 272.

138. Manna J, Begum G, Kumar K P, Misra S and Rana R K 2013. ACS Appl. Mater. Interfaces 5 4457.

139. Bajpai S K and Kumari M 2015 Int. J. Biol. Macromol. 80 177.

140. Radulescu M et al 2016 Rom. J. Morphol. Embryol. 57 107.

141. Atrak K, Ramazani A and Fardood S T 2019 Environ. Technol. 2019 1.

142. Fardood S T, Ramazani A, Golfar Z and Joo S W 2017 Appl. Organomet. Chem. 31 e3823.

143. Ahankar H, Ramazani A, Ślepokura K, Lis T and Kinzhybalo V 2019 Res. Chem. Intermed. 45 5007.

144. Fardood S T, Moradnia F and Ramazani A 2019 Micro Nano Lett. 14 986.

145. Azar B E, Ramazani A, Fardood S T and Morsali A 2020 Optik 208 164129.

146. Virender K, Sharma R, Yngard A and Yekaterina L 2009. Advances in Colloid and Interface Science 145 83.

147. Chaturvedi A, Bajpai A K, Bajpai J and Singh K 2016 Mater.Sci. Eng. C Mater. Biol. Appl. 65 408.

148. Rath G, Hussain T, Chauhan G, Garg T and Goyal A K 2016. Mater. Sci. Eng. C Mater. Biol. Appl. 58 242.

149. Sarika P R, Cinthya K, Jayakrishnan A, Anilkumar P R and James N R 2014 Mater. Sci. Eng. C Mater. Biol. Appl. 43 272

150. Badreldin A H, Ziada A and Blunden G 2009 Food Chem. Toxicol. 47 1.

151. Aderibigbe B A, Varaprasad K, Sadiku E R, Ray S S, Mbianda X Y, Fotsing M C, Owonubi S J and Agwuncha S C 2015 Int. J. Biol. Macromol. 73 115.

152. Sarika P R and Rachel N J 2016 Carbohydrate Polymer 148 354.

153. Singh B, Sharma S and Dhiman A 2013 Int. J. Pharm. 457 82.

154. Fardood S T, Golfar Z and Ramazani A 2017 J. Mater. Sci.: Mater. Electron. 28 17002

155. Fardood S T, Ramazani A and Moradi S 2017 J. Sol-Gel Sci.Technol. 82 432

156. Sarikaa P R, Cinthya K, Jayakrishnan A, Anilkumar P R and Rachel N J 2014 Materials Science and Engineering: C 43 272.

157. Rao H N, Lakshmidevi N, Pammia S V N, Kolluc P, Ganapaty S and Lakshmi P 2016 Materials Science and Engineering: C 62 553.

158. Chopra M, Bernela M, Kaur P, Manuja A, Kumar B and Thakur R 2015 Int. J. Biol. Macromol. 72 827.

159. Bajpai S K, Jadaun M and Tiwari S 2016 Carbohyd. Polym. 153 60

160. Singh K, Singh J and Rawat M 2019 SN Appl. Sci. 1 624.

161. Mehr E S, Sorbiun M, Ramazani A and Fardood S T 2018 J. Mater. Sci.: Mater. Electron. 29 1333.

162. Mina S, Ebrahim S M, Ramazani A and Fardood S T 2018 Int. J. Environ. Res. 12 29.

163. Iravani S 2011 Green Chem. 13 2638.

164. Pattanayak P, Behera P, Das D and Panda S K 2010. Pharmacogn. Rev. 4 95.

165. Cohen M M 2014 J. Ayurveda. Integr. Med. 5 251.

166. Juby K A, Dwivedi C, Kumar M, Kota S, Misra H S and Bajaja P N 2012 Carbohydrate Polymers 89 906.

167. Shivananjappa M and Joshi M 2012 J. Herbs Spices Med. Plants 18 331.

168. Lia J, Xu X, Chen Z, Wang T, Lu Z, Hu W and Wang L 2018 Carbohydrate Polymers 200 416.

169. Singh B, Sharma S and Dhiman A 2017 Carbohydrate Polymers 165 294.

170. Primikyri A, Mazzone G, Lekka C, Tzakos A G, Russo N and Gerothanassis I P 2015 J. Phys. Chem. B 119 83.

171. Bhattacharya D, Saha B, Mukherjee A, Santra C R and Karmakar P 2012 Nanosci. Nanotechnol. 2 14.

172. Chang Y N, Zhang M, Xia L, Zhang J and Xing G 2012 Materials (Basel) 5 2850.

173. Banerjee S et al 2018 Colloids Surf. B 171 300.

174. Chowdhuri A R, Das B, Kumar A, Tripathy S, Roy S and Sahu S K 2017 Nanotechnology 28 095102.

175. Mandal J, Ghorai P, Pal K, Karmakar P and Saha A 2019. J. Lum. 205 14.

176. Mandal J, Ghorai P, Brandão P, Pal K, Karmakar P and Saha A. 2018 New J. Chem. 42 19818.

177. Dey S, Purkait R, Pal K, Jana K and Sinha C 2019 ACS Omega. 4 8451

178. S. Chang, D.M. Sievert, J.C. Hageman, M.L. Boulton, F.C. Tenover, F.P. Downes, S. Shah, J.T. Rudrik, G.R. Pupp, W.J. Brown, S.K. D Cardo, Fridkin infection with,

vancomycin-resistant Staphylococcus aureus containing the van a resistance gene. New, Engl. J. Med. 348 (2003) 1342–1347, https://doi.org/10.1056/NEJMoa025025.

179. H. Ren, L. Zhang, J. An, T. Wang, L. Li, X. Si, L. He, X. Wu, C. Wang, Z. Su, Polyacrylic acid@zeolitic imidazolate framework-8 nanoparticles with ultrahigh drug loading capability for pH-sensitive drug release, Chem. Commun. 50 (2014). 1000–1002, https://doi.org/10.1039/C3CC47666A.

180. P. Horcajada, C. Serre, G. Maurin, A.N. Ramsahye, F. Balas, M. Vallet-Regí, M. Sebban, F. Taulelle, G. Férey, Flexible porous metal-organic frameworks for a controlled drug delivery, J. Am. Chem. Soc. 130 (2008) 6774–6780, https://doi.org/10.1021/ja710973k.

181. K.M.L. Taylor-Pashow, J.D. Rocca, Z. Xie, S. Tran, W. Lin, Postsynthetic modifications of iron-carboxylate nanoscale metal-organic frameworks for imaging and drug delivery, J. Am. Chem. Soc. 131 (40) (2009) 14261–14263, https://doi.org/10.1021/ja906198y.

182. J.A. Lemire, J.J. Harrison, R.J. Turner, Antimicrobial activity of metals: mechanisms, molecular targets, and applications, Nat. Rev. Microbiol. 11 (6) (2013) 371–385, https://doi.org/10.1038/nrmicro3028.

183. A. Azam, A.S. Ahmed, M. Oves, M.S. Khan, S.S. Habib, A memic antimicrobial activity of metal oxide nanoparticles against Gram-positive and Gram-negative bacteria: a comparative study, Int. J. Nanomedicine 7 (2012) 6003–6009, https://doi.org/10.2147/IJN.S35347.

184. A.T. George, S.K. Namasivayam, Raju S synthesis, characterization and antibacterial activity of chitosan stabilized nano zero-valent iron, BOPAMS 1 (1) (2013) 7–11.

185. D. Beyersmann, A hartwig carcinogenic metal compounds: recent insight into molecular and cellular mechanisms, Arch. Toxicol. 82 (8) (2008) 493–512.

186. U. Jungwrith, R.C. Kowol, B.K. Keppler, C.G. Hartinger, W. Berger, P heffeter anticancer activity of metal complexes: involvement of redox processes, Antioxid. Redox Signal 15 (4) (2011) 1085–1127, https://doi.org/10.1089/ars.2010.3663.

187. S.J. Dougan, A. Habtemariam, S.E. McHale, S. Parsons, P.J. Sadler, Catalytic organometallic anticancer complexes, Proc. Natl Acad. Sci. USA 105 (33) (2008) 11628–11633, https://doi.org/10.1073/pnas.0800076105.

188. B. Desoize, Metals and metal compounds in cancer treatment, Anticancer Res. 24. (3a) (2004) 1529–1544.

189. A.U. Wijenayake, C.L. Abayasekara, H.M.T.G.A. Pitawala, B.M.R. Bandara, Antimicrobial potential of two traditional herbometallic drugs against certain pathogenic microbial species, BMC Complement. Altern. Med. 16 (2016) 365.

190. X. Zhou, K. Zeng, Q. Wang, X. Yang, K. Wang, In vitro studies on dissolved substance of cinnabar: chemical species and biological properties, J. Ethnopharmacol. 131 (1) (2010) 196–202, https://doi.org/10.1016/j.jep.2010.06.018.

191. T.N. Aung, Z. Qu, R.D. Kortschak, D.L. Adelson, Understanding the effectiveness of natural compound mixtures in cancer through their molecular mode of action, Int. J. Mol. Sci. 18 (3) (2017) 656, https://doi.org/10.3390/ijms18030656.

192. M. Bhandari, A.S. Ravipati, N. Reddy, S.R. Koyyalamudi, Traditional ayurvedic medicines: pathway to develop anti-cancer drugs, J. Mol. Pharm. Org. Process Res. 3 (3) (2015) 130, https://doi.org/10.4172/2329-9053.1000130.

193. F.M. Millimouno, J. Dong, L. Yang, J. Li, X. Li Targeting, Apoptosis pathways in cancer and perspectives with natural compounds from mother nature, Cancer Prev. Res. 7 (11) (2014) 1081–1107, https://doi.org/10.1158/1940-6207.

194. M. Nafiujjaman, M. Nurunnabi, S.K. Saha, R. Jahan, Y.K. Lee, M rahmatullah anticancer activity of arkeshwara rasa – a herbometallic preparation, Ayur 36 (3) (2015) 346–350, https://doi.org/10.4103/0974-8520.182757.

195. P. Chaudhary, N. Lamba, S.K. Balian, Analytical study of vanga Bhasma International, Journal of Ayurvedic Medicine 5 (1) (2014) 82–90.

196. R. Hiremath, C. Jha, K. Narang, Vanga bhasma and its XRD analysis, Ancient Science of Life 29 (4) (2010) 24–28.

197. S.K. Singh, D.N. Gautam, M. Kumar, S.B. Rai, Synthesis characterization and histopathological study of lead based Indian traditional drug: naga bhasma, Indian J. Pharm Sci 72 (1) (2010) 24e30.

198. R.D. Umrani, D.S. Agrawal, K.M. Paknikar, Anti-diabetic activity and safety assessment of ayurvedic medicine, jasad bhasma (zinc ash) in rat, Indian J. Exp. Biol. 51 (2013) 811e22.

199. P. Verma, C.M. Prasad, Standardization and bioavailability of ayurvedic drug lauha bhasma part II comparative bioavailability studies, Anc Sci Life 15 (1995) 140e5.

200. M.L. Rajendraprasad, K. Shridhar, Study on vanga bhasma, Innovative pharmaceutical Sciences and Research 2 (5) (2014) 978–985.

201. B. Kale, N. Rajurkar, Synthesis and Characterization of Vanga Bhasma, (2017), pp. 1–9.

202. H. Baruah, R. Parveen, A.K. Chaudhary, Therapeutic uses of vanga bhasma: a critical review, Int J Res Ayurveda Pharma 5 (4) (2014) 566–570.

203. I. Bhaumik, K. Pal, U. Debnath, P. Karmakar, K. Jana, A.K. Misra, Natural product inspired allicin analogs as novel anti-cancer agents, Bioorg chem. 86 (2019). 259–272, https://doi.org/10.1016/j.bioorg.2019.01.057.

204. B. Ruidas, S.S. Chaudhury, K. Pal, P.K. Sarkar, C.D. Mukhopadhyay, A novel herbometallic nanodrug has the potential for antibacterial and anticancer activity through oxidative damage, Nanomedicine 14 (9) (2019) 1173–1189, https://doi.org/10.2217/nnm-2018-0187.

205. T. Manna, K. Pal, K. Jana, A.K. Misra, Anti-cancer potential of novel glycosylated 1,4-substituted triazolylchalcone derivatives, Bioorg. Med. Chem. Lett. 29 (19) (2019), https://doi.org/10.1016/j.bmcl.2019.08.019 126615.

206. B. Das, S.K. Dash, D. Mandal, T. Ghosh, S. Chattopadhyay, S. Tripathy, S. Das, S.K. Dey, D. Das, S. Roy, Green synthesized silver nanopartcless destroy multi drug bacteria via reactive oxygen spacies mediated me,brane damage, Arab. J. Chem. 10 (6) (2015) DOI:org/j.arabjc.2015.08.008.

207. M. Mar´ı, A. Morales, A. Colell, C. García-Ruiz, J.C. Fernández-Checa, Mitochondrial glutathione, a key survival antioxidant, Antioxid. Redox Signal 11 (11) (2009) 2685–2700, https://doi.org/10.1089/ARS.2009.2695.

208. S.H. Jo, M.K. Son, H.J. Koh, S.M. Lee, I.H. Song, Y.O. Kim, Y.S. Lee, K.S. Jeong, W.B. Kim, J.W. Park, B.J. Song, T.L. Huh, Control of mitochondrial redox balance and cellular defense against oxidative damage by mitochondrial NADP+-dependent isocitrate dehydrogenase, J. Biol. Chem. 276 (19) (2001) 16168–16176, https://doi.org/10.1074/jbc.M010120200.

209. M. Rai, A. Gade, A. Yadav, Biogenic nanoparticles: an introduction to what they are, how they are synthesized and their applications. In: Rai M, Duran N (eds), Metal nanoparticles in microbiology pp 1–16 (2011).

210. K. Yokohama, D.R. Welchons The conjugation of amyloid beta protein on the gold colloidal nanoparticles surfaces, Nanotechnology 18:105101–105107 (2007).

211. M.B. Mohamed, V. Volkov, S. Link, M.A.E. Sayed, The 'lightning' gold nanorods: fluorescence enhancement of over a million compared to the gold metal, Chem Phy Lett. 317 517–523 (2000).

212. P. Raveendran, J. Fu, S.L. Wallen, Completely green synthesis and stabilization of metal nanoparticles J Am Chem Soc. 125 13940–13941(2003).

213. S.A. kumar, S. Ravi, V. Kathiravan, S. Velmurugan, Synthesis, characterization and catalytic activity of silver nanoparticles using Tribulus terrestris leaf extract, Spectrochimica Acta Part A: Molecular and Biomolecular Spectroscopy 121 88-93 (2014).

214. S.P. Chandran, M. Chaudhary, R. Pasricha, A. Ahmed, M. Sastry, Synthesis of gold nanotriangles and silver nanoparticles using Aloe vera plant extract, Biotechnology Progress, 22 577-583 (2006).

215. S.P. Dubey, M. Lahtinen, M. Sillanpaa, Tansy fruit mediated greener synthesis of silver and gold nanoparticles, Process Biochemistry 45 1065-1071(2010).

216. R.N. Rati, P. Nilotpala, B. Debadhyan, M.P. Kshyama, M. Srabani, B.S. Lala, B.K. Mishra, Green synthesis of silver nanoparticle by Penicillium purpurogenum NPMF: the process and Optimization, Journal of Nanoparticles Research 13 3129-3137 (2011).

217. N. Duran, P.D. Marcarto, G.I.H. DeSouza, O.L. Alves, E. Esposito, Antibacterial effect of silver nanoparticles produced by fungal process on textile fabrics and their effluent treatment, Journal of biomedical nanotechnology 3 203-208 (2007).

218. S. Edgar, S. Sofia, M. Sonia, J. Correia, PVP coated silver nanoparticles showing antifungal improved activity against Dermatophytes, Journal of nanoparticles research 16 2726 (2014). A.M. Fayaz, K. Balaji, M. Girilal, R. Yadav, P.T. Kalaichelvan, R. Venketesan, Biogenic synthesis of silver nanoparticles and their synergistic effect with antibiotics: a study against gram-positive and gram-negative bacteria, Nanomedicine: Nanotechnology, Biology and medicine 6 103-109 (2010).

219. Q.L. Feng, J. Wu, G.Q. Chen, F.Z. Cui, T.N. Kim, J.O. Kim, A mechanistic study of the antibacterial effect of silver ions on Escherichia coli and Staphylococcus aureus, Journal of Biomedical Materials Research 52 662-668 (2001).

220. S. Ghosh, S. Patil, M. Ahire, R. Kitture, S. Kale, K. Pardesi, S.S. Cameotra, J. Bellare, D.D. Dhavale, A. Jabgunde, B.A. Chopade, Synthesis of silver nanoparticles using Dioscorea bulbifera tuber extract and evaluation of its synergistic potential in combination with antimicrobial agents, International journal of Nanomedicine 7 483-496 (2012).

221. S. Kaviya, J. Santhanalakshmi, B. Viswanathan, J. Muthumar, K. Srinivasan, Biosynthesis of silver nanoparticles using citrus sinensis peel extract and its antibacterial activity, Spectrochimica Acta Part A: Molecular and Biomolecular Spectroscopy, 79 594-598 (2011).

222. N. Singh, Y. Hoette, R. Miller, Tulsi: The Mother Medicine of Nature. 2nd ed. Lucknow: International Institute of Herbal Medicine pp. 28–47 (2010).

223. N. Mahajan, S. Rawal, M. Verma, M. Poddar, S. Alok, A phytopharmacological overview on Ocimum species with special emphasis on Ocimum sanctum, Biomed Prev Nutr. 3 185–92 (2013).

224. L. Mohan, M.V. Amberkar, M. Kumari, Ocimum sanctum linn. (TULSI)- an overview, Int J Pharm Sci Rev Res. 7 51-3(2011).

225. P. Pattanayak, P. Behera, D. Das, S.K. Panda, Ocimum sanctum Linn. A reservoir plant for therapeutic applications: An overview, Pharmacogn Rev. 4 95–105 (2010).

226. M.M. Cohen, Tulsi - Ocimum sanctum: A herb for all reasons, J Ayurveda Integr Med. 5(4) 251–259 (2014).

227. S. Mondal, B.R. Mirdha, S.C. Mahapatra, The science behind sacredness of Tulsi (Ocimum sanctum Linn.) Indian J Physiol Pharmacol. 53 291–306 (2009).

228. W. Wangcharoen, W. Morasuk, Antioxidant capacity and phenolic content of holy basil Songklanakarin, J Sci Technol. 29 1407–15 (2007).

229. V.S. Panda, S.R. Naik, Evaluation of cardioprotective activity of Ginkgo biloba and Ocimum sanctum in rodents, Altern Med Rev. 14 161–71 (2009).

230. M. Shivananjappa, M. Joshi, Aqueous extract of tulsi (Ocimum sanctum) enhances endogenous antioxidant defenses of human hepatoma cell line (HepG2) J Herbs Spices Med Plants 18 331–48 (2012).

231. S.P. Chakraborty, S.K. Sahu, S.K. Mahapatra, S. Santra, M. Bal, S. Roy, P. Pramanik, Nanoconjugated vancomycin: new opportunities for the development of anti-VRSA agents, Nanotechnology 21 105103–11 (2010).

232. J. Mandal, P. Ghorai, K. Pal, P. Karmakar, A. Saha, 2-hydroxy-5-methylisophthalaldehyde based fluorescent-colorimetric chemsensor for dual detection of Zn Cu2+ with high sensitivity and application in live cell imaging, Journal of Luminescence 205 14–22 (2019).

233. Ganguly, S., Das, S., & Dastidar, S. G. (2013). Distinct Antimicrobial Effects of Synthesized ZnS Nanoparticles Against Twelve Pathogenic Bacterial Strains. Open Science Repository Chemistry, Online(open-access), e70081948. doi:10.7392/Chemistry.70081948

234. Giridhar, M., Naik, H.S.B., Prabhakar M.C., Naik, M.M., Ballesh N., Mahesh, M.C. Synthesis, characterization and antibacterial activity of water-soluble dye-capped zinc sulphide nanoparticles form waste Zn-C battery. Bulletin of Material Science. 6:44(2021)

235. Chaliha, C., Nath, B.K., Verma, P.K., Kalita, P.K. Synthesis of functionalized Cu:ZnS nanosystems and its antibacterial potential. Arabian Journal of Chemistry. 13(4):515-524(2019)

236. Zhang, L., Goncalves, A.A.S., Jaroniec, M. Identification of preferencially exposed crystal facets by X-ray diffraction. RSC Advance. 10: 5585-5589(2020)

237. Nowaczyk, J., Kadac K., Tarach, I., Kruszkowska, E.O. Conducting polymer: silver interface, morphology and properties. Journal of Materials Science: Material in Electronics. 28(24):1-10 (2017)

238. Kumar, R.S., Veeravazhuthi, V., Muthukumarasamy, N., Thambidurai, M., Elango, M., Gnanaprakasam, A., Rajesh, G. Effect of gadolinium doped ZnS nanoparticles: ferro magnetic photocatalyst for efficient dye degradation. S.N Applied Sciences. 268(2019)

239. Gora, S. A review on biogenic synthesis of ZnS nanoparticles and potential applications. Special Issue J. Indian Chem. Society. 97(12c):2972-2980(2020)

240. Sathiya, P., Kumar, R.A., Geetha, K. Synthesis and characterisation of Gadolinium doped ZnS nanoparticles by chemical precipitation method and its antibacterial activity. Int. J. Nano Dimens., 13 (4):403-413(2022)

241. Mazhdi, M., Tafreshi, M.J. the effects of gadolinium doping on the structural, morphological, optical and photoluminescence properties of zinc oxide nanoparticles prepared by co-precipitation method. Appl. Phys. A., 124:863(2018).

242. Sonawane, H., Deore, J., Rajshri, S., Chavan, P. Synthesis of ZnS NAnomaterials and their applications via Green Approaches: An Overview. BioNanoScience. 13:879-890(2023)

243. K. Yokohama, D.R. Welchons The conjugation of amyloid beta protein on the gold colloidal nanoparticles surfaces, Nanotechnology 18:105101–105107 (2007).

244. Q.L. Feng, J. Wu, G.Q. Chen, F.Z. Cui, T.N. Kim, J.O. Kim, A mechanistic study of the antibacterial effect of silver ions on Escherichia coli and Staphylococcus aureus, Journal of Biomedical Materials Research 52 662-668 (2001).

245. S. Kaviya, J. Santhanalakshmi, B. Viswanathan, J. Muthumar, K. Srinivasan, Biosynthesis of silver nanoparticles using citrus sinensis peel extract and its antibacterial activity, Spectrochimica Acta Part A: Molecular and Biomolecular Spectroscopy, 79 594-598 (2011).

Functionalised biomimetic hydroxyapatite NPs as potential agent against pathogenic multidrug-resistant bacteria

Debbethi Bera[1,2]**, Kunal Pal**[3,4]**, Souravi Bardhan**[1]**, Shubham Roy**[1]**, Rubia Parvin**[3]**, Parimal Karmakar**[3]**, Papiya Nandy**[2] **and Sukhen Das**[1,2]

[1] Department of Physics, Jadavpur University, Kolkata-700032, India
[2] Centre for Interdisciplinary Research and Education, 404B, Jodhpur Park, Kolkata-700068, India
[3] Department of Life Science and Biotechnology, Jadavpur University, Kolkata-700032, India
[4] Division of Molecular Medicine and Centre for Translational Research, Bose Institute, Kolkata-700056, India

E-mail: sukhendas29@gmail.com

CrossMark

Abstract

The persistent dissemination of resistant bacterial strains is a grave contemporary global impediment in hospital-acquired infections which needs to be mitigated with immediate effect. In particular, infections from pathogenic multidrug-resistant (MDR) Gram-positive bacteria (like *Enterococcus faecalis*) which are resistant to conventional antibiotic therapy are attracting immediate global attention. Here we report the synthesis of nanoscale hydroxyapatites (HAPs), which are the well known biomimetic ceramic material having needle shaped morphologies. We have encapsulated vancomycin (VAN) within these nanoparticles and have conjugated the targeting ligand (folic acid) by a facile synthesis process in order to enhance the therapeutic efficacy against MDR *E. faecalis*. These functionalised HAPs are thoroughly characterised by employing field emission scanning electron microscopy (FESEM), powder x-ray diffraction (PXRD), ultraviolet–visible spectroscopy (UV-Vis) and dynamic light-scattering (DLS) techniques. Our results suggest that these functionalised HAPs could successfully transport vancomycin across the cell wall of MDR *E. faecalis* through endocytosis. The determination of selective antibacterial activity has been envisaged with the help of extensive *in-vitro* assays like the minimum inhibitory concentration (MIC), minimum bactericidal concentration (MBC) and the generation of reactive oxygen species (ROS). This study vividly establishes that this folic acid conjugated HAPs are promising antibacterial agents against MDR *E. faecalis* and related pathogenic resistant bacterial strains.

Keywords: hydroxyapatite nanoneedle, vancomycin, folic acid targeting, multidrug-resistant, enterococcus faecalis, antibacterial drug delivery

Classification numbers: 2.04, 2.05, 5.00, 5.08, 5.09

1. Introduction

The emergence of drug-resistant bacteria has posed a grave threat to the modern society. The antibiotic-resistant bacteria are the primary driving force behind millions of deaths that occur every year worldwide as mentioned in the previous reports [1, 2]. Furthermore an incessant decline in approved antibiotics in the past decade is responsible for aggravating this issue. This has given rise to the need of the development of alternate strategies that would help in overcoming the resistance in bacterial strains. Numerous active strategies including the development of novel antibiotics have been implemented for the treatment of multidrug-resistant (MDR) bacteria. The functionalisation of nanomaterials is a very effective process to develop antibacterial agents for the treatment of MDR bacteria. The fluorescent-carbon quantum

dots capped with spermidine have been successfully implemented against MDR bacteria by Li *et al* [3]. Furthermore, different nanoparticles mediated approaches are being implemented as ameliorative agents for infections caused by MDR bacteria [4]. These nanoparticles are not only undesirably hazardous but their process of synthesis is quite tedious. Therefore, there is an urgent need for the development of facile, effective synthesis of non-hazardous antibacterial agents. *Enterococcus faecalis* is a predominant pathogen that accounts for infection in the urinary tract, nosocomial bacteremia, post-surgical infections and is gradually developing resistance towards the conventional therapies. The lack of proper diagnosis and treatment in case of such infections could be responsible for the loss of innumerable lives. Furthermore, its MDR phenotype is posing a grave threat to the global public health [5]. In order to curb the *E. faecalis* infection, different antibiotics have been used, but recently none have been found to be effective against various strains of *E. faecalis* [6, 7]. The resistance to the different antibiotics like penicillin, vancomycin and methicillin has been found in more than 90% of *E. faecalis* strains [8]. The antibiotic drug vancomycin which was used clinically to treat *E. faecalis* infections is the latest inclusion in the list of the antibiotics to develop resistance after penicillin (in 1940), and methicillin (in 1961) [9, 10]. In order to overcome this drug resistance and to combat the MDR *E. faecalis* infection, there is a serious need for the development of antibacterial agent that could effectively overcome MDR *E. faecalis*. Although recently some work has been carried out on the modification of the materials that are effective against MDR pathogenic strains like *S. aureus* [11–13], there is an urgent need for the development of additional surface modifications that could amplify the antibacterial activities of glycopeptide antibiotics like vancomycin (VAN) [14]. Though, vancomycin is predominantly used for the treatment of Gram-positive bacteria, like *S. aureus* and *E. faecalis*, unfortunately these bacterial strains also exhibit a resistance towards it. In order to combat this problem, a number of researchers have implemented a series of VAN-modified nanoparticles that can be employed against multidrug-resistant *S. aureus* (MRSA) [15–19]. Taking clue from their work, here we report the development of nanoscale hydroxyapatite (HAPs) conjugated with VAN for the treatment of MDR *E. faecalis*. In recent years, HAPs have shown great potential in many applications, especially for bioactive molecule delivery [20, 21]. In recent times, the modification of HAPs for therapeutic applications has drawn considerable interests. This is primarily due to their attributes like large surface area, very high porosity and easily modified surface [22, 23]. Wu *et al* and Ghosh *et al* have established that hydroxyapatites possess the ability to enhance the antibacterial effects of common antibiotics like vancomycin [24, 25]. Due to all these attributes, we here emphasise the development of functionalised HAPs for the treatment of MDR *E. faecalis*. It is also well known that folic acid (FA) is a vital nutrient required for nucleotide synthesis for bacteria. Therefore the folic acid conjugated antibiotic encapsulated nanoparticles are readily internalised by the bacteria through the process of endocytosis and thereby the delivery of the encapsulated antibiotic to the bacterial cells can be aggravated to a great extent. The folic acid targeting has been previously implemented for the delivery of antibiotics to the resistant cells [15, 16].

In our present study, we have designed folic-acid-modified HAP nanoparticles conjugated with VAN as an ameliorative agent against vancomycin resistant bacteria strains. The detailed *in vitro* assays like minimum inhibitory concentration (MIC), minimum bactericidal concentration (MBC), agar diffusion method have been used in order to envisage the antibacterial efficacy of our prepared sample. The results vividly implicate that our prepared material has the potential to emerge as a promising ameliorative agent for different disease-causing MDR bacterial strains. Our present work depicts that functionalised HAPs are endowed with such attributes that could unlock new vistas in the treatment of MDR *E. faecalis* as well as other similar pathogenic resistant bacterial strains.

2. Experimental section

2.1. Materials and bacterial strains used in this study

Calcium nitrate tetrahydrate [$Ca(NO_3)_2 \cdot 4H_2O$] (0.1 M) and di-ammonium hydrogen phosphate [$(NH_4)_2 \cdot HPO_4$] (0.1 M) were obtained from Merck, India. The antibiotic, vancomycin, a pure drug was procured from HiMedia, India. Ultrapure grades of bacterial culture media, fluorescence stains, various chemicals and reagents used for biological purposes were procured from Merck Ltd, and SRL Pvt. Ltd, Mumbai, India. Therefore mentioned reagents were utilised without any type of purification or modification. All the experiments were performed with deionised (Millipore) water with a resistivity of at least 18 MΩcm. The glass-wares were thoroughly cleaned with aqua regia solution and were subsequently rinsed with ultrapure water.

MDR pathogenic bacterial strain and antibiotic sensitive strains were used throughout the antibacterial study. The antibiotic resistant *E. faecalis* (ATCC 52199) and antibiotic sensitive *E. faecalis* bacteria (ATCC 29212) were obtained from ATCC. The resistant strain, *E. faecalis* (ATCC 52199) is totally resistant to the various traditional antibiotics like vancomycin, amikacin, ciprofloxacin, tetracyclin, penicillin, methicillin, and erythromycin. All the synthesised HAPs and drugs were sterilised by UV radiation technique prior to the antibacterial experiments.

2.2. Synthesis of nano-hydroxyapatite (HAP)

Stock solution was prepared by dissolving calcium nitrate tetrahydrate [$Ca(NO_3)_2 \cdot 4H_2O$] (0.1 M) and di-ammonium hydrogen phosphate [$(NH_4)_2 \cdot HPO_4$] (0.1 M) in 50 ml distilled water. To yield the final solution, di-ammonium hydrogen phosphate was added dropwise to calcium nitrate tetrahydrate (figure 1). The pH of the reacting suspension was maintained
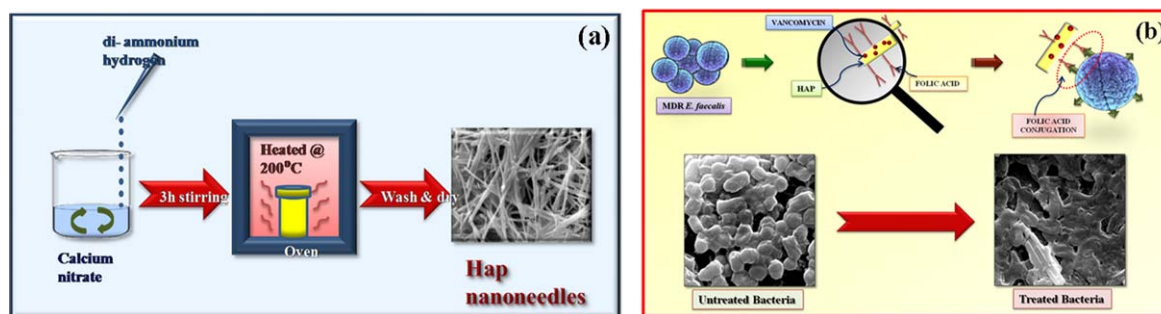
Figure 1. (a) Schematic representation of synthesis of HAP nanoparticles, (b) schematic representation of the delivery of vancomycin by the functionalised HAP nanoparticles for selective recognition and killing of pathogenic MDR *E. faecalis*.

at 5. After vigorous stirring for 2–3 h the solution was transferred to a Teflon-lined stainless steel hydrothermal reactor. Reactions were performed by placing the unit in a dust-free electric oven for 48 h at a temperature of 200 °C and naturally then cooled to room temperature. The reacted solutions were washed several times with distilled water followed by air drying at ∼50 °C for 72 h. The obtained sample was named as HAP and was sent for further characterisations.

2.3. Synthesis of vancomycin encapsulated nanoscale HAP (HAP@VAN)

The synthesised HAP was dissolved in Millipore water and vigorously stirred for 24 hrs. The vancomycin was solubilised in water in another glass tube and stirred for 4 hrs. The vancomycin solution was then introduced dropwise into the HAP solution. The resulting solution was vigorously stirred for 24 hrs. vancomycin encapsulated HAP nanoparticles were collected by means of centrifugation at a speed of 10,000 rpm for 10 mins. Afterwards, the solution was dried by normal lyophilisation method. Finally, the dried powder was mortared in an agate mortar to achieve finer grains. The sample, HAP@VAN was used for further characterisations.

2.4. Folic acid tailoring on vancomycin loaded HAP NPs (HAP@VAN@FA)

The ethyl (dimethylaminopropyl) carbodiimide/N-hydroxysuccinimide (EDC/NHS) reaction was carried out to activate the carboxyl group (–COOH) of folic acid (FA). At first, FA was solubilised in dimethylformamide (DMF). The EDC/NHS was incorporated into the FA solution in order to activate the FA. In a dark condition the activated FA was added dropwise into HAP@VAN solution maintaining the pH of the solution at 7. The FA conjugated HAP@VAN NPs (HAP@VAN@FA) were subjected to centrifugation at 10,000 rpm for about 10 mins and washed thoroughly. Ultimately, the FA conjugated HAP@VAN was obtained employing lyophilisation method.

2.5. Characterisation of HAP NPs

The x-ray diffraction (XRD) patterns of the powdered nanoparticle samples were analysed by x-ray diffractometer

model-D8 Bruker AXS, Winconsin, USA, employing Cu-Kα target with the help of a target wavelength of 1.5418 Å. The XRD was operated at 35 kV with a scan speed of 1 s/step. The Fourier transform infrared spectroscopy (FTIR) study was done using FTIR-8400S, Shimadzu, Japan in the wavenumber range from 400 cm^{-1} to 4000 cm^{-1}. The field emission scanning electron microscope (FESEM) was carried out for the morphological study employing INSPECT F50 (FEI, the Netherland). The nanoparticles were thoroughly dispersed in MilliQ water in a bath-type ultrasonicator for 30 mins to form a suspension having a concentration of 2 mg ml^{-1}. The UV visible spectrophotometer (Epoch microplate reader, Bio-Tek, USA) was used to estimate the absorbance intensity of the nanoparticles after being dispersed completely in MilliQ water. The average particle diameter, size distribution and zeta potential of HAP NPs were measured by employing Zetasizer (NANO ZS90, Malvern Instruments Ltd, UK).

2.6. Antibacterial activity determination

2.6.1. Determination of minimum inhibitory concentration (MIC) and minimum bactericidal concentration (MBC).
The microdilution method was employed in order to envisage the MIC and MBC values [26]. Precisely, 10 μl of bacterial culture containing 2.5×10^5 CFU/ml bacteria was individually added to the several 1-ml nutrient broths (NBs) which were exposed to different concentrations of our synthesised HAPs and were incubated for 24 hrs at 37 °C. Prior to this, the HAP nanoparticles were thoroughly sonicated in a bath ultrasonicator in order to prepare a pure suspension. The MIC values were then estimated by examining the turbidity of the bacterial growth which can be correlated to the near absolute (99%) inhibition of the bacterial growth.

The MBC was performed with the MIC dilutions of bacterial cultures grown onto agar plates. The cultures were then incubated for 24 hrs at a temperature of 37 °C. The minimum concentration required for total killing of the bacteria is regarded as its MBC value. The assays were meticulously performed in a biosafety cabinet.

2.6.2. Tolerance level.
The values of MIC and MBC also gave a clear indication about the tolerance levels of each

bacterial strain towards our synthesised samples. This tolerance level was determined with the help of the following formula [27].

$$\text{Tolerance level} = (\text{MBC})/(\text{MIC}). \qquad (1)$$

2.6.3. Agar well diffusion method.
The agar well diffusion method gives a clear indication about the efficacy of our samples HAP@VAN and HAP@VAN@FA against the pathogenic MDR bacterial strain E. faecalis. The strain was grown until the turbidity of the bacterial culture reached 0.5 McFarland standards which are approximately 10^8 CFU/ml. Then 100 μl of this bacterial culture was inoculated on petridish having a diameter of 90 mm and was filled with 30 ml of Mueller Hinton agar (MHA). Afterwards, the wells having a diameter of approximately 0.563 cm were punched within the agar plates and were treated with HAP, HAP@VAN, HAP@VAN@FA NPs at their respective MBC concentrations. The resistant *E. faecalis* strains were grown on the MHA and incubated overnight at a temperature of 37 °C. Then, the zone of inhibition or the inhibitory diameter was measured [28]. The autoclaved distilled water was used as negative control and standard antibiotic, methicillin was used as positive control in this experiment.

2.6.4. Bacterial cell viability assay.
The bacterial cell survivability was envisaged with the help of the 3-(4, 5-dimethylthiazol-2-yl) -2, 5-diphenyltetrazolium bromide (MTT) assay following a standard protocol [26]. The cell viability was examined after exposure to different concentrations of HAPs and was incubated for 24 hrs at 37 °C. The bacterial cells were then collected and were centrifuged at 1400 rpm for 10 mins at 4 °C. The collected cells were then washed thrice with the help of autoclaved phosphate buffered saline (PBS, pH 7.4). The fresh culture media containing 0.5 mg ml^{-1} of MTT reagent were then added by replacing the previous medium and were incubated for 3 hrs at a temperature of 37 °C. The solution of HCl-isopropanol was added and was incubated for 15 mins at room temperature. Then the absorbance of solubilised MTT formazan product was estimated by UV-vis spectrophotometer (Epoch microplate reader, Bio-Tek, USA) at a wavelength of 570 nm.

2.6.5. Study of intracellular uptake.
The HAP nanoparticles were labeled with quinine sulfate (QS), a fluorescent dye in order to establish the successful internalisation of the drug encapsulated nanoparticles by the bacteria. At first, the freshly grown bacterial cultures were subjected to centrifugation at 1400 rpm at 4 °C for 10 mins. Then, the obtained pellet was thoroughly washed with PBS (pH 7.4), treated with QS-labelled HAPs) and incubated in the dark at 37 °C for 12 hrs. Meanwhile, the bacterial cells treated with unlabelled HAP nanoparticles were taken as negative control. The cells were then washed and re-suspended in PBS. A drop of this suspension was then placed onto a glass slide. The images

were taken with the help of a fluorescence microscope (DM 2500, Leica, Germany) at excitation wavelengths of 330–360 nm.

2.6.6. Intracellular ROS generation.
2, 7-dichlorofluorescein diacetate (DCFH$_2$-DA) assay was used to determine the amount of intracellular ROS generation within the bacteria followed by a standard protocol [26]. The generated ROS readily reacts with the DCFH$_2$-DA which in turn leads to its oxidisation which results in the production of a highly fluorescent compound, 2, 7-dichlorofluorescein (DCF). After the exposure of bacteria cells with HAPs, they were cultured overnight. The overnight culture was then centrifuged at 5000 rpm for 5 mins and was thoroughly washed with PBS solutions. Afterwards, the cells were incubated with DCFH2-DA in the dark conditions at 37 °C for a period of 30 mins. Ultimately, the images of bacteria cells were obtained with a fluorescence microscope (DM 2500, Leica, Germany) at an excitation wavelength of 504 nm and emission wavelength of 529 nm.

2.6.7. Morphology change of bacterial cells.
The bacterial cells were grown in 5 ml culture media and were incubated in shaking condition at 198 rpm at 37 °C for 12 hrs [26]. Then the cells were treated with three different concentrations of HAP@VAN@FA (with respect to the MBC concentration). The cells which were not treated with the HAPs were taken as negative control. Then the cells were centrifuged at 5000 rpm for 5 mins and were washed thoroughly with PBS. The obtained bacterial pellet was later fixed with the help of 2.5% glutaraldehyde and was then washed thrice with sterile PBS. Afterwards, one drop of the fixed pellet was placed on the surface of a glass plate and was vacuum oven dried. The plate was then gold coated and alterations in the bacterial cell morphology were observed with a scanning electron microscope (SEM, EVO 18 Special Edition, Carl Zeiss, Germany).

2.6.8. Cell survivability assay.
The cell survivability of the human lung fibroblast cells WI-38 when treated with HAP nanoparticles 4*s* were envisaged by employing a standard protocol [29, 30]. Briefly, the WI-38 cells were exposed to different concentrations of HAP nanoparticles and were then examined by MTT assay. The cells were grown in each well of 96-well plates at a density of 1×10^4 cells per well at 37 °C for 22–24 hrs. The cells were then exposed to HAP NPs at different concentrations of 0–500 μg ml^{-1} for 24 hrs. The cells after incubation were thoroughly washed with $1 \times$ PBS and incubated with solution of MTT at a concentration of 450 μg ml^{-1} for a period of 3–4 hrs at 37 °C. The resulting formazan crystals were then dissolved in a buffer which could solubilise the crystals. Then, the absorbances were measured at a
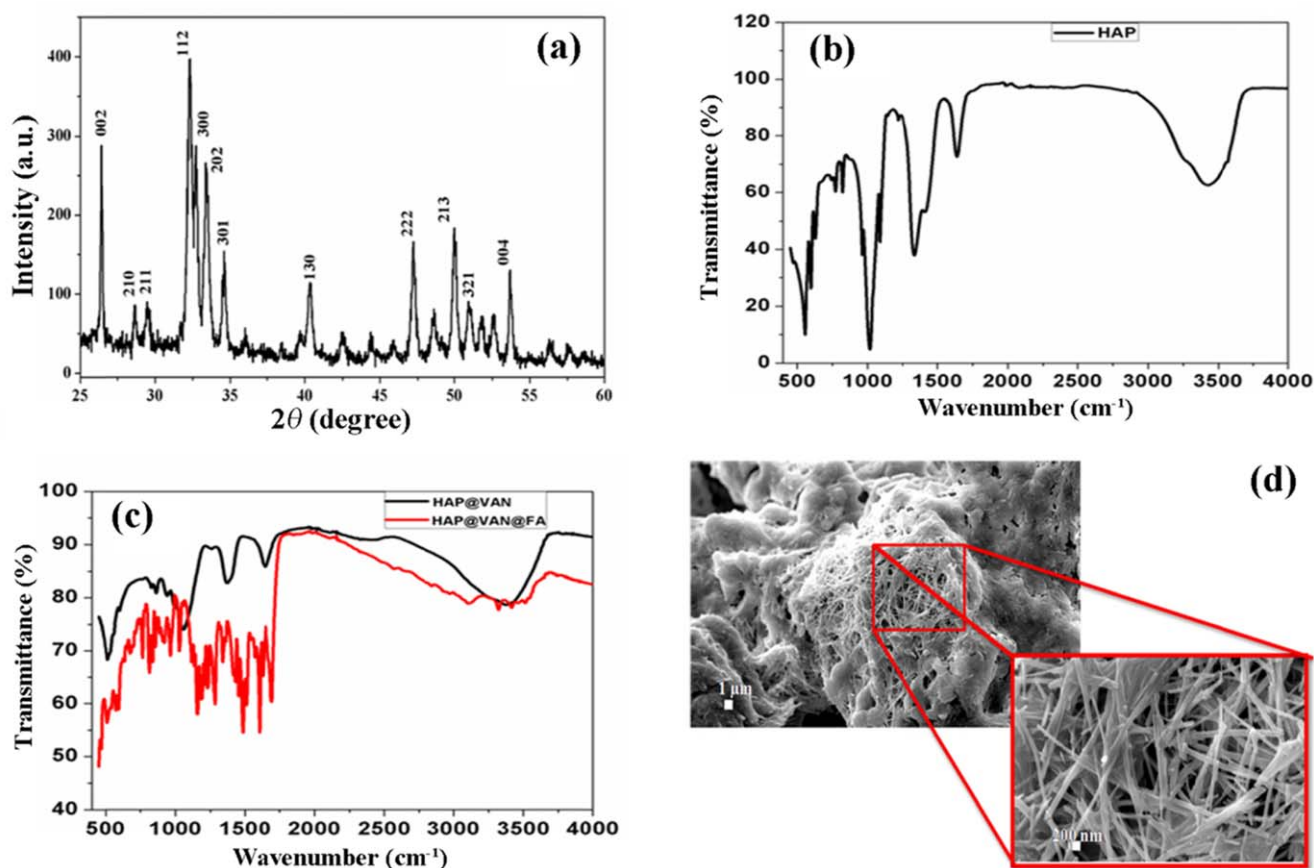
Figure 2. (a) XRD analysis of HAP nanoparticles, (b) FTIR spectra of HAP, (c) HAP@VAN and HAP@VAN@FA, and (d) FESEM analysis of HAP nanoneedles.

wavelength of 570 nm with the help of a spectrophotometer (Epoch microplate reader, BioTek, USA).

2.7. Statistical analysis

We repeated these experiments three times and the data were expressed by calculating the standard deviation of all the experiments. Comparisons of the mean of bacterial cells treated with HAP nanoparticles were made by a model I ANOVA test (using a statistical package, Origin Pro 8, Northamptom, MA 01060, USA) with multiple comparison *t*-tests, $p < 0.05$ as a limit of significance. The data is the average of three experiments $\pm$ SD. $*$ = represents p value < 0.05, $**$ = represents p value < 0.01, $***$ = represents p value < 0.001.

3. Results and discussions

3.1. Structural and morphological characterisations of the nano-HAP

Synthesised nano-HAP sample shows prominent diffraction maxima which corresponds to the fact that this ceramic nanomaterial is well crystalline (figure 2(a)) [31, 32]. The formation of hexagonal phase pure synthesised HAP nanoneedles has been confirmed by using the JCPDS card (No:

74–0566). Absence of any unwanted diffraction maxima confirms the purity of the sample.

In case of our synthesised HAP nanoneedles, absorption peaks at 1460, 882 and 670 cm^{-1} correspond to the presence of the carbonate ions [33, 34]. The carbonate ions may arise due to a reaction between atmospheric carbon dioxide and solution during the synthesis process (figure 2(b)). The characteristic bands for PO_4^{3-} are exhibited at 471.2 (v_2 PO_4^{3-}) [35], 565 and 602.7 (v_4 PO_4^{3-}) [36], 962 (v_1 PO_4^{3-}) [36], 1031 and 1095 (v_3 PO_4^{3-}) [37], and 1248 cm^{-1} (P–O stretching vibration of PO_4^{3-}) [38]. The band at 1382 cm^{-1} occurs due to the N-O stretching mode of NO_3^- [39]. A broad band at 1633 and 3197 cm^{-1} corresponds to the presence of adsorbed water [37, 38]. The medium band at 1355 is attributed due to the OH in-plane bend [40].

The presence of the characteristic peaks of the bare folic acid at 3549, 3115, 1679, 1600, 834 cm^{-1} establishes that folic acid is successfully attached on the surface of the HAP nanoparticles as shown in figure 2(c). The peak of vancomycin and folic acid in case of HAP@VAN@FA gets almost merged since they possess identical functional groups. The broadness of the region 2900–3300 cm^{-1} with prominent FA peaks confirms the presence of VAN within the matrix of HAP nanoparticles and the folic acid conjugation on the surface of HAP nanoparticles. Thus we can conclude that the FTIR spectra confirm the successful conjugation of the drug

Adv. Nat. Sci.: Nanosci. Nanotechnol. **10** (2019) 045017

D Bera *et al*
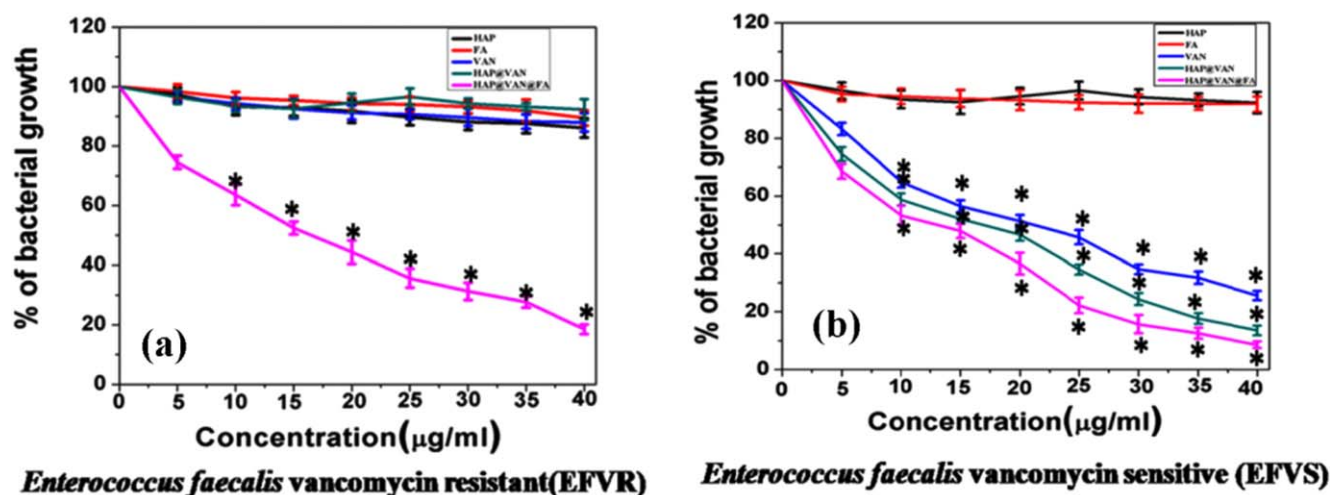
Figure 3. Analysis of activity of HAP, HAP@VAN, HAP@VAN@FA by MIC method in (a) MDR *E. faecalis* strain and (b) vancomycin sensitive *E. faecalis* strain.

Table 1. The hydrodynamic size and zeta potential of the synthesised nanoparticles.

Samples	DLS size (d.nm)	PDI	Zeta potential (mV)
HAP	83.8 ± 2.43	0.225 ± 0.08	11.23 ± 1.82
HAP@VAN	181.4 ± 3.47	0.261 ± 0.07	4.84 ± 1.97
HAP @VAN@FA	343.9 ± 4.86	0.295 ± 0.0	-9.87 ± 2.35

molecule (VAN) and targeting ligand (FA) with the HAPs (HAP@VAN@FA).

The surface morphology and size of biomimetic HAP nano-carrier were investigated by FESEM analysis, as shown in figure 2(d). The synthesised HAP NPs represents very well dispersed and nearly needle-like uniform nanostructures having a thickness of 70–80 nm and length of these needles are in the range of 1 μm. The small size of these HAP nanoneedles leads to the highest amount of cohesive force between the grains of this sample, which may be the reason for high agglomeration rate in HAP.

3.2. Determination of hydrodynamic size and surface charge of synthesised HAP nanoparticles

Vancomycin encapsulated HAP NPs show a hydrodynamic diameter of 181.4 ± 3.47 d.nm and a zeta potential of 4.84 ± 1.97 mV (table 1). The encapsulation of vancomycin does not reverse the zeta potential, but leads to the enhancement of its hydrodynamic diameter. The bare HAP nanoparticles possess hydrodynamic size of 83.8 ± 2.43 d.nm. The conjugation of folic acid to the HAP nanoparticle increases the hydrodynamic diameter of the nanoparticles to 343.9 ± 4.86 d. nm and the zeta potential of the nanoparticles reduces to -9.87 ± 2.35 mV [31]. This moderate negative zeta potential of the nanoparticle increases their stability. The polydispersity index (PDI) values of the samples are quite low, which is an indication that they form a homogenous solution [30]. This homogenous solution is quite conducive for biological applications.

3.3. Functionalised HAP nanoparticles successfully overcomes bacterial resistance in E. faecalis

Bare vancomycin does not exhibit any antibacterial activity against the MDR *E. faecalis* [41]. HAP nanoparticle and the targeting ligand folic acid also do not show any antibacterial activity (figure 3) but VAN encapsulated HAP (HAP@VAN) and folic acid conjugated HAP@VAN(HAP@VAN@FA) show antibacterial activity to combat bacterial resistance in the case of *E. faecalis*. The bactericidal activity of our synthesised HAPs, HAP@VAN and HAP@VAN@FA was envisaged separately against vancomycin sensitive *E. faecalis* and vancomycin resistant *E. faecalis* strains. In the case of vancomycin sensitive *E. faecalis* strain the MIC values of HAP@VAN and HAP@VAN@FA were 18.46 ± 1.2 μg ml^{-1} and 15.54 ± 1.43 μg ml^{-1} respectively, while that of bare vancomycin was 22.77 ± 1.03 μg ml^{-1}. Again in the case of resistant *E. faecalis* strain vancomycin and HAP@VAN nanoparticles failed to show any effect while HAP@VAN@FA showed considerable antibacterial effect with a MIC value of 19.88 ± 2.04 μg ml^{-1}.

The misinterpretation due to the turbidity of insoluble HAPs in the broth tube was avoided by performing the MBC assay. Briefly, both the bacterial strains were cultured with the MIC dilutions on the sterile agar plates and the MBC was examined [26].

The MBC concentrations are noted in cases where no visible bacteria growth was observed on the agar plates. The MBC values of HAP@VAN@FA were observed to be 70 μg ml^{-1} in case of the resistant *E. faecalis* strains as shown in figure 4(a). The decrease in bacterial growth is contingent

Figure 4. (a) Determination of MBC value of HAP@FA against MDR *E. faecalis* and vancomycin sensitive *E. faecalis* strain, (b) Antibacterial activity of HAP, VAN, HAP@VAN, HAP@VAN@FA by disc agar diffusion method. The data is the average of three experiments $\pm$ SD. $*$ = represents p value < 0.05, $**$ = represents p value < 0.01, $***$ = represents p value < 0.001.

upon the increase in the concentration of HAP@VAN@FA. In this method, the bacterial growths were effectively inhibited by the internalisation of HAP@VAN@FA into the resistant *E. faecalis* cells. Chakroborty *et al* reported that the MIC value of folic acid conjugated vancomycin encapsulated chitosan nanoparticles against vancomycin resistant *S. aureus* strain was $2 \, \mu g/ml$ [15]. Qi *et al* found that in case of mesoporous silica encapsulated vancomycin nanoparticles the MIC value against *S. aureus* was $200 \, \mu g \, ml^{-1}$ [17]. Chowdhuri *et al* have developed folic acid conjugated mesopporous ZIF nanoparticles for the delivery of vancomycin to multi-drug-resistant *Staphylococcus aureus* strains (MRSA). Their MIC and MBC values were $8 \, \mu g \, ml^{-1}$ and $16 \, \mu g \, ml^{-1}$ respectively [19]. Previous findings have depicted that hydroxyapatite nanoparticles have augmented the activity of vancomycin [24, 25]. Wu *et al* reported that the vancomycin loaded hydroxyapatites showed antibacterial activity at 0.5–$10 \, \mu g \, ml^{-1}$ against common non-resistant pathogenic bacterial strains [24]. Ghosh *et al* observed that a composite containing $0.02 \, g$ of vancomycin and hydroxyapatite is required for antibacterial activity against the pathogenic bacterial strains [25]. Therefore, we can conclude from this study that significant bactericidal activity is exhibited by the HAP@VAN@FA nanoparticles against resistant *E. faecalis* strains.

3.4. Selective bactericidal activity of HAP@VAN@FA confirmed by disc diffusion method

This study was performed to visualise the comparison of antibacterial activity of different HAP samples. The zone of inhibition of Gram-positive vancomycin resistant *E. faecalis* against HAP@VAN@FA, HAP@VAN, VAN, distilled water (as a negative control), standard antibiotic, methicillin (as a positive control) is shown in figure 4(b). In case of the HAP@VAN, VAN and distilled water no zone of inhibition was observed. But a clear zone of inhibition is observed around the disc in case of HAP@VAN@FA. Zone of inhibition having a diameter of around $18 \pm 0.5 \, mm$ is observed when MDR *E. faecalis* strain is treated with HAP@-VAN@FA at a concentration of $70 \, \mu g \, ml^{-1}$ (MBC conc.).

Chowdhuri *et al* have found that the zone of inhibition in case of disc agar diffusion study of ZIF@VAN@FA in case of MRSA is $14 \pm 0.5 \, mm$ [19]. This study vividly elucidates the efficacy of HAP@VAN@FA against the resistant *E. faecalis*.

3.5. Functionalised HAPs show excellent bactericidal activity

The tolerance level of *E. faecalis* strains against HAP@-VAN@FA was estimated from the respective MIC and MBC values. Our results suggest that the tolerance level of Gram-positive vancomycin resistant *E. faecalis* to HAP@-VAN@FA was 4.02. The values of the tolerance level help in the differentiation between the bactericidal agents and bacteriostatic agents. Previous studies [15] showed that the folic acid conjugated vancomycin loaded chitosan nanoparticles exhibited a tolerance level of 5 towards vancomycin resistant *S. aureus* strains. Chowdhuri *et al* observed that the value of tolerance level in case of the ZIF@VAN@FA against resistant *S. aureus* strain was 2.0 [19]. The bactericidal agents are known to be responsible for the killing of the bacteria while the bacteriostatic agents lead to the inhibition of bacterial growth. When the ratio of MBC/MIC is more than or equivalent to 16 for a specific bacterium, antibacterial agents are noted as bacteriostatic and when this ratio is equal to or less than 4, the nanoparticles are regarded as bactericidal agents [27]. Here, the MBC/MIC ratio is considered important paradigm in examining the antibacterial capability of our synthesised nanoparticles, HAP@VAN@FA. Our results reflect that HAP@VAN@FA has the potential to be considered as an effective bactericidal agent against the MDR *E. faecalis*.

3.6. HAP nanoparticles exhibit excellent biocompatibility

The *in vitro* cytotoxicity of the HAP nanoparticles is estimated for checking the biocompatibility on WI-38 cell line (figure 5). The HAP nanoparticles exhibit toxicity at a very high concentration of $0.1 \, g \, ml^{-1}$. No such toxicities were observed when the cells were treated with HAP nanoparticles at lower concentrations. Therefore we can conclude that the HAP NP has commendable biocompatibility and is ideal for biological application. According to previous report the IC_{50}
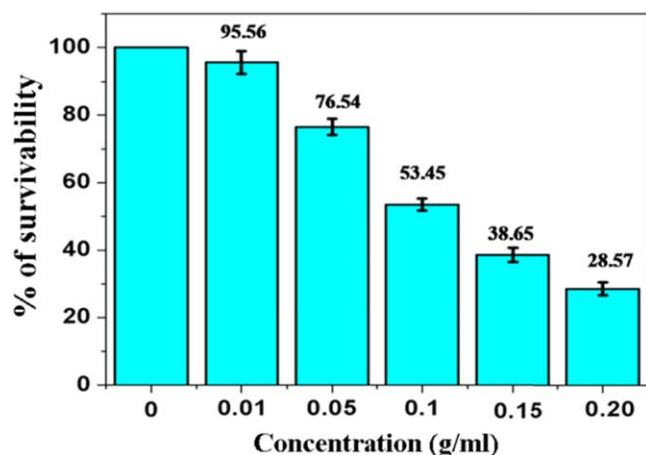
Adv. Nat. Sci.: Nanosci. Nanotechnol. **10** (2019) 045017

D Bera *et al*

Figure 5. Cell viability assay of HAP nanoparticles on human lung fibroblast cells, WI-38.

value of hydroxyapatite-silica nanocomposite was 0.1 g ml^{-1} [42]. In this case the IC$_{50}$ value of our synthesised hydroxyapite nanoparticles was 0.127 g ml^{-1}.

3.7. Treatment of MDR E. faecalis with HAP@VAN@FA significantly diminishes the bacterial cell viability

HAP@VAN@FA significantly decreased the viability of the MDR *E. faecalis* to 37.57% in comparison to the control group at 70 μg ml^{-1} (MBC conc.) as displayed in figure 6(a). This may take place due to the successful internalization of HAP@VAN@FA within the *E. faecalis* cells which in turn inhibits the bacterial growth and causes bacterial cell death. According to the previous report of Chowdhuri *et al*, the treatment with ZIF-8@FA@VAN diminished the cell viability of multidrug-resistant *S. aureus* at 8 μg ml^{-1} (MIC conc.) and 16 μg ml^{-1} (MBC conc.) by 38.57% and 84.03%, respectively [19]. The results suggest that the folic acid conjugated vancomycin encapsulated HAP nanoparticles show bacteriostatic as well as bactericidal activities.

3.8. Mechanisms behind bactericidal activity of functionalised HAP

3.8.1. Functionalised HAP exhibits promising intracellular internalisation. The primary requisite for the action of an antibiotic is binding with the cell wall and its subsequent cellular internalisation. To prove the HAPs uptake by MDR *E. faecalis*, QS-labelled HAPs were treated with bacterial strains and fluorescence images were taken (figure 7(a)). The results show that the QS-labelled HAP@FA is successfully internalised into the resistant *E. faecalis* cells, whereas the QS labelled HAP failed to do so. The QS labelled HAP@FA were found to be uniformly dispersed within the cytoplasm, which proves its successful internalisation within the *E. faecalis* cells. The internalisation of nanoparticles is generally contingent upon various physical characteristics like size, shape as well as surface charge. In general, this internalisation

takes place in two steps. At first the binding of the nanoparticles to the cell membrane occurs followed by their subsequent internalisation into the cells. In this scenario, the internalisation of QS labelled HAP@FA is mediated by endocytosis that occurs through the folate receptors that are present on the membrane of *E. faecalis*. The endocytosis process involves the uptake of HAPs by membrane invagination that leads to the formation of intracellular vesicles that encapsulate the nanoparticles and facilitate its transportation within the cells [19]. Similar internalisation mechanism was studied with FITC tagged vancomycin encapsulated mesoporous silica nanoparticles in *E. coli* and *S. aureus* bacterial strains by Qi *et al* [17]. Chowdhuri et al also delineated similar mechanism of internalisation of their synthesised functionalised nanoparticles, ZIF@VAN@FA [19]. From this observation we can conclude that following similar endocytotic pathway HAP@VAN@FA nanoparticles can successfully deliver vancomycin inside the MDR *E. faecalis*.

The photoluminescence studies confirm the distinct peak at 429 nm in case of the sample HAP@QS (figure 7(b)). This peak is congruent with that of the emission spectra of quinine sulphate [43, 44]. This indicates the successful encapsulation of quinine sulphate within the HAP nanoparticles. The bare HAP nanoparticles are optically inactive. However a prominent bend is observed at 468 nm in case of HAP@QS@FA which is possibly due to the conjugation of folic acid which has emission spectra at 490 nm [45].

3.8.2. HAP@VAN@FA enhances intracellular ROS generation which culminates in the bacterial cell death. The production of intracellular ROS was thoroughly envisaged in order to delve into the mechanisms behind the bactericidal activities of HAP@VAN@FA, as elucidated in figure 6(b and c). The DCFH-DA was used as intracellular ROS indicator for the estimation of ROS inside the HAP@VAN@FA-treated bacterial cells. The results clearly depicts the enhanced generation of ROS which is indicated by the augmented fluorescence intensity in case of the bacterial cells treated with HAP@VAN@FA while the untreated cells exhibits negligible fluorescence intensity. The enhancement of ROS also occurred in the case of delivery of vancomycin via ZIF@FA as observed by Chowdhuri *et al* [19]. Thus we can conclude enhancement of intracellular ROS generation is responsible for the antibacterial activity of the HAP@VAN@FA. The increased production of intracellular ROS is responsible for the disruption in the electronic transport chain, degradation of the genetic materials and also causes damage to the bacterial cell membrane [26].

3.8.3. Physical interactions of HAP@VAN@FA nanoparticles with the bacterial cells. The images obtained from SEM of vancomycin resistant *E. faecalis* cells treated with HAP@VAN@FA and untreated cells are displayed in figure 8. The SEM images reveal that the untreated cells are smooth, unaltered and possess features that are similar to the

Adv. Nat. Sci.: Nanosci. Nanotechnol. **10** (2019) 045017

D Bera *et al*
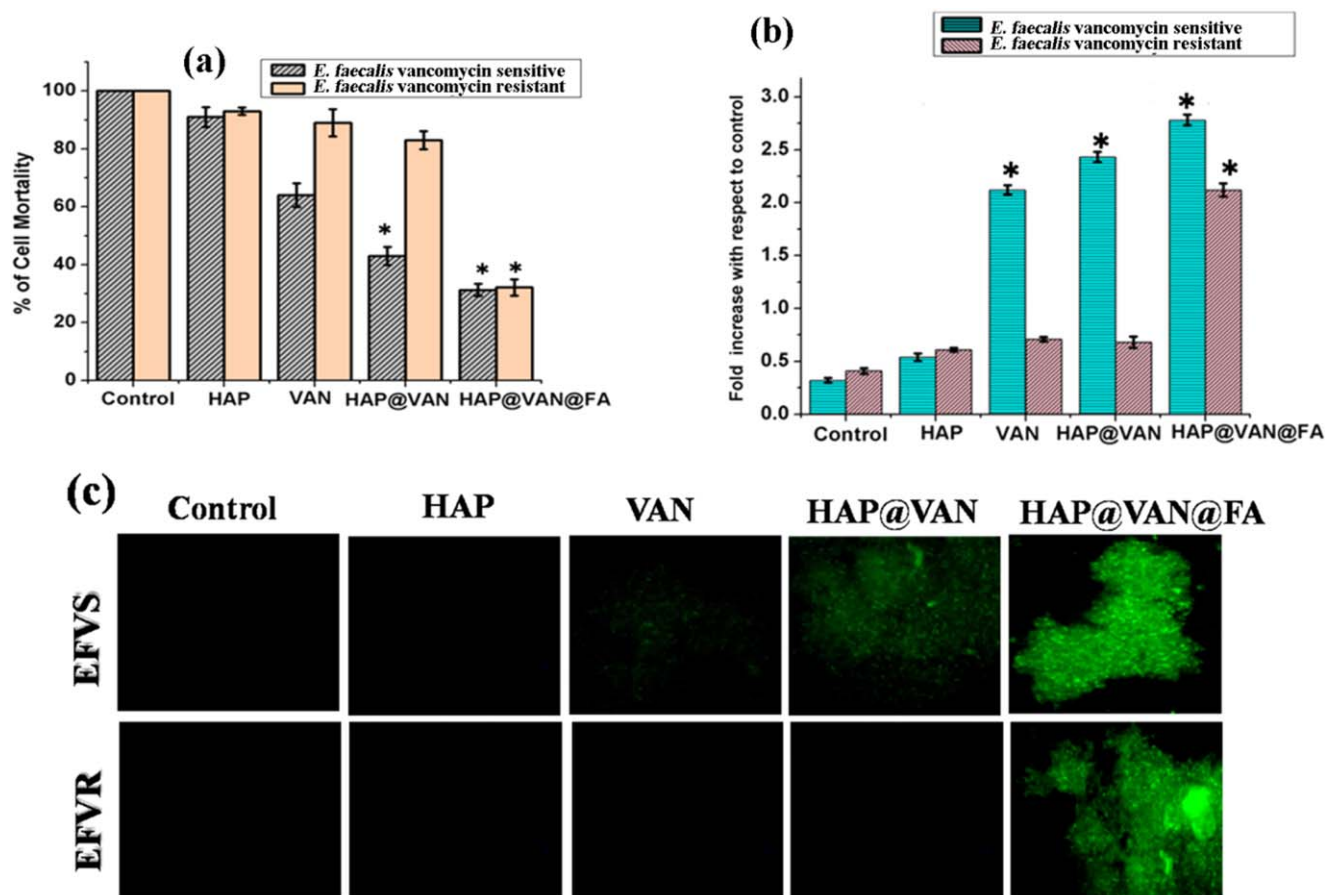
Figure 6. (a) Bacterial viability study upon treatment of HAP, HAP@VAN and HAP@VAN@FA nanoparticles by MTT assay.
(b) Intracellular ROS generation of control, VAN, HAP@VAN and HAP@VAN@FA in MDR *E. faecalis* strains by spectrophotometry.
(c) Intracellular ROS generation of control, VAN, HAP@VAN, HAP@VAN@FA in MDR *E. faecalis* strains by fluorescence microscopy.
The data is the average of three experiments ± SD. * = represents *p* value < 0.05, ** = represents *p* value < 0.01, *** = represents
p value < 0.001.
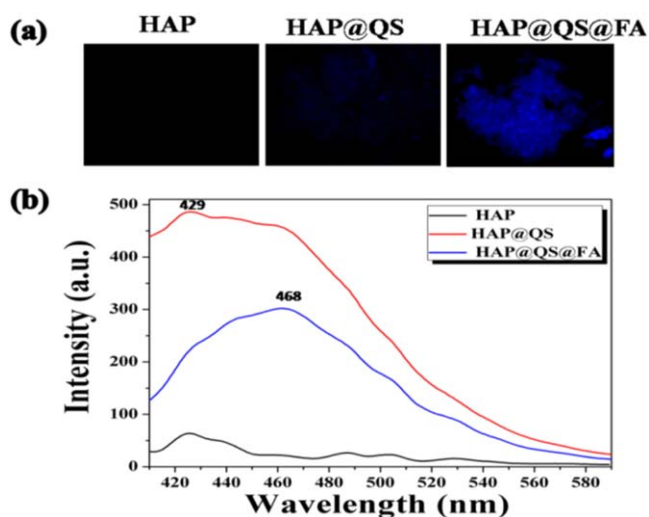
Figure 7. (a) Intracellular uptake of HAP@QS@FA, HAP @QS and HAP in MDR *E. faecalis* strains. (b) Photoluminescence spectra of HAP@QS@FA, HAP @QS and HAP nanoparticles at different excitations.

native cells. On the other hand, the treated resistant *E. faecalis* cells bear the signs of maximum membrane damage. A substantial number of treated *E. faecalis* cells exhibit signs of fragmentation, leakage, perforation and innumerable gaps in the cell membrane. Our study clearly depicts that the treatment with HAP@VAN@FA is the reason behind the aberration in the bacterial membrane morphology. This in turn leads to the enhanced permeability that crucially favors the cell membrane mediated transport of the nanoparticles. The damage in the DNA and the perturbance of cellular response are due to the penetration of the HAP@VAN@FA into the bacterial cells and its subsequent interaction with the DNA. According to the previous report by Qi *et al* vancomycin encapsulated mesoporous silica was able to cause intense membrane damage in *E. coli* and *S. aureus* bacterial strains [17]. Chowdhuri *et al* also reported that ZIF@VAN@FA caused cell membrane damage towards the multidrug-resistant *S. aureus* [19]. The most probable mechanism behind antibacterial activity of HAP@VAN@FA is that it can easily penetrate into the cell by means of endocytosis via the folate receptors and effectively

Adv. Nat. Sci.: Nanosci. Nanotechnol. **10** (2019) 045017

D Bera *et al*
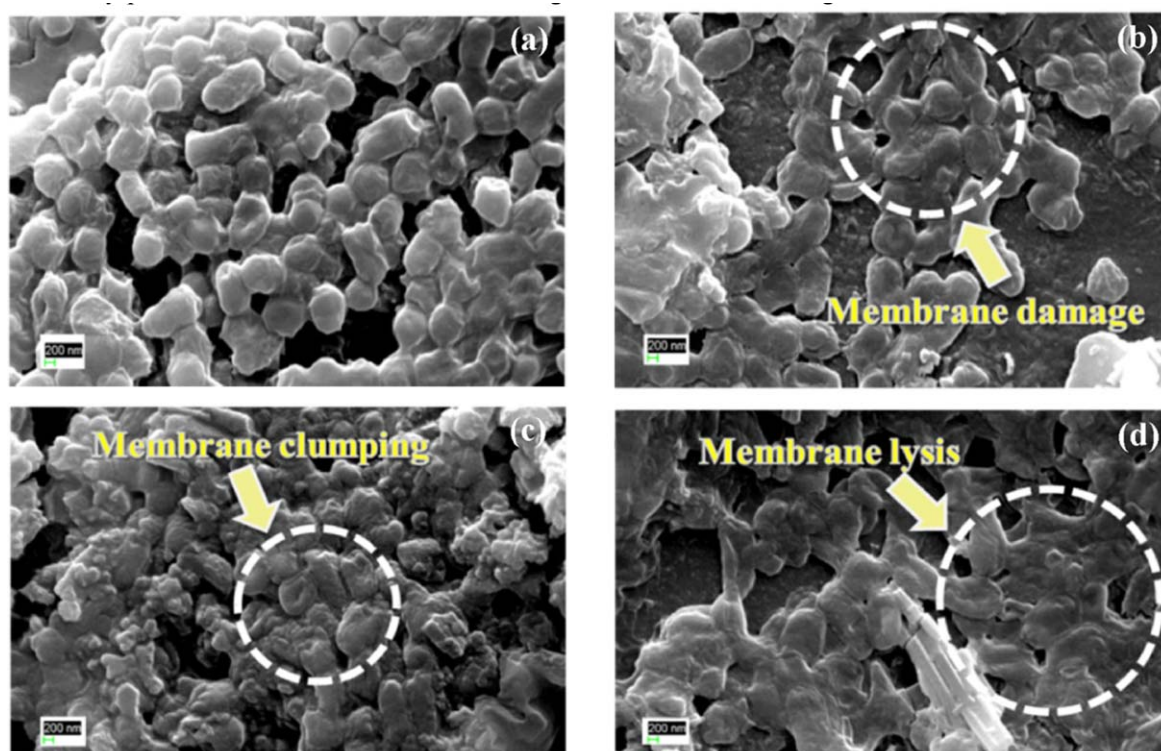
Figure 8. (a) FESEM images showing the morphology of untreated MDR *E. faecalis* cells, (b) FESEM images of MDR *E. faecalis* cells treated with HAP@VAN@FA at a concentration of 20 μg ml^{-1}, (c) FESEM images of MDR *E. faecalis* cells treated with HAP@VAN@FA at a concentration of 40 μg ml^{-1} and (d) FESEM images of MDR *E. faecalis* cells treated with HAP@VAN@FA at a concentration of 70 μg ml^{-1}.

produce ROS which in turn is leading into the bacterial cell growth inhibition.

4. Conclusion

Here we have successfully encapsulated vancomycin within the HAP nanoparticles and modified their surface through folic acid conjugation by a facile synthesis process. We have laid emphasis on the functionalisation of biocompatible hydroxyapatite nanoparticles by folic acid conjugation in order to deliver vancomycin to the resistant pathogenic MDR *E. faecalis*. Our results clearly depict that the functionalised HAPs exhibited good biocompatibility and excellent selective antibacterial activity towards the MDR *E. faecalis*. Our strategy could thus be instrumental in the delivery of several other conventional antibiotics such as penicillin, methicillin, erythromycin, amikacin, ciprofloxacin, tetracyclin, oxacillin, cefotaxime, etc. to the several multidrug-resistant strains similar to *E. faecalis*. Thus we can conclude that our synthesised biocompatible HAPs fulfill all the criteria to emerge as a promising ameliorative agent against a wide range of multidrug-resistant bacterial infections that are crippling the modern society.

References

[1] Li X, Robinson S M, Gupta A, Saha K, Jiang Z, Moyano D F, Sahar A, Riley M A and Rotello V M 2014 *ACS Nano* **8** 10682–6
[2] Neu H C 1992 *Science* **257** 1064–73
[3] Li Y J, Harroun S G, Su Y C, Huang C F, Unnikrishnan B, Lin H J, Lin C H and Huang C C 2016 *Adv. Healthc. Mater.* **5** 2545–54
[4] Chen C W, Hsu C Y, Lai S M, Syu W J, Wang T Y and Lai P S 2014 *Adv. Drug. Deliv. Rev.* **78** 88–104
[5] Chambers H F 2001 *Emerg. Infect. Dis.* **7** 178–82
[6] Dickgiesser N and Kreiswirth B N 1986 *Antimicrob. Agents Chemother.* **29** 930–2
[7] Levin T P, Suh B, Axelrod P, Truant A L and Fekete T 2005 *Agents Chemother.* **49** 1222–4
[8] Schmitz F J, Sadurski R, Kray A, Boos M, Geisel R, Kohrer K, Verhoef J and Fluit A C 2000 *J. Antimicrob. Chemother.* **45** 891–4
[9] Hiramatsu K, Hanaki H, Ino T and Tenover F C 1997 *J. Antimicrob. Chemother.* **40** 135–46

Adv. Nat. Sci.: Nanosci. Nanotechnol. **10** (2019) 045017

D Bera *et al*

[10] Chang S *et al* 2003 *New Engl. J. Med.* **348** 1342–7

[11] Singh R, Smitha M S and Singh S P 2014 *J. Nanosci. Nanotechnol.* **14** 4745–56

[12] Rai M K, Deshmukh S D, Ingle A P and Gade A K 2012 *J. Appl. Microbiol.* **112** 841–52

[13] Manikprabhu D, Cheng J, Chen W, Sunkara A K, Mane S B, Kumar R, Das M, Hozzein W, Duan N Y Q and Li W J 2016 *J. Photochem. Photobiol. B* **158** 202–5

[14] Eirich J, Orth R and Sieber S A 2011 *J. Am. Chem. Soc.* **133** 12144–53

[15] Chakraborty S P, Sahu S K, Kar Mahapatra S, Santra S, Bal M, Roy S and Pramanik P 2010 *Nanotechnology* **21** 105103–11

[16] Chakraborty S P, Sahu S K, Pramanik P and Roy S 2012 *Int. J. Pharma.* **436** 659–76

[17] Qi G, Li L, Yu F and Wang H 2013 *ACS Appl. Mater. Interfaces* **5** 10874–81

[18] Kell A J, Stewart G, Ryan S, Peytavi R, Boissinot M, Huletsky A, Bergeron M G and Simard B 2008 *ACS Nano* **2** 1777–88

[19] Chowdhuri A R, Das B, Kumar A, Tripathy S, Roy S and Sahu S K 2017 *Nanotechnology* **28** 095102

[20] Ren H, Zhang L, An J, Wang T, Li L, Si X, He L, Wu X, Wang C and Su Z 2014 *Chem. Commun.* **50** 1000–2

[21] Horcajada P, Serre C, Maurin G, Ramsahye A N, Balas F, Vallet-Regí M, Sebban M, Taulelle F and Férey G 2008 *J. Am. Chem. Soc.* **130** 6774–80

[22] Taylor-Pashow K M L, Rocca J D, Xie Z, Tran S and Lin W 2009 *J. Am. Chem. Soc.* **131** 14261–3

[23] Tamames-Tabar C E, Guillou I N, Serre C, Miller S R, Elkaïm E, Horcajada P and Blanco-Prieto M J 2015 *Cryst. Eng. Comm.* **17** 456–62

[24] Wu V M, Tang S and Uskoković V 2018 *ACS Appl. Mater. Interfaces* **10** 34013–28

[25] Ghosh S, Wu V, Pernal S and Uskoković V 2016 *ACS Appl. Mater. Interfaces* **8** 7691

[26] Bardhan S, Pal K, Roy S, Das S, Chakraborty A, Karmakar P, Basu R and Das S 2019 *J. Nanosci. Nanotechnol.* **19** 1–11

[27] May J, Shannon K and King A 1998 *J. Antimicrob. Chemother.* **42** 189–97

[28] Bhattacharya D, Saha B, Mukherjee A, Santra C R and Karmakar P 2012 *Nanoscience and Nanotechnology* **2** 14–21

[29] Pal K, Laha D, Parida P K, Roy S, Bardhan S, Dutta A, Jana K and Karmakar P 2018 *J. Nanosci. Nanotechnol.* **19** 3720–33

[30] Pal K, Roy S, Parida P K, Dutta A, Bardhan S, Das S, Jana K and Karmakar P 2019 *Materials Science & Engineering C* **95** 204–16

[31] Roy S, Maity A, Mandal P, Chanda D K, Pal K, Bardhan S and Das S 2018 *Cryst. Eng. Comm.* **20** 6338–50

[32] Roy S, Bardhan S, Pal K, Ghosh S, Mandal P and Das S 2018 *Journal of Alloys and Compounds* **763** 749–58

[33] Liu J B, Ye X Y, Wang H, Zhu M K, Wang B and Yan H 2003 *Ceram. Int.* **29** 629

[34] Zapanta L R 1965 *Nature* **206** 403–4

[35] Banerjee S *et al* 2018 *Colloids and Surfaces B: Biointerfaces* **171** 300–7

[36] He Q J and Huang Z L 2007 *Cryst. Res. Technol.* **42** 460

[37] Panda R N, Hsieh M F, Chung R J and Chin T S 2003 *J. Phys. Chem. Solids* **64** 193

[38] Blakeslee K C and Condrate R A 1971 *J. Am. Ceram. Soc.* **54** 559

[39] Anee T K, Ashok M, Palanichamy M and Narayana K 2003 *Mater. Chem. Phys.* **80** 725–30

[40] Liu Y, Hou D and Wang G 2004 *Mater. Chem. Phys.* **86** 69–73

[41] Esmaeilia A and Ghobadianpour S 2016 *Int. J. Pharm.* **501** 326–30

[42] Musa M, Kannan T P, Masudi S M and Rahman I A 2012 *Mol. Cell. Toxicol.* **8** 53–60

[43] Dixon J M, Taniguchi M and Lindsey J S 2005 *Photochem. Photobiol.* **81** 212–3

[44] Eaton D F 1988 *Pure Appl. Chem.* **60** 1107–14

[45] Tyagi A and Penzkofer A 2010 *Chem. Phys.* **367** 83–92

Gum acacia capped ZnO nanoparticles, a smart biomaterial for cell imaging and therapeutic applications

Debbethi Bera[1,2]**, Kunal Pal**[3,4]**, Dheeraj Mondal**[2]**, Parimal Karmakar**[3]**, Sukhen Das**[1,2] **and Papiya Nandy**[1]

[1] Centre for Interdisciplinary Research and Education, 404B, Jodhpur Park, Kolkata-700068, India
[2] Department of Physics, Jadavpur University, Kolkata-700032, India
[3] Department of Life Science and Biotechnology, Jadavpur University, Kolkata-700032, India
[4] Division of Molecular Medicine and Centre for Translational Research, Bose Institute, Kolkata-700056, India

E-mail: pnandy00@gmail.com

CrossMark

Abstract

The zinc oxide nanoparticles (ZnONPs) have gained prominence in different biomedical applications nowadays. The phytochemical mediated synthesis of ZnONPs (green synthesis) is cost-effective, facile and generates negligible hazardous impact. In the present study we have utilised the leaf extract of abundantly available well known medicinal plant, *Ocimum sanctum* (Tulsi) for the phytosynthesis of ZnONPs via a facile process. Gum acacia, a widely recognised natural polymer was used as a capping agent of the biogenic ZnONPs in order to enhance its bioavailability and its therapeutic efficacy. These nanoparticles were tagged with a fluorescent dye, rhodamine-B to observe the cellular imaging applications. The nanoparticles were characterised by different biophysical methods like UV–vis spectroscopy, XRD, FTIR and FESEM for confirmation of their successful synthesis and their antibacterial and anticancer efficacy was then validated. The result clearly suggests that these nanoparticles are able to induce the oxidative stress in both eukaryotic and prokaryotic cells which in turn is responsible for their efficacy against both the pathogenic bacterial strains and hepatocellular cancerous cells. Moreover, these nanoparticles possess pH responsive behaviour and hence it fulfils the essential criteria of cancer therapeutic delivery system. Furthermore, these rhodamine-B tagged nanoparticles are endowed with fluorescence property which can be utilised for bioimaging applications. These nanoparticles could be conjugated with cancer specific targeting ligands in the future that could further augment their therapeutic and diagnostic credentials. Therefore, these nanoparticles could truly emerge as unique promising multifunctional therapeutic intervention in the near future.

Keywords: phytochemical synthesis, zinc oxide nanoparticles, gum acacia, rhodamine-B, antibacterial activity, anticancer property

Classification numbers: 2.04, 2.05, 5.00, 5.08, 5.09

1. Introduction

ZnONP has a great reputation in biomedical field. In recent times research interest are increasing to modify ZnO for enhancing its property and making it more biocompatible. In recent past, ZnONPs have also gained fair reputation as an effective antimicrobial agent [1, 2]. Several natural polymers and green synthesised metals were used in biological field [3–12]. Many endeavours have been made to enhance the bioavailability of zinc by encapsulating within a natural or synthetic polymer matrix. [13–40]. For example, ZnONPs in combination with several natural polymers and synthetic

polymers like collagen, dextran, gelatine, polyvinyl alcohol have been widely reported as a wound dressing material by several researchers [41–51]. The natural polymers like gum acacia (GA) extracted from acacia tree have been recently used in extensive biomedical applications since it is highly biocompatible and biodegradable. [52–60]. Chopra *et al* [61] have designed alginate/gum acacia encapsulated GA@ZnONPs and have envisaged their antibacterial efficacy against pathogenic *Pseudomonas aeruginosa*. Bajpai *et al* [62] have also fabricated ZnONPs loaded gum acacia/poly sodium-acrylate hydrogels and have validated their antibacterial efficacy against *E. coli* (details in the supplementary table S). But no efforts had been previously made to augment the functionalities of these polymer encapsulated ZnONPs.

There are several studies of producing zinc from different plants [63–66]. In the present study, we have synthesised ZnONPs via an ecofriendly and cost-effective route by using well known medicinal plant, *Ocimum sanctum* (Tulsi). Aromatic and cooling leaves of this plant have anticancer, anti-inflammatory, diuretic and various other properties [67–71]. The Tulsi leaves contain several phenolic phytochemicals like quercetin, luteolin, cyclopropylidene, eugenol, germacrene, β-caryophyllene, β-elemene, carvacrol, etc [72]. The predominance of flavonoids like quercetin in the *Ocimum sanctum* helps in the formation of chelating complexes with the zinc ions that help in stabilisation of these metallic ions [73]. Moreover, these phenolic compounds are also capable of reducing the metallic salts into metal oxides with the transfer of electrons and functionalising the surface of the particles. Therefore, the aqueous extract of *O. sanctum* plays a pivotal role in synthesising the ZnONPs by colloidal precipitation method [72].

We have successfully encapsulated these biogenic ZnONPs with the biopolymeric matrix of GA and have thoroughly characterised them with the help of UV–vis spectroscopy, XRD, FTIR and FESEM. We have used both bacterial strains and hepatocellular cancer cell line as our study models and have found that our green synthesised polymer capped ZnONPs have a significant dual therapeutic effect through the initiation of oxidative stress in both eukaryotic and prokaryotic cells [74–77]. Bioimaging applications were also studied by incorporating rhodamine-B into the matrix of the GA@ZnONPs, which showed its ability to penetrate eukaryotic cells. Our synthesised GA@ZnONPs also possess pH sensitive rhodamine-B release attribute which can be utilised for the delivery of cancer therapeutics without exerting hazardous effects on the normal cells. Some future endeavours could be made for conjugating these nanoparticles with cancer specific targeting ligands for specific labelling and transporting the therapeutics to the cancer cells. We can conclude from our present study that biocompatible polymer GA@ZnONPs can emerge as a promising therapeutic intervention and bioimaging tool.

2. Experimental details

2.1. Materials

All the reagents and chemicals used for this study including bacterial culture media, fluorescence stains, MTT reagent, glutaraldehyde, rhodamine-B were purchased from Merck Ltd, and SRL Pvt. Ltd, Mumbai, India. AR-grade zinc nitrate ($ZnNO_3$) was purchased from Sigma-Aldrich Chemicals. Fresh *Ocimum sanctum* (Tulsi) leaves were purchased from the nearby market. Throughout the study deionised (Millipore) water of resistivity at least 18 MΩ-cm has been used.

2.1.1. Bacterial strains.
The Gram-positive strains used in microbiological experiments were *Staphylococcus aureus* 740 and *Enterococcus faecalis* 441. *Escherichia coli* 443 and *Pseudomonas aeruginosa* 1688 were the Gram-negative strains used in this study. These bacterial strains were procured from the Microbial Type Culture Collection (MTCC), IMTECH, Chandigarh, India.

2.2. Experimental methods

2.2.1. Preparations.
Preparation of Tulsi leaf extract: The leaves of Tulsi were washed thoroughly with deionised water and kept at room temperature for drying. Powder of dry leaves was prepared by mortar and pestle and about 2 g of the dried powder was taken into 100 ml distilled water for boiling for 2–3 min. Solution was then cooled at room temperature and filtered using Whatman filter paper.

Preparation of zinc nitrate solution: 1.0 mM $ZnNO_3$ was added into distilled water (20 ml) and stirred continuously for 2 to 4 h.

Synthesis of zinc xide nanoparticles: 10 ml of filtered leaf extract was added dropwise into 200 ml of prepared zinc nitrate stock solution. Then it was heated in a water bath at 90 °C for 1 h.

Purification of synthesised ZnO: The obtained ZnONPs were purified by centrifugation at 9000 rpm for 25 min in room temperature. The precipitate was re-dispersed in distilled water after removing the supernatant. The whole purification procedure was performed thrice.

Capping of ZnONP with gum acacia and tagging with rhodamine-B: GA was dissolved in lukewarm distilled water (kept at 45 °C) and continuously stirred for 24 h. Then the solution of ZnONPs was added to the GA solution in 2:1 *w*/*v* ratio. The rhodamine-B was solubilised in water and was mixed thoroughly by constant stirring for 12 h in a separate test tube. This rhodamine-B solution was then added slowly within the GA@ZnONPs solution in 1:4 *w*/*v* ratio and was continuously stirred for another 24 h. Ultimately, the final solution was centrifuged at 10 000 rpm for 10 min in room temperature to obtain the rhodamine-B labelled GA@ZnONP (GA@ZnONP@RB). After discarding the supernatant, precipitate was kept in vacuum desiccators at room temperature for drying. Ultimately, the dried powder was mortared to achieve fine grains for further characterisations.

2

Adv. Nat. Sci.: Nanosci. Nanotechnol. **11** (2020) 035015

D Bera *et al*

2.2.2. Physical characterisation of GA@ZnONPs. The GA@ZnONPs were characterised with the help of ultraviolet-visible spectrophotometer (BioTek); x-ray powder diffractometer model D8, Bruker AXS, Winconsin, USA, using Cu-K_α target operating at 35 kV ($\lambda = 1.5418$ Å and scan speed 1 s/step); field emission scanning electron microscope (FESEM) using INSPECTF50 (FEI, the Netherlands) and EVO 18 Special Edition, Carl Zeiss, Germany for bacterial image; ImageJ software for size distribution analysis; Fourier transform infrared spectroscope (FTIR)-8400S, Shimadzu, DLS (dynamic light scattering) (NANO ZS90, Malvern Instruments Ltd, UK), fluorescence microscope (DM 2500 Leica, Japan).

2.2.3. Antibacterial activity determination. Determination of minimum inhibitory concentration (MIC) and minimum bactericidal concentration (MBC): The microdilution method was applied to determine the MIC and MBC values [78]. Total assays were performed in a biosafety cabinet to prevent any undesirable contamination.

Tolerance level: Tolerance level of each bacterial strain towards GA@ZnONPs can be predicted by the values of MIC and MBC. Tolerance level was determined by using following formula [78].

$$\text{Tolerance level} = (\text{MBC})/(\text{MIC}). \qquad (1)$$

Agar well diffusion method: The susceptibility of pathogenic bacteria to GA@ZnONPs was examined by Mueller-Hinton agar well diffusion method according to a previously reported protocol [78].

Bacterial cell viability assay: The bacterial cell survivability was evaluated with the aid of 3-(4, 5-dimethylthiazol-2-yl) -2, 5-diphenyltetrazolium bromide (MTT) assay by adhering a standard protocol [79, 80].

Intracellular ROS generation: 2, 7-dichlorofluorescein diacetate (DCFH$_2$-DA) assay was employed to determine the bacterial intracellular ROS generation [75, 80].

Morphological change of bacterial cell observed by FESEM: The treated (at their MBC value) and untreated (control) bacterial strains were incubated for 16 h at 37 °C. Next, the cells were prepared following a standard protocol [78].

2.2.3.1. Anticancer activity determination. Cytotoxicity assay: The viability of HepG2 cells after exposure to various concentrations of GA@ZnONPs was determined by 3-(4, 5-dimethylthiazol-2-yl)-2,5-diphenyltetrazolium bromide (MTT) assay [76, 78].

2.2.3.2. Intracellular ROS generations were checked by DCFDA method. 2, 7-dichlorofluorescein diacetate (DCFH$_2$-DA) assay was employed to determine the bacterial intracellular ROS generation [77, 78].

Study of intracellular uptake: Biogenic GA@ZnONPs is labelled with the fluorescent dye, rhodamine-B for confirming the internalisation of nanoparticles within the bacterial surface

[81–84]. The images were obtained under a fluorescence microscope at an excitation wavelength of 510–550 nm.

Apoptotic cell quantification by AnnexinV-FITC staining: The quantification of the apoptotic cells was conducted with the help of AnnexinV-FITC/PI double staining method by following a standard protocol [79].

2.2.3.3. Drug release study. *In vitro* rhodamine-B released from the core of GA@ZnONP@RB was examined to confirm the amount of impregnated rhodamine-B released in different intervals of time by following a standard protocol [76, 77] at 544 nm from a standard curve of rhodamine-B [81].

3. Results and discussion

3.1. Structural, morphological and spectroscopic analyses of the GA@ZnONPs

XRD pattern of the biosynthesised GA@ZnONPs clearly indicates their crystalline nature, figure 1(a). The prominent diffraction peaks (2θ) were found at 31.48, 34.32, 36.36, 47.53, 56.52, 62.88, 67.82 and 76.5 degrees. The highest intense peak was considered for determining the average size of ZnONPs by employing the Debye–Scherrer equation.

$$D = 0.9\lambda/\beta \cos \theta. \qquad (2)$$

where β represents the full width at half maxima of the diffraction peak (radian), Bragg's angle is denoted by θ in degree. The particle size of these GA@ZnONPs was in accordance with the relevant literature [2, 41]. FWHM (β) = 0.011 17. Average diameter $\langle D_{101} \rangle$ of ZnO = 13.04 nm. These peaks are for crystallisation of GA@ZnONPs. All the peaks can be assigned with the PDF code No. #00-036-1451. The amorphous nature in the diffraction pattern for the 2θ value ranges from 10 to 20° and is also more scattering throughout the XRD pattern due to very low crystallisation of gum acacia extract.

The FTIR spectra of the biosynthesised GA@ZnONPs are displayed in figure 1(b). The FTIR was performed to determine the purity of the nanoparticles and confirmed the prevalence of different phytochemicals in the *O. sanctum* leaf extract. The characteristic peaks at 1634 and (600, 450) cm^{-1} for the synthesised ZnONPs are congruent with that of the Zn–O vibration arising due to stretching and deformation [69, 70]. The prominent bands are at 3408 cm^{-1} (–OH stretching), 2936 cm^{-1} (stretching of –CH) and characteristic peaks of vibration at 1624 cm^{-1} and 1427 cm^{-1} (asymmetric as well as symmetric stretching of –COO–) also suggest the presence of GA@ZnONPs.

In figure 1(c) results of UV–visible absorption are shown, which confirm the formation of GA@ZnONPs. The characteristic peak of GA@ZnONPs is found around 350 nm, due to their large excitation binding energy at room temperature [69].

The morphological modification of synthesised GA@ZnONPs is determined by the FESEM analysis (figures 1(d) and S1). The micrograph of GA@ZnONPs shows that they
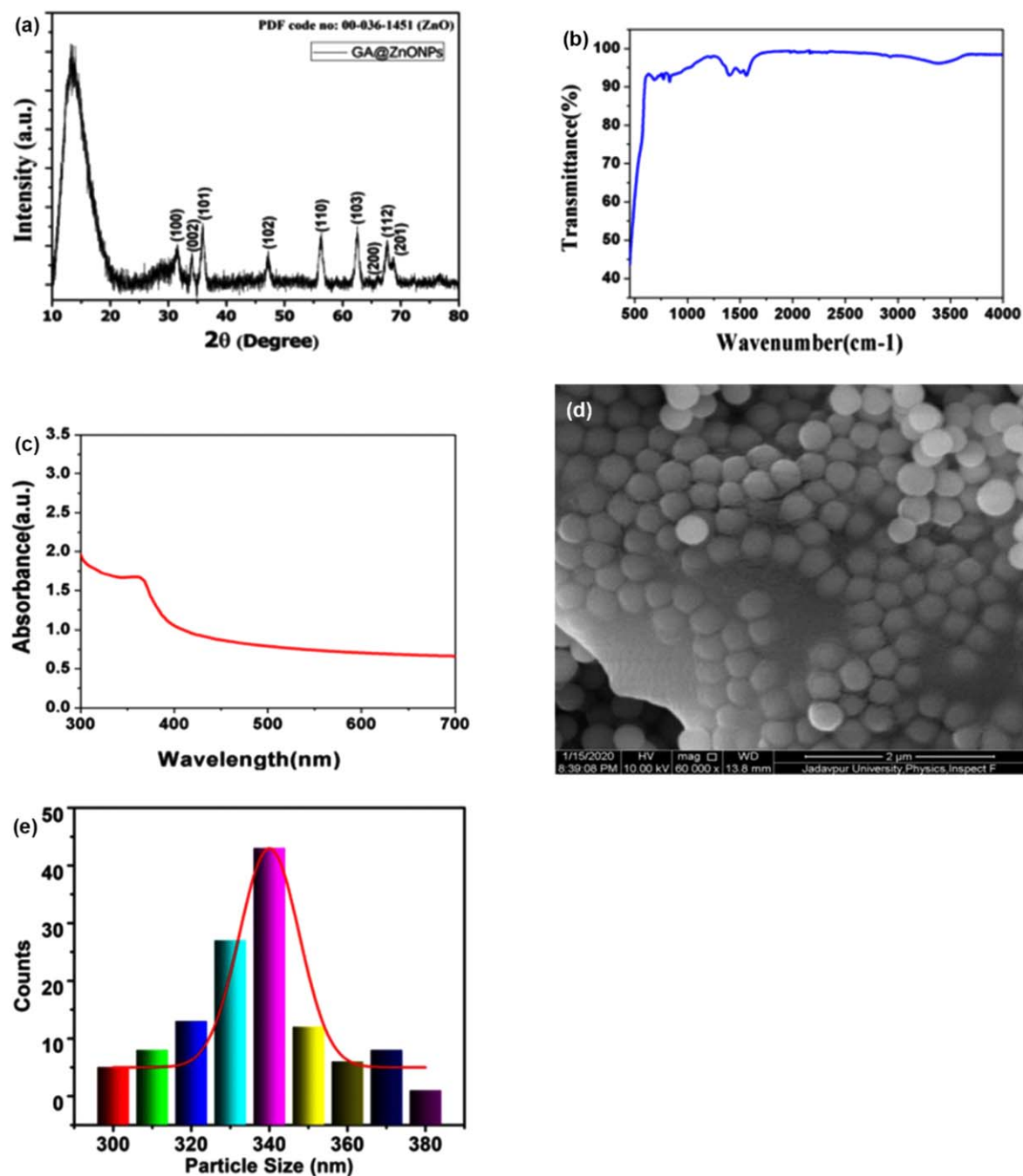
Figure 1. (a) XRD pattern, (b) FTIR spectra, (c) UV–vis spectra, (d) FESEM image, (e) Size distribution curve of gum acacia capped ZnONPs.

had a spherical shape and uniform distribution. The FESEM results explain the presence of spherical ZnONPs within a sheath of the biopolymer gum acacia with size range between 300–380 nm, figure 1(e) (average particle size of 340 nm). From the FESEM images GA@ZnONPs capping was confirmed.

The size distribution of the GA@ZnONPs was determined by DLS (table 1). Particle size distribution curve divulges that GA@ZnONPs obtained are homogeneous in nature, having a polydispersity index (PDI) of 0.225 with an average diameter about 254 nm. The zeta potential of the GA@ZnONP was 12.23 mV which indicates the moderate

Table 1. Hydrodynamic size and zeta potential of gum acacia capped ZnONPs.

Sample name	DLS size (nm)	PDI	Zeta potential (mV)
Gum acacia capped zinc nanoparticles	253.8 ± 4.4	0.225 ± 0.075	12.23 ± 1.4

Adv. Nat. Sci.: Nanosci. Nanotechnol. **11** (2020) 035015

D Bera *et al*
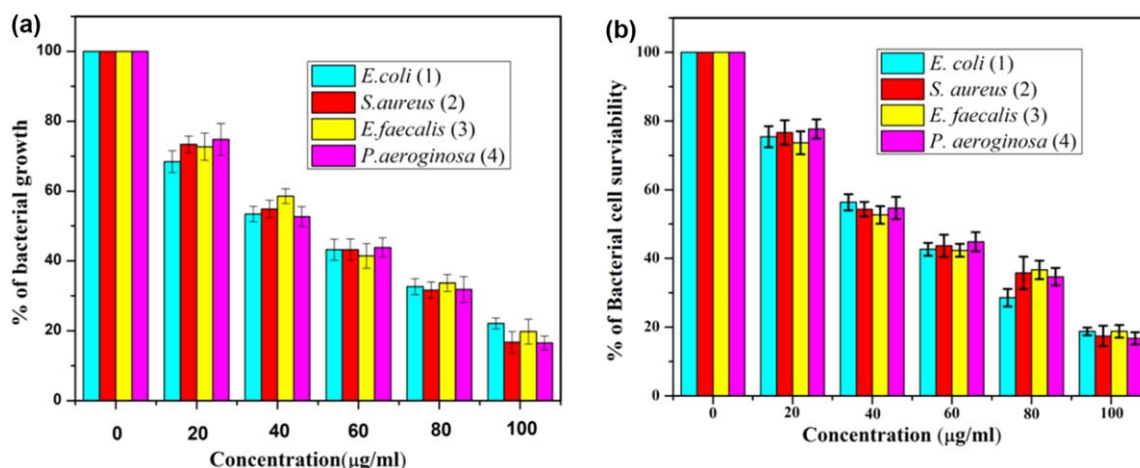
Figure 2. (a) Analysis of antibacterial activity by MIC, (b) Bacterial viability study upon treatment with GA@ZnONPs in pathogenic bacterial strains.

stability of the sample. DLS and zeta potential study suggests that the particle is quite conducive to biological applications.

3.2. Biosynthesised GA@ZnONPs exhibit significant antibacterial activity against pathogenic bacterial strains

The antibacterial activity of the synthesised GA@ZnONPs was determined by separate treatment against Gram-negative and Gram-positive bacterial strains. MIC values of GA@ZnONPs against *E. coli, P. aeruginosa*, *E. faecalis, S. aureus* were 36.46 ± 1.8, 42.32 ± 2.9, 15.54 ± 1.37 and $22.48 \pm 2.4 \, \mu\mathrm{g \, ml}^{-1}$ respectively as shown in figure 2(a).

The MIC dilutions of all the bacterial strains were streaked on the sterile agar plates and were kept at 37 °C for 18–22 h in order to evaluate their respective minimum bactericidal concentrations (MBC) [76, 80]. The concentration at which no visible bacterial growth is observed on the agar plate after treatment with GA@ZnONPs is considered as the MBC. The MBC values of GA@ZnONPs in case of *E. coli, P. aeruginosa, S. aureus, E. faecalis* are found to be 135, 148, 59, and 81 $\mu\mathrm{g \, ml}^{-1}$, respectively. The result clearly depicts significant bactericidal activity of GA@ZnONPs in different bacterial strains.

Tolerance level of bacterial strains *E. coli, P. aeruginosa, S. aureus, E. faecalis* against GA@ZnONPs is 3.7, 3.5, 3.9, 3.6, respectively. Tolerance level states the difference between bacteriostatic agents and bactericidal agents. When the value of MBC/MIC for a particular strain is greater than or equal to 16, this may be considered as bacteriostatic type and when the value is less than or equal to 4, it may be considered as bactericidal agent [76, 80]. The result clearly suggests that GA@ZnONPs exhibit significant bactericidal activity against pathogenic bacterial strains.

The agar diffusion study was performed to the compare the antibacterial activity of different strains treated with GA@ZnONPs. The inhibition zone of Gram-positive and Gram-negative bacteria is shown in figure S2. This study reconfirms the bactericidal activity of GA@ZnONPs against different pathogenic bacterial strains.

The bacterial MTT assay suggested that the GA@ZnONPs significantly decreased the cell viability significantly from the control group in the case of all the four pathogenic strains as shown in figure 2(b). Therefore the GA@ZnONPs can be considered as an ideal bactericidal agent.

The treatment with GA@ZnONPs causes alterations in the structural morphology of the bacterial cells as shown in the FESEM results. The untreated bacterial strains as shown in figure 3 retain their respective morphology. But in the case of treated bacterial cell we observe that the membrane is damaged, and cytoplasmic leakage leads to agglomerated cell debris. FESEM confirms that the bacterial membrane is disrupted and perforated due to penetration of GA@ZnONPs or due to ROS generation.

3.3. Anticancer activity of GA@ZnONPs

The *in vitro* cytotoxicity was estimated by exposing the HepG2 cells to different concentrations of GA@ZnONPs for 24 h. This was followed by MTT assay. It is noted that the GA@ZnONPs exhibit significant anticancer activity with an LD$_{50}$ of $48 \pm 3.24 \, \mu\mathrm{g \, ml}^{-1}$ as shown in figure 4(a). Therefore we can conclude that the GA@ZnONPs have promising anticancer property.

3.4. Mechanisms behind the bactericidal and anticancer activities of functionalised GA@ZnONPs

The content of intracellular ROS was intricately evaluated for investigating the cellular mechanisms responsible for the antibacterial activity of GA@ZnONPs as depicted in figure 5. The enhanced fluorescence intensity in case of GA@ZnONPs treated bacterial cells is a positive indicator of increased levels of intracellular ROS. On the other hand, the untreated bacterial cells exhibit negligible fluorescence intensity. The increased production of intracellular ROS is responsible for the disruption in the electronic transport chain, degradation of the genetic material and damage to the bacterial cell membrane [75, 76, 80].
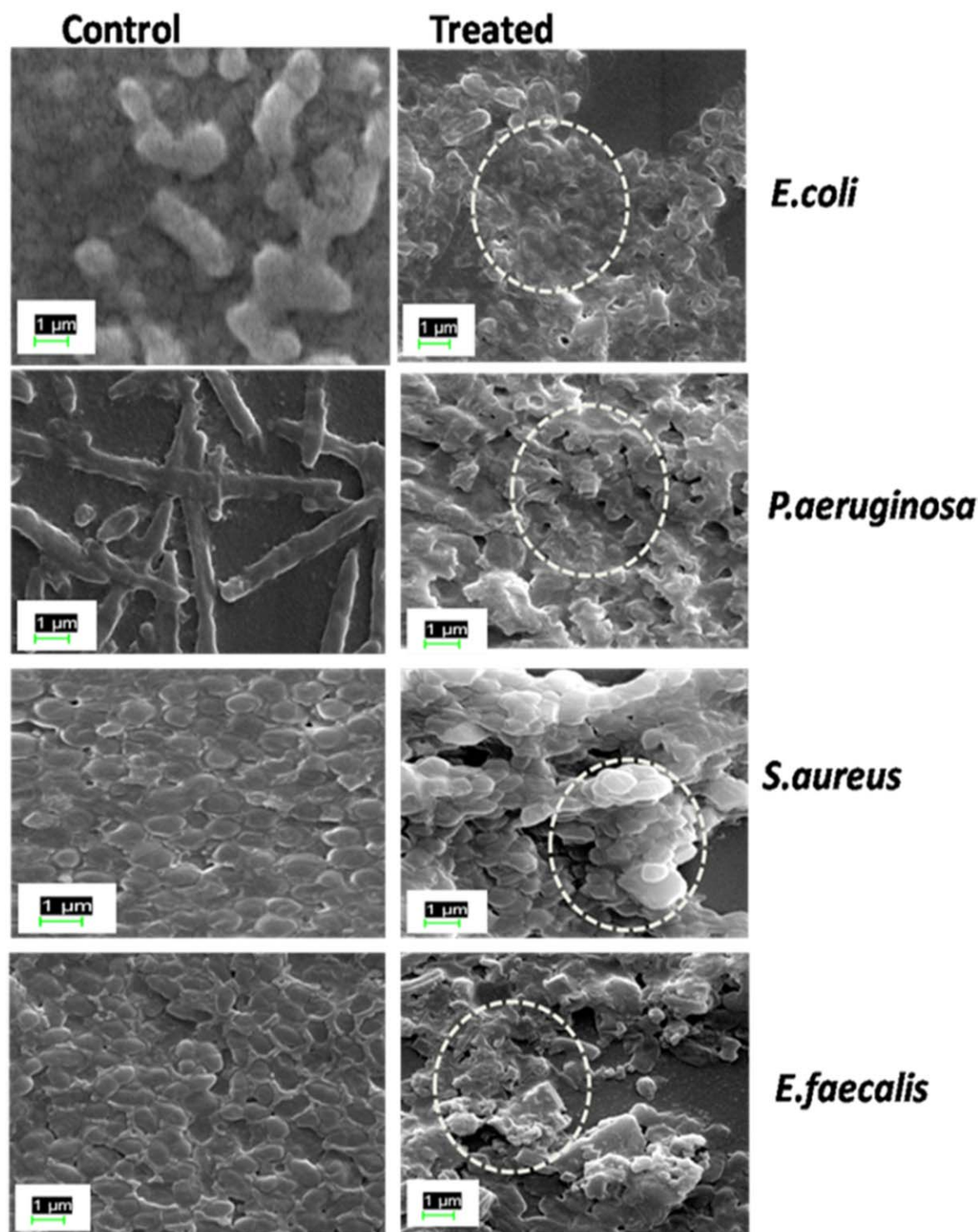
Figure 3. FESEM analysis of gum acacia capped ZnONPs treated pathogenic bacterial strains.

Similarly, in case of the eukaryotic cells, 2′, 7′ dichlorofluorscence diacetate (DCF-DA) is employed as a specific probe in order to envisage the reactive oxygen species (ROS) [77, 78]. The reactive oxygen production is measured in case of hepatocellular cancer cells, HepG2 where the cells are treated with GA@ZnONPs at their LD_{50} dose for a period of 12 h. The results procured from the fluorescence microscope and spectrofluorometer clearly delineate the enhancement of green colour fluorescent intensity in case of the treated HepG2 cells after the incubation time of 12 h as depicted in figures 4(b) and (c).

The confirmation of apoptosis was conducted with the aid of AnnexinV-FITC staining and was estimated by FACS Verse. Figure 6 depicts that upon treatment with 40 and 60 μg ml^{-1} of NPs, cells shifted towards early to late apoptosis with time. Almost 43% and 62.5% apoptotic cells were

Adv. Nat. Sci.: Nanosci. Nanotechnol. **11** (2020) 035015

D Bera *et al*
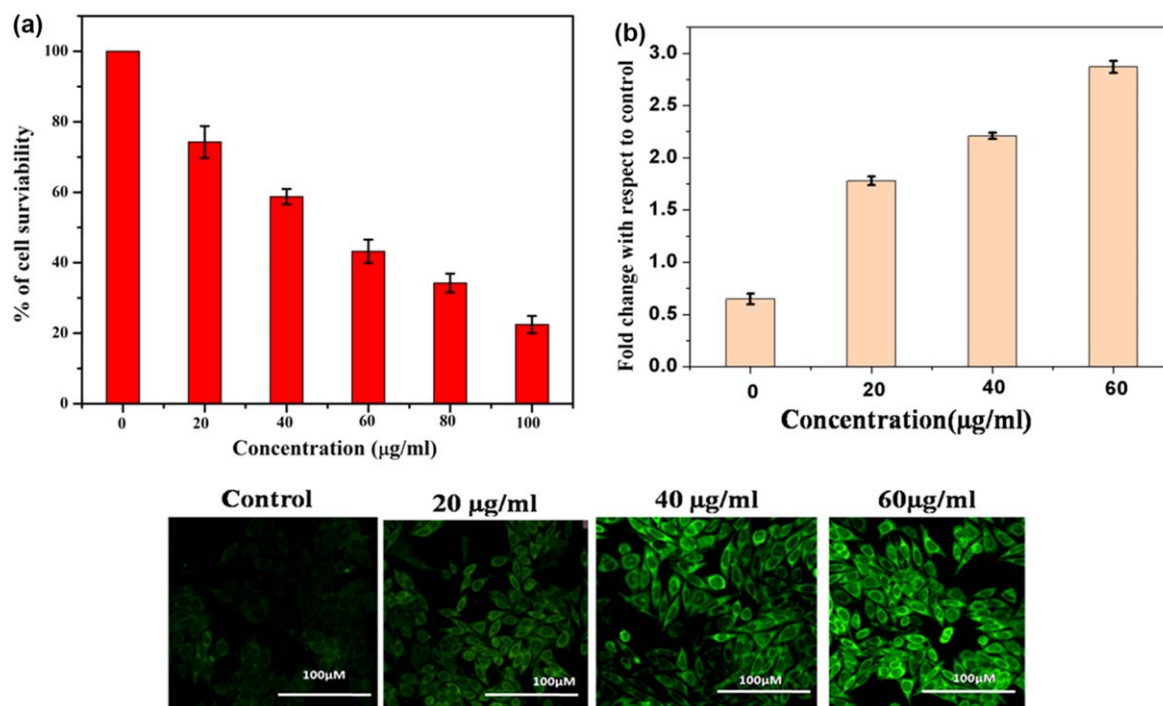
Figure 4. (a) Cell viability assay of GA@ZnONPs in human hepatocellular carcinoma, HepG2; Intracellular ROS generation by treatment with gum acacia capped ZnONPs in HepG2 cells observed by (b) Spectrofluorometer and (c) Fluorescence microscopy.
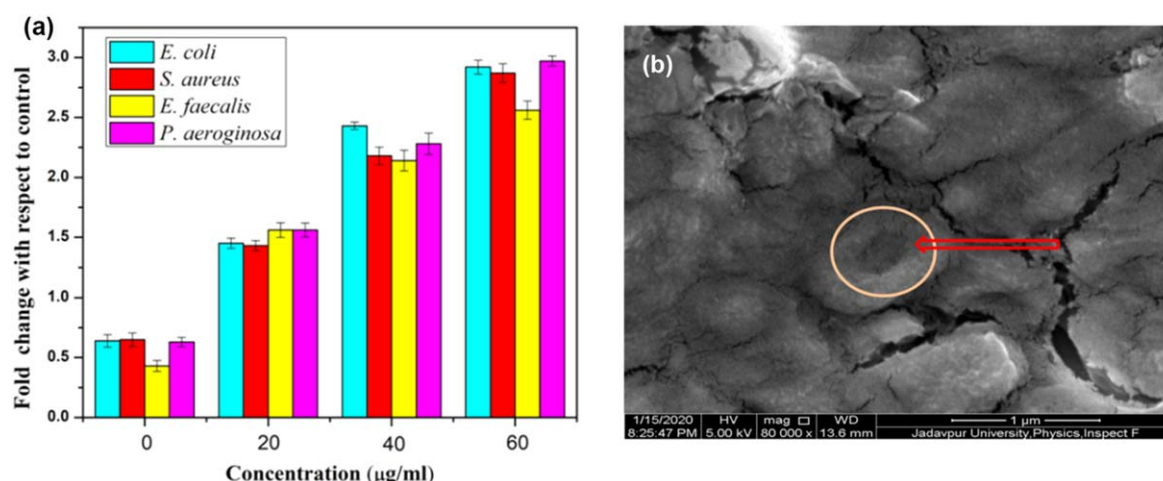
Figure 5. (a) Intracellular ROS generation by treatment with gum acacia capped ZnONPs in pathogenic bacterial strains and (b) FESEM image depicting bacterial membrane damage of *E. coli* due to the treatment of GA@ZnONPs.

observed in 40 and 60 μg ml^{-1} of GA@ZnONPs treated HepG2 cells for 24 h respectively.

3.5. Intracellular uptake of rhodamine-B encapsulated GA@ZnONPs

The rhodamine-B encapsulated GA@ZnONPs exhibit an absorbance peak at 544 nm which is quite similar to that of bare rhodamine-B as shown in figure 7(a). This confirms the encapsulation of rhodamine-B within the GA@ZnONP. The photoluminescence spectra of our synthesised GA@ZnONPs show a luminescent maximum centered at 575 nm shown in figure 7(b).

The incorporation of rhodamine-B dye in GA@ZnONP@RB is indicated by the peaks at 2740, 2407, 1362 cm^{-1} respectively corresponding to C–H stretching, NH$_3^+$ symmetric and C=S stretching vibration, which are similar to the absorbance peaks of rhodamine-B (figure S3(a)). This result confirms the conjugation of rhodamine-B within the matrix of GA@ZnONPs.

GA@ZnONPs tagged with rhodamine-B was successfully internalised into the HepG2 cells as seen in figure 7(c). The result clearly exhibits that the GA@ZnONP@RB was distributed throughout the cytoplasm, which indicates its successful internalisation into HepG2 cells. These nanoparticles possibly penetrate into the cells through the
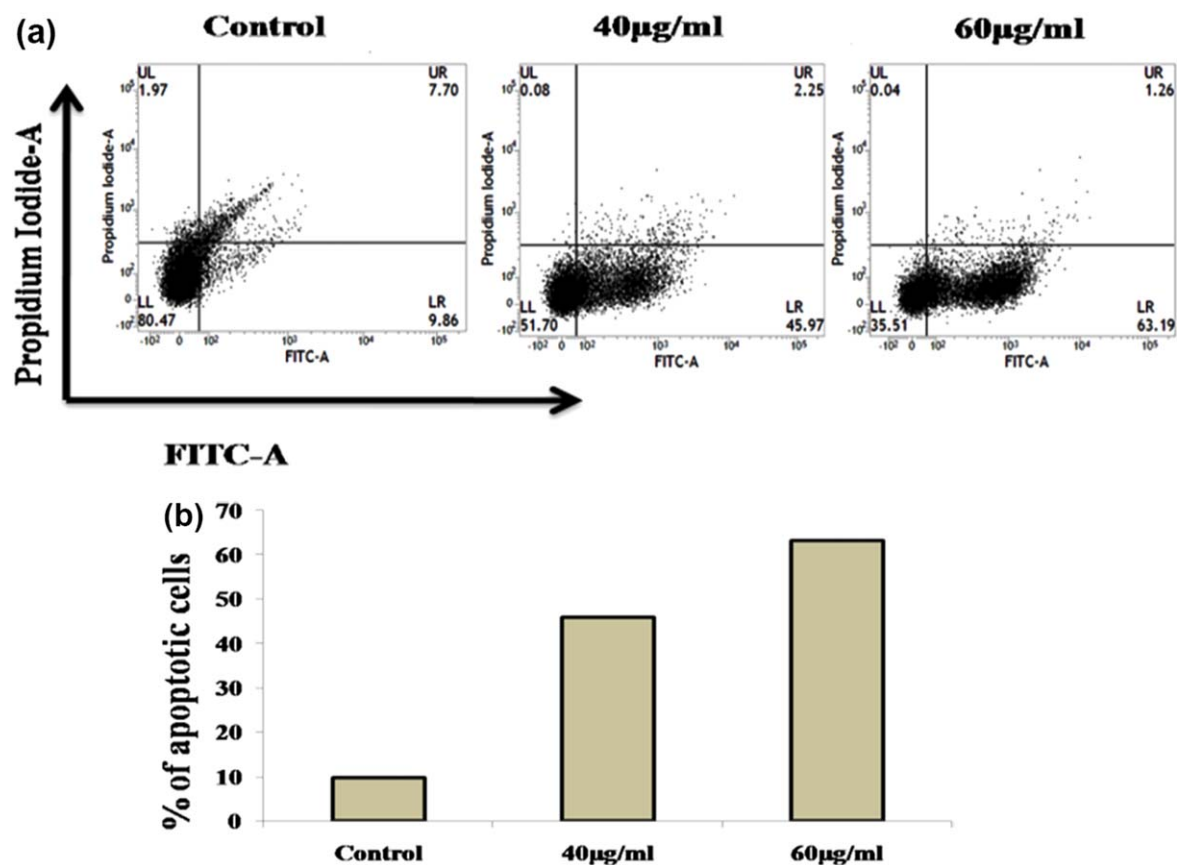
Figure 6. (a) Annexin-FITC analyses of HepG2 treated with 40 and 60 μg ml^{-1} of GA@ZnONPs and (b) Quantitative analysis of apoptotic cells.
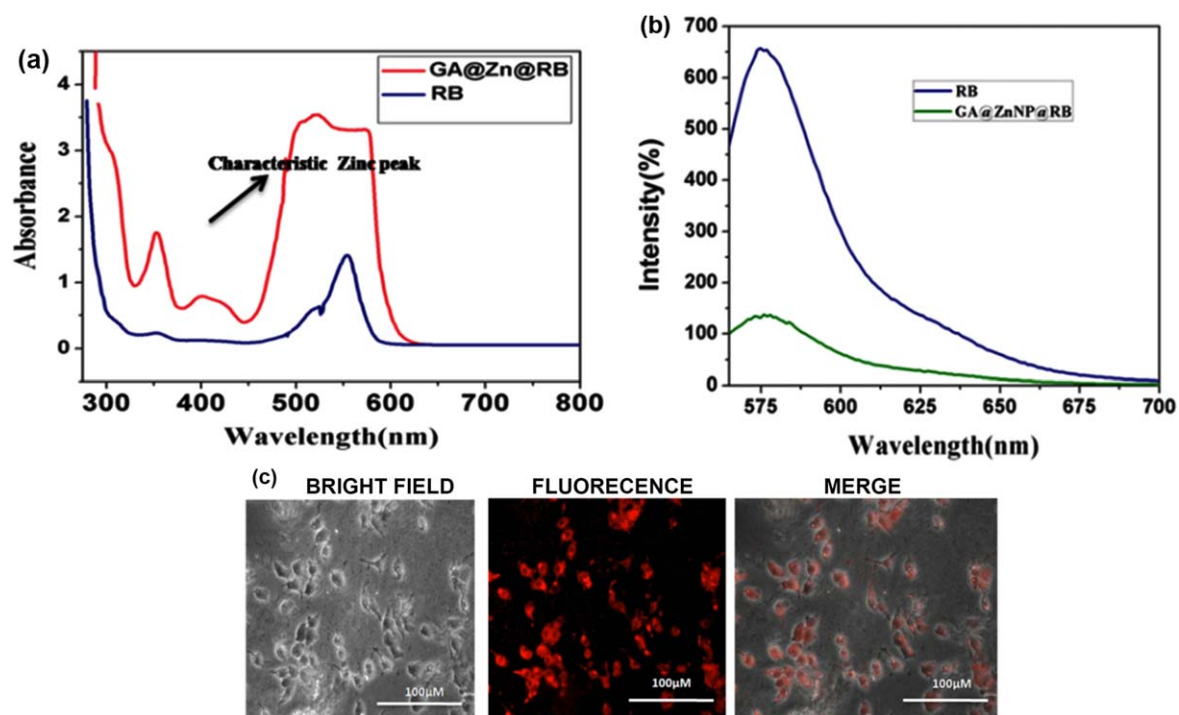
Figure 7. Physical characterisations of GA@ZnONP@RB (a) UV-Vis analysis, (b) Photoluminescence spectra and (c) Cellular internalisation.

Adv. Nat. Sci.: Nanosci. Nanotechnol. **11** (2020) 035015

D Bera *et al*
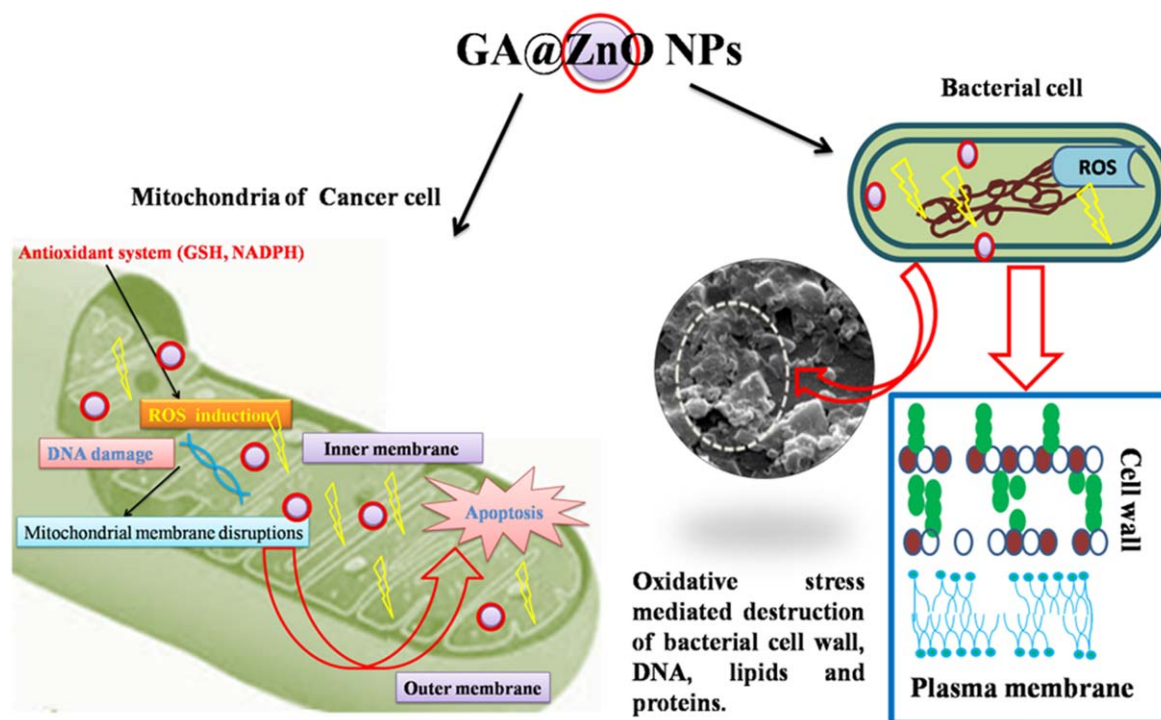
Figure 8. Schematic representation illustrating the mechanism behind the antibacterial and anticancer activities of GA@ZnONPs.

endocytotic pathway. Thus these fluorescent biocompatible nano-platforms are quite conducive to bioimaging applications.

Drug release study: Approximately 25 and 31% rhodamine-B are released from GA@ZnONP@RB after 12 and 24 h, respectively at pH 7.4 as shown in figure S4. On the other hand the release values are 41 and 55% respectively in case of pH 5.5. The results indicate that the discharge of rhodamine-B in pH 5.5 (similar to the pH of the cancer cells) is faster than that of the physiological pH of 7.4. This pH sensitive attribute is quite conducive to cancer amelioration and also circumvents adverse effects on the normal cells.

4. Conclusion

The present study depicts the synthesis, detailed physical characterisation and biological activity determination of gum acacia capped green synthesised ZnO nanoparticles (GA@ZnONPs). They have disrupted the cell wall synthesis or cross linking of polymers as well as degradation of intracellular DNA, lipids and proteins which in turn resulted in the pathogenic cell death. These nanoparticles exhibited quite significant activities against pathogenic bacterial strains like Gram-positive (*S. aureus, E. faecalis*) and Gram-negative (*E. coli, P. aeruginosa*), which was confirmed by performing MIC, MBC and agar well diffusion studies. The DCFDA assay results clearly suggested that GA@ZnONPs is effective in initiating augmented intracellular ROS which culminates in bacterial cell death. Furthermore, GA@ZnONPs also lead to the enhanced generation of ROS in human hepatoma cell as depicted by the DCFDA assay. The AnnexinV/FITC study

confirms the induction of oxidative stress mediated apoptosis in the HepG2 cells. The detailed schematic representation illustrating the mechanism behind the antibacterial and anticancer efficacy of GA@ZnONPs is depicted in figure 8. These nanoparticles were then tagged with rhodamine-B for facilitating the bioimaging applications. We have additionally performed a pH responsive drug release assay at two pH (5.5 and 7.4) keeping rhodamine-B as the model drug. The result suggests that the discharge of rhodamine-B over a period of time was significantly higher at lower pH (which corresponds to the intracellular pH of the cancer cells). Therefore this pH responsive behaviour of our nanoparticle can be instrumental for the transport of anticancer therapeutics, specifically to the cancer cells without having any adverse effect on the normal cells. Future endeavours could be made towards the conjugation of various cancer specific target molecules like folic acid, lactobionic acid, etc for specifically delivering therapeutics to the cancer cells. The attachments of these targeting moieties to these rhodamine-B tagged nanoparticles could also result in cancer specific labelling that in turn can be exploited for the cancer cell discrimination. To the best of our knowledge, this is the first time the biogenic GA@ZnONPs have been endowed with enhanced therapy diagnostic (i.e. both therapeutic and diagnostic) attributes. Henceforth, we can conclude that this hydrophilic GA@ZnONPs have undoubtedly paved the way for the development of a cost-effective platform for multiple therapeutic and bioimaging applications.

Acknowledgments

Conflicts of interest

Authors have no conflict of interest to declare.

References

[1] Patrinoiu G, Calderón-Moreno J M, Chifiriuc C M, Saviuc C, Birjega R and Carp O 2016 *J. Colloid Interface Sci.* **462** 64

[2] Petrochenko P E, Skoog S A, Zhang Q, Comstock D J, Elam J W, Goering P L and Narayan R J 2013 *Biomatter* **3** e25528

[3] Vijayakumar S, Vinoj G, Malaikozhundan B, Shanthi S and Vaseeharan B 2015 *Spectrochimica Acta Part A:Molecular and Biomolecular Spectroscopy* **137** 886

[4] Malekzadeh A M, Ramazani A, Rezaei S J T and Niknejad H 2017 *J. Colloid Interface Sci.* **490** 64

[5] Gholibeloo E, Mortezazadeh T, Salehian F, Forootanfar H, Firoozpour L, Foroumadi A, Ramazani A and Khooti M 2019 *J. Colloid Interface Sci.* **556** 128

[6] Dabbaghi A, Jahandideh A, Kabiri K, Ramazani A and Zohuriaan-mehr M J 2019 *J. Polym. Environ.* **27** 1988

[7] Fardood S T, Ramazani A, Moradi S and Asiabi P A 2017 *J. Mater. Sci.: Mater. Electron.* **28** 13596

[8] Singh G, Singh J, Jolly S S, Rawat R, Kukkar D, Kumar S, Basu S and Rawat M 2018 *J. Mater. Sci.: Mater. Electron.* **29** 7364

[9] Rezaei S, Seyed J T, Asemeh M, Ali R and Hassan N 2019 *Curr. Drug Deliv.* **16** 839

[10] Sadr S H, Davaran S, Alizadeh E, Salehi R and Ramazani A 2018 *J. Drug Deliv. Sci. Tec.* **45** 240

[11] Sadr S H, Davaran S, Alizadeh E, Salehi R and Ramazani A 2018 *J. Biomater. Sci. Polym. Ed.* **29** 277

[12] Singh J, Kumar S, Alok A, Upadhyay S K, Rawat M, Tsang D C W, Bolan N and Kim K H 2019 *J. Clean. Prod.* **214** 1061

[13] Sajjadifar S, Amini I and Amoozadeh T 2017 *Chem. Method.* **1** 1

[14] Elumalaia K and Velmuruganb S 2015 *Applied Surface Science* **345** 329

[15] Selvarajan E and Mohanasrinivasan V 2013 *Materials Letters* **112** 180

[16] Moradnia F, Ramazani A, Fardood S T and Gouranlou F 2019 *Mater. Res. Express.* **6** 075057

[17] Yu C, Zheng-Jun Y, Ping-Ze Z and Xi-Xi L 2020 *Mater. Res. Express* **6** 1250f4

[18] Fardood S T, Forootan R, Moradnia F, Afshari Z and Ramazani A 2020 *Mater. Res. Express.* **7** 015086

[19] Dayyani N, Ramazani A, Khoee S and Shafiee A 2018 *Silicon* **10** 595

[20] Hosseinzadeh Z, Ramazani A, Ahankar H, Ślepokura K and Lis T 2019 *Silicon* **11** 2933

[21] Atrak K, Ramazani A and Fardood S T 2019 *J. Photochem. Photobiol.* A **382** 111942

[22] Moradnia F, Fardood S T, Ali Ramazani A and Gupta V K 2020 *J. Photochem. Photobiol.* A **392** 112433

[23] Hassani H, Zakerinasab B and Nozarie A 2018 *Asian J. Green Chem.* **2** 59

[24] Lakshmeesha T R, Sateesh M K, Prasad B D, Sharma S C, Kavyashree D, Chandrasekhar M and Nagabhushana H 2014 *Cryst. Growth Des.* **14**

[25] Krishnaveni R and Thambidurai S 2013 *Industrial Crops and Products* **47** 160

[26] Karvani Z E and Chehrazi P 2011 *African Journal of Microbiology Resear.* **5**

[27] Raghupathi R, Koodali R T and Manna A C 2011 *Langmuir* **27** 4020

[28] Sorbiun M, Mehr S E, Ramazani A and Fardood S T 2018 *J. Mater. Sci.: Mater. Electron.* **29** 2806

[29] Atrak K, Ramazani A and Fardood S T 2018 *J. Mater. Sci.: Mater. Electron.* **29** 6702

[30] Bhadra P, Mitra M K, Das G C, Dey R and Mukherjee S 2011 *Mater Sci Eng C.* **31** 929

[31] Banoee M, Seif S, Nazari Z E, Fesharaki P J, Shahverdi H R, Moballegh A, Moghaddam K M and Shahverdi A R 2005 *J. Biomed. Mater. Res. B Appl. Biomater.* **93** 557

[32] Dutta R K, Nenavathu B P and Gangishetty M K 2013 *Journal of Photochemistry and Photobiology B: Biology* **126** 105

[33] Vikrant K, Roy K, Kim K H and Bhattacharya S S 2019 *Environ. Res.* **177** 108569

[34] Fardood S T, Ramazani A and Moradi S 2017 *Chem. J. Mold.* **12** 115

[35] Tarasi R, Khoobi M, Niknejad H, Ramazani A, Ma'mani L, Bahadorikhalili S and Shafiee A 2016 *J. Magn. Magn. Mater.* **417** 451

[36] Singh J, Dutta T, Kim K H, Rawat M, Samddar P and Kumar P 2018 *J. Nanobiotechnol.* **16** 84

[37] Singh J, Rathi A, Rawat M, Kumar V and Kim K H 2019 *Compos. B Eng.* **166** 361

[38] Aghahosseini H, Ramazani A, Slepokura K and Lis T 2018 *J. Colloid Interface Sci.* **511** 222

[39] Aghahosseini H and Ramazani A 2020 *Eurasian Chem. Commun.* **2** 410

[40] Singh J, Kaur S, Kaur G, Basu S and Rawat M 2019 *Green Processing and Synthesis* **8** 272

[41] Manna J, Begum G, Kumar K P, Misra S and Rana R K 2013 *ACS Appl. Mater. Interfaces* **5** 4457

[42] Bajpai S K and Kumari M 2015 *Int. J. Biol. Macromol.* **80** 177

[43] Radulescu M *et al* 2016 *Rom. J. Morphol. Embryol.* **57** 107

[44] Atrak K, Ramazani A and Fardood S T 2019 *Environ. Technol.* **2019** 1

[45] Fardood S T, Ramazani A, Golfar Z and Joo S W 2017 *Appl. Organomet. Chem.* **31** e3823

[46] Ahankar H, Ramazani A, Ślepokura K, Lis T and Kinzhybalo V 2019 *Res. Chem. Intermed.* **45** 5007

[47] Fardood S T, Moradnia F and Ramazani A 2019 *Micro Nano Lett.* **14** 986

[48] Azar B E, Ramazani A, Fardood S T and Morsali A 2020 *Optik* **208** 164129

[49] Virender K, Sharma R, Yngard A and Yekaterina L 2009 *Advances in Colloid and Interface Science* **145** 83

[50] Chaturvedi A, Bajpai A K, Bajpai J and Singh K 2016 *Mater. Sci. Eng. C Mater. Biol. Appl.* **65** 408

[51] Rath G, Hussain T, Chauhan G, Garg T and Goyal A K 2016 *Mater. Sci. Eng. C Mater. Biol. Appl.* **58** 242

[52] Sarika P R, Cinthya K, Jayakrishnan A, Anilkumar P R and James N R 2014 *Mater. Sci. Eng. C Mater. Biol. Appl.* **43** 272

[53] Badreldin A H, Ziada A and Blunden G 2009 *Food Chem. Toxicol.* **47** 1

[54] Aderibigbe B A, Varaprasad K, Sadiku E R, Ray S S, Mbianda X Y, Fotsing M C, Owonubi S J and Agwuncha S C 2015 *Int. J. Biol. Macromol.* **73** 115

[55] Sarika P R and Rachel N J 2016 *Carbohydrate Polymer* **148** 354

[56] Singh B, Sharma S and Dhiman A 2013 *Int. J. Pharm.* **457** 82

Adv. Nat. Sci.: Nanosci. Nanotechnol. **11** (2020) 035015

D Bera *et al*

[57] Fardood S T, Golfar Z and Ramazani A 2017 *J. Mater. Sci.: Mater. Electron.* **28** 17002

[58] Fardood S T, Ramazani A and Moradi S 2017 *J. Sol-Gel Sci. Technol.* **82** 432

[59] Sarikaa P R, Cinthya K, Jayakrishnan A, Anilkumar P R and Rachel N J 2014 *Materials Science and Engineering: C* **43** 272

[60] Rao H N, Lakshmidevi N, Pammia S V N, Kolluc P, Ganapaty S and Lakshmi P 2016 *Materials Science and Engineering: C* **62** 553

[61] Chopra M, Bernela M, Kaur P, Manuja A, Kumar B and Thakur R 2015 *Int. J. Biol. Macromol.* **72** 827

[62] Bajpai S K, Jadaun M and Tiwari S 2016 *Carbohyd. Polym.* **153** 60

[63] Singh K, Singh J and Rawat M 2019 *SN Appl. Sci.* **1** 624

[64] Mehr E S, Sorbiun M, Ramazani A and Fardood S T 2018 *J. Mater. Sci.: Mater. Electron.* **29** 1333

[65] Mina S, Ebrahim S M, Ramazani A and Fardood S T 2018 *Int. J. Environ. Res.* **12** 29

[66] Iravani S 2011 *Green Chem.* **13** 2638

[67] Pattanayak P, Behera P, Das D and Panda S K 2010 *Pharmacogn. Rev.* **4** 95

[68] Cohen M M 2014 *J. Ayurveda. Integr. Med.* **5** 251

[69] Juby K A, Dwivedi C, Kumar M, Kota S, Misra H S and Bajaja P N 2012 *Carbohydrate Polymers* **89** 906

[70] Shivananjappa M and Joshi M 2012 *J. Herbs Spices Med. Plants* **18** 331

[71] Lia J, Xu X, Chen Z, Wang T, Lu Z, Hu W and Wang L 2018 *Carbohydrate Polymers* **200** 416

[72] Singh B, Sharma S and Dhiman A 2017 *Carbohydrate Polymers* **165** 294

[73] Primikyri A, Mazzone G, Lekka C, Tzakos A G, Russo N and Gerothanassis I P 2015 *J. Phys. Chem.* B **119** 83

[74] Bhattacharya D, Saha B, Mukherjee A, Santra C R and Karmakar P 2012 *Nanosci. Nanotechnol.* **2** 14

[75] Chang Y N, Zhang M, Xia L, Zhang J and Xing G 2012 *Materials (Basel)* **5** 2850

[76] Pal K, Laha D, Parida P K, Roy S, Bardhan S, Dutta A, Jana K and Karmakar P 2019 *J. Nanosci. Nanotechnol.* **19** 3720

[77] Pal K, Roy S, Parida P K, Dutta A, Bardhan S, Das S, Jana K and Karmakar P 2019 *Mater. Sci. Eng* C **95** 204

[78] Bera D, Pal K, Bardhan S, Roy S, Parvin R, Karmakar P, Nandy P and Das S 2019 *Adv. Nat. Sci.: Nanosci. Nanotechnol.* **10** 045017

[79] Bera D, Pal K, Ruidase B, Mondal D, Pal S, Paul B K, Karmakar P, Das S and Nandy P 2020 *Mater. Today Commun.* **24** 101099

[80] Banerjee S *et al* 2018 *Colloids Surf.* B **171** 300

[81] Chowdhuri A R, Das B, Kumar A, Tripathy S, Roy S and Sahu S K 2017 *Nanotechnology* **28** 095102

[82] Mandal J, Ghorai P, Pal K, Karmakar P and Saha A 2019 *J. Lum.* **205** 14

[83] Mandal J, Ghorai P, Brandão P, Pal K, Karmakar P and Saha A 2018 *New J. Chem.* **42** 19818

[84] Dey S, Purkait R, Pal K, Jana K and Sinha C 2019 *ACS Omega* **4** 8451

A mechanistic insight into the bioaccesible herbometallic nanodrug as potential dual therapeutic agent

Debbethi Bera[a,b,1], Kunal Pal[c,d,1], Bhuban Ruidas[e], Dheeraj Mondal[b], Shinjini Pal[b], Biplab Kumar Paul[b], Parimal Karmakar[c], Sukhen Das[b], Papiya Nandy[a,*]

[a] Centre for Interdisciplinary Research and Education, 404B, Jodhpur Park, Kolkata, 700068, India
[b] Department of Physics, Jadavpur University, Kolkata, 700032, India
[c] Department of Life Science and Biotechnology, Jadavpur University, Kolkata, 700032, India
[d] Division of Molecular Medicine and Centre for Translational Research, Bose Institute, Kolkata, 700056, India
[e] Centre for Healthcare Science & Technology, Indian Institute of Engineering Science & Technology, Shibpur, Howrah, 711103, West Bengal, India

ARTICLE INFO

ABSTRACT

Vanga Bhasma, a herbometallic mixture compound is used as gastrointestinal digestive medicine in ayurveda. Here, we have studied its bioaccessbility as antibacterial and anti cancer agent. Their characteristic FESEM, XRD, FTIR, UV absorption spectra were determined, which indicates high mineral content in Vanga Bhasma nanoparticles. Biological studies like MIC, MBC evaluate its antibacterial property, bacterial ROS generation enhance the ravages of peptidoglycan layer of bacterial cell wall. Further anti-cancerous potential of synthesized Vanga Bhasma nanoparticles was also studied on breast cancer cell line showing its potential to induce apoptosis through oxidative damage and mitochondrial membrane damage. Our studies thus successfully establish the dual therapeutic attribute of Vanga Bhasma nanoparticles as anticancer and antibacterial agent.

1. Introduction

Antibiotics treatments are common and in recent times enormous antibiotics are available in the market worldwide. However, because of their rampant use and sometime due to incompletion of prescribed course, the bacterial strains become resistant. Also many of the antibiotics are not used because of their side effects. Evidences shows that resistant pathogenic strains of *Staphylococcus aureus*, *Pseudomonas aeruginosa* has the potential to cause enormous deaths. Penicillin in 1940, methicillin (in 1961) and in recent times vancomycin-resistant *S. aureus* strains were found in U.S.A (in 2002) and in India (in 2005) [1] were found to be resistant. Infact this causes become a challenge for researchers to develop new drug or to modify the previous ones. Moreover, now-a-days, new system called metal-organic frameworks are showing their potential in biological field [2–4]. In recent days, herbometallic compound also has come into spotlight because of their novel synthesis process.

From centuries, metal and metallic ions have been utilized at very low concentration as antimicrobial and anticancer agent due to their minimal toxic effects [5–11]. In eastern countries herbometallic drugs had been used traditionally against diseases [12–17] without

understanding their action mechanism. In our present studies, we attempt to understand the mechanism and their physical character of one of the drug, locally named as Vanga Bhasma (VB) with the help of advance technologies.

Vanga Bhasma(VB) is mainly used as ayurvedic medicine, are organometallic compound with reduced particle size [18]. VB is composed of some elements which are essential for the body. Main composites in it is Tin oxide (SnO_2) [18,19]. VB is tasteless and odourless fine powder. pH of VB is 8.75 [18]. VB is carefully prepared to focus on immunodulation and ability of drug targeting to the site [20–22]. In previous studies only the synthesis, purification [23] and physical characterization and biocapability for gastric digestion and gastro-intestinal digestion of VB were observed [24]. VB was used to determined as a gastrointestinal drug used for diabetes, urinary disorders, anaemia, asthma and gastric ulcer [25]. But its antibacterial and anticancer activity has not been delved in details.

In our present study, we have investigated the mechanism of a naturally processed drug VB which has been in use for years as an ameliorative agent against gastro-intestinal diseases in oriental medicine. We have also established the potential of Vanga Bhasma nanoparticles (VBNP) as antibacterial and anticancer agent. The detailed

---

* Corresponding author.
  E-mail address: pnandy00@gmail.com (P. Nandy).
[1] Both authors have contributed equally.

physical characterisations like XRD, FTIR, UV–vis Spectra, DLS, Zeta Potential, FESEM were performed to confirm its nano-size, structure, functional group and bonding. The assays like Minimum Bactericidal Concentration (MBC), Minimum Inhibitory Concentration (MIC), Agar well diffusions were carried out to confirm its antibacterial property. The efficacy of the VBNPs was envisaged against the MDA-MB 468, human breast carcinoma cells and was observed to have significant lethal activities. Furthermore we have also delved into the mechanism leading to the cancer cell death. Our detailed studies have established that the VBNP induces the enhancement of the intracellular ROS and disrupts the mitochondrial membrane potential which in turn initiates apoptosis that culminates in cell death. Thus our results implicate the mechanism behind the promising anticancer and bactericidal activities of this herbometallic nanodrug and we can also conclude that the VBNPs could emerge as effective dual therapeutic agent.

2. Materials and methods

2.1. Materials

All analytical grade of chemicals were used for mentioned experiments and were purchased from Sigma-Aldrich. Reagents used for bacterial studies, MTT reagents, glutaraldehyde, fluorescence stains were of Himedia. All the glass wares were washed with Aqua regia solution, then rinsed with the aid of ultrapure water and was ultimately dried. For the synthesis and characterization of material ion-free water (Millipore) was employed with a minimum resistivity at 18Ω. For further use the deionised water was utilised.

2.2. Bacterial strain and cell line

Bacterial strains used in our study are gram negative *Pseudomonas aeruginosa* 1688, *Escherichia coli* 443 and gram positive *Staphylococcus aureus* 740, *Enterococcus faecalis* 441. Bacterial strain were procured from the Microbial Type Culture Collection (MTCC), IMTECH, Chandigarh, India.

MDA-MB-468 and MCF-7 (human breast cancer cell) and WI38 (human lung fibroblast) cell lines were procured from the Central Cell repository of National Center for Cell Science (NCCS), Pune, India. All the above cell lines were cultured in the presence of Dulbecco's Modiefied Eagles Media (DMEM) supplemented with 10 % FBS, 1 mM sodium pyruvate, 2 mM L-glutamine, non–essential amino acids, in the presence of antibiotic solution comprising of 100 mg/L penicillin and 100 mg/L streptomycin. The cells were grown in a humidified atmosphere at a temperature of 37° C in presence of 5% CO_2.

2.3. Drug description

Vanga Bhasma (VB) was provided by the Department of Pharmacy, J. B. Roy State Ayurvedic Medical College and Hospital, Kolkata, West Bengal, India. It was further purified following other improved extraction method.

2.4. Extraction procedure of VBNPs

As per reference the extraction procedure included three stages namely, purification and incineration. In brief, the general purification was done by using lime water for seven times. Then the specific purification process was done by adding Nirgundi (*Vitex nigundo Linn.*) and powderised Haridra (*Curcuma longa Linn.*, Turmeric) for three times. Then the mixture was incinerated by heating and rubbing the purified Vanga along with whole plant of *Achyranthes aspera* in open atmosphere. The roasted Vanga was triturated with Aloe vera juice and incinerated using electric muffle furnace at temperature 600 °C for an hour. This was repeated six times in order to obtain Vanga Bhasma following classical literature [19].

2.5. Physical characterisations

Inductively coupled plasma optical emission spectra (ICP-OES); Thermo iCAP 7000 series, (Thermo Fisher Scientific, USA) and atomic absorption spectra (AAS; Perkin Elmer 2800, USA) were checked to find out the total cation concentration of the VBNPs after acid digestion (HNO3:HCl; 1:3ratio) reported elsewhere [22]. To perform ICP-OES, a standard solution (1000 μg/ml) compatible with multiple parameter was procured from Merck, Kolkata, India. Each individual element was characterized at RF power 1160 W, plasma and nebulizer argon flow rate of 10.00 and 0.50 L/min, respectively, at a auxiliary argon flow rate of 0.50 L/min. During each cycle of operation, the callibration supported by an intermediate standard after every five samples and was repeated thrice. The AAS analysis was performed by keeping VBNPs in water at a horizontal shaker for 6 h at room temperature following an 18 h equilibration for filtration of the aqueous solution. The instruments were fine-tuned using standard solutions (analytical grade) of each element and the analytical procedure was checked by blank analysing reagents routinely as per manufacturer's protocol. Elemental detection ranges were varied from 1 to 0.001 μg/ml for the experiment. Final data were recorded following the formula: (Instrument reading × final volume make up) / actual weight or volume of sample. To investigate the functional groups in the biomolecules possibly present in the material, we have examined the Fourier transform infrared spectroscopy (FTIR) with the help of FTIR-8400S (Shimadzu) between the wavelengths of 400 cm^{-1} and 4000 cm^{-1}. To observe the crystalline property of VBNP, X-ray diffraction (XRD) pattern were analysed using the Model D8, Bruker AXS, Wincosin, USA with a voltage of 40kv having a scan speed of 0.2 s/step in the range of 2θ from 20° to 80° and with Cu Kα radiation-1.5418 Å. To measure the absorbance spectra of VBNPs at a wavelength of 250 − 800 nm, Ultraviolet-visible spectrophotometer were used (Bio-tek, India). Dynamic light scattering (DLS) were performed by employing Zetasizer (NANO ZS90, Malvern Instruments Ltd., UK) to determine the size distribution of VB nanoparticles. With the help of Field Emission Scanning Electron Microscope we visualize fine morphological character of the material by using INSPECT F50 (FEI, Netherland). Biological effect of VBNP were confirmed by Bacterial SEM (ZEISS). Energy-dispersive X-ray (EDX) spectroscopy of synthesized VBNPs were examined with Supra 55 (ZEISS).For determining the shape and size of the material we have performed the TEM analysis using JEOL JEM 2100 h.

3. Experimental section

3.1. Antibacterial activity screening

The antibacterial activity of VBNPs against the two Gram negative and two Gram positive bacterial strains were envisaged with the help of MIC, MBC and agar diffusion processes.

3.2. Minimum inhibition concentration

Fresh culture of *E. coli, E. feacalis, S. aureus and P. aeroginosa* were prepared in nutrient broth, which were used for treatment at different concentration of VBNPs. These were kept in a shaker and incubated for 18 − 20 hrs. After incubation uv-absorption spectrum was observed to obtain MIC against positive control.

3.3. Minimal bactericidal concentration

The above mentioned four strains were streak with MIC dilutions growth on agar plate to observe the MBC. They were incubated for 18 − 20 hrs at 37° C. MBC is the minimum concentration of VBNP at which bacterial strain is completely killed. Bacterial assays were done in a biosafety cabinet in order to prevent contamination.
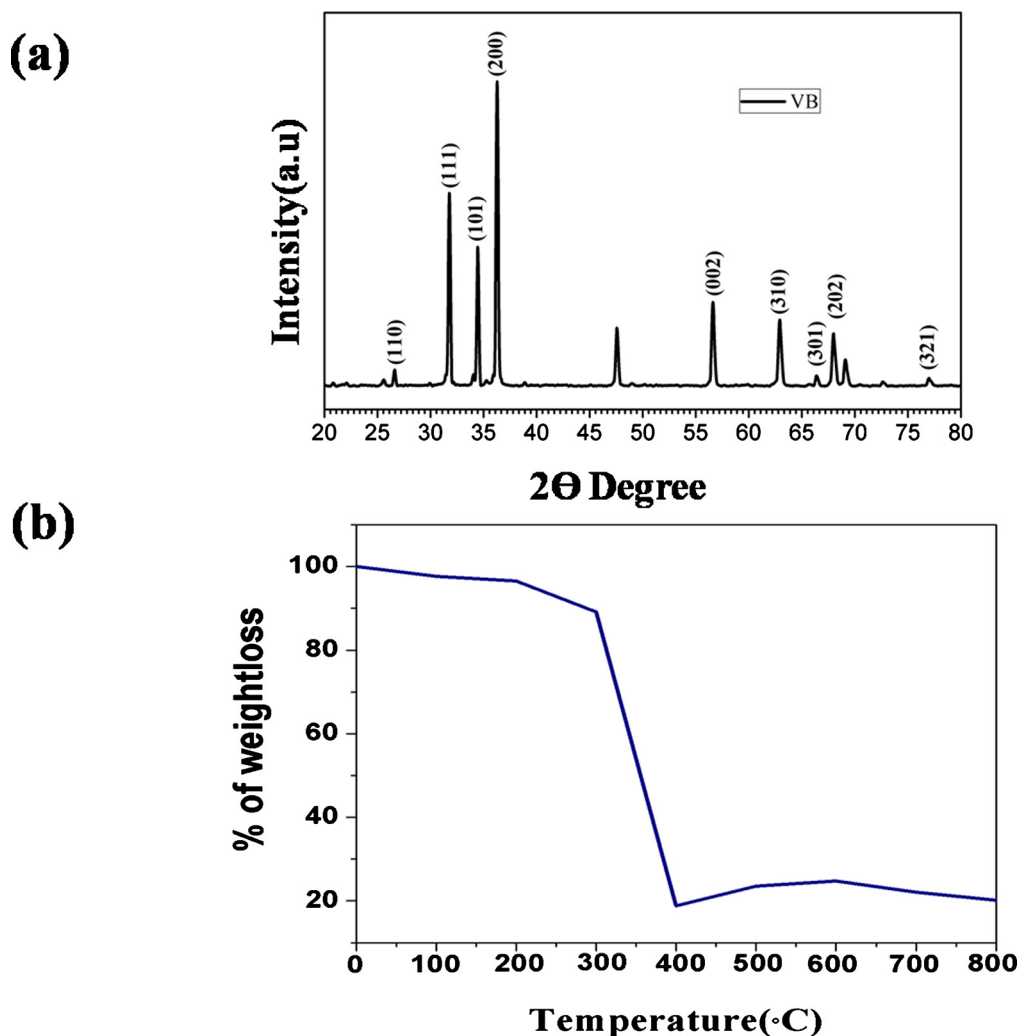
Fig. 1. (a) XRD analysis of VBNP and (b) Thermogravimetric analysis of VBNP.

3.4. Tolerance level

To evaluate tolerance level of bacterial strain against VBNP, we use the following equation,

$$\text{Tolerance} = (MBC) / (MIC) \tag{1}$$

3.5. Agar well diffusion method

Fresh culture of two Gram negative and Gram positive bacterial strains were spread on Muller Hinton agar plate for disc diffusion. After that wells of 90 mm were made to add VB at their MIC concentration along with a negative control i.e. sterile water and a positive control and incubated for overnight. A growth inhibition zone will be observed. To determine the susceptibility of the drug VB, the zone of inhibition diameter were measured surrounding the well.

3.6. Bacterial cell survivability assay

The survivability of the bacterial cells were determined with the aid of 3-(4, 5-dimethylthiazol-2-yl) -2, 5-diphenyltetrazolium bromide (MTT) [26]. The bacterial cells were treated with various concentrations of VBNPs and were incubated for a time span of 24 h at a temperatute of 37° C. These bacterial cells were collected via centrifugation at 1400 rpm for 10 min. and were then washed thrice with the help of sterilised phosphate buffered saline (PBS) having a pH of 7.4. Then the

fresh culture media containing $0.5 \, \text{mg.ml}^{-1}$ of MTT reagent was added by replacing the previous culture medium and was then incubated in dark condition at a temperature of 37° C for 3 h. Then, a solution of HCl-isopropanol was added and was incubated for 15 min. at room temperature. Ultimately the absorbance of the MTT formazan product after being solubilised in HCl-isopropanol was examined in a Shimadzu UV–vis 1800 spectrophotometer at a wavelength of 570 nm.

3.7. Study of the intracellular ROS generation

The 2,7-dichlorofluorescein diacetate ($DCFH_2$-DA) was used as a specific probe for envisaging the amount of ROS generation withion the bacterial cells. The $DCFH_2$-DA shows passive intracellular pentetration and subsequently reacts with the cellular ROS,which in turn results in the generation of 2, 7-dichlorofluorescein (DCF), which is a fluorescent compound [27]. The bacterial cells were at first treated with different concentrations of VBNPs and were incubated overnight at 37° C. The bacterial cells were collected with the help of centrifugation and were washed thoroughly with PBS solutions. Afterwards the cells were incubated with adequate $DCFH_2$-DA solution for 30 min. at a temperature of at 37° C. Ultimately, the visualisation of the bacterial cells were performed with the help of a fluorescence microscope (Leica).

3.8. Study of bacterial cells by SEM

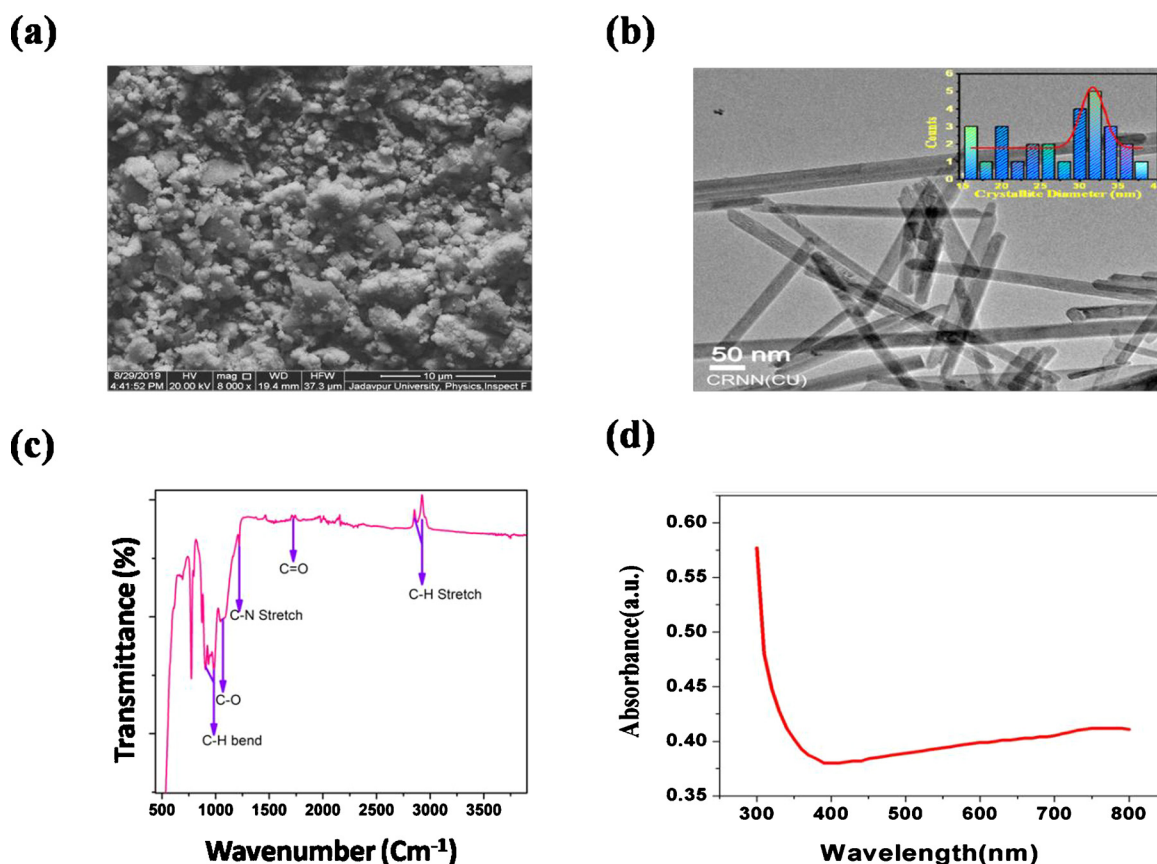The degree of damage to the bacterial cells, post-treatment, by

(a)

(b)

(c)

(d)

Fig. 2. (a) FESEM of VBNPs, (b) TEM with size distribution curve, (c) FTIR spectra of VBNPs (c) UV–vis analysis of VBNPs.

Table 1
Determination of hydrodynamic size and surface charge of synthesized VBNP nanoparticles.

SAMPLE NAME	DLS SIZE (d.nm)	PDI	ZETA POTENTIAL (mV)
VBNP	124.8 ± 2.13	0.185 ± 0.09	10.83 ± 1.48

VBNP was analysed by SEM. Samples subjected to SEM study were prepared following overnight incubation of both the treated and control bacterial cells at 37 °C [26]. Centrifugation (4 min., 4000 rpm) of 1 mL of these incubated cultures (both control and treated) were performed to obtain the pellet. After washing the pellet three times with sterile and filtered PBS containing 2% glutaraldehyde, the bacterial cells were dehydration. Bacterial cells were then fixed on cover slips using drop-casting method and were finally dried by placing under laminar air flow. SEM analysis was then performed followed by gold coating and placing on carbon tape (FEI, INSPECT F50, Netherlands).

3.9. Cytotoxicity assay

The 3-(4, 5-dimethylthiazol-2-yl)-2,5-diphenyltetrazolium bromide (MTT) dye was used to determine the survivability of the breast cancer cells and normal lung fibroblast cells treated with different concentrations of VBNPs [27]. Briefly, around 1×10^4 cells per well of cell culture plates containing 96 wells were treated with different concentrations (0, 20, 40, 60, 80, 100 μg/mL) of VBNPs at 37° C for 24 h in the presence of 5% CO_2. Following this, 10 μl MTT solution at a temperature of 37° C were kept for 4 h in the presence of 5% CO_2. These, generated crystals of MTT-formazan were dissolved in a MTT solubilization buffer. Ultimately a microplate reader (Biorad) was employed to analyse the absorbance at a wavelength of 570 nm. The data were formulated comparing with the control ones.

3.10. Intracellular ROS generations were checked by DCFDA method

Normally, the DCFDA makes intracellular penetration and it subsequently reacts with the reactive oxygen which results in the generation of a green fluorescent colour compound, dichlorofluorescein (DCF). DCFDA stock solution(10 mM) was prepared in methanol. The stock solution was diluted in PBS in order to make a working concentration (100 μM). At first, MDA-MB 468 cells were exposed to VBNPs for a timespan of 12 h at a temperature of 37° C. The cells were washed thoroughly with ice-cold $1 \times$ PBS and were then incubated with DCFDA for 30 min. in dark condition at a temperature of 37° C [28]. The fluorescence intensity was examined both spectroscopically (Hitachi, Japan) and under a fluorescence microscope in MDA-MB 468 cells (Leica) at wavelengths of 485 nm (excitation) and 520 nm (emission).

3.11. Intracellular GSH & NADPH measurement

In order to examine the intracellular antioxidant level in MDA-MB-468 cells on treatment with different concentrations of VBNPs, the intracellular GSH (Glutathione) and NADPH sensing luminescence were performed. GSH-Glo™ are used to record the experimental data. Glutathione Assay kit (Promega) for GSH measurement and Amplite™ Fluorometric NADPH Assay kit (Advancing Assay & Test technologies [AAT] Bioquest, USA) for NADPH measurement with the aid of Microplate reader (Bio-Tek).

3.12. Assessment of mitochondrial membrane potential with JC-1 staining

The mitochondrial membrane potential was examined with the help of JC1 staining [30]. JC-1 dye was used for specific indication of
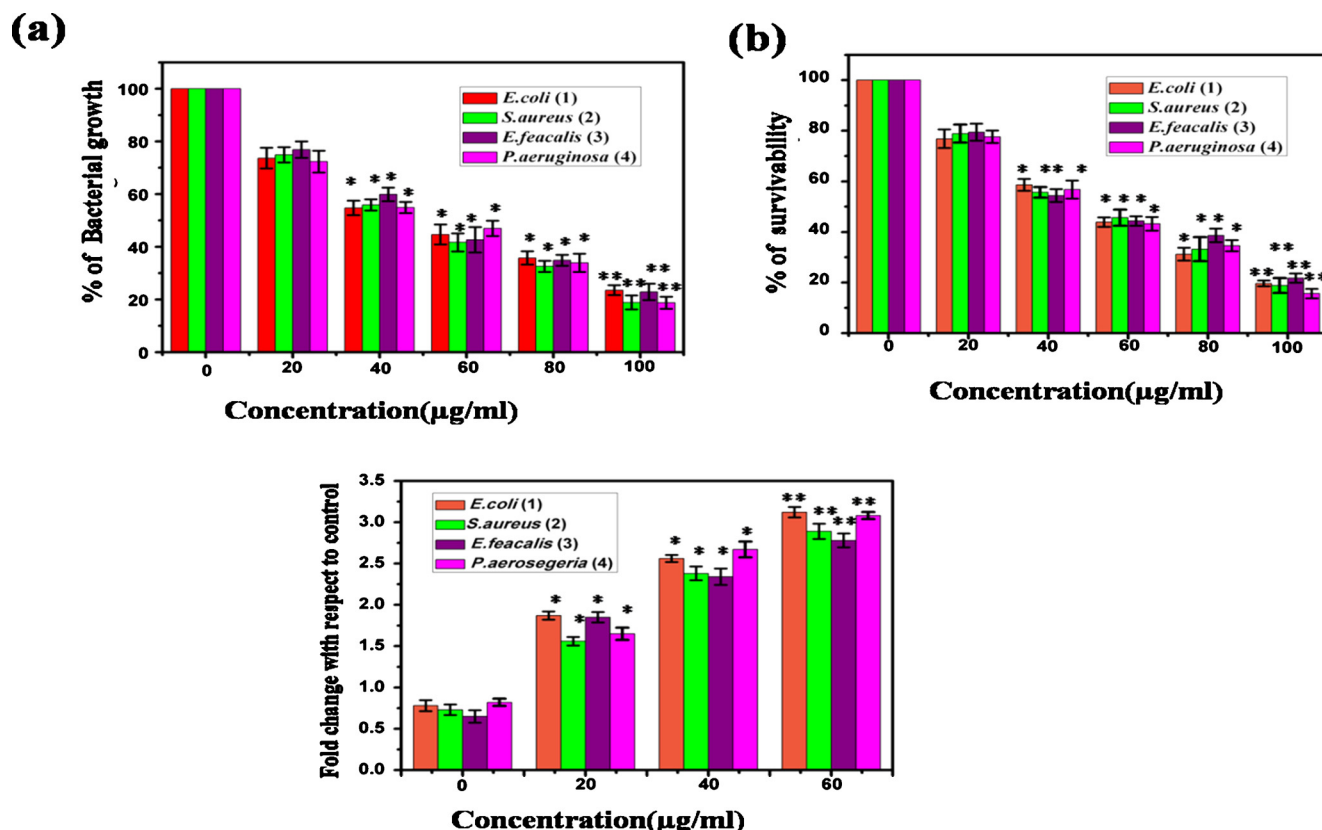
(a)

(b)

Fig. 3. (a) Analysis of activity of VBNP by MIC method in pathogenic bacterial strains *E.coli, S.aureus, E.faecalis, P.aeroginosa*, (b) Bacterial viability study upon treatment of VBNP by MTT assay (c) Intracellular ROS generation in bacterial strains treated with VBNPs.

Table 2
Determination of MIC and MBC values of VBNPs.

Antibacterial effectiveness of VBNPs		
Bacterial strain	MIC value (µg/mL)	MBC value (µg/mL)
Enterococcus faecalis	26.0 ± 2.64	100.88 ± 2.12
Staphylococcus aureus	24.8 ± 1.64	98.2 ± 2.43
Pseudomonas aeruginosa	38.7 ± 2.51	147.06 ± 3.23
Escherichia coli	34.0 ± 1.70	122.4 ± 4.56

Table 3
Evaluation of antibacterial efficacy of VBNPs by disc diffusion assay.

Bacterial strain	Inhibitory diameter
Enterococcus faecalis	16.0 ± 2.64
Staphylococcus aureus	18.8 ± 1.64
Pseudomonas aeruginosa	19.7 ± 2.51
Escherichia coli	18.2 ± 1.80

mitochondria depolarization. A cationic dye, JC-1 shows accumulation within the mitochondria in a potential-dependent manner. This is indicated by a transition of fluorescence from red to green which takes place due to the mitochondrial damage and subsequent loss of membrane potential. The treated MDA-MB-468 cells were afterwards washed thoroughly with the help of phosphate buffered saline (PBS) and incubated in dark for 30 min. with (10 µg/mL) JC-1at 37° C. Finally images were captured with the aid of fluorescent microscope (Leica).

3.13. Mitochondrial ROS measurement with the help of MitoSOX™

MitoSOX™ Red is a fluorescent dye which acts as a specific probe for quantifying the superoxide present within the mitochondria of live cells. At first, 5×10^4 cells cultured on coverslips and were then exposed to the different concentrations of VBNPs. The cell were afterwards fixed with the help of 3.7 % formaldehyde and was thoroughly washed with $1 \times$ PBS. Subsequently, the cells were incubated for 10 min. at 37° C in dark using a working solution of MitoSOX™ Red reagent(5 µM). Ultimately the coverslips were mounted on slides and were immediately observed with the help of a fluorescence microscope (Leica). Again, a spectrofluometer (BioTek) was used to analyse the Fluorescence intensity at excitation of 510 nm and emission at 580 nm.

3.14. Nuclear morphology examination with the help of DAPI staining

The nuclear morphology of the treated and untreated breast cancer cells werer envisaged by by DAPI staining. The cells were exposed with different doses (40 µg/mL and 60 µg/mL) of VBNPs for a time span of 12 h. Afterwards, the cells were washed with $1 \times$ PBS and were stained with the help 4′,6-diamidino- 2-phenylindole (DAPI) (Vector Laboratories Inc.). The nuclear morphology of the cells were ultimately observed with the aid of a fluorescence microscope (Leica).

3.15. Apoptotic cell quantification by Annexin V-FITC staining

The Annexin V-FITC/PI staining was performed after flow cytometry in order to confirm the initiation of apoptosis by employing the Thermo Fischer kit [31]. In brief, the cells were treated with different concentrations of VBNPs.Then the cells were washed thoroughly in ice-cold $1 \times$ PBS. These cells were then resuspensed in a binding buffer (100 µL) and were incubated for 15 min after the addition of Annexin V-FITC (5 µL) and PI (5 µL). The cells were incubated in dark condition at room temperature following the guidelines of the manufacturer. Afterwards the Flow cytometric analysis was performed by employing a FACS Verse instrument (BD).
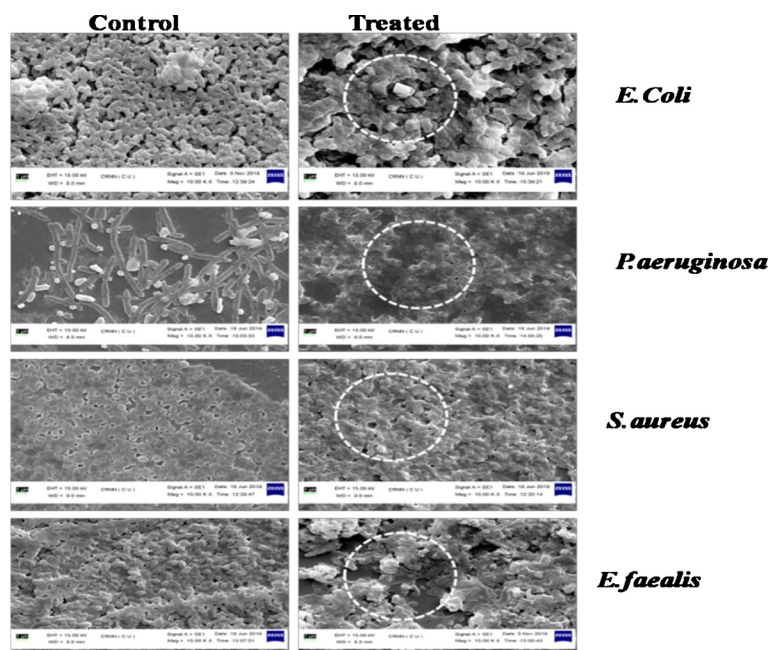
Fig. 4. FESEM images showing the morphology of untreated and treated bacterial strains *E.coli,S.aureus,E.faecalis,P.aeroginosa*.

Table 4
Determination of LD 50 values of VBNPs.

Compound	MDA-MB 468	MCF-7
VBNPs	58.7 ± 3.4	60.2 ± 4.8

3.16. Statistical analysis

We repeated these experiments three times and the data were expressed by calculating the standard deviation of all the experiments. Comparisons of the mean were done with the help of by a model I ANOVA test (using a statistical package, Origin Pro 8, Northamptom, MA 01060, USA) with multiple comparison t-tests, $p < 0.05$ as a limit of significance. The data is the average of three experiments $\pm$ SD. ∗ = represents p value < 0.05, ∗∗ = represents p value < 0.01, ∗∗∗ = represents p value < 0.001.

4. Result and discussions

4.1. Morphological and structural analysis of VBNPs

The results of ICP-OES of VBNPs (ST1) clearly exhibit the presence of water-soluble elements like magnesium (Mg), potassium (K), calcium (Ca), sodium (Na) and iron (Fe) at a low concentration. The heavy metals manganese (Mn), Silver (Ag), zinc (Zn), copper (Cu) and Arsenic (As) were also prevalent but at low concentration. On the other hand Sn is quite predominant in the amalgamate of VBNPs. Henceforth we can conclude that the prevalence of these cationic elements are responsible for the antibacterial and anticancer activity of the VBNPs.

Fig.1a represent the X-ray diffraction (XR) of VBNP. The diffraction peaks are approximately at 26.5°, 31.7°, 34.5°, 36.2°, 56.5°, 62.9°, 66.26°, 67.7°, 72.4°, 76.9° corresponding to (110), (111), (101), (200), (002), (310), (301), (202), (321) plane. The formation of VB NPs has been in good agreement with the Joint Committee on Powder Diffraction Standards (JCPDS) card no. −71-0652 for SnO_2 and 37–1497 for CaO. The average nanocrystalline diameter of all the samples has been
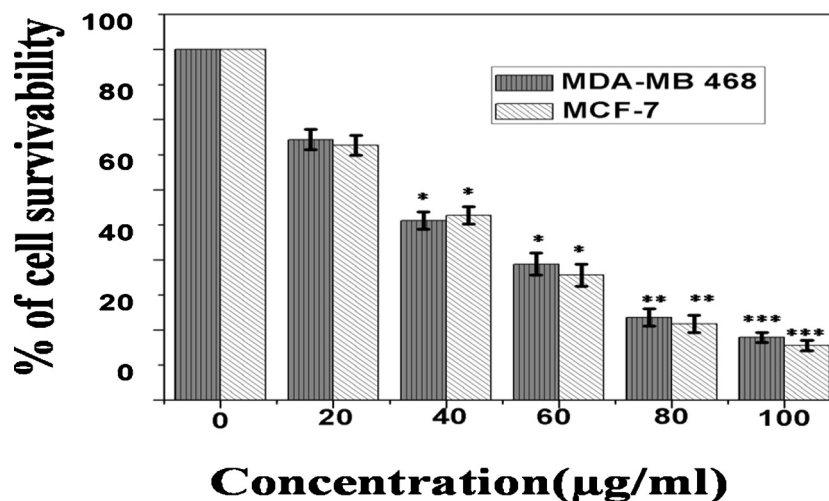

Fig. 5. Assessment of cytotoxicity on triple negative breast cancer cell lines, MDA-MB 468, MCF-7 by MTT assay which shows dose dependent decrease in cell survivability in cells treated with VBNPs.
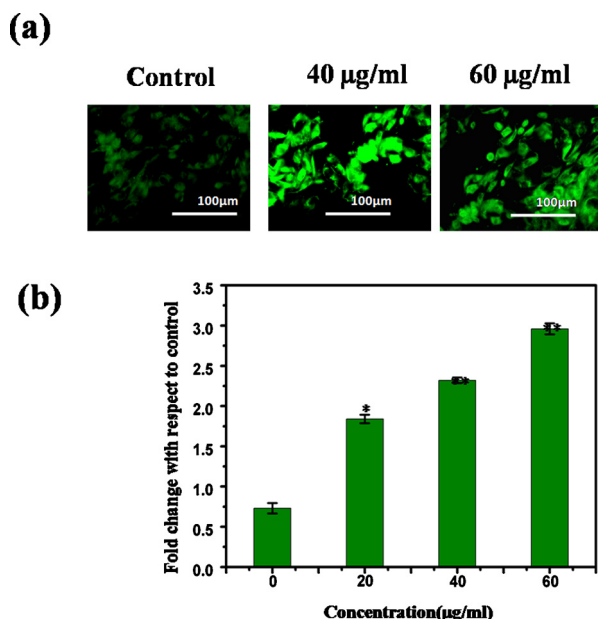
(a)

(b)

Fig. 6. Determination of cellular ROS by DCFDA assay. (a) Fluorescence microscopic image of treated cells and (b) Spectrophotometric fluorescence intensity measurement which indicates the enhancement of ROS in cells treated with VBNPs at doses 40 μg/mL and 60 μg/mL.

estimated using Debye-Scherrer equation from the broadening of the most intense peak (200) present in the diffraction pattern.

$$<D>_{(200)} = \frac{K\lambda}{\beta_{1/2}\cos\theta} \tag{2}$$

Here, D is the average nanocrystalline size, λ is the wavelength of the incident Cu-K^{aa} beam (λ = 1.54 Å), θ is the corresponding Bragg's angle, $\beta_{1/2}$ is the full width at half maximum (FWHM) of the (200) peak and K is the shape factor having the constant value of $\simeq$ 0.9. The FWHM ($\beta_{1/2}$) of the sample has been calculated after broadening the (200) peak and it is around 0.00424. Also the corresponding average nanocrystalline diameter (D) is found to be $\sim$ 34.4 nm.

In thermogravimetric analysis, nearly 85 % weight loss was observed at 464 °C due to the decrease in the labile organic as well as mineral contents of VBNPs (Fig. 1b) whereas, other identified minerals were found to be thermally stable within this temperature. Thus from the TGA data it could be assumed that the major fractions of VBNPs contain organic substances along with a relatively lower amount of metallic components which are quite capable for the antibacterial and

anticancer activities.

For further morphological confirmation of VB were studied by FESEM. Microstructure of VB is shown in Fig. 2b which has rod shaped morphology.

The elemental composition was determined using EDX analysis. The presence of Tin, Zinc, Calcium, Iron were predominant in EDX spectra (Fig.S1).

From the TEM image it is demonstrated that the VBNPs is nearly monodisperse, nanosized crystals. The average crystallite diameter has been estimated through Gaussian distribution and found to be around 31.8 nm (Size histogram shown in Fig. 2b). Particles are crystalline with very low agglomeration and visualized mostly regular rod in shape.

4.2. Spectroscopic analysis of VBNPs

In Fig. 2c The presence of organic compounds in VBNP was clearly observed by FTIR analysis reflecting the presence of different types of organic bonds like C–H, C−N, C−O, C═O, and so on.

In Fig. 2d the UV–vis spectrum of VBNP does not show any characteristic peak or hump upon spectral scanning within a range of 300 − 800 nm.

4.3. The determination of hydrodynamic size and surface charge of VBNPs

As depicted in Table 1 VBNPs exhibit a hydrodynamic diameter of 124.8 ± 2.13 nm with a low P.D.I value of 0.185 ± 0.09. This low P.D.I value indicates that the solution is aqueous solution of VBNP is homogenous in nature which is quite conducive for biological applications. The Zeta potential of VBNPs are 10.83 ± 1.48 mV.The colloidal stability of the prepared samples was studied by dynamic light scattering (DLS) measurements. No observable aggregation ofnanoparticles was found even after 21 days as observed in DLS results shown in Fig. S2. The hydrodynamic diameter of water dispersed VBNP nanoparticles after 21 days wasalmost the same (suggesting the higher colloidal stability of the nanoparticles.

4.4. The antibacterial activity determination of VBNPs

To determine the bactericidal activity of VBNPs against both the gram negative as well as and gram positive strains were treated with different concentrations of VBNPs. In Fig. 3a depicts a dose dependent inhibition of growth in different bacterial strains due to the treatment with VBNPs. Table 2 represents the respective MIC values in case of *E. coli, E. feacalis, S. aureus* and *P. Aeroginosa* bacterial strains.

MIC dilution was streaked to sterile agar plates to estimate the MBC value. The repective MBC values for *E. coli, E. feacalis, S. aureus* and *P.*
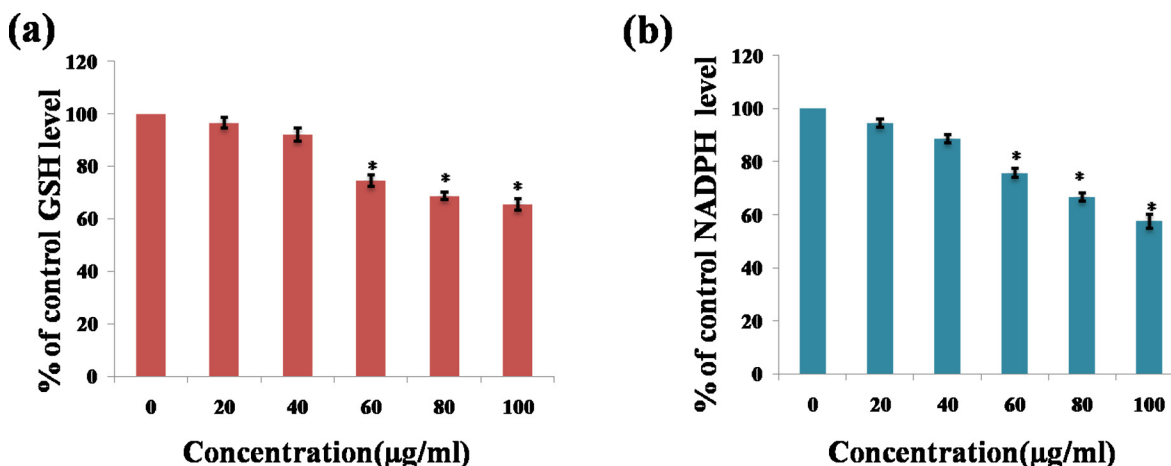
(a)

(b)

Fig. 7. Intracellular antioxidant level determination in MDA-MB 468 cells treated with VBNPs.
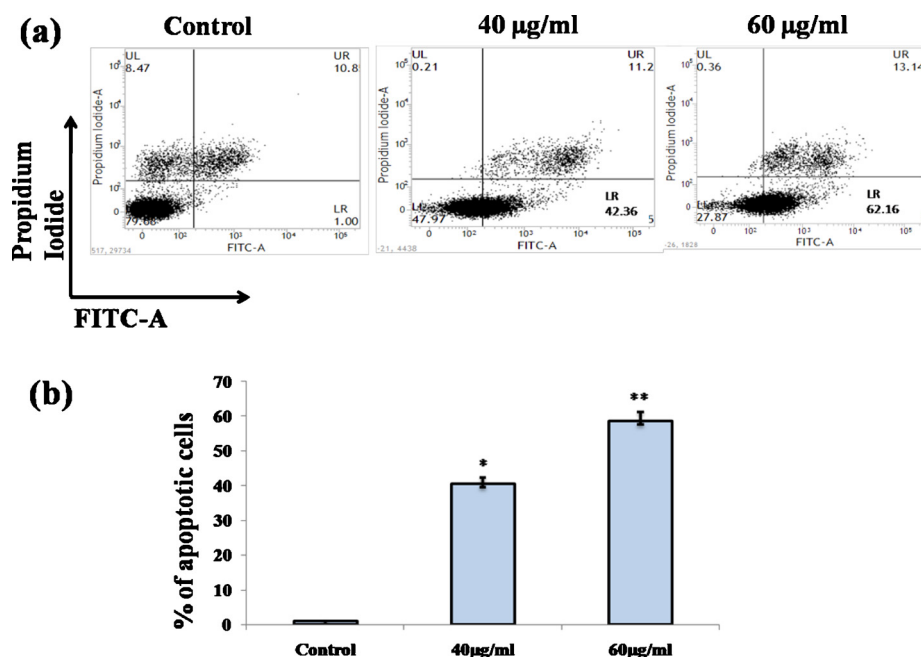
Fig. 8. Dot plot of Annexin V-FITC/PI for evaluation of apoptosis in MDA-MB 468, MCF-7 and WI-38 cells treated with VBNPs; (b) Quantification of apoptotic cells for evaluation of apoptosis in these cells treated with VBNPs at doses 40 µg/mL and 60 µg/mL.
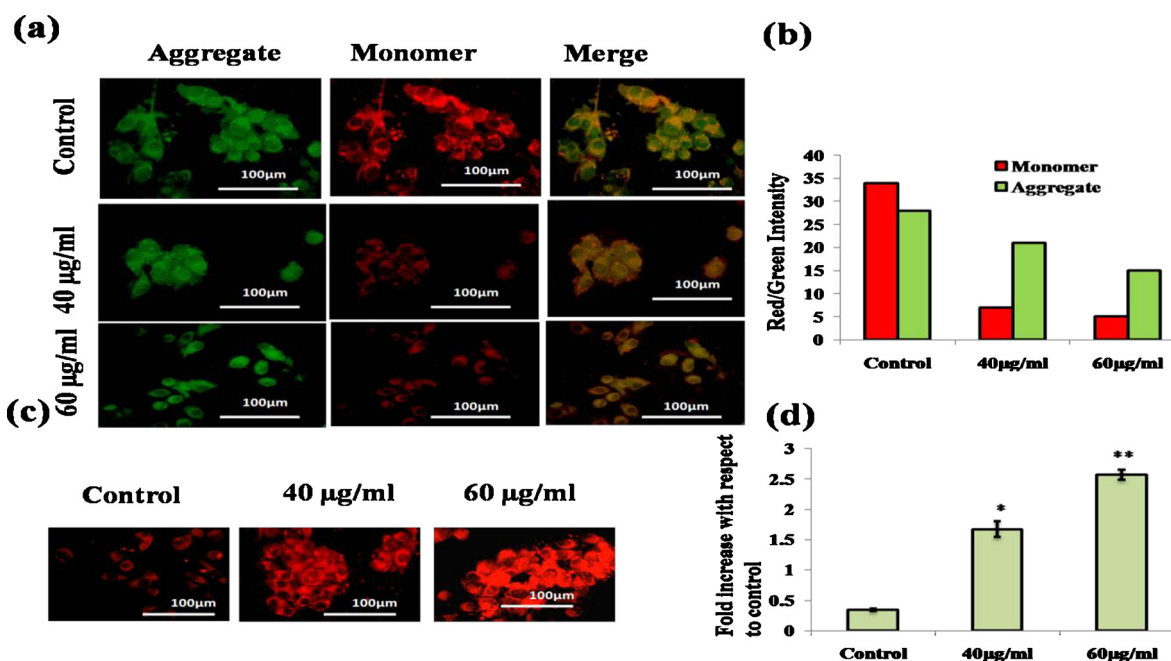
Fig. 9. (a),(b)Mitochondrial membrane potential measurement by JC1 on MDA-MB 468 along with quantification data which clearly indicates the mitochondrial membrane potential transition in cells treated with the compound VBNPs;(c),(d),Mitochondrial ROS determination by Mitosox on MDA-MB 468 along with quantification data which clearly indicates the generation of mitochondrial ROS in cells treated with VBNPs.

aeroginosa are also given in Table 2. The results clearly depicts that the VBNPs exhibit significant bactericidal activity against a wide range of bacterial strains.

4.5. Vanga bhasma nanoparticles exhibit excellent bacteriocidal activities against pathogenic strains

Tolerance level was calculated from MBC and MIC value [32]. When the MBC/MIC ratio is greater or equal to 16, the agent is considered to be bacteriostatic for specific bacteria.On the other hand when this ratio is less than or equal to 4 it is considered to be bactericidal for that

specific bacteria. The values of the tolerance level of VBNPs in case of *E. feacalis, S. aureus, P. aeroginosa, E. coli* were 3.88,3.96,3.8,3.6 which further confirms the bactericidal charecteristics of VBNPs.

4.6. Antibacterial efficacy confirmation of VBNPs by agar well diffusion methods

The agar well diffusion method was performed in order to confirm the growth inhibition of different strains at their MIC concentration with the control treated with sterile water [32]. As depicted in the Fig S3 distinct zones of inhibition are observed in case of the pathogenic

strains like *E. coli, E. feacalis, S. aureus* and *P. aeroginosa*. The values of the diameter of Zones of inhibition of different bacterial strains are given Table 3.

4.7. Treatment of E.coli, E.feacalis, S.aureus and P.aeruginosa with VBNPs significantly diminishes the bacterial cell viability

VBNPs are responsible for reducing the bacterial cell survivability at their respective MBC conc. as depicted in Fig. 3b. The reason behind it may be the intracellular ingression of VBNPs. This penetration of the VBNPs are responsible for cutailing the survivability of the bacterial cells. Hence we can conclude that these VBNPs can be considered as promising bactericidal agent [32].

4.8. Mechanisms behind bactericidal activity of VBNPs

The VBNPs had the capability to induce intracellular ROS generation which in results culminates in the bacterial cell death. In order to envisage the mechanisms behind the bactericidal activities of VBNPs, the DCF-DA solution was used as a specific probe for determining the amount of ROS generated within the bacterial cells as depicted in Fig. 3c. The results indicate that the treated pathogenic bacterial cells enhanced the generation of ROS. This augmented intracellular ROS production contributes to the bacterial cell membrane, disruption in the cellular genetic content which subsequently leads to the death of the bacterial cells [33].

4.9. Treatment with VBNPs exerts significant effect on bacterial morphology

After analysing the SEM images (Fig. 4) it can easily be concluded that, membrane was severely damaged in case of VBNP treated bacterial cells resulting in loss of morphological integrity of the cells. On the other hand, membrane integrity was intact in case of control cells. Bacterial cell death was an obvious consequence as a result of membrane destruction and perforations leading to expulsion of cytoplasmic contents [26].

4.10. Anticancer activity of VBNPs

In-vitro cytotoxicity of the VBNPs are evaluated for determining the cytotoxic effects on MDA-MB 468 and MCF-7 cell line [27]. The cells were treated with various concentrations of VBNPs ($0 - 120\,\mu g/mL$) for a time span of 24 h and was afterwards followed by MTT assay. It was observed that, VBNPs depicted a decrease in the cell survivability in a dose dependent manner. The details of LD_{50} values in case of these two cell lines are provided in Table 4. The VBNPs showed negligible toxicities on the normal WI38 cells. Therefore the results clearly suggest that the VBNPs could exert encouraging anticancer activity without exhibiting any significant toxicity on the normal cells exhibited in Figs. 5 and S4.

5. The treatment of VBNPs induces the generation of intracellular reactive oxygen species

The Reactive oxygen species (ROS) is examined with the help of both Spectro fluorometer and fluorescence microscopy with the help of 2′, 7′ dichlorofluorscence in diacetate (DCF-DA) as a probe [31]. The generation of reactive oxygen species is evaluated in case of human breast carcinoma cells, MDA-MB 468 with VBNPs at concentrations of $40\,\mu g/mL$ and $60\,\mu g/mL$ for 12 h.The fluorescence microscopic images clearly depicts the occurrence of enhanced green fluorescence intensity in case of treated MDA-MB 468 cell lines after 12 h (Fig. 6).

5.1. The intracellular redox balance is impaired due to the treatment with VBNPs

The homoestasis of the ROS level is critically maintained inside the cell and solely regulated by intracellular antioxidant level (NADPH and GSH) in mitochondria and cytosol. Therefore, the investigation of the intracellular antioxidant system was in the central concern, as it eliminates NADPH and GSH, which are very important antioxidants in mitochondria and cytosol to defend cells against the oxidative stress mediated cellular death [34,35]. In this experiment, the results exhibit a drastic dose dependent diminish in the percentage of GSH and NADPH level with 100 µg/ml of VBNP treatment compared with control one (Fig. 7).

VBNPs mediate the mitochondrial membrane permeability transition which inculminates in the initiation of apoptosis mediated cell death in breast cancer cells

Moreover, reports suggest that a pivotal role is played by the intracellular ROS in altering the mitochondrial permeability [30]. Therefore we envisaged mitochondrial damage by JC-1 upon treatment with VBNPs (Fig. 8a and b). The mitochondrial membrane permeability transition is depicted by the drastic transition of fluorescence from red to green and by a decreased the red/green ratio. Henceforth, these results confirm that the VBNPs mediate intracellular ROS generation which in turn drastically disrupts the mitochondrial membrane potential [30].

The mitochondrial ROS production in presence of the MitoSOX™ Red reagent was also envisaged. MitoSOX™ Red reagent effectively penetrates into the mttochondria of the live cells and gets immediately oxidosed by the mitochondrial superoxide. The oxidized product emits a prominent red fluorescence when it binds to nucleic acid. A distinctly augmented level of fluorescence is observed in case of cells treated with different concentrations of VBNPs as seen in Fig. 8c and d. Henceforth, we can conclude that the VBNP mediates the enhanced mitochondrial ROS production which in turn leads to the apoptosis mediated cell death.

Apoptotic morphology were evaluated in case of the breast cancer cells treated with VBNPs for 12 h with the aid of DAPI staining. In case of the untreated cells no morpholical anomalies like nucleus shrinking or polynuclear fragmentation were observed. While in case of the treated cells, a distinct polynuclear fragmentation and nucleus shrinking was prevalent [Fig. S5]. Our results show that 34 % and 46 % of cells showed dominant signs of apoptosis when treated with a dose of 40 ug/mL and 60 ug/mL of VBNPS.

As a confirmation of apoptosis,Annexin V-FITC staining was carried out with the help of FACS Caliber. As depicted in Fig. 9a and b, the treatment with LD_{50} dose of VBNPs resulted in the drastic transition of the cells shifted towards early to late apoptosis.The percentage (%) of apoptotic cells were predominant in case of the breast carcinoma cells treated VBNPs for 24 h compared to the untreated cells. In case of the MDA-MB 468 cells treated with VBNP, approximately 60 % of the cells depicted the signs of apoptosis after 24 h. On the other hand, only 1% of apoptotic cells were oberved in case of the untreated cells. The results suggests that the VBNPs are capable of initiating apoptosis mediated cell death in the breast cancer cells via a series of intracellular events like enhancement of ROS generation, impairment of the intracellular redox balance and mitochondrial membrane damage [31].

6. Conclusion

Both the field of cancer and resistant antibiotics becoming threaten in these days. Moreover, the side effects of promising chemotherapy required more efficient therapeutics in order to diminish this problem. Our studies confirm that these nano material, VBNP is applicable for combined therapeutic system which are in great demand nowadays. From our studies we believe that these nanoparticles can emerge as a promising ameliorative agent against a broad range of diseases like

cancer as well as bacterial diseases including urinary tract infection, surgical infection, skin infection, etc In the present study with VBNPs, the probable reason behind the bacterial cell wall destruction might be the disruption in the steps of signaling cascades that in turn is the reason behind the disrupted synthesis of cell wall resulting from enhanced ROS generation [26,29] in case of both Gram-negative and Gram-positive strains of bacteria. Furthermore, our study clearly depicts the enhancement of intracellular ROS generation in breast carcinoma cells brought about by the treatment of Vanga Bhasma nanoparticles.This aggravated ROS is responsible for the transition of the mitochondrial membrane potential of the cells which in turn culminates in the apoptosis mediated breast cancer cell death. In conclusion, our studies suggest that these Vanga Bhasma nanoparticles can emerge as a dual ameliorative agent against pathogenic bacterial strains and breast cancer cells.

CRediT authorship contribution statement

Debbethi Bera: Conceptualization, Resources, Methodology, Investigation, Writing - original draft. **Kunal Pal:** Investigation, Methodology. **Bhuban Ruidas:** Investigation. **Dheeraj Mondal:** Investigation. **Shinjini Pal:** Investigation. **Biplab Kumar Paul:** Investigation. **Parimal Karmakar:** Resources. **Sukhen Das:** Resources. **Papiya Nandy:** Supervision.

Declaration of competing Interest

The authors have no competing conflicts of interest related to this work.

Acknowledgement

Appendix A. Supplementary data

Supplementary material related to this article can be found, in the online version, at doi:https://doi.org/10.1016/j.mtcomm.2020.101099.

References

[1] S. Chang, D.M. Sievert, J.C. Hageman, M.L. Boulton, F.C. Tenover, F.P. Downes, S. Shah, J.T. Rudrik, G.R. Pupp, W.J. Brown, S.K. D Cardo, Fridkin infection with vancomycin-resistant Staphylococcus aureus containing the van a resistance gene New, Engl. J. Med. 348 (2003) 1342–1347, https://doi.org/10.1056/NEJMoa025025.

[2] H. Ren, L. Zhang, J. An, T. Wang, L. Li, X. Si, L. He, X. Wu, C. Wang, Z. Su, Polyacrylic acid@zeolitic imidazolate framework-8 nanoparticles with ultrahigh drug loading capability for pH-sensitive drug release, Chem. Commun. 50 (2014) 1000–1002, https://doi.org/10.1039/C3CC47666A.

[3] P. Horcajada, C. Serre, G. Maurin, A.N. Ramsahye, F. Balas, M. Vallet-Regí, M. Sebban, F. Taulelle, G. Férey, Flexible porous metal-organic frameworks for a controlled drug delivery, J. Am. Chem. Soc. 130 (2008) 6774–6780, https://doi.org/10.1021/ja710973k.

[4] K.M.L. Taylor-Pashow, J.D. Rocca, Z. Xie, S. Tran, W. Lin, Postsynthetic modifications of iron-carboxylate nanoscale metal-organic frameworks for imaging and drug delivery, J. Am. Chem. Soc. 131 (40) (2009) 14261–14263, https://doi.org/10.1021/ja906198y.

[5] J.A. Lemire, J.J. Harrison, R.J. Turner, Antimicrobial activity of metals: mechanisms, molecular targets, and applications, Nat. Rev. Microbiol. 11 (6) (2013) 371–385, https://doi.org/10.1038/nrmicro3028.

[6] A. Azam, A.S. Ahmed, M. Oves, M.S. Khan, S.S. Habib, A memic antimicrobial activity of metal oxide nanoparticles against Gram-positive and Gram-negative bacteria: a comparative study, Int. J. Nanomedicine 7 (2012) 6003–6009, https://doi.org/10.2147/IJN.S35347.

[7] A.T. George, S.K. Namasivayam, Raju S synthesis, characterization and antibacterial activity of chitosan stabilized nano zero-valent iron, BOPAMS 1 (1) (2013) 7–11.

[8] D. Beyersmann, A hartwig carcinogenic metal compounds: recent insight into molecular and cellular mechanisms, Arch. Toxicol. 82 (8) (2008) 493–512.

[9] U. Jungwrith, R.C. Kowol, B.K. Keppler, C.G. Hartinger, W. Berger, P heffeter anticancer activity of metal complexes: involvement of redox processes, Antioxid. Redox Signal 15 (4) (2011) 1085–1127, https://doi.org/10.1089/ars.2010.3663.

[10] S.J. Dougan, A. Habtemariam, S.E. McHale, S. Parsons, P.J. Sadler, Catalytic organometallic anticancer complexes, Proc. Natl Acad. Sci. USA 105 (33) (2008) 11628–11633, https://doi.org/10.1073/pnas.0800076105.

[11] B. Desoize, Metals and metal compounds in cancer treatment, Anticancer Res. 24 (3a) (2004) 1529–1544.

[12] A.U. Wijenayake, C.L. Abayasekara, H.M.T.G.A. Pitawala, B.M.R. Bandara, Antimicrobial potential of two traditional herbometallic drugs against certain pathogenic microbial species, BMC Complement. Altern. Med. 16 (2016) 365.

[13] X. Zhou, K. Zeng, Q. Wang, X. Yang, K. Wang, In vitro studies on dissolved substance of cinnabar: chemical species and biological properties, J. Ethnopharmacol. 131 (1) (2010) 196–202, https://doi.org/10.1016/j.jep.2010.06.018.

[14] T.N. Aung, Z. Qu, R.D. Kortschak, D.L. Adelson, Understanding the effectiveness of natural compound mixtures in cancer through their molecular mode of action, Int. J. Mol. Sci. 18 (3) (2017) 656, https://doi.org/10.3390/ijms18030656.

[15] M. Bhandari, A.S. Ravipati, N. Reddy, S.R. Koyyalamudi, Traditional ayurvedic medicines: pathway to develop anti-cancer drugs, J. Mol. Pharm. Org. Process Res. 3 (3) (2015) 130, https://doi.org/10.4172/2329-9053.1000130.

[16] F.M. Millimouno, J. Dong, L. Yang, J. Li, X. Li Targeting, Apoptosis pathways in cancer and perspectives with natural compounds from mother nature, Cancer Prev. Res. 7 (11) (2014) 1081–1107, https://doi.org/10.1158/1940-6207.

[17] M. Nafiujjaman, M. Nurunnabi, S.K. Saha, R. Jahan, Y.K. Lee, M rahmatullah anticancer activity of arkeshwara rasa – a herbometallic preparation, Ayur 36 (3) (2015) 346–350, https://doi.org/10.4103/0974-8520.182757.

[18] P. Chaudhary, N. Lamba, S.K. Balian, Analytical study of vanga bhasma International, Journal of Ayurvedic Medicine 5 (1) (2014) 82–90.

[19] R. Hiremath, C. Jha, K. Narang, Vanga bhasma and its XRD analysis, Ancient Science of Life 29 (4) (2010) 24–28.

[20] S.K. Singh, D.N. Gautam, M. Kumar, S.B. Rai, Synthesis characterization and histopathological study of lead based Indian traditional drug: naga bhasma, Indian J Pharm Sci 72 (1) (2010) 24e30.

[21] R.D. Umrani, D.S. Agrawal, K.M. Paknikar, Anti-diabetic activity and safety assessment of ayurvedic medicine, jasad bhasma (zinc ash) in rat, Indian J. Exp. Biol. 51 (2013) 811e22.

[22] P. Verma, C.M. Prasad, Standardization and bioavailability of ayurvedic drug lauha bhasma part II comparative bioavailability studies, Anc Sci Life 15 (1995) 140e5.

[23] M.L. Rajendraprasad, K. Shridhar, Study on vanga bhasma, Innovative pharmaceutical Sciences and Research 2 (5) (2014) 978–985.

[24] B. Kale, N. Rajurkar, Synthesis and Characterization of Vanga Bhasma, (2017), pp. 1–9.

[25] H. Baruah, R. Parveen, A.K. Chaudhary, Therapeutic uses of vanga bhasma: a critical review, Int J Res Ayurveda Pharma 5 (4) (2014) 566–570.

[26] S. Bardhan, K. Pal, S. Roy, S. Das, A. Chakraborty, P. Karmakar, R. Basu, S. Das, J. Nanosci. Nanotechnol. 9 (2019) 1–11, https://doi.org/10.1166/jnn.2019.16658.

[27] I. Bhaumik, K. Pal, U. Debnath, P. Karmakar, K. Jana, A.K. Misra, Natural product inspired allicin analogs as novel anti-cancer agents, Bioorg chem. 86 (2019) 259–272, https://doi.org/10.1016/j.bioorg.2019.01.057.

[28] K. Pal, D. Laha, P.K. Parida, S. Roy, S. Bardhan, A. Dutta, K. Jana, P. Karmakar, J. Nanosci. Nanotechnol. 18 (2018) 1–14, https://doi.org/10.1166/jnn.2018.16292.

[29] B. Ruidas, S.S. Chaudhury, K. Pal, P.K. Sarkar, C.D. Mukhopadhyay, A novel herbometallic nanodrug has the potential for antibacterial and anticancer activity through oxidative damage, Nanomedicine 14 (9) (2019) 1173–1189, https://doi.org/10.2217/nnm-2018-0187.

[30] K. Pal, S. Roy, P.K. Parida, A. Dutta, S. Bardhan, S. Das, K. Jana, P. Karmakar, Folic acid conjugated curcumin loaded biopolymeric gum acacia microsphere for triple negative breast cancer therapy in invitro and invivo model, Materials Science & Engineering C 95 (2019) 204, https://doi.org/10.1016/j.msec.2018.10.071.

[31] T. Manna, K. Pal, K. Jana, A.K. Misra, Anti-cancer potential of novel glycosylated 1,4-substituted triazolylchalcone derivatives, Bioorg. Med. Chem. Lett. 29 (19) (2019), https://doi.org/10.1016/j.bmcl.2019.08.019 126615.

[32] D. Bera, K. Pal, S. Bardhan, S. Roy, R. Parvin, P. Karmakar, P. Nandy, S. Das, Functionalised biomimetic hydroxyapatite NPs as potential agent against pathogenic multidrug-resistant bacteria, Adv. Nat. Sci.: Nanosci. Nanotechnol. 10 (4) (2019) 045017, https://doi.org/10.1088/2043-6254/ab5104.

[33] B. Das, S.K. Dash, D. Mandal, T. Ghosh, S. Chattopadhyay, S. Tripathy, S. Das, S.K. Dey, D. Das, S. Roy, Green synthesized silver nanopartcless destroy multi drug bacteria via reactive oxygen spacies mediated me,brane damage, Arab. J. Chem. 10 (6) (2015) DOI:org/j.arabjc.2015.08.008.

[34] M. Mar´ı, A. Morales, A. Colell, C. García-Ruiz, J.C. Fernández-Checa, Mitochondrial glutathione, a key survival antioxidant, Antioxid. Redox Signal 11 (11) (2009) 2685–2700, https://doi.org/10.1089/ARS.2009.2695.

[35] S.H. Jo, M.K. Son, H.J. Koh, S.M. Lee, I.H. Song, Y.O. Kim, Y.S. Lee, K.S. Jeong, W.B. Kim, J.W. Park, B.J. Song, T.L. Huh, Control of mitochondrial redox balance and cellular defense against oxidative damage by mitochondrial NADP + -dependent isocitrate dehydrogenase, J. Biol. Chem. 276 (19) (2001) 16168–16176, https://doi.org/10.1074/jbc.M010120200.

PHYTOFABRICATION OF SILVER NANO PARTICLES USING *OCIMUM SANCTUM* LEAF EXTRACT AND THEIR ANTIBACTERIAL AND ANTICANCER ACTIVITY THROUGH OXIDATIVE DAMAGE

Debbethi Bera [a,b], Kunal Pal [c,d], Parimal Karmakar [c], Sukhen Das [b], Papiya Nandy [a]*

*[a] Department of Physics, Jadavpur University
Kolkata-700032, India*
*[b]Centre for Interdisciplinary Research and Education
404B, Jodhpur Park, Kolkata-700068, India*
*[c]Department of Life Science and Biotechnology, Jadavpur University
Kolkata-700032, India*
*[d]Division of Molecular Medicine and Centre for Translational Research,
Bose Institute, Kolkata-700056, India*
.

Address for Correspondence: Papiya Nandy, pnandy00@gmail.com

Graphical Abstract	Abstract
Green synthesized AgNPs increase intracellular ROS generation in the cells ROS — Decrease bacterial cell viability Nucleus / ROS — Apoptosis of cancer cell	*The silver nanoparticles have found prominence in different fields such as medicine, catalysis, nanoelectronics, textile field, pollution and water treatment due to their unique attributes. Applications of silver nanoparticles are increasing rapidly in the medical purpose including drug delivery, treatment, diagnosis, medical device coating. Various chemical and physical methods are use to synthesize the silver nanoparticles (AgNP) conventionally. But these synthesis processes are expensive and also involves side effects. To solve these savior problems by modification in synthesis process for safer and more efficiency, Green Nanotechnology comes to play a very crucial role for synthesis of*
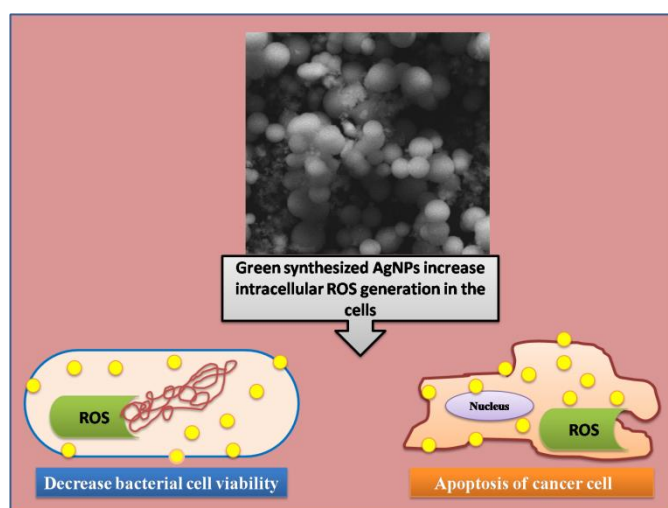
silver nanoparticles. Synthesis of biogenic silver nanoparticles from plant extract is referred as Green Nanotechnology. In this study, we have mentioned the green synthesis of silver nanoparticles using by Ocimum sanctum (Tulsi) leaf extract, which act as reducing agent as well as capping agent. Synthesized Ag nanoparticles were thoroughly characterized and their antibacterial and anticancer activities were observed. The development of brown color by the addition of Ocimum sanctum (Tulsi) signifies the formation of silver nanoparticles. UV-Vis absorption spectroscopy, XRD and zeta potential were applied to estimate the quantitative formation of silver nanoparticles. FTIR analysis was applied to reveal that the AgNPs were stabilized by eugenols, terpenes, and other aromatic compounds present in the extract. The antimicrobial and anticancer properties of AgNPs were assessed by various in vitro cellular assays. Our present study confirms that AgNP can be used as a dual therapeutic option for combating pathogenic microbial strains and hepatocellular cancer.

Introduction

Nanotechnology is the field for development of more consistent process for the synthesis of nanomaterials more than a range of size (with good monodispersity) and chemical composition [1]. Metallic nanoparticles have been gaining a lot of significance in the past few years due to their applicability in the field of physics, chemistry, medicine, biology and material science [2]. Metallic nanoparticles due to their high specific surface area and surface atoms have outstanding physicochemical characteristics, including optical, catalytic, electronic, magnetic and antibacterial properties. Synthesized metallic nanoparticles are enormous due to their influential applicability in various fields such as electronics, chemistry, energy, and medicine development [3]. Metallic nanoparticles, particularly noble metals are influential mainly because of their dominant optical absorption in the visible region caused by the exciting group of the free electron gas [4]. The silver nanoparticles have a wide range of interest as they have a larger number of apposite: nonlinear optics, spectrally selective coating for solar energy absorption, good electrical conductors, bio-labeling, antibacterial materials, intercalation materials for electrical batteries as optical receptors, chemically stable materials and catalyst in chemical reactions [5, 6] In the medical field, silver and silver nanoparticles have broad applications, especially in skin ointments and creams to avoid infection of burns and open wounds [10]. Silver possess an inhibitory action toward many bacterial strains and microorganisms commonly present in medical and industrial processes [7]. The general method of synthesizing silver nanoparticles in chemical reduction is as colloidal dispersions in water or organic solvents [8]. The green synthesis method is an imperative

technique, utilizes nontoxic chemicals, eco-friendly solvent and renewable materials [9] and has capability to reduce metal by specific metabolic pathway. Many biological approaches of green synthesis have been reported till date using plant leaf extracts from different plants [9, 10, 11]. These biosynthesized nanoparticles act as an antibacterial agent [12-18].

From ancient time leaves of *Ocimum sanctum* (Tulsi) is used as a remedy to cure stomachache, headache, diarrhea, dysentery, cough and cold, intestinal infections, etc. [19-24]. The leaves of the plant is aromatic, cooling, mucilaginous, diuretic and anti-inflammatory and used to treat digestive, carminative, spasmodic affections, vitiated conditions of inflammations well as a anticancer agent [25, 26, 27]. The major phytochemicals eugenol, β-caryophyllene, β-elemene, cyclopropylidene, carvacrol, linalool, germacrene, etc. present in *O. sanctum* plant are supposed to be responsible for bioreduction of silver metal ions followed by stabilization of the nanoparticles formed.

Here we have observed the effect of these biogenic AgNPs on the prokaryotic and eukaryotic cell. The phytofabricated AgNPs had a positive effect against Gram-positive (*S. aureus, B. subtilis*) and Gram-negative (*E. coli, P. aeruginosa*) pathogenic bacterial species. We have also studied the mechanism behind the bacterial growth inhibition. Our present experiments with biogenic AgNP, destruction of bacterial cell wall might have caused due to one or multiple steps of signaling cascades resulting in defective cell wall synthesis or impaired cross-linking of polymer units, which have occurred due to the ROS generation in both Gram-positive and Gram-negative bacterial strains [28, 29].

Silver ions have a great impact on altered cellular metabolism inhibiting proliferation and metastasis of cancer cells. Reactive oxygen species (ROS) generation plays a crucial role in the maintenance of the redox balance in most cancer cells and an elevated ROS level may promote oxidative damage leading to cellular abnormalities or death [30, 31]. In this study, we investigated (AgNPs) and their antimicrobial as well as anticancer activities against different pathogenic bacterial strains and hepatocellular cancer cell lines. Thus, the development of these phytofabricated, non hazardous, eco-friendly AgNPs has the potential to emerge as an effective dual therapeutic agent.

Materials and Methods

1. Materials

AR-grade silver nitrate (AgNO$_3$) was purchased from Sigma-Aldrich Chemicals and fresh *Ocimum sanctum* leaves were collected from local area Kolkata, India. All the chemicals and reagents required for bacterial culture media, MTT reagent, glutaraldehyde, fluorescence stains, different chemicals and reagents used for biological purposes were pruchased from Merck Ltd, and SRL Pvt. Ltd, Mumbai, India at the highest grade available. All the reagents were used without further purification. Deionised (Millipore) water was used throughout the experiment with resistivity at least 18 MΩ-cm. All the glass-wares used in our experiments were cleaned with aqua regia solution followed by rinsing with ultrapure water.

Bacterial strain and Cell line

Gram-positive (*Staphylococcus aureus* 740 and *Bacillus subtilis* 441) and Gram-negative (*Escherichia coli* 443 and *Pseudomona aeruginosa* 1688) used for the bacterial experiment were procured from Microbial Type Culture Collection (MTCC), IMTECH, Chandigarh, India.

Hep G2 are used for determine the cytotoxicity assay was obtained from Central Cell repository of National Center for Cell Science (NCCS), Pune, India.

2. Methods

Preparation of plant leaf extract

The leaves of *Ocimum sanctum* were washed by diionized water to remove the dust and dirt particles. The leaves are then dried at room temperature. About 2 grams of the dried powder leaves was taken in to the 100 ml distilled water. The leaves were boiled for 5 minutes and then it was allowed to cool. The solution was filtered and then stored at 4° C. All synthesis was performed within a week after preparation of leaf extract.

Preparation of Silver Nitrate Solution

1.0 mM AgNO$_3$ added in to distilled water and stirred continuously at 2 to 4 hours.

Synthesis of Silver Nanoparticles

150 ml of prepared silver nitrate stock solution was taken in a 250 ml beaker. After that, 10ml of leaf extract was added. At 90°C the mixture was heated in a water bath for 1hr.

Purification of Synthesized Particles

After heating, precipitation was obtained by centrifugation at 9000 rpm for 25 minutes. Then the precipitation was washed by centrifuged repeatedly (3 times). Thus purified Ag Nps was obtained.

Physical Characterisation of Silver Nanoparticle

The absorbance spectra were measured using Ultraviolet-visible spectrophotometer (Bio-tek) at a wavelength of 250-800 nm. Silver nano particles were synthesized by reducing silver metal ions solution with Tulsi leaf extract were initially characterized using UV-Visible Spectrophotometer. The XRD (X Ray Diffractometer) patterns of the silvernano particle samples were recorded by X-ray powder Diffractometer model D8, Bruker AXS, Winconsin, USA, using Cu-Kα target employing wavelength of 1.5418 Å and operating at 35 kV with scan speed of 2s/step. Particle size and its distribution were assessed with field emission Scanning Electron Microscope (FESEM) using ZEISS. Electron interacts with the electrons in the sample, producing various signals that can be detected and that contain information about surface topography and composition of the samples. The Fourier transform infrared spectroscopy (FTIR) study was done using FTIR-8400S, Shimadzu in the wavenumber range from 400 cm^{-1} to 4000 cm^{-1}. FTIR Spectrometer to detect the possible functional groups in biomolecules present in the plant extract. The particle size distribution and stability were measured by DLS (Dynamic light Scattering) using Zetasizer (NANO ZS90, Malvern Instruments Ltd., UK). The surface charges of the nanoparticles were also measured by the Zetasizer.

Antibacterial activity determination

(a)   Determination of minimum inhibitory concentration (MIC) and minimum bactericidal concentration (MBC)

According to our previously reported protocol [28, 29], MIC and MBC were evaluated by microdilution method in Luria broth. Different concentrations of AgNPs were added to the bacterial media containing the inoculums and incubated for 24 hrs. After incubation, the MIC values were obtained by checking the turbidity of the bacterial growth with UV absorption. The MBC values were determined by spreading the MIC dilutions of growth i.e. 10 μl of bacterial strain containing 2.5×10^5 CFU ml^{-1} bacteria were separately added to the several 1 ml nutrient broths (NBs) onto agar plates and incubating them for 24 hrs at 37° C. The lowest concentration of AgNPs, at which the bacterial strains were completely inhibited, was noted as the MBC value. This MBC value of the particles denotes the minimum

concentration of particles required for 100% bacterial killing compared to the positive control (no treatment). All assays were performed in a laminar air flow.

(b)   Tolerance level

The tolerance levels of each bacterial strain against AgNP were determined by using the following formula [28, 30].

$$\text{Tolerance} = (MBC)/ (MIC) \ldots\ldots\ldots \qquad (1)$$

(c)   Agar well diffusion method

The susceptibility of pathogenic bacteria to AgNP was examined according to a previously reported protocol by the Agar well diffusion method. The pathogenic strains were grown on LB Broth at 37°C overnight till a turbidity of 0.5 Mac Farland standards (10^8 CFU per ml). About 50µl of this suspension was used to inoculate 90mm diameter petridish filled with 30ml of Mueller Hinton Agar. Wells (diameter^2= $0.563cm^2$) were punched in the agar plates and treated with AgNPs at their MBC concentrations. The zone of inhibition diameter in the bacterial growth surrounding the disc (including the disc) was measured [28, 30].

(d)   Bacterial cell-viability assay

The viability of bacterial cells was analysed with help of 3-(4, 5-dimethylthiazol-2-yl) -2, 5-diphenyltetrazolium bromide (MTT) following a standard protocol [28]. Cell viability was determined after exposure to different concentrations of AgNPs for 24 hrs at 37° C. After incubation, the bacterial cells were collected and centrifuged at 1400 rpm for 10 mins at 4° C then washed three times with sterile phosphate buffered saline (PBS, pH 7.4). Subsequently, the medium was replaced with fresh culture media containing 0.5 mg.ml^{-1} of MTT reagent and incubated for 3 hrs at 37° C. Then, HCl-isopropanol solution was added and after 15 mins of incubation at room temperature, absorbance of solubilized MTT formazan product was measured spectrophotometrically at 570 nm in a Shimadzu UV–Vis 1800 spectrophotometer.

(e)   ROS generation in Bacterial cell

The bacterial intracellular ROS generation was measured by using 2, 7-dichlorofluorescein diacetate (DCFH$_2$-DA) according to our previously reported protocol [29]. The DCFH$_2$-DA passively enters the cells, reacts with the generated ROS and oxidizes as well as forming a highly fluorescent compound: 2, 7-dichlorofluorescein (DCF). After the exposure of bacteria cells with AgNPs, they were then cultured overnight and washed with PBS solutions. Then, the cells were incubated with the required amount of DCFH$_2$-DA at 37° C for 30 mins. Finally, the bacteria cells were visualized under fluorescence microscope.

Anticancer Activity Determination

(a) Cytotoxicity assay

The viability of Hep G2 cells after exposure to various concentrations of AgNP was determined by 3-(4, 5-dimethylthiazol-2-yl)-2,5-diphenyltetrazolium bromide (MTT) assay [31, 32, 33]. Briefly, around 1×10^4 cells per well of 96-well plates were exposed to AgNPs at the concentrations of untreated as control, 20, 40, 60, 80, 100 µg/ml for 24 hrs of incubation at 37° C and 5% CO$_2$. Following this, the cells were incubated again with 10 µl MTT solution (stock 1 mg/ml) for 4 h at 37°C and 5% CO$_2$ following a wash with 1× phosphate-buffered saline (PBS), and the resulting formazan crystals were dissolved in

MTT solubilization buffer to measure the absorbance at 570 nm by using a microplate reader (Biorad). The data were formulated comparing with the control ones.

(b)   Intracellular ROS generations were checked by DCFDA method in Hep G2 cells

Normally, the DCFDA enters the cell and reacts with the reactive oxygen to give a green fluorescent color compound dichlorofluorescein (DCF). Briefly, a stock solution of DCFDA (10mM) was prepared in methanol and was further diluted with PBS to a working concentration of 100μM. Hep G2 cells were treated with AgNP at LD_{50} for 12hrs at 37°C, and washed with ice-cold 1× PBS followed by an incubation with 100μM of DCFDA for 30mins in the dark at 37°C [32, 33]. The fluorescence intensity was measured both spectroscopically (Hitachi, Japan) and under a fluorescence microscope in Hep G2 cells (Leica, Japan) at excitation and emission wavelengths of 485 nm and 520 nm respectively.

Results and Discussion

X-ray diffraction (XRD)

The crystalline character of these sythesized nanoparticles was confirmed by X-ray crystallography. The XRD pattern of AgNPs is given in Fig 1a. The pattern clearly shows the main peaks at (2θ) 38.19 and 44.37 corresponding to the (111) and (200) planes, respectively. By comparing with JCPDS (file no: 89-3722), the typical pattern of green-synthesized AgNPs is found to possess a prominent structure. The average crystalline size of the silver nanoparticles was estimated using (Eq. 2), the Debye–Scherrer's equation

$$D=0.9λ/β \cosθ………………………….. (2)$$

    By calculating the width of (111) Bragg's reflection, we evaluate average size of the particle is 14 nm. In addition, three unassigned peaks appeared at 27.78^o, 32.34^o and 46.29^o. These peaks were weaker than those of silver. This may be due to the bioorganic compounds occurring on the surface of the AgNPs.

Fourier Transform Infrared Spectroscopy (FTIR)

FTIR experiment was carried out in order to identify the presence of various functional groups in biomolecules responsible for the bioreduction of Ag and capping/stabilization silver nanoparticles. The obtained intense bands were compared with standard values to identify the functional groups as in Figure 2b. The bands at 3422 cm^{-1} in the spectra corresponds to O–H stretching vibration indicating the presence of alcohol and phenol group. Bands at 2921 cm^{-1} region arising from C–H stretching of aromatic compound were observed. The band at 1631 cm^{-1} assigned to C–N and C–C stretching indicating the presence of proteins. The band at 1450 cm^{-1} was assigned for N–H stretch vibration present in the amide linkages of the proteins. These functional groups have role in stability/capping of AgNP as reported in other studies. The bands at 1450 cm^{-1} were corresponds to N–H and C–N (amines) stretch vibration of the proteins respectively. The band at 1377 cm^{-1} exemplifies the N- O symmetry stretching typical of the nitro group.

The strong bands at 1074 cm^{-1} are corresponds to ether linkages and suggest the presence of flavanones adsorbed on the surface of synthesized metal nanoparticles. The immediate reduction and capping of silver ion into silver nanoparticles in this analysis might be due to flavanoids and proteins. The flavonoids present in the leaf extract are powerful reducing agents which may be actively involved and responsible for the reduction of Ag$^+$ to Ag^0.
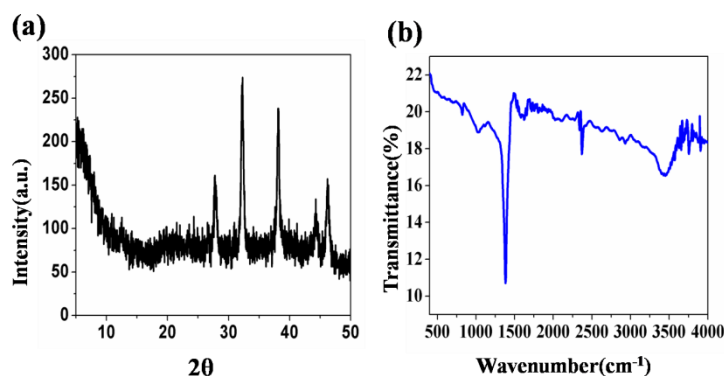
Figure.1.(a) XRD analysis of silver nanoparticles and (b) FTIR spectra

UV-Visible absorption studies

The synthesized AgNPs in aqueous solution was monitored to obtain the absorption spectra at a wavelength range of 250-800 nm as shown in Figure.2a. It was observed that solution of silver nitrate turned dark brown on addition of leaves extract; it indicated the formation of AgNPs, while no color change was observed in the absence of plant extract. In the UV Vis spectrum; a single, strong and broad Surface plasmon resonance (SPR) peak was observed at 450 nm that assign the synthesis of AgNPs. Particle size distribution and surface charge measurement

Size Determination of Silver Nanoparticle

Size distribution of the AgNPs was determined by DLS (Figure.2b). Particle size distribution curve reveals that AgNPs obtained are polydispersed in nature having a P.D.I (Polydispersive Index) of 0.231 with average diameter ∼100 nm. The low P.D.I value indicates that the solution is homogenous in nature which is ideal for biological applications. The silver nanoparticles had quite high negative zeta potential which indicates the stability of the particles in aqueous solution. The details are given in the table below.
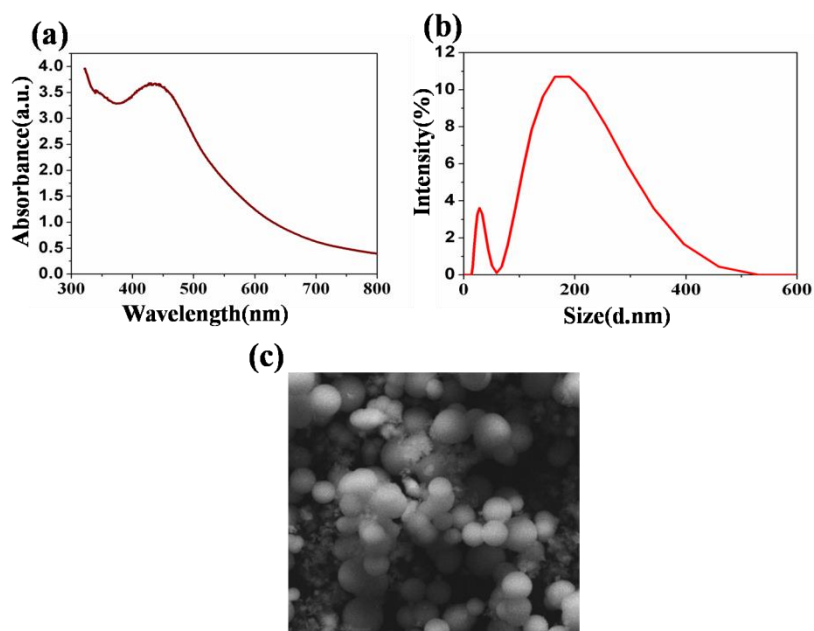
Figure.2.(a) UV-Vis spectra, (b) hydrodynamic size distribution study by DLS and (c)FESEM analysis of silver nanoparticles.

SAMPLE NAME	DLS SIZE (d.nm)	PDI	ZETA POTENTIAL (mV)
AgNP	101.8	0.231	-21.4

Table.1. Hydrodynamic Size Distribution

Field Emission Scanning Electron Microscope (FESEM) analysis

The FESEM images of the silver nanoparticles are shown in Figure.2c. The surface morphology of silver nanoparticles showed rod AgNP structure. In the present study, the particle size ranges from 25 to 100 nm.

Biosynthesized AgNP nanoparticles exhibits significant antibacterial activity against pathogenic bacterial strains

(a) **Determination of minimum inhibitory concentration (MIC) and minimum bactericidal concentration (MBC)**

To evaluate the bactericidal activity of the synthesized AgNPs have been treated separately against Gram negative *E.coli, P.aeruginosa* and *Gram positive S.aureus, B.subtilis.* In the case of *E.coli, P.aeruginosa* strains the MIC values of AgNP was 38.46 ± 1.2 µg/ml, 44.65 ± 2.2 µg/ml and that in case of *S.aureus,*

B.subtilis the MIC value was 35.54 ± 1.43µg/ml, 41.3 ± 2.83 µg/ml respectively as shown in Figure.3. All bacterial strains were grown with the MIC dilutions on the sterile agar plates to obtain the MBC [28, 29]. The MBC concentrations are noted where complete bacteria growth was inhibited on the agar plate after treatment with AgNPs. The MBC values of AgNP were at 135 ± 3.2 µg/ml, 143 ± 4.2 µg/ml, 132 ± 1.8 µg/ml, 140 ± 3.7µg/ml in case of *E. coli, P. aeruginosa, S. aureus, B. subtilis* bacterial strains respectively. Bacterial growth decreases with an increase in the concentration of AgNP. In the microdilution method, these may be inhibited due to the easy penetration of AgNP into the cells followed by bacteriostatic in different bacterial strains.
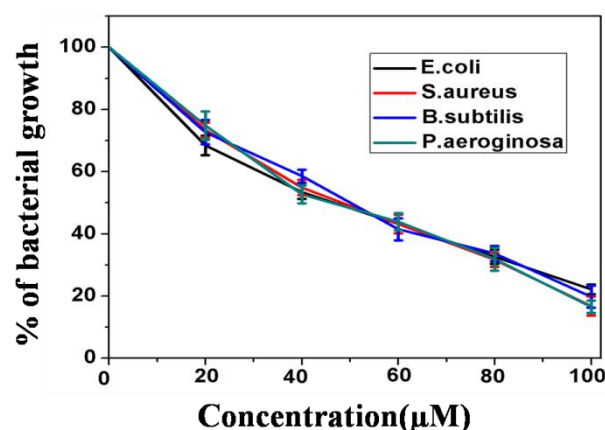

Figure.3. Analysis of activity of AgNPs by MIC method in pathogenic strains

(b)   *Phytofabricated AgNPs show excellent bactericidal activity*

The tolerance level of pathogenic strains against AgNP was evaluted from the respective MIC and MBC values. From these result, it is measured that the tolerance level to AgNP was 3.5, 3.2 in case of *E. coli, P. aeruginosa* and 3.7, 3.4 in case of *S. aureus, B. subtilis* respectively. The implication of the tolerance level is the difference between bactericidal agents from bacteriostatic agents. Bactericidal agents always kill microbes, but bacteriostatic agents inhibit the growth. When the MBC/MIC ratio is greater than or equal to 16 for particular bacteria, the antibacterial agents are considered as bacteriostatic type and when this ratio is less than or equal to 4, then the particles are considered as a bactericidal agent [28].Thus, the MBC/MIC ratio is an important parameter which reflects the bactericidal capacity of the AgNP. In this study, AgNP exhibits significant bactericidal activity against *E. coli, S. aureus, P. aeruginosa, B. subtilis* pathogenic strains.

(c)   *Selective bactericidal activity of AgNP confirmed by Disc diffusion method*

This experiment was performed to observe the comparison of antibacterial activity of different AgNP samples. The zone of inhibitions of Gram-positive and Gram negative are given in Figure 4. Zone of inhibition having a diameter is significant when strain is treated with AgNP at their MBC concentration. So, from this study, it has become clear that the AgNP has really proved to be beneficial and needs to be administered for pathogenic *E.coli, S.aureus, B.subtilis, P.aeruginosa* growth inhibition.
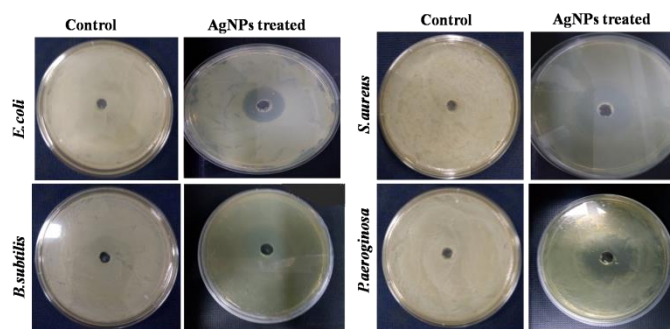
Figure.4. Antibacterial assaessment of biogenic silver nanoparticles in pathogenic strains by disc agar diffusion method.

(d)   Treatment of E.coli, S.aureus, B.subtilis, P.aeruginosa with AgNP significantly diminishes the bacterial cell viability

AgNP is responsible for diminishing the bacterial cell survivability at their respective MBC conc. as depicted in Figure.5. This may be due to the ingression of AgNPs into the bacterial cells that can hinder the growth of the bacteria and acts as an ideal bactericidal agent.
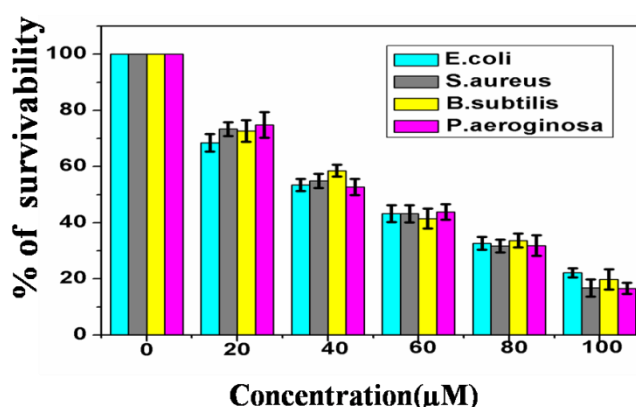

Figure.5. Bacterial viability study upon treatment with AgNPs in pathogenic bacterial strains

(e)   Mechanisms behind bactericidal activity of functionalized AgNPs

The phytofabricated AgNPs had the capability to induce intracellular ROS generation which in turn culminates in the bacterial cell death. In order to envisage the mechanisms behind the bactericidal activities of AgNPs, the intracellular ROS generation in the bacterial cells was determined by employing DCFH-DA as an intracellular ROS indicator which is depicted in Figure.6. The results indicate that the AgNP treated pathogenic bacterial cells augment the generation of ROS which is responsible for bacterial cell death. The enhanced ROS production is correlated with bacterial cell death. The intracellular ROS production contributes to the bacterial cell membrane damage, disruption in the electronic transport chain and the genetic material detonation [29, 30].
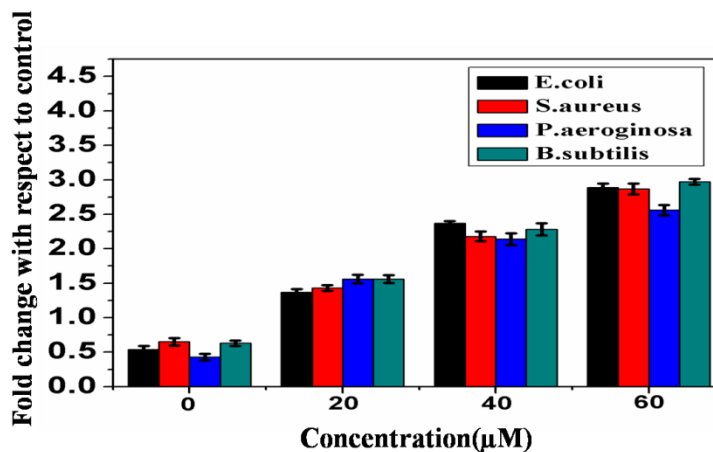
Figure. 6. Intracellular ROS generation by treatment with AgNPs in pathogenic bacterial strains.

Anticancer activity of AgNPs

(a)   Cytotoxicity of AgNPs

The in vitro cytotoxicity of the AgNPs is evaluated for determining the cytotoxic effects on HepG2 cell line. The cells were exposed to different concentrations of AgNPs (0-120 µg/ml) for a time span of 24hrs and was afterwards followed by MTT assay. It was observed that the AgNPs depicted a dose dependent decrease in the cell survivability. The LD_{50} of AgNP was calculated to be 46 ± 3.2 µM. Thus we can conclude that the synthesized phytofabricated AgNPs could exert encouraging anticancer activity as exhibited in Figure.7.
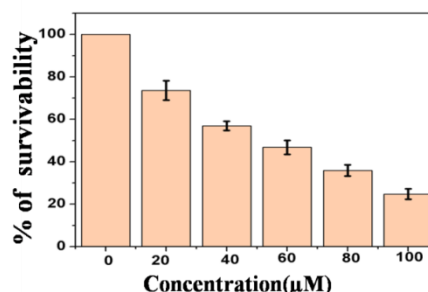
Figure. 7. Cell viability assay of HAP in human hepatocellular carcinoma, HepG2

(b)   Intracellular Reactive oxygen species generation induced by treatment of AgNP

The Reactive oxygen species (ROS) is analysed with the the dual aid of fluorescence microscopy and Spectro fluorometer by employing 2′, 7′ dichlorofluorscence in diacetate (DCF-DA) as a probe. The generation of reactive oxygen species is evaluated in case of hepatocellular carcinoma cells, Hep G2 with AgNPs at concentrations of 80 µM and 100 µM for 12hrs. The fluorescence microscopic images

clearly depicts that the enhancement of green color fluorescent intensity occurred in case of treated HepG2 cell lines after 12hrs (Figure. 8a and 8b).

Figure.8. Intracellular ROS generation by treatment with AgNPs in HepG2 cells observed by (a) spectrofluometry and (b) fluorescence microscopy

Conclusions

The synthesis of phytofabricated silver nanoparticle is inexpensive, non toxic and ecofriendly. The AgNPs were thoroughly charecterised with the UV-Vis, FTIR, XRD, DLS and FESEM. The results from UV–Vis spectral studies testified the prese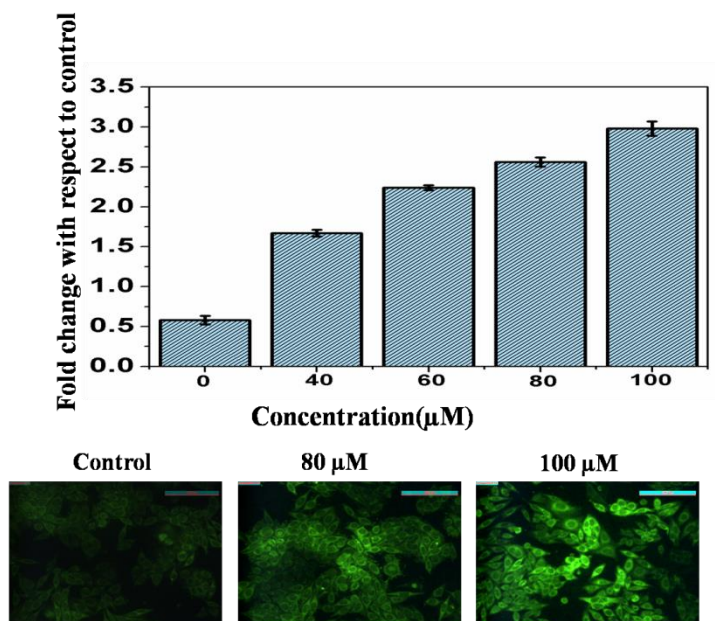nce of surface plasmon resonance of these biogenic silver nanoparticles. The biomolecules predominant in the *O. sanctum* leaves were primarily responsible for reducing and capping of AgNPs which were then analysed by FTIR measurements. Particle size and stabilization were determined with the aid of DLS and zeta potential techniques. FESEM studies depicted the formation of rod and uniform shaped silver nanoparticles with a size range of 25-100 nm. The XRD pattern additionally confirmed the development of the silver nanoparticles via the eco-friendly green synthetic route.

Although there has been significant progress in cancer diagnosis and treatment, cancer is still posing   a worldwide grave threat. On the other hand, the global dissemination of pathogenic bacterial strains has emerged as a serious cotemporary challenges with respect to public health. Our results clearly depicts that the biogenic AgNPs are responsible for initiating the oxidative damage through augmented ROS generations both in case of prokaryotic and eukaryotic cells. The generated reactive oxygen or superoxide has the potential to directly interact with the cell metabolism in order to generate the hydroxyl radicals, which is responsible for damaging the DNA, lipid and proteins. Our results clearly suggest that these phytofabricated AgNPs can be considered as potential antibacterial agent against Gram-positive (*S. aureus, B. subtilis*) and Gram-negative (*E. coli, P. aeruginosa*) pathogenic bacterial strains.

In the present study with AgNPs, the probable reason behind the bacterial cell wall destruction might be the disruption in the steps of signaling cascades that leads to the defective cell wall synthesis. This phenomenon takes place due to the enhanced ROS generation in both Gram-positive and Gram-negative bacterial strains. Additionally, the phytofabricated leads to the death of human liver cancer due to enhanced intracellular ROS. In conclusion, our studies suggest that our phytofabricated AgNPs can emerge as potential anticancer and antibacterial agents.

References

1. M. Rai, A. Gade, A. Yadav, Biogenic nanoparticles: an introduction to what they are, how they are synthesized and their applications. In: Rai M, Duran N (eds), *Metal nanoparticles in microbiology* pp 1–16 (2011).
2. K. Yokohama, D.R. Welchons The conjugation of amyloid beta protein on the gold colloidal nanoparticles surfaces, *Nanotechnology* **18**:105101–105107 (2007).
3. A. Saxena, R.M. Tripathi, F. Zafar, P. Singh, Green synthesis of silver Nanoparticles using aqueous solution of *Ficus benghalensis* leaf extract and characterization of their antibacterial activity, *Mater Lett*. **67** 91–94 (2012).
4. M.B. Mohamed, V. Volkov, S. Link, M.A.E. Sayed, The 'lightning' gold nanorods: fluorescence enhancement of over a million compared to the gold metal, *Chem Phy Lett.* **317** 517–523 (2000).
5. M. Zargar, S. Shameli, N. G. Reza, F. Farahani, Plant mediated green biosynthesis of silver nanoparticles using *Vitex negundo* L. extract. *J Ind Eng Chem*. **20(6)** 4169–4175 (2014).
6. H. Jiang, S. Manolache, A.C.L. Wong, F.S. Denes, Plasma enhanced deposition of silver nanoparticles onto polymer and metal surfaces for the generation of antimicrobial characteristics, *J Appl Polym Sci*. **93** 1411–1422 (2004).
7. V.K. Sharma, R.A. Yngard, Y. Liny, Silver nanoparticles; green synthesis and their antimicrobial activities, *Adv Coll Interface Sci.* **145** 83–96 (2009).
8. P. Raveendran, J. Fu, S.L. Wallen, Completely green synthesis and stabilization of metal nanoparticles *J Am Chem Soc*. **125** 13940–13941(2003).
9. S.A. kumar, S. Ravi, V. Kathiravan, S. Velmurugan, Synthesis, characterization and catalytic activity of silver nanoparticles using *Tribulus terrestris* leaf extract, *Spectrochimica Acta Part A: Molecular and Biomolecular Spectroscopy* **121** 88-93 (2014).
10. S.P. Chandran, M. Chaudhary, R. Pasricha, A. Ahmed, M. Sastry, Synthesis of gold nanotriangles and silver nanoparticles using *Aloe vera* plant extract, *Biotechnology Progress*, **22** 577-583 (2006).
11. S.P. Dubey, M. Lahtinen, M. Sillanpaa, Tansy fruit mediated greener synthesis of silver and gold nanoparticles, *Process Biochemistry* **45** 1065-1071(2010).
12. R.N. Rati, P. Nilotpala, B. Debadhyan, M.P. Kshyama, M. Srabani, B.S. Lala, B.K. Mishra, Green synthesis of silver nanoparticle by Penicillium purpurogenum NPMF: the process and Optimization, *Journal of Nanoparticles Research* **13** 3129-3137 (2011).
13. N. Duran, P.D. Marcarto, G.I.H. DeSouza, O.L. Alves, E. Esposito, Antibacterial effect of silver nanoparticles produced by fungal process on textile fabrics and their effluent treatment, *Journal of biomedical nanotechnology* **3** 203-208 (2007).
14. S. Edgar, S. Sofia, M. Sonia, J. Correia, PVP coated silver nanoparticles showing antifungal improved activity against Dermatophytes, *Journal of nanoparticles research* **16** 2726 (2014).
15. A.M. Fayaz, K. Balaji, M. Girilal, R. Yadav, P.T. Kalaichelvan, R. Venketesan, Biogenic synthesis of silver nanoparticles and their synergistic effect with antibiotics: a study against gram-positive and gram-negative bacteria, *Nanomedicine: Nanotechnology, Biology and medicine* **6** 103-109 (2010).
16. Q.L. Feng, J. Wu, G.Q. Chen, F.Z. Cui, T.N. Kim, J.O. Kim, A mechanistic study of the antibacterial effect of silver ions on *Escherichia coli* and *Staphylococcus aureus*, *Journal of Biomedical Materials Research* **52** 662-668 (2001).
17. S. Ghosh, S. Patil, M. Ahire, R. Kitture, S. Kale, K. Pardesi, S.S. Cameotra, J. Bellare, D.D. Dhavale, A. Jabgunde, B.A. Chopade, Synthesis of silver nanoparticles using *Dioscorea bulbifera* tuber extract and evaluation of its synergistic potential in combination with antimicrobial agents, *International journal of Nanomedicine* **7** 483-496 (2012).
18. S. Kaviya, J. Santhanalakshmi, B. Viswanathan, J. Muthumar, K. Srinivasan, Biosynthesis of silver nanoparticles using citrus sinensis peel extract and its antibacterial activity, *Spectrochimica Acta Part A: Molecular and Biomolecular Spectroscopy*, **79** 594-598 (2011).
19. N. Singh, Y. Hoette, R. Miller, Tulsi: The Mother Medicine of Nature. 2nd ed. Lucknow: *International Institute of Herbal Medicine* pp. 28–47 (2010).
20. N. Mahajan, S. Rawal, M. Verma, M. Poddar, S. Alok, A phytopharmacological overview on *Ocimum* species with special emphasis on *Ocimum sanctum*, *Biomed Prev Nutr.* **3** 185–92 (2013).

21. L. Mohan, M.V. Amberkar, M. Kumari, *Ocimum sanctum* linn. (TULSI)- an overview, *Int J Pharm Sci Rev Res*. **7** 51-3(2011).
22. P. Pattanayak, P. Behera, D. Das, S.K. Panda, *Ocimum sanctum* Linn. A reservoir plant for therapeutic applications: An overview, *Pharmacogn Rev*. **4** 95–105 (2010).
23. M.M. Cohen, Tulsi - *Ocimum sanctum*: A herb for all reasons, J Ayurveda Integr Med. **5(4)** 251–259 (2014).
24. S. Mondal, B.R. Mirdha, S.C. Mahapatra, The science behind sacredness of Tulsi (*Ocimum sanctum* Linn.) *Indian J Physiol Pharmacol*. **53** 291–306 (2009).
25. W. Wangcharoen, W. Morasuk, Antioxidant capacity and phenolic content of holy basil Songklanakarin, *J Sci Technol*. **29** 1407–15 (2007).
26. V.S. Panda, S.R. Naik, Evaluation of cardioprotective activity of Ginkgo biloba and *Ocimum sanctum* in rodents, *Altern Med Rev*. **14** 161–71 (2009).
27. M. Shivananjappa, M. Joshi, Aqueous extract of *tulsi* (*Ocimum sanctum*) enhances endogenous antioxidant defenses of human hepatoma cell line (HepG2) *J Herbs Spices Med Plants* **18** 331–48 (2012).
28. Bera D, Pal K, Bardhan S, Roy S, Parvin R, Karmakar P, Nandy P, Das Sukhen 2019 Functionalised biomimetic hydroxylapatite NPs as potential agent against pathogenic multidrug- resistant bacteria Advances in Natural Sciences: Nanoscience and Nanotechnology **10** 045017
29. S. Bardhan, K. Pal, S. Roy, S. Das, A. Chakraborty, P. Karmakar, R. Basu, S. Das, Nanoparticle size-depandent antibacterial activities in natural minaerals, *Journal of Nanoscience and Nanotechnology* doi: 10.1166/jnn.2019.16658
30. S.P. Chakraborty, S.K. Sahu, S.K. Mahapatra, S. Santra, M. Bal, S. Roy, P. Pramanik, Nanoconjugated vancomycin: new opportunities for the development of anti-VRSA agents, *Nanotechnology* **21** 105103–11 (2010).
31. J. Mandal, P. Ghorai, K. Pal, P. Karmakar, A. Saha, 2-hydroxy-5-methylisophthalaldehyde based fluorescent-colorimetric chemsensor for dual detection of Zn Cu^{2+} with high sensitivity and application in live cell imaging, *Journal of Luminescence* **205** 14–22 (2019).
32. K. Pal, S. Roy, P.K. Parida, A. Dutta, S. Bardhan, S. Das, K. Jana, P. Karmakar, Folic acid conjugated curcumin loaded biopolymeric gum acacia microshere for triple negative breast cancer therapy in invitro and invivo model, *Materials Science & Engineering C* **95** 204-216 (2019).
33. K. Pal, D. Laha, P.K. Parida, S. Roy, S. Bardhan, A. Dutta, K. Jana, P. Karmakar, An in vivo study for targeted delivery of curcumin in Human triple negative breast carcinoma cells using biocompatible PLGA microspheres conjugated with folic acid, *Journal of Nanoscience and Nanotechnology* **19** 3720-3733 (2019).

Certificate
OF RECOGNITION

EuroSciCon and the Editors of Journal of Single cell Biology
wish to thank

Ms. *Debbethi Bera*

Jadavpur University, India

for her phenomenal and worthy oral presentation on

"Phytofabrication of biomimetic nanoparticle as a potential dual therapeutic agent"

at the "6th Annual Congress on Plant Science and Biology

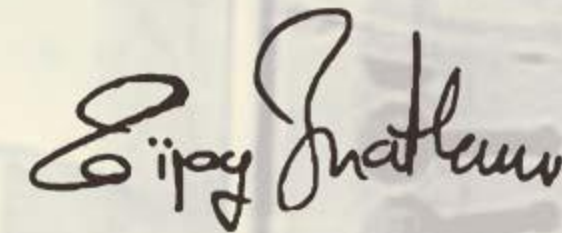held during November 09-10, 2020 in Webinar

The award has been attributed in recognition of research paper quality, novelty and significance.

Andrea Wilson
Andrea Wilson
Program Manager

"आत्मनिर्भरभारताय विश्वकल्याणाय च विज्ञानम्"
Science for Self-Reliant India and Global Welfare

MINISTRY OF SCIENCE AND TECHNOLOGY
MINISTRY OF EARTH SCIENCES
MINISTRY OF HEALTH & FAMILY WELFARE
GOVERNMENT OF INDIA

INDIA INTERNATIONAL SCIENCE FESTIVAL 2020

Certificate of Participation and Oral Presentation

This is to certify that Prof./Dr./Mrs./Mr./Ms. **DEBBETHI BERA** of

JADAVPUR UNIVERSITY has participated and delivered

an oral presentation entitled "**PHYTOFABRICATION OF BIOMMETIC NANOPARTICLES AS A POTENTIAL**

DUAL THERAPEUTIC AGENT "

under the theme " **FRONTIERS AREA OF RESEARCH - LIFE SCIENCES** " in the **Young**

Scientists' Conference organized during **22-12-2020** to **24-12-2020** as a part of **India**

International Science Festival- 2020 by the Ministry of Science and Technology, Ministry of

Earth Sciences, and Ministry of Health and Family Welfare, Govt. of India in collaboration

with Vijnana Bharati (VIBHA).

Dr. Shekhar C. Mande
DG, CSIR & Secretary, DSIR

Dr. Vijay P. Bhatkar
President, Vijnana Bharati

"आत्मनिर्भरभारताय विश्वकल्याणाय च विज्ञानम्"
Science for Self-Reliant India and Global Welfare

MINISTRY OF SCIENCE AND TECHNOLOGY
MINISTRY OF EARTH SCIENCES
MINISTRY OF HEALTH & FAMILY WELFARE
GOVERNMENT OF INDIA

INDIA INTERNATIONAL SCIENCE FESTIVAL 2020

SCIENCE FOR SELF-RELIANT INDIA AND GLOBAL WELFARE

Certificate of Participation

This is to certify that

SMT DEBBETHI BERA

from _____ - _____ has successfully participated in

Young Scientists Conference (YSC) conducted from **22-12-2020** to **25-12-2020**, as part of

INDIA INTERNATIONAL SCIENCE FESTIVAL 2020 (IISF 2020)

organised by Ministry of Science and Technology; Ministry of Earth Sciences,

and Ministry of Health and Family Welfare, Govt. of India

in collaboration with Vijnana Bharati (VIBHA)

by Council of Scientific & Industrial Research (CSIR).

Dr. Shekhar C. Mande
Director General, CSIR

Dr. Vijay P. Bhatkar
President, Vijnana Bharati

ONE DAY SEMINAR
ON
Recent Trend in Frontier Research in Physics

Organised By :

Department of Physics, Jadavpur University, Kolkata

CERTIFICATE OF PARTICIPATION

This is to certify that Mr/Mrs/Dr/Prof. *Debbethi Bera*

has participated/presented (oral/poster) a paper entitled *Synthesis of Dual Therapeutic Material:*

Antibacteria and Anticancer .... In the one day seminar

on "Recent trend in Frontier research in Physics" on 6th March, 2018 held at Department of Physics, Jadavpur

University, Kolkata-700 032.

Dr. Sanat Karmakar
Dr. Soumen Mondal
Dr. Abhijit Samanta
Dr. Subrata Sarkar
(Conveners)

Prof. Debasish Lohar
Head, Department of Physics
Jadavpur University

Materials Research Society of India (MRSI)
(Kolkata Chapter)

Certificate of Participation

This is to certify that **Debbethi Bera** of **Jadavpur University** (JU) has participated at the

"Young Scientists' Colloquium 2022"

Organised by

Materials Research Society of India (MRSI), Kolkata Chapter
On Friday, December 16, 2022
at CSIR-Central Glass and Ceramic Research Institute, Kolkata

Dr. Jui Chakraborty
Secretary, MRSI, Kolkata

Dr. Mrinal Pal
Chairman, YSC 2022

Prof. N. R. Bandyopadhyay
Chairman, MRSI, Kolkata

DST-SERB Sponsored

One Day Workshop on Material Synthesis & Characterization Techniques

Organized by: Department of Physics, Jadavpur University, Kolkata-700032

Certificate of Presentation

This Certificate is awarded to

Mr./ Ms. Debbethi Bera .... *for successfully presenting a paper entitled* .. Anti-Bacterial Application .... *in the Workshop organized by Department of Physics, Jadavpur University, Kolkata on 29th February 2020.*

29/02/2020

Head, Department of Physics, Jadavpur University

Professor and Head
Department of Physics
Jadavpur University
Kolkata – 700 032

National Seminar on
New Directions in Physical Sciences 2020 (NDPS 2020)

Organised by

Department of Physics, Jadavpur University
In association with
Indian Photobiology Society

Certificate of Participation

This is to certify that Prof./Dr./Mr./Ms. _____ Debdatti Bera _____ of

_____ Department of Physics, Jadavpur University _____ has participated/ presented a poster entitled

_____ Highly Fluorescent Carbon Nanoparticle : An Emerging Bioimaging Intervention at the

seminar on 'New Directions in Physical Sciences 2020' at Jadavpur University, Kolkata on February 25, 2020.

25/2/2020

Dr. Soumen Mondal
Convener, NDPS 2020

Prof. Mitali Mondal
Convener, NDPS 2020

25/02/2020

Prof. Sukhen Das
Head, Dept. of Physics

RESEARCH INNOVATION SCIENCE EMPOWERING NATION

INDIA INTERNATIONAL SCIENCE FESTIVAL 2019

CERTIFICATE OF PARTICIPATION

THIS IS TO CERTIFY THAT

PROF./DR./MRS./MR./MS./ ___ *Debbethi Bera*

HAS ACTIVELY PARTICIPATED IN THE **YOUNG SCIENTISTS' CONFERENCE**
AS A PART OF "INDIA INTERNATIONAL SCIENCE FESTIVAL – 2019" HELD AT
BISWA BANGLA CONVENTION CENTRE, KOLKATA DURING NOVEMBER 5-8, 2019.

SHE/HE HAS ALSO PRESENTED A PAPER ON THE THEME

Frontier areas of Research

TITLED

Functionalised biomimetic Hydroxyapatite NPs as a smart material against pathogenic multidrug-resistant bacteria

PROF. ASHUTOSH SHARMA
SECRETARY, DST

DR. VIJAY BHATKAR
PRESIDENT, VIJNANA BHARATI

CIRE

CENTRE FOR INTERDISCIPLINARY RESEARCH AND EDUCATION

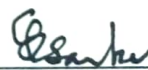404B, Jodhpur Park, Kolkata – 700068

25th March, 2017

CERTIFICATE OF PARTICIPATION

This is to certify that

Debbethi Bera

has contributed through Lecture / Oral Presentation / Poster Presentation / Participation to the success

of the One Day National Symposium on Nanotechnology:

From Materials to Medicine and their Social Impact held on 25th March, 2017

at Birla Industrial and Technological Museum, Kolkata.

Prof Sanjib Sarkar
President, CIRE

UGC-SAP (DRS II)-Sponsored National Symposium on
Modern Perspectives of Research & Development in Biochemistry & Biophysics (MPRDBB)

14th & 15th March 2019
Organized by

Department of Biochemistry & Biophysics, University of Kalyani

This is to certify that Prof./Dr./Mr./Mrs./Ms. Debbethi Bera

participated in the UGC-SAP (DRS II)-sponsored National Symposium on **MPRDBB**, as

Invited Speaker/for presenting a paper (Oral /Poster)/Organizer/participant held on

14th & 15th March 2019 at the Department of Biochemistry & Biophysics, University of

Kalyani, Nadia, West Bengal.

Joint Conveners
Dr. Rakhi Dasgupta &
Dr. Utpal Ghosh

Dean, Faculty of Science
Prof. Rita Ghosh

Vice-chancellor
Prof. Sankar Kumar Ghosh